DISSERTATION

EVALUATING THE EFFECTS OF FIRE ON CARBON AND NITROGEN BIOGEOCHEMISTRY IN FORESTED ECOSYSTEMS

Submitted by

Holly Roth

Department of Chemistry

In partial fulfillment of the requirements

For the Degree of Doctor of Philosophy

Colorado State University

Fort Collins, Colorado

Spring 2023

Doctoral Committee:

Advisor: Thomas Borch

Chuck Henry
Melissa Reynolds
Jessica Prenni
Mike Wilkins

ABSTRACT

EVALUATING THE EFFECTS OF FIRE ON CARBON AND NITROGEN BIOGEOCHEMISTRY IN FORESTED ECOSYSTEMS

Forests provide ecosystem services (e.g., carbon storage, nutrient processing, and water filtration) valued at ~$5 trillion per year which are vulnerable to disturbances such as wildfire. Although fires are a natural component of healthy forests, climate change has begun to increase the size, frequency, and severity of wildfires outside of their historic range. Expected increases in burn severity have implications for carbon (C) and nitrogen (N) cycling, with the potential to shift forests from C sinks to C sources due to long delays in tree re-establishment. There is great interest in resolving changes to soil organic matter (SOM) composition, especially organic nitrogen, to predict how forests respond to wildfires. Therefore, the purpose of the work included in this dissertation was to improve nitrogen analysis in fire-impacted forest systems and apply these methods to soil and water samples. In the following work, a suite of advanced analytical approaches were used to determine the molecular composition of SOM, which was evaluated for the impacts of severe wildfires on microbially-mediated SOM processing and water quality in fire-impacted watersheds. Field-based soil and water samples were collected from subalpine forests in the Colorado Rocky Mountains and investigated for shifts in the water-soluble and solid fractions of SOM in lodgepole pine-dominated forests and their influence on microbial processing and water quality was determined. The objectives of this study were to leverage ultrahigh mass spectrometry to improve N analysis in fire-impacted systems (Objective 1), determine the post-fire changes to

surface water C and N chemistry in reducing conditions (Objective 2) and to characterize how fire severity influences SOM composition along soil burn severity gradients (Objective 3).

Fourier transform ion cyclotron resonance mass spectrometry (FT-ICR MS) currently achieves the highest mass resolving power in the world, which allows for the study of complex mixtures with tens of thousands of compounds that are separated by the mass of an electron across a wide molecular weight range. The most widely used FT-ICR MS analytical approach uses negative-ion mode electrospray ionization (-ESI) to selectively ionize highly abundant carboxylic acids in SOM. The application of this approach has allowed for rigorous analysis of C composition; however, -ESI FT-ICR MS vastly underestimates N-dense species which are formed during combustion. The biases associated with ionization are propagated in chemical property calculations that are determined by elemental compositions and which must be fully understood for proper use in C and N cycling models. We compared traditional -ESI with positive-ion mode electrospray ionization (+ESI) of burned soil extracts and found that +ESI increased compositional coverage by 87%, including nearly 10,000 additional N species (Objective 1).

We applied our +ESI FT-ICR MS findings on a burn severity gradient (low, moderate, and high severity) to evaluate the compositional changes to SOM with increasing severity, with a specific focus on organic nitrogen. We collected soils from burned lodgepole pine forests along the Colorado-Wyoming border from two depths to characterize changes to organic N chemistry. Since organic N is the most abundant form of soil N in conifer forests, a better understanding of post-fire organic N will help address a critical gap in our understanding of fire severity-induced changes in the molecular composition of soil organic nitrogen. Nuclear magnetic resonance spectroscopy and FT-ICR MS analysis showed that N content and aromaticity of water-extractable SOM (0-5 cm depth) increased with burn severity, while minimal changes to the 5-10 cm depth

were observed. Heterocyclic N species are generally higher in toxicity compared to their non-nitrogenated counterparts, which prompted soil toxicity measurements. We used Microtox ® to determine that soil toxicity increased with increasing burn severity, which may be partly attributed to newly formed N-species (Objective 2).

In conjunction with increased fire activity, North American beaver (C. canadensis) populations have steadily increased since the early 1900s. The ponds that beavers create slow or impound hydrologic and elemental fluxes, increase soil saturation, and have a high potential to transform redox active elements (e.g., oxygen, nitrogen, sulfur, and metals). While surface water runoff composition has been studied in many environments, the effects of reducing conditions (i.e., beaver ponds) on these products are not well known. We collected surface water and sediment samples to investigate the impact of beaver ponds on the chemical properties and molecular composition of dissolved forms of C and N, and the microbial functional potential encoded within these environments from a combination of FT-ICR MS and metagenomics. We found that N-containing compounds and aromaticity increased in the surface water of burned beaver ponds, and that C/N and O/C ratios decreased. Microbial communities within the ponds did not have the capacity to process aromatic species, but they did have the potential for anaerobic metabolism and the potential to respire on microbial necromass (Objective 3).

Fires burn heterogeneously across the landscape, and overstory vegetation likely plays a large role both in the way fires burn and how soils recover post-fire. Site factors such as soil type affect the interactions of SOM with abiotic soil components and can have cascading effects on soil C storage, including SOM partitioning between particulate organic matter (POM) and mineral associated organic matter (MAOM). POM is generally considered to have a faster turnover time than MAOM, which is physically protected from microbial degradation. Soil under two common

trees in Colorado (lodgepole pine and aspen) are known to differ in SOM quantity and composition, including their relative proportions of POM and MAOM but post-fire products in these soils are relatively uncharacterized. To determine the differences in post-fire SOM between aspen and pine soils, we collected soils from under aspen and pine stands and burned them in open-air pyrocosms to minimize environmental variables which confound field-based studies. We concluded that fire influenced the dissolved fraction of the soils, with higher concentrations of dissolved organic carbon, dissolved total nitrogen, ammonium-N, and nitrate-N in burned aspen soil extracts. To determine the implications for less bioavailable carbon fractions, we will determine %C and %N in soils that have only been dried and sieved, as well as separated into POM and MAOM. We will also characterize the dissolved fractions using FT-ICR MS and NMR to evaluate differences in soil functional groups. Complementary microbiome analyses will be performed to determine the implications of shifts in soil functionality for microbial processing and C and N sequestration.

The novel application of +ESI in this dissertation allowed for the identification of increasingly N-dense species at high burn severities which were not previously observed in field samples. N-dense species are enriched under reducing conditions as they are unable to be processed by local microbial communities. In total, these findings contribute to our understanding of newly formed organic C and N species in soils, with implications for microbial activity in fire-affected watersheds.

ACKNOWLEDGEMENTS

I am extremely grateful to my advisor, Thomas Borch, who provided me with the help, guidance, and support I needed to grow as a person and a scientist over the last five years. I am lucky to have had a kind and caring advisor who was able to push me outside of my comfort zone while still offering me a great deal of encouragement. You have always been extremely generous with your time, and I've always appreciated that I could come to you for anything.

I am also incredibly grateful to Amy McKenna, whose mentorship has been invaluable to me. I am so appreciative for all the time you spent facilitating all the projects I was involved in and for reassuring me when it all became a bit too much. Thank you for inspiring my curiosity and for being such a fantastic mentor and role model.

I have been lucky to be a part of a lab group which consciously works towards maintaining a great group dynamic. Our research group fostered a welcoming and supportive environment that made our time in and out of work very enjoyable. I am thankful for the thoughtful critiques related to science and the opportunity to grow as a person through all the wonderful people I was surrounded by.

My family has provided me with a massive amount of support while I've been at CSU, and I couldn't be more appreciative of that. I am thankful for my parents, my sisters, and Nate who were always encouraging and listened to all of my stories and complaints, at any time of day. I have always counted myself lucky to be a part of a family that prioritizes each other, now more than ever. I am also thankful for all of my friends who have become my second family and made graduate school a much more enjoyable experience.

Lastly, there are many people who supported this research. I am grateful to Chuck Rhoades

and Tim Fegel, who were always willing to share their expertise and truly took the time to make sure that every product in this dissertation was of the best quality it could be. I am also grateful for Mike Wilkins and Amelia Nelson, whose kindness and generosity made all of our field trips and collaborations a lot of fun. I'd also like to thank Robert Young, who has always been willing to chat and without whom the coding aspects of this dissertation would have taken a lot longer. Finally, I would like to thank all of my other outstanding collaborators who not only contributed to this work but have supported my development as a scientist. This includes Huan Chen, Myrna Simpson, Nivetha Srikanthan, William Bahureksa, and Jacob VanderRoest.

Samples from this work were analyzed at the Rocky Mountain Research Station, the National High Magnetic Field Laboratory, and the University of Toronto. Portions of this work were supported by the NSF Division of Chemistry and Division of Materials Research through DMR-1644779 and the State of Florida. This work was funded through a variety of sources: NSF under grant number 1512670 and 2114868, USDA NIFA through AFRI grant number 2021-6701903-4608, NSF and AFRI grant number 2021-67019-33726, and the Discovery Grant and Tier 1 Canada Research Chair in Integrative Molecular Biogeochemistry through the Natural Sciences and Engineering Research Council of Canada.

TABLE OF CONTENTS

CHAPTER 1: INTRODUCTION

1. FIRES ARE IMPORTANT ECOSYSTEM DISTURBANCES

Wildfires are a natural component of many ecosystems and represent a key ecological driver across the globe.[1] While some ecosystems are adapted to wildfires, their size, frequency, and severity have increased in recent decades,[2–5] with potential negative implications for forest resilience under climate change scenarios.[6] High-elevation forests are particularly vulnerable to changes in fire regime (i.e., typical frequency, intensity, and duration of wildfires in a particular ecosystem),[7] as fires have advanced upslope in the western United States during the last three decades.[8] Forests provide ecosystem services (e.g., terrestrial carbon (C) storage, nutrient processing, water filtration) valued at ~$5 trillion/year.[9,10] Therefore, understanding the effects of wildfires on ecosystem services is critical for the management of present day and future ecosystem conditions.

2. FIRES INFLUENCE SOIL ORGANIC MATTER CHARACTERISTICS

Soils store more C than that in the atmosphere,[11] and thus play an important role in C sequestration.[12] Carbon stored in soils is released through the combustion of plant biomass and soil organic matter (SOM), which produces 56-129 T of pyrogenic C per year.[13] The soil that remains is at increased risk of erosion as organic soil cover is consumed and soil water repellency increases,[14] subsequently resulting in losses of nutrients and C.[15] Both sources (e.g., plant litter) and processing (e.g., microbes) affect SOM composition,[16] and changes to the chemical composition of SOM by wildfire strongly affect its role in the C and nutrient cycles of ecosystems.[17,18] Common changes to soils after fire include increased pH, higher electrical conductivity, and changes to the quantity of total and dissolved C.[19–21] Previous studies have also

shown that fire-induced SOM changes include increased aromatic C and N and shifts in major functional groups.[22–25] Nitrogen (N) is a critical element in SOM which is highly sensitive to heat-induced transformations and is commonly used as a soil and water quality indicator. Organic N comprises ~80% of N in forest soils;[26] however, the impact of fire on organic N is poorly constrained despite its important implications for microbial activity and ecosystem processes.

3. Studying complex Soil Organic Matter requires high-resolution tools

SOM is a highly complex mixture, the polydispersity and polyfunctionality of which presents a large analytical challenge.[27] Fourier transform ion cyclotron resonance mass spectrometry (FT-ICR MS) revolutionized complex mixture analysis due to the high resolution it provides which allows the differentiation of tens of thousands of peaks that differ by as little as the mass of an electron.[28–31] Instrumentation advances over the last two decades have improved the depth of compositional information obtained by FT-ICR MS, which has substantially increased its application for complex mixtures analysis.[32] The development of the 21 tesla FT-ICR MS allowed for 49,000 additional assignments than the 9.4 tesla FT-ICR MS,[33] as increasing the magnetic field results in a linear increase of mass resolving power, among other parameters.[34] While orbitrap mass spectrometry also provides ultrahigh resolving power, the mass resolving power and mass accuracy are ~10x higher for FT-ICR MS than orbitrap MS for ions of $m/z < 2000$, making FT-ICR MS uniquely suited to measure ions with high molecular weight.[35] The high mass accuracy provided by FT-ICR MS results in accurate assignment of elemental compositions to individual molecules[36] and allows improved analysis of composition, distribution, and transformation of SOM.

Conventional FT-ICR MS analyses rely on electrospray ionization, a soft ionization technique which primarily results in the formation of intact molecular ions.[37] Negative-ion mode

ESI (-ESI) is the most common for SOM analyses due to the prevalence of acidic functional groups in organic matter, relatively fast data analysis, and straightforward formula assignments. However, -ESI is highly susceptible to ion suppression as ionization is based on pKa, which generally results in a mass spectrum dominated by species containing carboxylic acids.[38–42] While -ESI is well-suited for the analysis of highly oxygenated CHO species, matrix effects and ion suppression can result in low detection of organic N species, which contain basic functional groups such as pyridines.[43] This can partially be addressed through the use of positive-ion mode electrospray ionization (+ESI), which forms ions based on pKb and can increase the analytical coverage provided by FT-ICR MS. Therefore, I hypothesized that the combination of -ESI and +ESI would improve compositional coverage in mixtures which are expected to contain basic N species, such as wildfire-impacted soils.[44] Results and discussion about improved N analysis in fire-impacted soils by +ESI 21 tesla FT-ICR MS compared to -ESI are presented in Chapter 2.

4. Burn severity is an important driver of SOM chemistry

Changes to modern fire regimes are expected to include increases in burn severity, defined by the degree of consumption of organic soil layers and vegetation.[45,46] Higher wildfire severities can lead to greater tree mortality and higher C emissions due to more complete combustion.[47] There can be considerable variation in the magnitude of impacts to SOM which occur within fires; understanding the heterogeneity derived from variations in burn severity is critical for anticipating the scale of effects under predicted future wildfire severity increases.[48] Burn severity is a primary driver for impacts to duff, mineral soils, and local soil microbiomes, with high fire severities having the greatest influence on SOM composition.[49] In general, heterogeneity in SOM composition increases with fire, partly attributed to the formation of polyaromatic biopolymers.[50] While many studies have evaluated the effects of fire on C composition, fire-induced

transformations to organic N remain poorly understood. To improve our understanding of the effects of burn severity on SOM molecular composition, I used 21 tesla FT-ICR MS to analyze water-extractable SOM from four soils burned at different severities at two depths. I hypothesized that distinct C and N chemical profiles would be formed in response to burn severity, which would yield organic matter with lower lability (i.e., compounds harder to mineralize by bacteria) and more heterocyclic N compounds at higher burn severities. Results and discussion from this study are presented in Chapter 3.

5. Reducing conditions influence surface water speciation and microbiomes

Wildfires can affect hydrological processes that result in enhanced runoff and erosion, which introduces sediment, nutrients, and potential contaminants to surface waters. The magnitude of such changes are determined by many factors (e.g., fire severity, topography, and vegetation),[51–54] as well as postfire storm events and snowmelt.[55–57] Water quality may be impacted for decades after fire, determined by the extent of high-severity wildfire and post-fire vegetation recovery.[58–61] Concurrent to increases in wildfire frequency and severity, North American beaver (*Castor canadensis*) populations have steadily increased since their near eradication in the northern U.S. in the early 1900s.[62] Beaver-generated wetlands can retain sediment and mobilized nutrients, but geochemical conditions may also drive shifts in nutrient processing, particularly N, in wetlands and wetland sediments through decreased oxygen availability. Wetland nutrient availability is important for microbial community composition and activity, which may experience additional stressors from the introduction of fire-impacted organic matter. I hypothesized that fire inputs and anaerobic conditions would influence microbial communities in beaver pond sediments due to higher N concentrations and more aromatic, high molecular weight organic matter. Results and discussion from this study are presented in Chapter 4.

6. SOM COMPOSITION IS HIGHLY DEPENDENT ON FIRE BEHAVIOR AND LITTER TYPE

The effects of wildfires are highly heterogeneous across the landscape due to a variety of factors (i.e., fuel load, soil moisture, vegetation).[63–67] Vegetation is important as one of the soil forming factors[68] and in turn influences variables that control burn characteristics at a specific location.[69–71] Forests in Colorado are primarily comprised of pine, spruce, fir, and aspen, representing a mix of coniferous and deciduous trees,[72–74] thus, investigating the differences in burned pine and aspen soils will help us to constrain our understanding of the heterogeneity of burns in Colorado. Soils associated with aspen stands are known to have higher C and nutrient stocks than those under conifer forests[75,76] and are typically characterized by lower C:N ratios and more mineral-associated organic matter.[77–80] Therefore, fire is expected to have different impact on soils under coniferous and deciduous trees. I hypothesized that higher mineral-associated organic matter in aspen soils would help shield its organic matter from fire and protect the C in aspen soils from combustion and heat-induced transformations. Preliminary results and discussion from this study are presented in Appendix A.

7. PUBLICATIONS AND PRESENTATIONS

This dissertation explores the development of analytical methodology for analyzing fire-impacted organic nitrogen (Chapter 2) and the effects of fire on dissolved organic matter composition in field settings (Chapters 3, 4). Most of this dissertation work is either submitted to or already published in peer-reviewed journals. Chapter 2 (Roth et al., 2022a) was published in *Analytical Chemistry*.[44] Chapter 3 (Roth et al.) was submitted to *Soil and Environmental Health* in February 2023. Chapter 4 (Roth et al., 2022b) was published in *Environmental Science: Processes & Impacts*.[81] Appendix A is in preparation to be submitted to *Environmental Science & Technology*.

My collaborations with other researchers involved two coauthored publications (Appendices E and F). First, the work in Appendix E "PFAS Analysis with Ultrahigh Resolution 21T FT-ICR MS: Suspect and Nontargeted Screening with Unrivaled Mass Resolving Power and Accuracy" was published in *Environmental Science & Technology* (Young et al., 2022).[82] Second, the work in Appendix F "Wildfire-dependent changes in soil microbiome diversity and function" was published in *Nature Microbiology* (Nelson et al., 2022).[83] Additionally, an invited review on the impacts of wildfire on human and ecosystem health entitled "Vegetation fire impacts on molecular soil biogeochemistry" is in preparation to be submitted to *Nature Reviews Earth & Environment*, for which I am a coauthor. An additional coauthored work studying the impact of pyrolysis temperature on photodegradation and toxicity of wheatgrass biochar entitled "Impact of Temperature on Wheat Straw Biochar Production on Photodegradation, Toxicity, and Surface Morphology" is in preparation for submission to *Biochar*. I am also a co-author on a paper investigating the short-term impacts of precipitation and burn extent on water chemistry and dissolved organic matter in fire-affected watersheds entitled "Impacts of Seasonal Storm on Stream Water Chemistry following the Cameron Peak Fire: Disinfection Byproduct Precursors Decrease During Storm", in preparation to be submitted to *Environmental Science & Technology*. A coauthored manuscript evaluating the effects of low and moderate wildfire severities over a 10-year chronosequence entitled "Distinct fungal and bacterial responses to fire severity and soil depth across a ten-year wildfire chronosequence in beetle-killed lodgepole pine forests" is in review for *Forest Ecology and Management*. Finally, a coauthored manuscript is in preparation studying the effects of pile burning on soil microbiomes over a 60-year chronosequence. According to CRediT criteria, my roles in these coauthored papers include Conceptualization, Data curation, Investigation, Methodology, and Writing – review and editing.

Parts of this research have also been presented at several conferences including American Chemical Society conferences (Roth et al., 2021a, Roth et al., 2021b) and the American Geophysical Union conference (Roth et al., 2021). I also served as a co-organizer and moderator for a session at the Soil Science Societies of America 2022 annual meeting entitled “Fire Induced Soil Transformations: Impacts on Human & Ecosystem Health”, for which I also prepared a talk (Roth et al., 2022). My publication record and commitment to outreach allowed me to be selected for the School of Global Environmental Sustainability 2021-2022 Sustainable Leadership Fellows program and as a 2023 Graduate Student Awardee in Environmental Chemistry through the Division of Environmental Chemistry of the American Chemical Society.

REFERENCES

(1) Bond, W. J.; Keeley, J. E. Fire as a Global "Herbivore": The Ecology and Evolution of Flammable Ecosystems. *Trends in Ecology and Evolution*. July 2005, pp 387–394. https://doi.org/10.1016/j.tree.2005.04.025.
(2) Westerling, A. L. R. Increasing Western US Forest Wildfire Activity: Sensitivity to Changes in the Timing of Spring. *Philosophical Transactions of the Royal Society B: Biological Sciences* **2016**, *371* (1696). https://doi.org/10.1098/rstb.2015.0178.
(3) Westerling, A. L.; Hidalgo, H. G.; Cayan, D. R.; Swetnam, T. W. Warming and Earlier Spring Increase Western U.S. Forest Wildfire Activity. *Science (1979)* **2006**, *313* (5789), 940–943. https://doi.org/10.1126/science.1128834.
(4) Keyser, A. R.; Westerling, A. L. R. Predicting Increasing High Severity Area Burned for Three Forested Regions in the Western United States Using Extreme Value Theory. *For Ecol Manage* **2019**, *432* (October 2018), 694–706. https://doi.org/10.1016/j.foreco.2018.09.027.
(5) Flannigan, M.; Cantin, A. S.; de Groot, W. J.; Wotton, M.; Newbery, A.; Gowman, L. M. Global Wildland Fire Season Severity in the 21st Century. *For Ecol Manage* **2013**, *294*, 54–61. https://doi.org/10.1016/j.foreco.2012.10.022.
(6) Stevens-Rumann, C. S.; Kemp, K. B.; Higuera, P. E.; Harvey, B. J.; Rother, M. T.; Donato, D. C.; Morgan, P.; Veblen, T. T. Evidence for Declining Forest Resilience to Wildfires under Climate Change. *Ecol Lett* **2018**, *21* (2), 243–252. https://doi.org/10.1111/ele.12889.
(7) Heinselman, M. L. Fire and Succession in the Conifer Forests of Northern North America. In *Forest Succession: Concepts and Application*; West, D. C., Shugart, H. H., Botkin, D. B., Eds.; Springer-Verlag New York, Inc.: New York, New York, 1981; pp 374–405.
(8) Alizadeh, M. R.; Abatzoglou, J. T.; Luce, C. H.; Adamowski, J. F.; Farid, A.; Sadegh, M. Warming Enabled Upslope Advance in Western US Forest Fires. *PNAS* **2021**, *118*. https://doi.org/10.1073/pnas.2009717118/-/DCSupplemental.
(9) de Groot, R.; D'Arge, R.; Sutton, P.; Grasso, M.; Limburg, K.; Farber, S.; Raskin, R.; van den Belt, M.; Costanza, R.; Hannon, B.; Paruelo, J.; O'Neill, R.; Naeem, S. The Value of the the World's Ecosystem Services and Natural Capital. *Nature* **2003**, No. 387, 253–260.
(10) Costanza, R.; de Groot, R.; Sutton, P.; van der Ploeg, S.; Anderson, S. J.; Kubiszewski, I.; Farber, S.; Turner, R. K. Changes in the Global Value of Ecosystem Services. *Global Environmental Change* **2014**, *26* (1), 152–158. https://doi.org/10.1016/j.gloenvcha.2014.04.002.
(11) Wardle, D. A.; Walker, L. R.; Bardgett, R. D. Ecosystem Properties and Forest Decline in Contrasting Long-Term Chronosequences. *Science (1979)* **2004**, *305* (5683), 509–513. https://doi.org/10.1126/science.1098778.
(12) Lal, R. Forest Soils and Carbon Sequestration. *For Ecol Manage* **2005**, *220* (1–3), 242–258. https://doi.org/10.1016/j.foreco.2005.08.015.
(13) Bird, M. I.; Wynn, J. G.; Saiz, G.; Wurster, C. M.; McBeath, A. The Pyrogenic Carbon Cycle. *Annu Rev Earth Planet Sci* **2015**, *43*, 273–298. https://doi.org/10.1146/annurev-earth-060614-105038.
(14) Doerr, S. H.; Woods, S. W.; Martin, D. A.; Casimiro, M. "Natural Background" Soil Water Repellency in Conifer Forests of the North-Western USA: Its Prediction and Relationship to Wildfire Occurrence. *J Hydrol (Amst)* **2009**, *371* (1–4), 12–21. https://doi.org/10.1016/j.jhydrol.2009.03.011.

(15) Hill, B. H.; Kolka, R. K.; McCormick, F. H.; Starry, M. A. A Synoptic Survey of Ecosystem Services from Headwater Catchments in the United States. *Ecosyst Serv* **2014**, *7*, 106–115. https://doi.org/10.1016/j.ecoser.2013.12.004.
(16) Bolan, N. S.; Adriano, D. C.; Kunhikrishnan, A.; James, T.; McDowell, R.; Senesi, N. *Dissolved Organic Matter. Biogeochemistry, Dynamics, and Environmental Significance in Soils.*; 2011; Vol. 110. https://doi.org/10.1016/B978-0-12-385531-2.00001-3.
(17) Kaiser, K.; Kalbitz, K. Cycling Downwards - Dissolved Organic Matter in Soils. *Soil Biol Biochem* **2012**, *52*, 29–32. https://doi.org/10.1016/j.soilbio.2012.04.002.
(18) Stubbins, A.; Silva, L. M.; Dittmar, T.; van Stan, J. T. Molecular and Optical Properties of Tree-Derived Dissolved Organic Matter in Throughfall and Stemflow from Live Oaks and Eastern Red Cedar. *Front Earth Sci (Lausanne)* **2017**, *5*. https://doi.org/10.3389/feart.2017.00022.
(19) Kong, J.; Xiang, X.; Yang, J. Wildfire Alters the Linkage between Total and Available Soil C:N:P Ratios and the Stoichiometric Effects on Fine Root Growth in a Chinese Boreal Larch Forest. *Plant Soil* **2021**. https://doi.org/10.1007/s11104-021-05215-1.
(20) Certini, G. Effects of Fire on Properties of Forest Soils: A Review. *Oecologia* **2005**, *143* (1), 1–10. https://doi.org/10.1007/s00442-004-1788-8.
(21) Knicker, H.; Hilscher, A.; González-Vila, F. J.; Almendros, G. A New Conceptual Model for the Structural Properties of Char Produced during Vegetation Fires. *Org Geochem* **2008**, *39* (8), 935–939. https://doi.org/10.1016/j.orggeochem.2008.03.021.
(22) Alcañiz, M.; Outeiro, L.; Francos, M.; Úbeda, X. Effects of Prescribed Fires on Soil Properties: A Review. *Science of the Total Environment* **2018**, *613–614*, 944–957. https://doi.org/10.1016/j.scitotenv.2017.09.144.
(23) Agbeshie, A. A.; Abugre, S.; Atta-Darkwa, T.; Awuah, R. A Review of the Effects of Forest Fire on Soil Properties. *Journal of Forestry Research*. Northeast Forestry University 2022. https://doi.org/10.1007/s11676-022-01475-4.
(24) Coppola, A. I.; Wagner, S.; Lennartz, S. T.; Seidel, M.; Ward, N. D.; Dittmar, T.; Santín, C.; Jones, M. W. The Black Carbon Cycle and Its Role in the Earth System. *Nature Reviews Earth and Environment*. Springer Nature August 1, 2022, pp 516–532. https://doi.org/10.1038/s43017-022-00316-6.
(25) Pellegrini, A. F. A.; Harden, J.; Georgiou, K.; Hemes, K. S.; Malhotra, A.; Nolan, C. J.; Jackson, R. B. Fire Effects on the Persistence of Soil Organic Matter and Long-Term Carbon Storage. *Nature Geoscience*. Nature Research January 1, 2022, pp 5–13. https://doi.org/10.1038/s41561-021-00867-1.
(26) Smolander, A.; Kitunen, V.; Mälkönen, E.; Smolander, A.; Kitunen, V.; Mälkönen, E. *Dissolved Soil Organic Nitrogen and Carbon in a Norway Spruce Stand and an Adjacent Clear-Cut*; Springer-Verlag, 2001; Vol. 33.
(27) Bahureksa, W.; Tfaily, M. M.; Boiteau, R. M.; Young, R. B.; Logan, M. N.; McKenna, A. M.; Borch, T. Soil Organic Matter Characterization by Fourier Transform Ion Cyclotron Resonance Mass Spectrometry (FTICR MS): A Critical Review of Sample Preparation, Analysis, and Data Interpretation. *Environmental Science and Technology*. American Chemical Society July 20, 2021, pp 9637–9656. https://doi.org/10.1021/acs.est.1c01135.
(28) Emmett, M. R.; White, F. M.; Hendrickson, C. L.; Shi, D. H.; Marshall, A. G. Application of Micro-Electrospray Liquid Chromatography Techniques to FT-ICR MS to Enable High-Sensitivity Biological Analysis. *J Am Soc Mass Spectrom* **1998**, *9* (4), 333–340. https://doi.org/10.1016/S1044-0305(97)00287-0.

(29) Stubbins, A.; Spencer, R. G. M.; Chen, H.; Hatcher, P. G.; Mopper, K.; Hernes, P. J.; Mwamba, V. L.; Mangangu, A. M.; Wabakanghanzi, J. N.; Six, J. Illuminated Darkness: Molecular Signatures of Congo River Dissolved Organic Matter and Its Photochemical Alteration as Revealed by Ultrahigh Precision Mass Spectrometry. *Limnol Oceanogr* **2010**, *55* (4), 1467–1477. https://doi.org/10.4319/lo.2010.55.4.1467.
(30) Kujawinski, E. B.; del Vecchio, R.; Blough, N. v.; Klein, G. C.; Marshall, A. G. Probing Molecular-Level Transformations of Dissolved Organic Matter: Insights on Photochemical Degradation and Protozoan Modification of DOM from Electrospray Ionization Fourier Transform Ion Cyclotron Resonance Mass Spectrometry. In *Marine Chemistry*; 2004; Vol. 92, pp 23–37. https://doi.org/10.1016/j.marchem.2004.06.038.
(31) Dittmar, T.; Koch, B. P. Thermogenic Organic Matter Dissolved in the Abyssal Ocean. *Mar Chem* **2006**, *102* (3–4), 208–217. https://doi.org/10.1016/j.marchem.2006.04.003.
(32) Hendrickson, C. L.; Quinn, J. P.; Kaiser, N. K.; Smith, D. F.; Blakney, G. T.; Chen, T.; Marshall, A. G.; Weisbrod, C. R.; Beu, S. C. 21 Tesla Fourier Transform Ion Cyclotron Resonance Mass Spectrometer: A National Resource for Ultrahigh Resolution Mass Analysis. *J Am Soc Mass Spectrom* **2015**, *26* (9), 1626–1632. https://doi.org/10.1007/s13361-015-1182-2.
(33) Banerjee, S.; Mazumdar, S. Electrospray Ionization Mass Spectrometry: A Technique to Access the Information beyond the Molecular Weight of the Analyte. *Int J Anal Chem* **2012**, *2012*, 1–40. https://doi.org/10.1155/2012/282574.
(34) Ohno, T.; Sleighter, R. L.; Hatcher, P. G. Comparative Study of Organic Matter Chemical Characterization Using Negative and Positive Mode Electrospray Ionization Ultrahigh-Resolution Mass Spectrometry. *Anal Bioanal Chem* **2016**, *408* (10), 2497–2504. https://doi.org/10.1007/s00216-016-9346-x.
(35) Kruve, A.; Kaupmees, K.; Liigand, J.; Leito, I. Negative Electrospray Ionization via Deprotonation: Predicting the Ionization Efficiency. *Anal Chem* **2014**, *86* (10), 4822–4830. https://doi.org/10.1021/ac404066v.
(36) Hertzog, J.; Carré, V.; le Brech, Y.; Mackay, C. L.; Dufour, A.; Mašek, O.; Aubriet, F. Combination of Electrospray Ionization, Atmospheric Pressure Photoionization and Laser Desorption Ionization Fourier Transform Ion Cyclotronic Resonance Mass Spectrometry for the Investigation of Complex Mixtures – Application to the Petroleomic Analysis . *Anal Chim Acta* **2017**, *969*, 26–34. https://doi.org/10.1016/j.aca.2017.03.022.
(37) Fenn, J. B.; Mann, M.; Meng, C. K.; Wong, S. F.; Whitehouse, C. M. ELECTROSPRAY IONIZATION - PRINCIPLES AND PRACTICE. *Mass Spectrom Rev* **1990**, *9* (1), 37–70.
(38) Oss, M.; Kruve, A.; Herodes, K.; Leito, I. Electrospray Ionization Efficiency Scale of Organic Compound. *Anal Chem* **2010**, *82* (7), 2865–2872. https://doi.org/10.1021/ac902856t.
(39) Torres-Rojas, D.; Hestrin, R.; Solomon, D.; Gillespie, A. W.; Dynes, J. J.; Regier, T. Z.; Lehmann, J. Nitrogen Speciation and Transformations in Fire-Derived Organic Matter. *Geochim Cosmochim Acta* **2020**, *276*, 170–185. https://doi.org/10.1016/j.gca.2020.02.034.
(40) Roth, H. K.; Borch, T.; Young, R. B.; Bahureksa, W.; Blakney, G. T.; Nelson, A. R.; Wilkins, M. J.; McKenna, A. M. Enhanced Speciation of Pyrogenic Organic Matter from Wildfires Enabled by 21 T FT-ICR Mass Spectrometry. *Anal Chem* **2022**, *94* (6), 2973–2980. https://doi.org/10.1021/acs.analchem.1c05018.
(41) Keeley, J. E. Fire Intensity, Fire Severity and Burn Severity: A Brief Review and Suggested Usage. *Int J Wildland Fire* **2009**, *18* (1), 116–126. https://doi.org/10.1071/WF07049.
(42) Parsons, A.; Robichaud, P. R.; Lewis, S. A.; Napper, C.; Clark, J. T. Field Guide for Mapping Post-Fire Soil Burn Severity. *General Technical Report RMRS-GTR-243* **2010**.

(43) Ghimire, B.; Williams, C. A.; Collatz, G. J.; Vanderhoof, M. Fire-Induced Carbon Emissions and Regrowth Uptake in Western U.S. Forests: Documenting Variation across Forest Types, Fire Severity, and Climate Regions. *J Geophys Res Biogeosci* **2012**, *117* (3). https://doi.org/10.1029/2011JG001935.
(44) Miesel, J. R.; Hockaday, W. C.; Kolka, R. K.; Townsend, P. A. Soil Organic Matter Composition and Quality across Fire Severity Gradients in Coniferous and Deciduous Forests of the Southern Boreal Region. *Journal of Geophysical Research G: Biogeosciences* **2015**, *120* (6), 1124–1141. https://doi.org/10.1002/2015JG002959.
(45) Miesel, J.; Reiner, A.; Ewell, C.; Maestrini, B.; Dickinson, M. Quantifying Changes in Total and Pyrogenic Carbon Stocks across Fire Severity Gradients Using Active Wildfire Incidents. *Front Earth Sci (Lausanne)* **2018**, *6*. https://doi.org/10.3389/feart.2018.00041.
(46) Knicker, H. How Does Fire Affect the Nature and Stability of Soil Organic Nitrogen and Carbon? A Review. *Biogeochemistry* **2007**, *85* (1), 91–118. https://doi.org/10.1007/s10533-007-9104-4.
(47) Abney, R. B.; Berhe, A. A. Pyrogenic Carbon Erosion: Implications for Stock and Persistence of Pyrogenic Carbon in Soil. *Frontiers in Earth Science*. Frontiers Media S.A. March 20, 2018. https://doi.org/10.3389/feart.2018.00026.
(48) Moody, J. A.; Shakesby, R. A.; Robichaud, P. R.; Cannon, S. H.; Martin, D. A. Current Research Issues Related to Post-Wildfire Runoff and Erosion Processes. *Earth Sci Rev* **2013**, *122*, 10–37. https://doi.org/10.1016/j.earscirev.2013.03.004.
(49) Abney, R. B.; Kuhn, T. J.; Chow, A.; Hockaday, W.; Fogel, M. L.; Berhe, A. A. Pyrogenic Carbon Erosion after the Rim Fire, Yosemite National Park: The Role of Burn Severity and Slope. *J Geophys Res Biogeosci* **2019**, *124* (2), 432–449. https://doi.org/10.1029/2018JG004787.
(50) Pierson, D. N.; Robichaud, P. R.; Rhoades, C. C.; Brown, R. E. Soil Carbon and Nitrogen Eroded after Severe Wildfire and Erosion Mitigation Treatments. *Int J Wildland Fire* **2019**, *28* (10), 814–821. https://doi.org/10.1071/WF18193.
(51) Moody, J. A.; Martin, D. A. Post-Fire, Rainfall Intensity-Peak Discharge Relations for Three Mountainous Watersheds in the Western USA. *Hydrol Process* **2001**, *15* (15), 2981–2993. https://doi.org/10.1002/hyp.386.
(52) Murphy, S. F.; Writer, J. H.; McCleskey, R. B.; Martin, D. A. The Role of Precipitation Type, Intensity, and Spatial Distribution in Source Water Quality after Wildfire. *Environmental Research Letters* **2015**, *10* (8). https://doi.org/10.1088/1748-9326/11/7/079501.
(53) Ebel, B. A.; Hinckley, E. S.; Martin, D. A. Soil-Water Dynamics and Unsaturated Storage during Snowmelt Following Wildfire. *Hydrol Earth Syst Sci* **2012**, *16* (5), 1401–1417. https://doi.org/10.5194/hess-16-1401-2012.
(54) Rust, A. J.; Saxe, S.; McCray, J.; Rhoades, C. C.; Hogue, T. S. Evaluating the Factors Responsible for Post-Fire Water Quality Response in Forests of the Western USA. *Int J Wildland Fire* **2019**, *28* (10), 769–784. https://doi.org/10.1071/WF18191.
(55) Rhoades, C. C.; Chow, A. T.; Covino, T. P.; Fegel, T. S.; Pierson, D. N.; Rhea, A. E. The Legacy of a Severe Wildfire on Stream Nitrogen and Carbon in Headwater Catchments. *Ecosystems* **2018**. https://doi.org/10.1007/s10021-018-0293-6.
(56) Malone, S. L.; Fornwalt, P. J.; Battaglia, M. A.; Chambers, M. E.; Iniguez, J. M.; Sieg, C. H. Mixed-Severity Fire Fosters Heterogeneous Spatial Patterns of Conifer Regeneration in a Dry Conifer Forest. *Forests* **2018**, *9* (1). https://doi.org/10.3390/f9010045.

(57) Chambers, M. E.; Fornwalt, P. J.; Malone, S. L.; Battaglia, M. A. Patterns of Conifer Regeneration Following High Severity Wildfire in Ponderosa Pine – Dominated Forests of the Colorado Front Range. *For Ecol Manage* **2016**, *378*, 57–67. https://doi.org/10.1016/j.foreco.2016.07.001.
(58) Naiman, R. J.; Johnston, C. A.; Kelley, J. C. Alteration of North American Streams by Beaver. *Bioscience* **1988**, *38* (11), 753–762. https://doi.org/10.2307/1310784.
(59) Santín, C.; Doerr, S. H.; Kane, E. S.; Masiello, C. A.; Ohlson, M.; de la Rosa, J. M.; Preston, C. M.; Dittmar, T. Towards a Global Assessment of Pyrogenic Carbon from Vegetation Fires. *Glob Chang Biol* **2016**, *22* (1), 76–91. https://doi.org/10.1111/gcb.12985.
(60) Hanan, E. J.; Kennedy, M. C.; Ren, J.; Johnson, M. C.; Smith, A. M. S. Missing Climate Feedbacks in Fire Models: Limitations and Uncertainties in Fuel Loadings and the Role of Decomposition in Fine Fuel Accumulation. *Journal of Advances in Modeling Earth Systems*. John Wiley and Sons Inc March 1, 2022. https://doi.org/10.1029/2021MS002818.
(61) SCHOENNAGEL, T.; VEBLEN, T. T.; ROMME, W. H. The Interaction of Fire, Fuels, and Climate across Rocky Mountain Forests. *Bioscience* **2004**, *54* (7), 661. https://doi.org/10.1641/0006-3568(2004)054[0661:TIOFFA]2.0.CO;2.
(62) Larson, A. J.; Churchill, D. Tree Spatial Patterns in Fire-Frequent Forests of Western North America, Including Mechanisms of Pattern Formation and Implications for Designing Fuel Reduction and Restoration Treatments. *Forest Ecology and Management*. March 1, 2012, pp 74–92. https://doi.org/10.1016/j.foreco.2011.11.038.
(63) Czimczik, C. I.; Masiello, C. A. Controls on Black Carbon Storage in Soils. *Global Biogeochem Cycles* **2007**, *21* (3), 1–8. https://doi.org/10.1029/2006GB002798.
(64) Jenny, hans. *Factors of Soil Formation*; Dover Publications Inc: New York, NY, 1994.
(65) Stephens, S. L.; Burrows, N.; Buyantuyev, A.; Gray, R. W.; Keane, R. E.; Kubian, R.; Liu, S.; Seijo, F.; Shu, L.; Tolhurst, K. G.; van Wagtendonk, J. W. Temperate and Boreal Forest Mega-Fires: Characteristics and Challenges. *Frontiers in Ecology and the Environment*. Ecological Society of America 2014, pp 115–122. https://doi.org/10.1890/120332.
(66) Jenkins, M. J.; Hebertson, E.; Page, W.; Jorgensen, C. A. Bark Beetles, Fuels, Fires and Implications for Forest Management in the Intermountain West. *For Ecol Manage* **2008**, *254* (1), 16–34. https://doi.org/10.1016/j.foreco.2007.09.045.
(67) Chen, H.; Wang, J.-J.; Ku, P.-J.; Tsui, M. T.-K.; Abney, R. B.; Berhe, A. A.; Zhang, Q.; Burton, S. D.; Dahlgren, R. A.; Chow, A. T. Burn Intensity Drives the Alteration of Phenolic Lignin to (Poly) Aromatic Hydrocarbons as Revealed by Pyrolysis Gas Chromatography–Mass Spectrometry (Py-GC/MS). *Environ Sci Technol* **2022**. https://doi.org/10.1021/acs.est.2c00426.
(68) Fall, P. L. Fire History and Composition of the Subalpine Forest of Western Colorado during the Holocene. *J Biogeogr* **1997**, *24* (3), 309–325. https://doi.org/10.1046/j.1365-2699.1997.00094.x.
(69) Diskin, M.; Rocca, M. E.; Nelson, K. N.; Aoki, C. F.; Romme, W. H. Forest Developmental Trajectories in Mountain Pine Beetle Disturbed Forests of Rocky Mountain National Park, Colorado. *Canadian Journal of Forest Research* **2011**, *41* (4), 782–792. https://doi.org/10.1139/x10-247.
(70) Chai, R. K.; Andrus, R. A.; Rodman, K.; Harvey, B. J.; Veblen, T. T. Stand Dynamics and Topographic Setting Influence Changes in Live Tree Biomass over a 34-Year Permanent Plot Record in a Subalpine Forest in the Colorado Front Range. *Canadian Journal of Forest Research* **2019**, *49* (10), 1256–1264. https://doi.org/10.1139/cjfr-2019-0023.

(71) Vesterdal, L.; Clarke, N.; Sigurdsson, B. D.; Gundersen, P. Do Tree Species Influence Soil Carbon Stocks in Temperate and Boreal Forests? *For Ecol Manage* **2013**, *309*, 4–18. https://doi.org/10.1016/j.foreco.2013.01.017.
(72) Jandl, R.; Ledermann, T.; Kindermann, G.; Weiss, P. Soil Organic Carbon Stocks in Mixed-Deciduous and Coniferous Forests in Austria. *Frontiers in Forests and Global Change* **2021**, *4*. https://doi.org/10.3389/ffgc.2021.688851.
(73) Quigley, K. M.; Kolka, R.; Sturtevant, B. R.; Dickinson, M. B.; Kern, C. C.; Donner, D. M.; Miesel, J. R. Prescribed Burn Frequency, Vegetation Cover, and Management Legacies Influence Soil Fertility: Implications for Restoration of Imperiled Pine Barrens Habitat. *For Ecol Manage* **2020**, *470–471*. https://doi.org/10.1016/j.foreco.2020.118163.
(74) Woldeselassie, M.; van Miegroet, H.; Gruselle, M.-C.; Hambly, N. Storage and Stability of Soil Organic Carbon in Aspen and Conifer Forest Soils of Northern Utah. *Soil Science Society of America Journal* **2012**, *76* (6), 2230–2240. https://doi.org/10.2136/sssaj2011.0364.
(75) Boča, A.; Miegroet, H. van. Can Carbon Fluxes Explain Differences in Soil Organic Carbon Storage under Aspen and Conifer Forest Overstories? *Forests* **2017**, *8* (4). https://doi.org/10.3390/f8040118.
(76) Dobarco, M. R.; van Miegroet, H. Soil Organic Carbon Storage and Stability in the Aspen-Conifer Ecotone in Montane Forests in Utah, USA. *Forests* **2014**, *5* (4), 666–688. https://doi.org/10.3390/f5040666.
(77) Roth, H. K.; Nelson, A. R.; McKenna, A. M.; Fegel, T. S.; Young, R. B.; Rhoades, C. C.; Wilkins, M. J.; Borch, T. Impact of Beaver Ponds on Biogeochemistry of Organic Carbon and Nitrogen along a Fire-Impacted Stream. *Environ Sci Process Impacts* **2022**, *24* (10), 1661–1677. https://doi.org/10.1039/D2EM00184E.
(78) Young, R. B.; Pica, N. E.; Sharifan, H.; Chen, H.; Roth, H. K.; Blakney, G. T.; Borch, T.; Higgins, C. P.; Kornuc, J. J.; McKenna, A. M.; Blotevogel, J. PFAS Analysis with Ultrahigh Resolution 21T FT-ICR MS: Suspect and Nontargeted Screening with Unrivaled Mass Resolving Power and Accuracy. *Environ Sci Technol* **2022**, acs.est.1c08143. https://doi.org/10.1021/acs.est.1c08143.
(79) Nelson, A. R.; Narrowe, A. B.; Rhoades, C. C.; Fegel, T. S.; Daly, R. A.; Roth, H. K.; Chu, R. K.; Amundson, K. K.; Young, R. B.; Steindorff, A. S.; Mondo, S. J.; Grigoriev, I. v.; Salamov, A.; Borch, T.; Wilkins, M. J. Wildfire-Dependent Changes in Soil Microbiome Diversity and Function. *Nat Microbiol* **2022**. https://doi.org/10.1038/s41564-022-01203-y.

CHAPTER 2: ENHANCED SPECIATION OF PYROGENIC ORGANIC MATTER FROM WILDFIRES ENABLED BY 21 T FT-ICR MASS SPECTROMETRY[1]

1. INTRODUCTION

Forests provide a myriad of ecosystem services, including the storage of ~30-40% of terrestrial carbon (C),[1] but are highly susceptible to ecosystem disturbances such as wildfires, which dramatically change foliage and landscape, and produce 256 Tg of pyrogenic C per year.[2] Although fires occur naturally across many ecosystems,[3] wildfire size, frequency, and severity in has substantially increased in recent decades in forested systems.[4,5] Incomplete combustion of soil organic matter (SOM) during wildfire forms by-products (e.g., char and soot)[6] that can impact the quantity and quality of soil C and nitrogen (N).[7,8] Pyrogenic organic matter (pyOM) exists as a continuum that spans macroscopic (i.e., char and soot) to microscopic scales (i.e., condensed polycyclic aromatic molecules)[6] across a range of physical and chemical properties. The composition of pyOM is determined by the type and amount of biomass, and burn conditions (e.g., intensity, moisture, fuel density).[9,10] Collectively, pyOM is characterized by increased hydrophobicity, lower C:N ratios, coarser soil textures, increased pH and higher electrical conductivity compared to non-fire impacted soil.[9,11]

Nitrogen is an essential and often limiting nutrient,[12,13] and inherent heating and post-fire ecosystem dynamics change N lability and bioavailability.[14,15] In unburned or low temperature-impacted soils, nitrogen is in the form of slightly acidic compounds (e.g., pyrrole, a ring structure composed of four carbon atoms and one nitrogen atom). As temperature increases, pyridinic

[1] Reproduced with permissions from Roth, H., Borch, T., Young, R., Bahureksa, W., Blakney, G., Nelson, A., Wilkins, M., McKenna, A. Enhanced Speciation of Pyrogenic Organic Matter from Wildfires Enabled by 21 T FT-ICR Mass Spectrometry. Analytical Chemistry 2022, 94(6): 2973-2980. Copyright 2022, American Chemical Society.

structures (aromatic, basic functional groups) have been reported.[16] Although many studies focus on the connection between pyOM persistence and C composition,[16] there are limited reports on the connection between N composition and pyOM mineralization in fire-impacted soil.

The compositional complexity, polydispersity, and polyfunctionality of complex organic mixtures (SOM, pyOM, dissolved organic matter) challenges all analytical techniques. Fourier transform ion cyclotron resonance mass spectrometry (FT-ICR MS) routinely achieves resolving power sufficient to identify species that differ in mass by less than the mass of an electron, prevalent in natural organic matter (NOM).[17–20] The most widely used FT-ICR MS analytical approach for SOM combines solid-phase extraction (SPE) to enrich SOM from aqueous samples and negative-ion electrospray ionization (-ESI) to selectively ionize highly abundant carboxylic acids in SOM.[21] However, studies that compare analyte selectivity in different ionization modes for pyOM remain limited.[22,23]

The first step in all mass spectral techniques is ionization to yield pseudo-molecular ions and is selected based on the analyte of interest. Negative ion electrospray (-ESI) yields deprotonated molecular ions based on the ionization efficiency of acidic functional groups.[22,24,25] In -ESI, stronger acids are efficiently ionized,[22] and the most abundant peaks correspond to low pK_a carboxylic acids (see **Table B1** for pKa's of common soil functional groups), and phenolic groups formed as lignin degradation products.[26] Negative ESI is also sensitive to chemical contamination (i.e., linear alkylbenzene surfactants), which cause suppression of analyte ions and result in a mass spectrum dominated by chemical noise.[27] Ionization in -ESI is primarily dominated by low molecular weight carboxylic acids, and basic species and those with lower acidity can be detected by positive-ion ESI (+ESI). The pK_b distribution of basic functional groups in pyOM (e.g., pyridines and amides) results in less ion suppression due to more equal charge competition.

Each ionization mode selectively ionizes a subset of species in a single SOM sample,[28] and no one soft ionization technique can equally access all of the compositional window of SOM species. Ohno et. al. benchmarked the field by comparing +/- ESI for unburned SOM and reported that the combination of elemental compositions from both modes increased the number of assignments by 43% compared to -ESI alone.[21] In addition, while other studies compare +/-ESI composition for soil- or water-derived SOM and refinery wastewater,[21,29–31] this study focuses on detailed characterization of pyOM, an understudied system in the field.

The improved resolving power, high dynamic range, and increased sensitivity of the 21 T FT-ICR MS system identifies previously unresolved mass differences in $C_cH_hN_nO_oS_s$ formulas within pyOM at high mass ranges (> *m/*z 750).[32,33] The combination of high magnetic field, unique custom hardware, internal mass calibration, absorption mode data processing available on the custom-built 21 T FT-ICR mass spectrometer achieves high resolving power ($m/\Delta m_{50\%}$ = 2,000,000 at *m/z* 200), sub-ppm mass accuracy (20-80 ppb), and high dynamic range that allows assignment of more than 30,000 species in a single mass spectrum.[32] Here, we leverage the 21 T FT-ICR MS to illuminate the unique compositional window detected by +ESI, compare the same speciation to -ESI, and expand the compositional window of wildfire-impacted SOM. This is the first study to probe the molecular complexity of pyOM in positive ion mode with 21 T FT-ICR mass spectrometry. We identify species that remain unresolved and thus undetected by lower resolution mass spectrometers and highlight the minimal resolving power requirements necessary to accurately assign elemental compositions. For the first time, more than 35,000 species are assigned at 30 ppb RMS error by +ESI 21 T FT-ICR MS, a new record for pyOM characterization.

2. Materials and Methods

2.1 Soil Sampling and Preparation

Soil was sampled in a lodgepole pine (*Pinus contorta*)-dominated region of the Medicine Bow National Forest which burned in the 2018 Ryan fire. A high severity burned site was identified according to the amount of organic matter cover (<20%) and sampled from the organic horizon approximately one year after the fire's containment (additional information: Nelson, *et. al*. 2021 (Sample # R89).[34] All solvents were HPLC grade, purchased from Sigma-Aldrich Chemical Co., St. Louis, MO, USA. Soil samples were weighed in acid-washed and combusted 250 mL Erlenmeyer flasks. A volume (in mL) of MilliQ water twice the mass (in grams) added to each flask and shaken (170 rpm for 10 h). Subsequently, the liquid was transferred into 50 mL centrifuge tubes and centrifuged for 10 minutes at 7500 rpm followed by filtering through a 0.2 um polyethersulfone filter. 50 mL of each water sample was acidified to pH 2 with trace-metal grade HCl, followed by SPE with styrene-divinylbenzene (SDVB) polymer modified with a proprietary nonpolar surface (Bond Elut Priority Pollutant™, Agilent Technologies).[29] Water-soluble organics were eluted with HPLC grade methanol and stored in precombusted glass vials at 4 °C in the dark prior to analysis.

2.2 21 Tesla FT-ICR Mass Spectrometry

Ions were generated at atmospheric pressure via a microelectrospray source[35] and analyzed by 21 T FT-ICR MS.[32,33] Peaks with signal magnitude greater than 6 times the baseline root-mean-square (rms) noise at *m/z* 500 were exported to peak lists, phase-corrected,[36] and internally calibrated based on the "walking" calibration method.[37] Molecular formula assignments were performed with PetroOrg© software.[38]

FT-ICR Mass Spectrometry and Data Analysis

Ions were initially accumulated in an external multipole ion guide (1-5 ms) and released m/z-dependently by a decreasing auxiliary radio frequency potential between the multipole rods and the end-cap electrode.[39] Ions were excited to m/z-dependent radius to maximize the dynamic range and number of observed mass spectral peaks (m/z 200-1500; 32-64%), and excitation and detection were performed on the same pair of electrodes.[40,41] The dynamically harmonized ICR is operated with 6 V trapping potential.[42,43] Time-domain transients of 3.1 seconds were acquired with the Predator data station, with 100 time-domain acquisitions averaged for all experiments,[44] which were initiated by a TTL trigger from the commercial Thermo data station.[33] Experimentally measured masses were converted from the International Union of Pure and Applied Chemistry (IUPAC) mass scale to the Kendrick mass scale[45] for rapid identification of homologous series for each heteroatom class (i.e., species with the same $C_cH_hN_nO_oS_s$ content, differing only be degree of alkylation).[46] For each elemental composition, $C_cH_hN_nO_oS_s$, the heteroatom class, type (double bond equivalents, DBE = number of rings plus double bonds to carbon, DBE = $C - h/2 + n/2 + 1$) and carbon number, c, were tabulated for subsequent generation of heteroatom class relative abundance distributions and graphical relative-abundance weighted DBE versus carbon number images.[47]

Molecular Formula Calculations

Bulk characteristics of molecular species detected in each ionization mode were determined based on neutral elemental compositions, including H/C, O/C, and N/C ratios, double-bond equivalents (DBE) and nominal oxidation state of carbon (NOSC). Equations for DBE and NOSC can be found below:

$$DBE = 1 + \frac{1}{2}(2C - H + N) \qquad \text{(EQ 1)}$$

where DBE conveys hydrogen deficiency as the number of rings plus double bonds to C, which calculates the number of π bonds and rings within the sample.[48,49]

$$NOSC = 4 - \frac{5C+H-3N-2O-2S}{C} \quad \text{(EQ 2)}$$

in which NOSC is dependent on the number of carbon (C), hydrogen (H), nitrogen (N), oxygen (O), and sulfur (S) atoms.[50] NOSC provides valuable information on the oxidative state of the sample, with higher values indicating DOM sources that are more oxidized.[50,51] Often, NOSC is used to estimate energetic limitations associated with microbial metabolism of C sources in different environments.[52–55] All FT-ICR mass spectra files and assigned elemental compositions are publicly available via the Open Science Framework at https://osf.io/758ux/ DOI 10.17605/OSF.IO/758UX.

3. Results and Discussion

3.1 Positive ESI 21T FT-ICR MS of pyOM identifies new isobaric overlaps

Figure 2.1 shows the broadband +ESI FT-ICR mass spectrum for a pyOM extract. More than 35,000 assigned mass spectral (signal magnitude of six times greater than the baseline noise level) between *m/z* 200-1300, centered at *m/z* 480 (bottom left). The achieved resolving power ($m/\Delta m_{50\%}$, in which $\Delta m_{50\%}$ is mass spectral peak full width at half-maximum peak height)[17] is 1,800,000 at *m/z* 400, which enables resolution and assignment of 35,100 peaks at root-mean-square error of 41 ppb. The mass scale-expanded segment at *m/z* 611 highlights the immense spectral density, with ~123 peaks within a 0.3 mDa window assigned with RMS error of 5 ppb (**Fig. 2.1 top left**). The theoretical resolving power required to separate equally abundant species that differ in mass by ~640 μDa at *m/z* 600 is 950,000. Here, the achieved resolving power ($m/\Delta m_{50\%}$ = 1,400,000 at *m/z* 611) enables the separation of species with the same nominal mass

(59 Da) that differ in exact mass by 640 μDa ($NO_2{}^{13}C$ versus $^{12}C_2SH_3$), approximately the mass of an electron (548 μDa).[56–58] **Table 2.1** shows isobaric overlaps and minimum achieved resolving power requirements for equally abundant species in pyOM samples by +ESI. Importantly, resolving power requirements will exceed the minimum for species of varying abundance.[17,59,60]

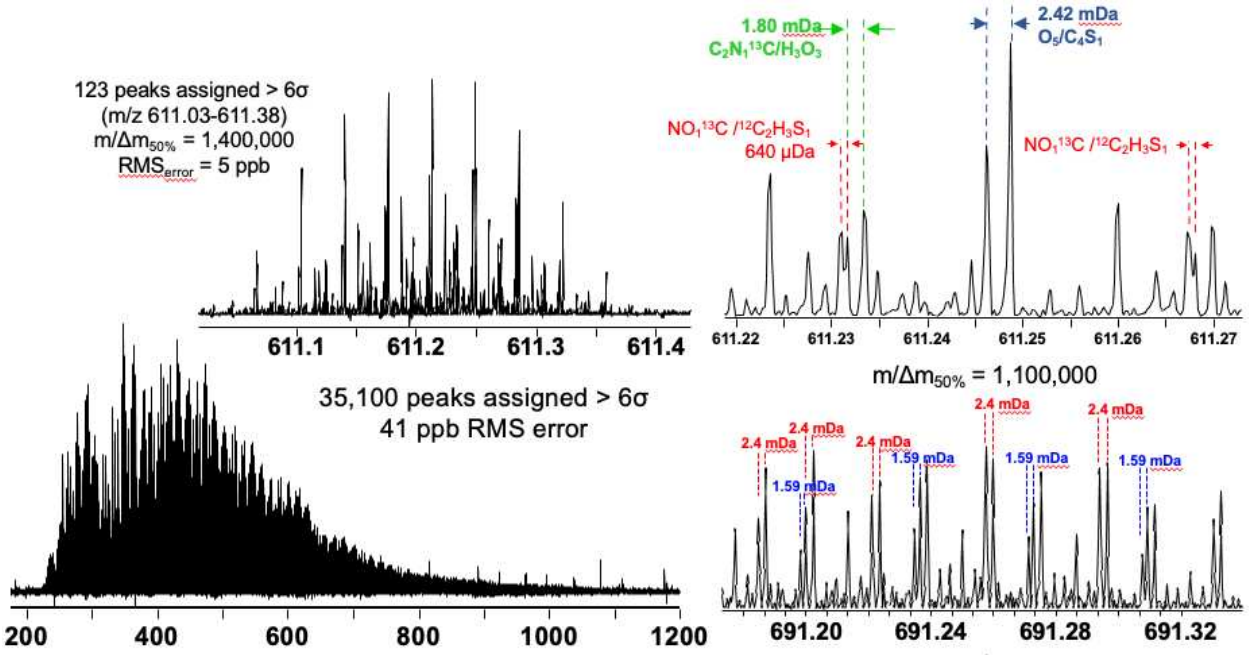

Figure 2.1. Positive-ion ESI 21 T FT-ICR mass spectrum of a pyOM extract. Bottom left: Broadband FT-ICR mass spectrum containing more than35 000 assigned mass spectral peaks (m/z200−1200) with a root-mean-square mass error of 41 ppb, each with a signal magnitude greater than 6σof baseline noise, withm/Δm50%= 1 800 000 atm/z400. Top left: 350 mDa mass scale-expanded segment, showing resolution of more than 120mass spectral peaks atm/z611. Bottom right: mass scale-expanded segment acrossm/z691.1−691.4, showing the +increase in the number ofisobaric overlaps at higherm/z. Top right:~60 mDa mass scale-expanded segment, showing resolution of three isobaric overlaps: 2.42 mDa, 1.80mDa, and 640μDa (mass of an electron is 548 μDa).

Table 2.1. Isobaric overlaps detected by +ESI 21 T FT-ICR MS and resolving power requirement for equally abundant species of a pyOM extract.

	Nominal Mass (Da)	**Δ Exact Mass (mDa)**	**$m/\Delta m_{50\%}$**	**$m/\Delta m_{50\%}$**	**$m/\Delta m_{50\%}$**	**$m/\Delta m_{50\%}$**
			***m/z* 200**	***m/z* 400**	***m/z* 600**	***m/z* 800**
$NO_2{}^{13}C$ /$^{12}C_2SH_3$	**59 Da**	0.640 mDa	310,000	625,000	930,000	1,200,000
$C_2N_1{}^{13}C/H_3O_3$	**51 Da**	1.80 mDa	110,000	220,000	330,000	440,000
O_5/C_4S_1	**80 Da**	2.40 mDa	83,000	160,000	250,000	330,000
CN_4/H_4O_4	**68 Da**	1.35 mDa	150,000	290,000	440,000	590,000

The polyfunctionality and polydispersity in molecular composition and structure of pyOM systems results in a highly complex mass spectrum for all ionization modes, including -ESI. **Figure 2.2** shows the -ESI 21 T FT-ICR mass spectrum, with more than 32,000 acidic species assigned between *m/z* 200-1000, with mass distribution centered at *m/z* ~375 (**Figure 2.2 bottom left**). Negative-ion ESI remains dominated by carboxylic acid moieties, yet still results in a highly complex mass spectrum. The mass scale-expanded segment at *m/z* 611 shows 66 peaks assigned with RMS error of 7 ppb (**Figure 2.2 top left**) and highlights the mass spectral complexity in -ESI. However, comparison of the same nominal mass range shows that +ESI detects more than twice the number of peaks (123 peaks) compared to -ESI (66 peaks) and illustrates the dominance of carboxylic acid ionization in negative-ion mode. Improved speciation of pyOM, especially lower abundant species, requires more than one ionization mode to more accurately identify compositional trends across a wide molecular weight range.

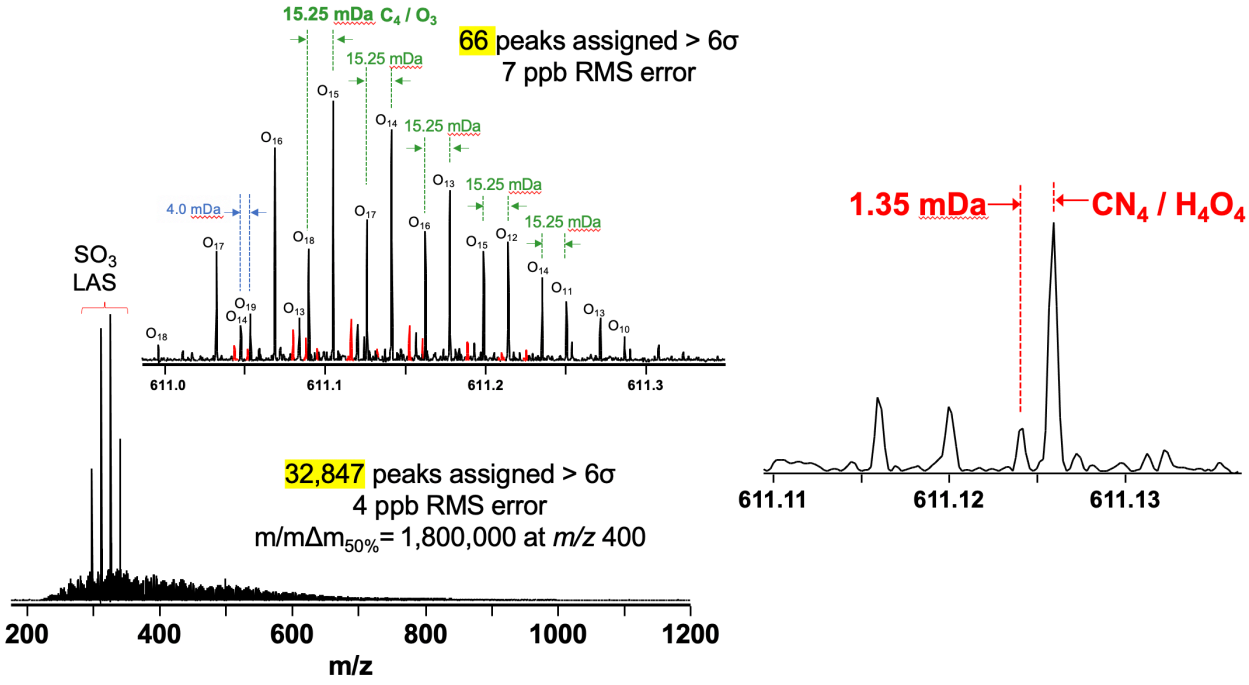

Figure 2.2. Negative-ion ESI 21 tesla FT-ICR mass spectrum of a pyOM extract. Bottom: Broadband FT-ICR mass spectrum, containing more than 32,000 resolved and assigned mass spectral peaks, each with signal magnitude greater than 6σ of baseline noise, with achieved $m/\Delta m_{50\%}$ = 1,800,000 at *m/z* 400 and root-mean-square mass error of 4 ppb. Middle: 350 mDa mass scale-expanded segment, showing resolution of more than 60 mass spectral peaks, each corresponding to a unique elemental composition. Right: ~30 mDa mass scale-expanded segment, showing resolution of isobaric species with the same nominal mass that differ in exact mass by 1.35 mDa, roughly the mass of two electrons.

3.2 Ionization Efficiency: +ESI vs -ESI

Efficient ionization of O_x species in -ESI can be rapidly visualized when compared to +ESI for the same sample across the same narrow mass range. **Figure 2.3** shows mass-scale expanded zoom insets for +ESI (top) and -ESI (bottom) across *m/z* 609.5-614.5. Species in both spectra are comprised of singly charged species, based on the unit *m/z* separation between $^{12}C_n$ and $^{13}C_1{}^{12}C_{n-1}$ isotopic variants of the same elemental composition[61]. The most abundant peaks in positive and negative mode correspond to odd nominal mass species (e.g., *m/z* 611 and 613). Mass spectral peaks with the highest signal magnitude detected by -ESI correspond to O_x species at odd nominal mass, and $^{13}C_1O_x$ at even nominal mass.[62] Conversely, +ESI across the same mass window shows

approximately equal signal magnitude for even and odd nominal mass species, and results in the detection of twice as many species. This is likely due to a combination of the narrow range of basicity in SOM compared to acidity and the relative concentrations of basic functional groups, which leads to more equal ionization in +ESI.

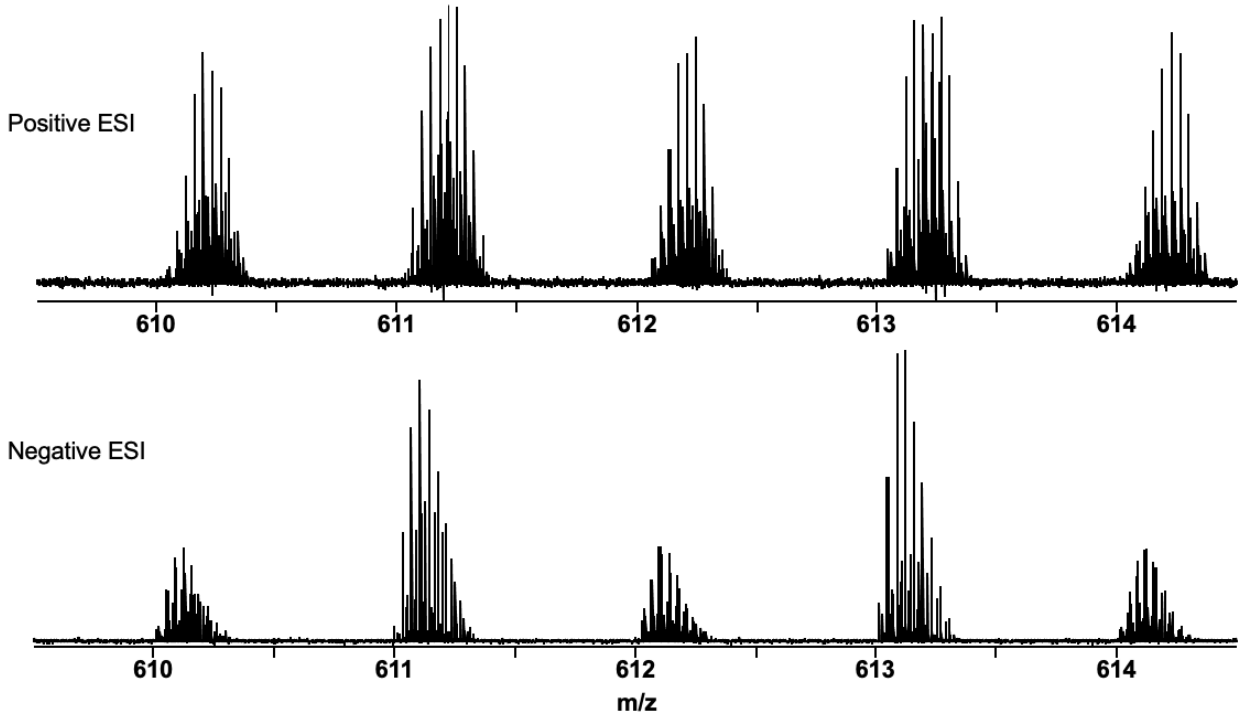

Figure 2.3. Mass-scale expanded zoom insets for +ESI (top) and -ESI (bottom) across m/z 609.5-614.5 of a pyOM extract.

Tables A2 and **A3** show the *m/*z, mass error, resolving power, S/N, DBE and neutral elemental composition for all mass spectral peaks detected above 6σ at *m/*z 611 and 612 by +ESI (**Table B2**) and -ESI (**Table B3**). Across a 348 mDa region, >120 peaks are assigned elemental compositions with RMS mass error of 6 ppb by +ESI (**Table B2a**) compared to 66 peaks across a similar mass range (RMS error of 6 ppb, error plot in **Figure 2.4**) by -ESI for the same sample. Shifting one nominal mass unit higher across each spectrum to *m/z* 612 (**Table B2b** and **B3b**) shows a similar trend, with 96 peaks assigned at RMS error of 5 ppb by +ESI (across 312 mDa)

compared to 54 peaks at 9 ppb RMS error by -ESI (285 mDa). Positive ESI contains more isobaric overlaps with tighter mass splits (1.59 mDa), which are resolved by 21T FT-ICR MS (**Table 2.1**). Additionally, +ESI detects more N species (56 at *m/z* 611 and 67 at *m/z* 612) compared to -ESI (25 at *m/z* 611 and 31 at *m/z* 612), and further highlights the increased compositional coverage for +ESI compared to -ESI for pyOM.

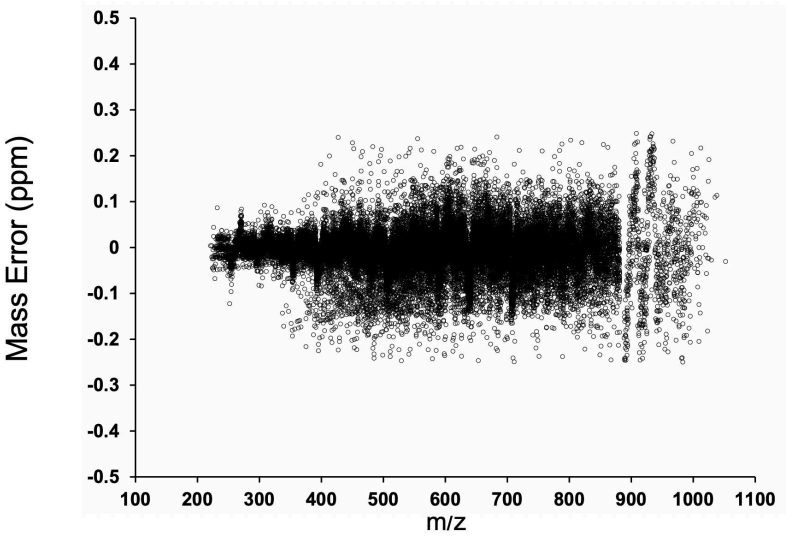

Figure 2.4. Error plot of a +ESI a pyOM ample with m/z on the x-axis and error on the y-axis.

3.3 Positive-ion ESI identifies 12,475 unique species not observed in negative ESI

The differences in spectra result in detection of unique species by each ionization mode, shown in **Table 2.2**. Positive ESI results 24,189 formulas compared to 11,301 by -ESI, a more than two-fold increase in identified species. Removal of the sodiated adducts from +ESI reduces the number of formulas assigned to 21,010 (only the CHO species resulted in sodiated adducts). For simplicity, further discussion of the elemental assignments will be limited to the non-sodiated fraction. Between -ESI and the +ESI, there are 8,535 formulas common to both modes – 4,371 CHO and 4,164 CHNO – which comprise nearly all the -ESI assignments. Stated another way, ~

76% of the total -ESI formulas and nearly 86% and 91% of the CHO and CHNO are also detected by +ESI. However, common assignments represent only ~41% of assignments by +ESI (~65% of CHO and ~30% of the CHNO).

Table 2.2. Formula assignments and elemental class distributions of the CHO and CHNO fractions of the negative-ion and +ESI spectra of a pyOM extract.

+/-	**-ESI**	**+ESI**	**+ESI (no Na)**	**Common**
Formulas assigned	11301	24189	21010	8535
Unique Formulas	2766	15654	12475	N/A
CHO	5112	9911	6732	4371
Unique CHO	741	5540	2361	N/A
CHNO	4568	14015	14015	4164
Unique CHNO	404	9851	9851	N/A

The unique formulas assigned for each mode were determined by eliminating neutral elemental compositions assigned in both spectra. However, it is important to note that it is possible that structural isomers may be present that have the same elemental composition and thus cannot be differentiated by mass alone. For unique CHO species, only 741 species were assigned in negative mode, whereas 2,361 species were assigned positive mode. However, for CHNO species, 9,851 unique species were assigned by +ESI compared to only 404 unique formulas in -ESI, an increase of ~87% and over 2x the number previously reported.[21] Out of 21,010 non-sodiated species assigned in positive-ion mode, 12,475 are unique; put generally, *+ESI displays more unique formulas than it has in common with negative-ion mode*. Thus, the use of +ESI identifies organic N species in pyOM that remain undetected by -ESI, and results in an expansion of the analytical window into complex fire-impacted systems.

3.4 CHEMICAL PROPERTIES ARE INFLUENCED BY IONIZATION LIMITATIONS

Chemical property calculations from elemental compositions detected by FT-ICR MS analysis are common in NOM systems to rapidly identify qualitative trends between samples. For example, nominal oxidation state of carbon (NOSC) describes a molecule's lability because it is directly related to the Gibbs free energy (DG°) of the reduction half-reaction between organic matter as the electron donor and the available terminal electron acceptor (e.g., oxygen). (**EQ 1**).[50] However, calculated properties based on elemental compositions will change based on the number and type of species detected. **Table 2.3** shows average H/C, O/C, N/C, NOSC, and double-bond equivalents (DBE) (**EQ 2**), plus the average C, H, O and N number per formula, for both +/- ESI spectra. For both polarities, the H/C ratio is ~1, with ~10 more C and 12 more H in +ESI than in -ESI. The average number of oxygens is 1.3 higher in -ESI, in agreement with Hertkorn, et. al. 2008, due to the preferential ionization of O-rich molecules.[63] The differences in average C, H, and N are propagated by differences in DBE, which is four units higher for +ESI, demonstrating how the differences in species detected are propagated through calculated indices. Finally, the distribution of the NOSC assignments displays a distinct shift towards higher oxidation and lower C# in the -ESI sample (**Figure 2.5, top**). This shift is even more distinct in the CHNO class (**Figure 2.5, bottom**), which shows a dramatic shift towards lower, more reduced NOSC values in +ESI. Together, these properties clearly demonstrate that any calculation based on elemental composition must be evaluated with caution.

Table 2.3. Calculated chemical parameters for a pyOM sample analyzed by positive and negative ESI. The first two rows represent the calculations for all the assigned formulas, while the bottom two rows represent the calculations for only the unique formulas assigned.

Mode	H/C	O/C	N/C	NOSC	DBE	Avg C	Avg H	Avg O	Avg N
-ESI all	1.02	0.478	0.0300	0.0422	13.8	25.1	25.4	11.8	0.642
+ESI all	1.09	0.381	0.0460	-0.192	15.1	29.4	31.8	10.9	1.18
-ESI unique	1.10	0.567	0.0155	0.141	10.7	21.2	23.2	11.7	0.266
+ESI unique	1.15	0.344	0.0522	-0.302	15.3	31.0	34.9	10.4	1.41

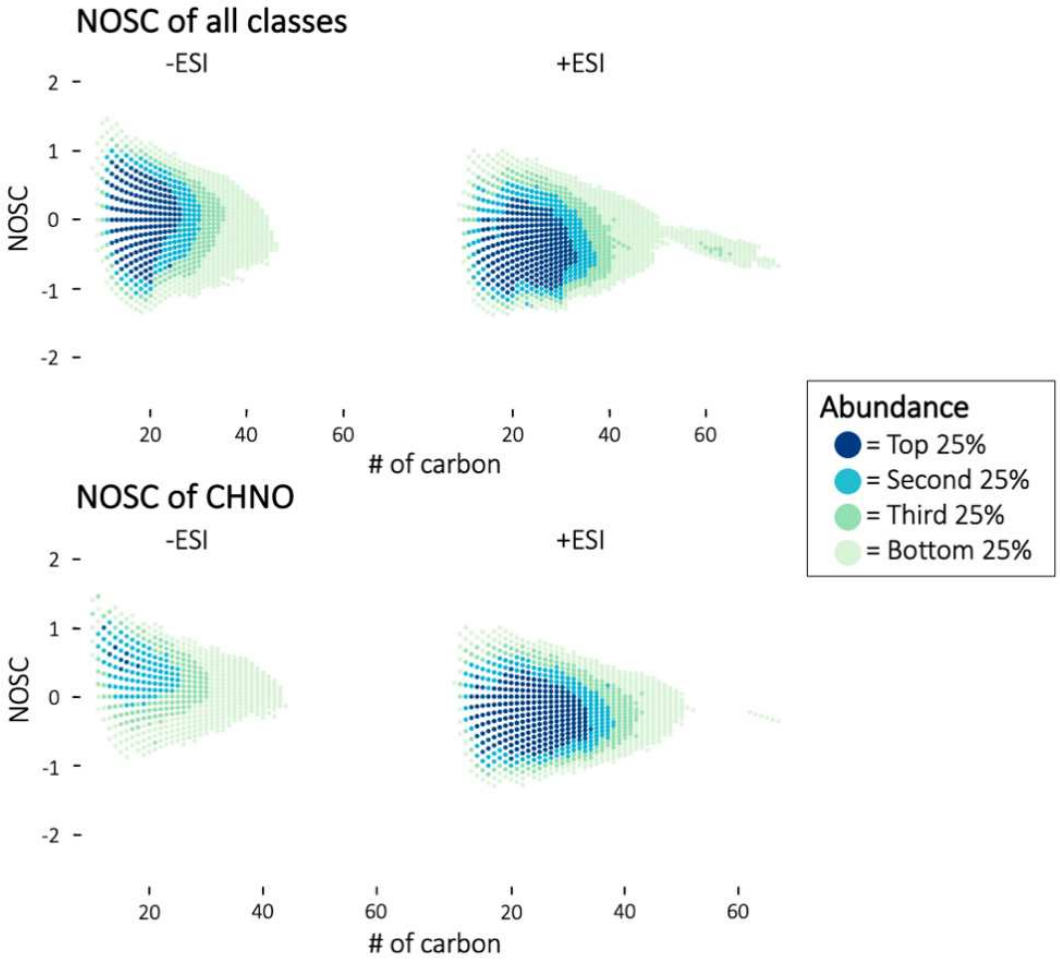

Figure 2.5. Kroll diagrams for a pyOM extract depicting the number of carbon atoms on the x-axis and the nominal oxidation state of carbon (NOSC) on the y-axis;[51] -ESI plotted on the left and +ESI on the right. Top: Kroll diagrams for all formulas assigned. Bottom: Kroll diagrams for CHNO formulas only.

3.5 Positive ESI at 21 T FT-ICR MS resolves and identifies dissolved organic nitrogen

Compared to -ESI, +ESI more efficiently ionizes N-containing species (**Table 2.2**). **Figure B1** shows the heteroatom class distribution comparison for the same sample of pyOM by +/-ESI **(**see **Figure B2** for relative abundances). Nitrogen species detected by +ESI contain a higher number of nitrogen atoms per molecule (i.e., N_3, N_4, and N_5), likely comprised of a range of basic functionalities (e.g., pyridines and amides). Species with high N substitution (e.g., N_5) are not detected in -ESI. Additionally, +ESI identifies a higher number of low oxygen-number classes (e.g., O_2 and O_3). In fact, six CHN_1 classes were assigned in +ESI, in addition to CHN_1O_2, $CHN_2O_{2\text{-}3}$, $CHN_3O_{2\text{-}4}$, $CHN_4O_{4\text{-}6}$, and all CHN_5O_x that were not detected by -ESI. This suggests that speciation and molecular detection of dissolved organic N in SOM systems could be significantly improved by 21 T FT-ICR MS in positive ion mode.

3.6 Van Krevelen diagrams highlight the increased compositional coverage of +ESI at 21 T

Van Krevelen diagrams plot H/C ratio versus O/C ratio of neutral species, and different regions of the H/C and O/C space correspond to the molar ratios of major biogeochemical precursors (e.g., lignin-like, peptide-like, and lipid-like).[64] Because FT-ICR MS results in tens of thousands of elemental compositions in a single mass spectrum, van Krevelen diagrams are widely applied to rapidly visualize compositional changes between samples.[65] **Figure 2.6** (**top**) shows van Krevelen diagrams derived from both ionization modes for all assigned species. Elemental compositions unique to -ESI are shown in blue (left), those identified in both spectra in gray

(middle), and species unique to +ESI shown in red (right). Unique species in -ESI primarily have O/C between 0.3-0.9, whereas species unique to +ESI span O/C 0.1 to 0.9. As shown in **Table 2**, 2,766 formulas are unique to -ESI and 12,475 are unique to +ESI. These species span similar compositional range but are lower in total number of species in -ESI.

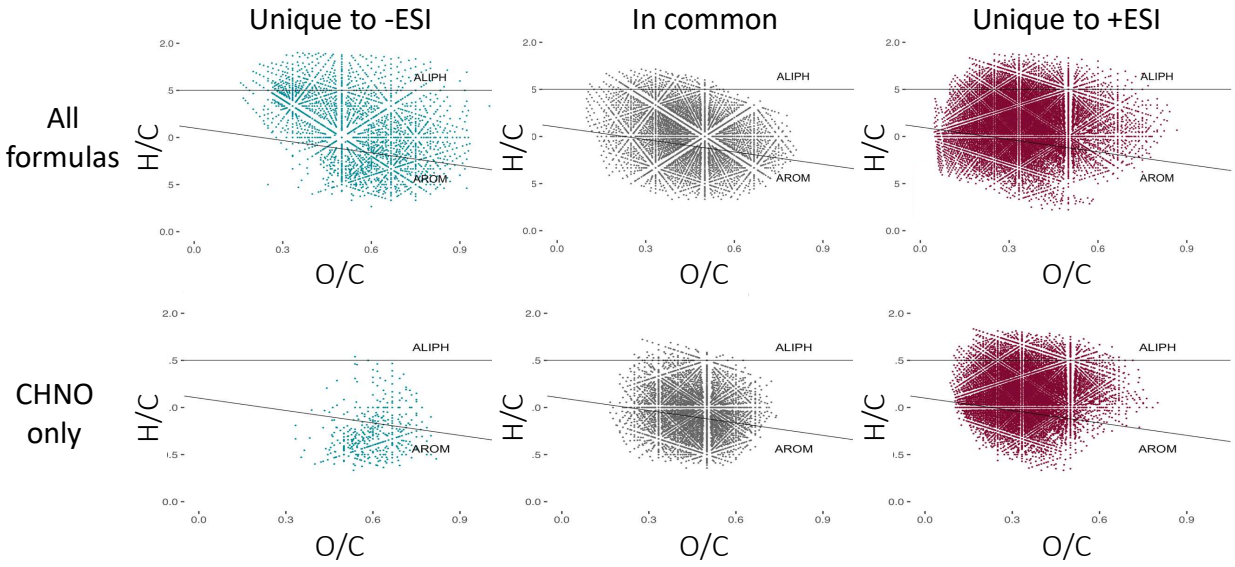

Figure 2.6. Top: van Krevelen diagrams of all the assigned formulas of the pyOM extract. Bottom: van Krevelen diagrams of only the CHNO class assignments. Unique formulas assigned for -ESI are on the left (blue); formulas in common are in the middle (grey), and formulas unique to +ESI are on the right (red).

3.7 Unique compositional space of nitrogen species by +ESI 21 T FT-ICR MS

Figure 2.6 (**bottom**) shows van Krevelen diagrams for unique N-containing species by +/- ESI. Importantly, across a wide range of H/C and O/C, positive-ion mode species occupy a much more diverse compositional range compared to -ESI, with only 404 peaks in -ESI compared to 9,851 peaks in +ESI (more than 24x the formula assignments in -ESI) (**Table 2.2**). These figures demonstrate that across a wide range of compositional and structural classes, +ESI identifies a wide range of N species. Importantly, species that correspond to H/C ratios >1.0 and O/C ratios >0.3 are uniquely detected by +ESI and remain undetected by -ESI. This region of van Krevelen

space (H/C > 1.0 and O/C >0.35) has previously reported as indicator for the presence of potential toxicants due to inhibition of aquatic photosynthetic organisms.[66] Therefore, characterization of pyOM by +ESI identifies potentially toxic species not detected by -ESI. Differences in O/C ratio are illustrated in **Figure B3**, which shows that -ESI identifies more species with high oxygen content, while +ESI can more efficiently ionize those with lower oxygen content.

3.8 Modified van Krevelen diagrams: H/C versus N/C

A useful complement to the traditional van Krevelen diagram is H/C vs N/C plots, shown for the total assigned CHNO fraction (**Figure 2.7a**) and the unique CHNO assignments (**Figure 2.7b**). Each panel is further divided by ionization mode (-ESI on top) and N# (1-5 from left to right). The compositional space for the total assigned species spans similar compositional ranges for N_1 (N/C > 0.1) and N_2 (N/C > 0.2) species, but becomes more evident for N_3-N_5, with only 25 N_4 species identified by negative-ion mode and no N_5 species detected (**Figure 2.7a**). For the unique formula assignments, the difference in N/C spans across all N classes. For N_{1-3} the unique formulas in negative-ion mode are clustered towards lower H/C ratios (H/C < 1.0), while N_4 and N_5 do not display any unique formulas (**Figure 2.7b**), further highlighting the increased speciation of CHNO by positive-ion mode. Thus, for research that is focused on changes in N content, +ESI should be utilized as the preferred method. Importantly, previous studies utilizing both negative and positive ESI were not able to provide the level of resolution for the nitrogenated molecules that we report here.[21,23,63] Therefore, this key element for microbial processing and ecosystem productivity is relatively understudied within the field of FT-ICR MS.

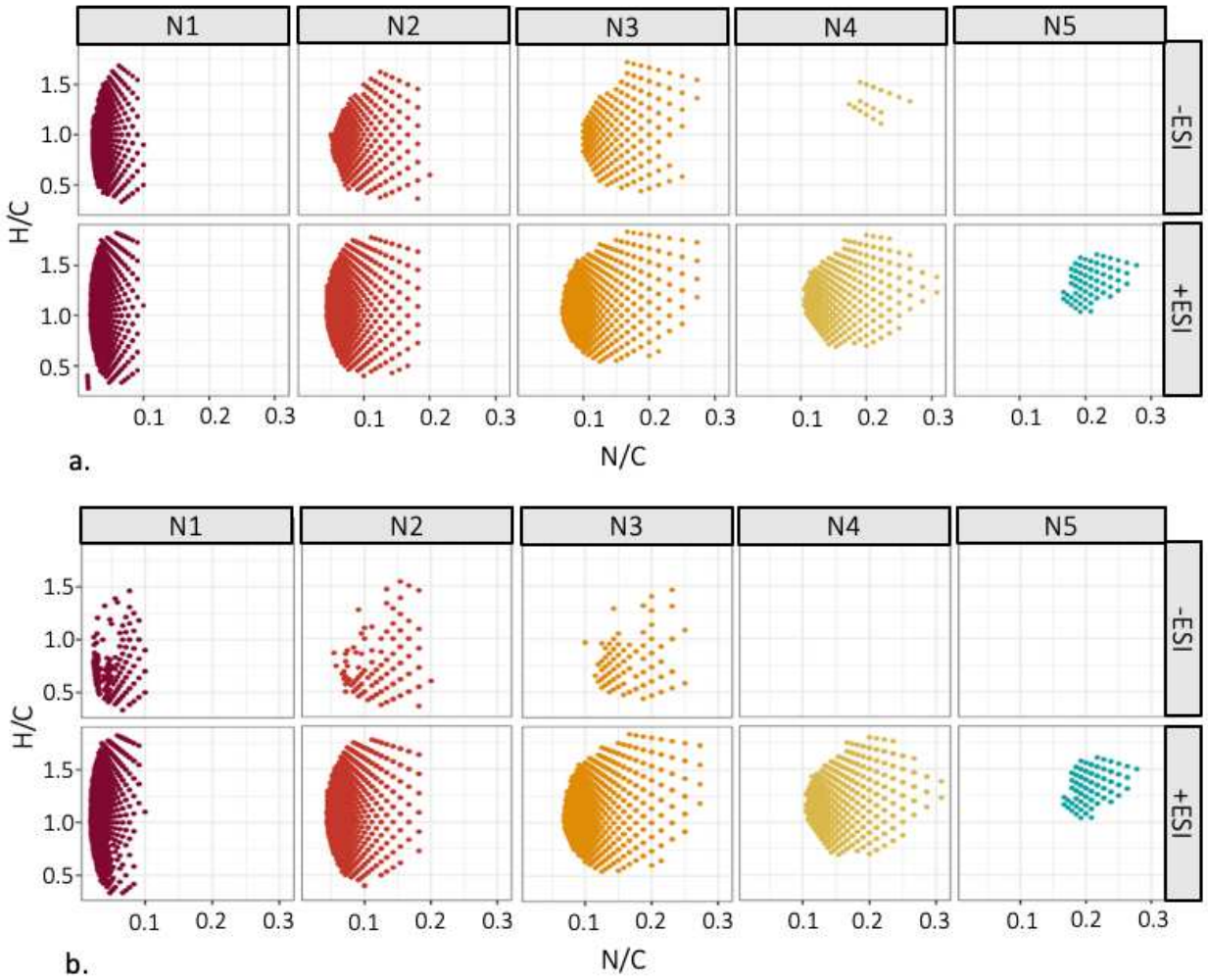

Figure 2.7. Atomic H/C vs N/C ratios of neutral species detected in a pyOM extract. (a) All CHNO assigned, -ESI assignments on the top row and +ESI assignments on the bottom row. (b) Only the unique CHNO assigned, again with -ESI on the top row and +ESI on the bottom row. Both panels are separated by N number, which increases from left to right.

4. Conclusion

21 T FT-ICR MS in +ESI displayed clear shifts in pyOM composition compared to -ESI, highlighting differences in the ionization mechanism that proliferate into the resulting spectrum. The addition of +ESI resulted in an 87% increase (12,475 additional formulas) in the non-sodiated species compared to the traditional -ESI-only analysis. This included 9,851 unique CHNO formulas, which spanned a wider compositional range and demonstrate that a large fraction of organic N is overlooked with analysis only by -ESI. Additionally, the calculated chemical

parameters displayed that the biases associated with calculating chemical parameters by any ionization mechanism (e.g., NOSC) must be fully understood for proper use in C and N cycling models. Finally, while no one ionization mode can address the complexity of SOM, combining ESI in positive- and negative-mode substantially expands the analytical window for fire-impacted systems.

5. Author Contributions

According to CRediT criteria, my contributions to this work included conceptualization, data curation, formal analysis, investigation, methodology, visualization, writing – original draft, and writing – reviewing and editing. Contributions by T.B. included funding acquisition, project administration, resources, and writing- review and editing. Contributions by R.B.Y., W.B., and G.T.B. included validation, resources, software, writing – review and editing. Contributions by A.R.N. included resources and writing – review and editing. Contributions by M.J.W. included resources, funding acquisition, project administration, and writing – review and editing. Contributions by A.M.M. included conceptualization, data curation, investigation, supervision, validation, writing – original draft, and writing – review and editing.

REFERENCES

(1) Bladon, K. D.; Emelko, M. B.; Silins, U.; Stone, M. Wildfire and the Future of Water Supply. *Environ Sci Technol* **2014**, *48* (16), 8936–8943. https://doi.org/10.1021/es500130g.
(2) Jones, M. W.; Santín, C.; van der Werf, G. R.; Doerr, S. H. Global Fire Emissions Buffered by the Production of Pyrogenic Carbon. *Nat Geosci* **2019**, *12* (9), 742–747. https://doi.org/10.1038/s41561-019-0403-x.
(3) Giglio, L.; Randerson, J. T.; van der Werf, G. R. Analysis of Daily, Monthly, and Annual Burned Area Using the Fourth-Generation Global Fire Emissions Database (GFED4). *J Geophys Res Biogeosci* **2013**, *118* (1), 317–328. https://doi.org/10.1002/jgrg.20042.
(4) Abatzoglou, J. T.; Williams, A. P. Impact of Anthropogenic Climate Change on Wildfire across Western US Forests. *Proc Natl Acad Sci U S A* **2016**, *113* (42), 11770–11775. https://doi.org/10.1073/pnas.1607171113.
(5) Dennison, P. E.; Brewer, S. C.; Arnold, J. D.; Moritz, M. A. Large Wildfire Trends in the Western United States, 1984-2011. *Geophys Res Lett* **2014**, *41* (8), 2928–2933. https://doi.org/10.1002/2014GL059576.
(6) Bird, M. I.; Wynn, J. G.; Saiz, G.; Wurster, C. M.; McBeath, A. The Pyrogenic Carbon Cycle. *Annu Rev Earth Planet Sci* **2015**, *43*, 273–298. https://doi.org/10.1146/annurev-earth-060614-105038.
(7) González-Pérez, J. A.; González-Vila, F. J.; Almendros, G.; Knicker, H. The Effect of Fire on Soil Organic Matter - A Review. *Environ Int* **2004**, *30* (6), 855–870. https://doi.org/10.1016/j.envint.2004.02.003.
(8) Knicker, H. How Does Fire Affect the Nature and Stability of Soil Organic Nitrogen and Carbon? A Review. *Biogeochemistry* **2007**, *85* (1), 91–118. https://doi.org/10.1007/s10533-007-9104-4.
(9) Viedma, O.; Quesada, J.; Torres, I.; de Santis, A.; Moreno, J. M. Fire Severity in a Large Fire in a Pinus Pinaster Forest Is Highly Predictable from Burning Conditions, Stand Structure, and Topography. *Ecosystems* **2015**, *18* (2), 237–250. https://doi.org/10.1007/s10021-014-9824-y.
(10) Pierson, D. N.; Robichaud, P. R.; Rhoades, C. C.; Brown, R. E. Soil Carbon and Nitrogen Eroded after Severe Wildfire and Erosion Mitigation Treatments. *Int J Wildland Fire* **2019**, *28* (10), 814–821. https://doi.org/10.1071/WF18193.
(11) Santín, C.; Doerr, S. H.; Kane, E. S.; Masiello, C. A.; Ohlson, M.; de la Rosa, J. M.; Preston, C. M.; Dittmar, T. Towards a Global Assessment of Pyrogenic Carbon from Vegetation Fires. *Glob Chang Biol* **2016**, *22* (1), 76–91. https://doi.org/10.1111/gcb.12985.
(12) Geisseler, D.; Horwath, W. R.; Joergensen, R. G.; Ludwig, B. Pathways of Nitrogen Utilization by Soil Microorganisms - A Review. *Soil Biology and Biochemistry*. December 2010, pp 2058–2067. https://doi.org/10.1016/j.soilbio.2010.08.021.
(13) Acquisti, C.; Elser, J. J.; Kumar, S. Ecological Nitrogen Limitation Shapes the DNA Composition of Plant Genomes. *Mol Biol Evol* **2009**, *26* (5), 953–956. https://doi.org/10.1093/molbev/msp038.
(14) Adkins, J.; Sanderman, J.; Miesel, J. Soil Carbon Pools and Fluxes Vary across a Burn Severity Gradient Three Years after Wildfire in Sierra Nevada Mixed-Conifer Forest. *Geoderma* **2019**, *333*, 10–22. https://doi.org/10.1016/j.geoderma.2018.07.009.
(15) Miesel, J. R.; Hockaday, W. C.; Kolka, R. K.; Townsend, P. A. Soil Organic Matter Composition and Quality across Fire Severity Gradients in Coniferous and Deciduous Forests of

the Southern Boreal Region. *Journal of Geophysical Research G: Biogeosciences* **2015**, *120* (6), 1124–1141. https://doi.org/10.1002/2015JG002959.
(16) Torres-Rojas, D.; Hestrin, R.; Solomon, D.; Gillespie, A. W.; Dynes, J. J.; Regier, T. Z.; Lehmann, J. Nitrogen Speciation and Transformations in Fire-Derived Organic Matter. *Geochim Cosmochim Acta* **2020**, *276*, 170–185. https://doi.org/10.1016/j.gca.2020.02.034.
(17) Marshall, A. G.; Hendrickson, C. L.; Jackson, G. S. *FOURIER TRANSFORM ION CYCLOTRON RESONANCE MASS SPECTROMETRY: A PRIMER*.
(18) Stubbins, A.; Spencer, R. G. M.; Chen, H.; Hatcher, P. G.; Mopper, K.; Hernes, P. J.; Mwamba, V. L.; Mangangu, A. M.; Wabakanghanzi, J. N.; Six, J. Illuminated Darkness: Molecular Signatures of Congo River Dissolved Organic Matter and Its Photochemical Alteration as Revealed by Ultrahigh Precision Mass Spectrometry. *Limnol Oceanogr* **2010**, *55* (4), 1467–1477. https://doi.org/10.4319/lo.2010.55.4.1467.
(19) Kujawinski, E. B.; del Vecchio, R.; Blough, N. v.; Klein, G. C.; Marshall, A. G. Probing Molecular-Level Transformations of Dissolved Organic Matter: Insights on Photochemical Degradation and Protozoan Modification of DOM from Electrospray Ionization Fourier Transform Ion Cyclotron Resonance Mass Spectrometry. In *Marine Chemistry*; 2004; Vol. 92, pp 23–37. https://doi.org/10.1016/j.marchem.2004.06.038.
(20) Dittmar, T.; Koch, B. P. Thermogenic Organic Matter Dissolved in the Abyssal Ocean. *Mar Chem* **2006**, *102* (3–4), 208–217. https://doi.org/10.1016/j.marchem.2006.04.003.
(21) Ohno, T.; Sleighter, R. L.; Hatcher, P. G. Comparative Study of Organic Matter Chemical Characterization Using Negative and Positive Mode Electrospray Ionization Ultrahigh-Resolution Mass Spectrometry. *Anal Bioanal Chem* **2016**, *408* (10), 2497–2504. https://doi.org/10.1007/s00216-016-9346-x.
(22) Kruve, A.; Kaupmees, K.; Liigand, J.; Leito, I. Negative Electrospray Ionization via Deprotonation: Predicting the Ionization Efficiency. *Anal Chem* **2014**, *86* (10), 4822–4830. https://doi.org/10.1021/ac404066v.
(23) Hockaday, W. C.; Purcell, J. M.; Marshall, A. G.; Baldock, J. A.; Hatcher, P. G. Electrospray and Photoionization Mass Spectrometry for the Characterization of Organic Matter in Natural Waters: A Qualitative Assessment. *Limnol Oceanogr Methods* **2009**, *7* (1), 81–95. https://doi.org/10.4319/lom.2009.7.81.
(24) Whitehouse, C. M.; Dreyer, R. N.; Yamashita, M.; Fenn, J. B. Electrospray Interface for Liquid Chromatographs and Mass. *Anal Chem* **1985**, *149* (3), 675–679.
(25) Fenn, J. B.; Mann, M.; Meng, C. K.; Wong, S. F.; Whitehouse, C. M. Electrospray Ionization for Mass Spectrometry of Large Biomolecules. *Science (1979)* **1989**, *246* (4926), 64–71.
(26) Qi, Y.; Fu, P.; Volmer, D. A. Analysis of Natural Organic Matter via Fourier Transform Ion Cyclotron Resonance Mass Spectrometry: An Overview of Recent Non-Petroleum Applications. *Mass Spectrom Rev* **2020**. https://doi.org/10.1002/mas.21634.
(27) Young, R. B.; Avneri-Katz, S.; McKenna, A. M.; Chen, H.; Bahureksa, W.; Polubesova, T.; Chefetz, B.; Borch, T. Composition-Dependent Sorptive Fractionation of Anthropogenic Dissolved Organic Matter by Fe(III)-Montmorillonite. *Soil Syst* **2018**, *2* (1), 1–19. https://doi.org/10.3390/soilsystems2010014.
(28) Brown, T. L.; Rice, J. A. Effect of Experimental Parameters on the ESI FT-ICR Mass Spectrum of Fulvic Acid. *Anal Chem* **2000**, *72* (2), 384–390. https://doi.org/10.1021/ac9902087.

(29) Dittmar, T.; Koch, B.; Hertkorn, N.; Kattner, G. A Simple and Efficient Method for the Solid-Phase Extraction of Dissolved Organic Matter (SPE-DOM) from Seawater. *Limnol Oceanogr Methods* **2008**, *6*, 230–235.
(30) He, C.; Fang, Z.; Li, Y.; Jiang, C.; Zhao, S.; Xu, C.; Zhang, Y.; Shi, Q. Ionization Selectivity of Electrospray and Atmospheric Pressure Photoionization FT-ICR MS for Petroleum Refinery Wastewater Dissolved Organic Matter. *Environ Sci Process Impacts* **2021**. https://doi.org/10.1039/d1em00248a.
(31) Li, Y.; Xu, C.; Chung, K. H.; Shi, Q. Molecular Characterization of Dissolved Organic Matter and Its Subfractions in Refinery Process Water by Fourier Transform Ion Cyclotron Resonance Mass Spectrometry. *Energy and Fuels* **2015**, *29* (5), 2923–2930. https://doi.org/10.1021/acs.energyfuels.5b00333.
(32) Hendrickson, C. L.; Quinn, J. P.; Kaiser, N. K.; Smith, D. F.; Blakney, G. T.; Chen, T.; Marshall, A. G.; Weisbrod, C. R.; Beu, S. C. 21 Tesla Fourier Transform Ion Cyclotron Resonance Mass Spectrometer: A National Resource for Ultrahigh Resolution Mass Analysis. *J Am Soc Mass Spectrom* **2015**, *26* (9), 1626–1632. https://doi.org/10.1007/s13361-015-1182-2.
(33) Smith, D. F.; Podgorski, D. C.; Rodgers, R. P.; Blakney, G. T.; Hendrickson, C. L. 21 Tesla FT-ICR Mass Spectrometer for Ultrahigh-Resolution Analysis of Complex Organic Mixtures. *Anal Chem* **2018**, *90* (3), 2041–2047. https://doi.org/10.1021/acs.analchem.7b04159.
(34) Nelson, A. R.; Narrowe, A. B.; Rhoades, C. C.; Fegel, T. S.; Roth, H. K.; Chu, R. K.; Amundson, K. K.; Geonczy, S. E.; Young, R. B.; Steindorff, A. S.; Mondo, S. J.; Grigoriev, I. v; Salamov, A.; Borch, T.; Wilkins, M. J.; author, C. Playing with FiRE: A Genome Resolved View of the Soil Microbiome Responses to High Severity Forest Wildfire. *bioRxiv* **2021**. https://doi.org/10.1101/2021.08.17.456416.
(35) Emmett, M. R.; White, F. M.; Hendrickson, C. L.; Shi, D. H.; Marshall, A. G. Application of Micro-Electrospray Liquid Chromatography Techniques to FT-ICR MS to Enable High-Sensitivity Biological Analysis. *J Am Soc Mass Spectrom* **1998**, *9* (4), 333–340. https://doi.org/10.1016/S1044-0305(97)00287-0.
(36) Xian, F.; Hendrickson, C. L.; Blakney, G. T.; Beu, S. C.; Marshall, A. G. Automated Broadband Phase Correction of Fourier Transform Ion Cyclotron Resonance Mass Spectra. *Anal Chem* **2010**, *82* (21), 8807–8812. https://doi.org/10.1021/ac101091w.
(37) Savory, J. J.; Kaiser, N. K.; McKenna, A. M.; Xian, F.; Blakney, G. T.; Rodgers, R. P.; Hendrickson, C. L.; Marshall, A. G. Parts-per-Billion Fourier Transform Ion Cyclotron Resonance Mass Measurement Accuracy with a Walking Calibration Equation. *Anal Chem* **2011**, *83* (5), 1732–1736. https://doi.org/10.1021/ac102943z.
(38) Corilo, Y. E. PetroOrg Software. Florida State University, Omics LLC: Tallahassee, FL 2014.
(39) Kaiser, N. K.; Savory, J. J.; Hendrickson, C. L. Controlled Ion Ejection from an External Trap for Extended m/z Range in FT-ICR Mass Spectrometry. *J Am Soc Mass Spectrom* **2014**, *25* (6), 943–949. https://doi.org/10.1007/s13361-014-0871-6.
(40) Kaiser, N. K.; McKenna, A. M.; Savory, J. J.; Hendrickson, C. L.; Marshall, A. G. Tailored Ion Radius Distribution for Increased Dynamic Range in FT-ICR Mass Analysis of Complex Mixtures. *Anal Chem* **2013**, *85* (1), 265–272. https://doi.org/10.1021/ac302678v.
(41) Chen, T.; Beu, S. C.; Kaiser, N. K.; Hendrickson, C. L. Note: Optimized Circuit for Excitation and Detection with One Pair of Electrodes for Improved Fourier Transform Ion Cyclotron Resonance Mass Spectrometry. *Review of Scientific Instruments* **2014**, *85* (6). https://doi.org/10.1063/1.4883179.

(42) Boldin, I. A.; Nikolaev, E. N. Fourier Transform Ion Cyclotron Resonance Cell with Dynamic Harmonization of the Electric Field in the Whole Volume by Shaping of the Excitation and Detection Electrode Assembly. *Rapid Communications in Mass Spectrometry* **2011**, *25* (1), 122–126. https://doi.org/10.1002/rcm.4838.
(43) Kaiser, N. K.; Savory, J. J.; McKenna, A. M.; Quinn, J. P.; Hendrickson, C. L.; Marshall, A. G. Electrically Compensated Fourier Transform Ion Cyclotron Resonance Cell for Complex Mixture Mass Analysis. *Anal Chem* **2011**, *83* (17), 6907–6910. https://doi.org/10.1021/ac201546d.
(44) Blakney, G. T.; Hendrickson, C. L.; Marshall, A. G. Predator Data Station: A Fast Data Acquisition System for Advanced FT-ICR MS Experiments. *Int J Mass Spectrom* **2011**, *306* (2–3), 246–252. https://doi.org/10.1016/j.ijms.2011.03.009.
(45) Kendrick, E. A Mass Scale Based Resolution Mass Spectrometry of Organic Compounds. *Anal Chem* **1963**, *35* (13), 2146–2154.
(46) Hughey, C. A.; Hendrickson, C. L.; Rodgers, R. P.; Marshall, A. G.; Qian, K. Kendrick Mass Defect Spectrum: A Compact Visual Analysis for Ultrahigh-Resolution Broadband Mass Spectra. *Anal Chem* **2001**, *73* (19), 4676–4681. https://doi.org/10.1021/ac010560w.
(47) McLafferty, F. W.; Turecek, F. *Interpretation of Mass Spectra*, 4th ed.; University Science Books: Mill Valley, CA, 1993.
(48) Koch, B. P.; Dittmar, T. From Mass to Structure: An Aromaticity Index for High-Resolution Mass Data of Natural Organic Matter. *Rapid Communications in Mass Spectrometry* **2006**, *20* (5), 926–932. https://doi.org/10.1002/rcm.2386.
(49) Koch, B. P.; Dittmar, T. Erratum: From Mass to Structure: An Aromaticity Index for High-Resolution Mass Data of Natural Organic Matter (Rapid Communications in Mass Spectrometry (2006) 20 (926-932) DOI: 10.1002/Rcm.2386). *Rapid Communications in Mass Spectrometry* **2016**, *30* (1), 250. https://doi.org/10.1002/rcm.7433.
(50) LaRowe, D. E.; van Cappellen, P. Degradation of Natural Organic Matter: A Thermodynamic Analysis. *Geochim Cosmochim Acta* **2011**, *75* (8), 2030–2042. https://doi.org/10.1016/j.gca.2011.01.020.
(51) Kroll, J. H.; Donahue, N. M.; Jimenez, J. L.; Kessler, S. H.; Canagaratna, M. R.; Wilson, K. R.; Altieri, K. E.; Mazzoleni, L. R.; Wozniak, A. S.; Bluhm, H.; Mysak, E. R.; Smith, J. D.; Kolb, C. E.; Worsnop, D. R. Carbon Oxidation State as a Metric for Describing the Chemistry of Atmospheric Organic Aerosol. *Nat Chem* **2011**, *3* (2), 133–139. https://doi.org/10.1038/nchem.948.
(52) Noël, V.; Tfaily, M. M.; Fendorf, S.; Bone, S. E.; Boye, K.; Williams, K. H.; Bargar, J. R. Thermodynamically Controlled Preservation of Organic Carbon in Floodplains. *Nat Geosci* **2017**, *10* (6), 415–419. https://doi.org/10.1038/ngeo2940.
(53) Boye, K.; Herrmann, A. M.; Schaefer, M. v.; Tfaily, M. M.; Fendorf, S. Discerning Microbially Mediated Processes during Redox Transitions in Flooded Soils Using Carbon and Energy Balances. *Front Environ Sci* **2018**, *6* (MAY). https://doi.org/10.3389/fenvs.2018.00015.
(54) Zhang, J.; Feng, Y.; Wu, M.; Chen, R.; Li, Z.; Lin, X.; Zhu, Y.; Delgado-Baquerizo, M.; Zhang, C. J. *Evaluation of Microbe-Driven Soil Organic Matter Quantity and Quality by Thermodynamic Theory*; 2021. https://doi.org/10.
(55) Naughton, H. R.; Keiluweit, M.; Tfaily, M. M.; Dynes, J. J.; Regier, T.; Fendorf, S. Development of Energetic and Enzymatic Limitations on Microbial Carbon Cycling in Soils. *Biogeochemistry* **2021**, *153* (2), 191–213. https://doi.org/10.1007/s10533-021-00781-z.

(56) Wapstra, A. H.; Audi, G.; Thibault, C. The Ame2003 Atomic Mass Evaluation - (I). Evaluation of Input Data, Adjustment Procedures. *Nucl Phys A* **2003**, *729* (1), 129–336. https://doi.org/10.1016/j.nuclphysa.2003.11.002.
(57) Audi, G.; Bersillon, O.; Blachot, J.; Wapstra, A. H. The NUBASE Evaluation of Nuclear and Decay Properties. *Nucl Phys A* **2003**, *729* (1), 3–128. https://doi.org/10.1016/j.nuclphysa.2003.11.001.
(58) Mohr, P. J.; Taylor, B. N.; Newell, D. B. CODATA Recommended Values of the Fundamental Physical Constants: 2006. *Rev Mod Phys* **2008**, *80* (2), 633–730. https://doi.org/10.1103/RevModPhys.80.633.
(59) Marshall, A. G.; Rodgers, R. P. *Petroleomics: Chemistry of the Underworld*; 2008. www.pnas.orgcgidoi10.1073pnas.0805069105.
(60) G. Marshall, A.; T. Blakney, G.; Chen, T.; K. Kaiser, N.; M. McKenna, A.; P. Rodgers, R.; M. Ruddy, B.; Xian, F. Mass Resolution and Mass Accuracy: How Much Is Enough? *Mass Spectrometry* **2013**, *2* (Special_Issue), S0009–S0009. https://doi.org/10.5702/massspectrometry.s0009.
(61) Senko, M. W.; Beu, S. C.; Mclafferty, F. W. *Automated Assignment of Charge States from Resolved Isotopic Peaks for Multiply Charged Ions*; 1995.
(62) Kujawinski, E. B.; Freitas, M. A.; Zang, X.; Hatcher, P. G.; Green-Church, K. B.; Jones, R. B. *The Application of Electrospray Ionization Mass Spectrometry (ESI MS) to the Structural Characterization of Natural Organic Matter*. www.elsevier.com/locate/orggeochem.
(63) Hertkorn, N.; Frommberger, M.; Witt, M.; Koch, B. P.; Schmitt-Kopplin, P.; Perdue, E. M. Natural Organic Matter and the Event Horizon of Mass Spectrometry. *Anal Chem* **2008**, *80* (23), 8908–8919. https://doi.org/10.1021/ac800464g.
(64) Kim, S.; Kramer, R. W.; Hatcher, P. G. Graphical Method for Analysis of Ultrahigh-Resolution Broadband Mass Spectra of Natural Organic Matter, the Van Krevelen Diagram. *Anal Chem* **2003**, *75* (20), 5336–5344. https://doi.org/10.1021/ac034415p.
(65) Rivas-Ubach, A.; Liu, Y.; Bianchi, T. S.; Tolić, N.; Jansson, C.; Paša-Tolić, L. Moving beyond the van Krevelen Diagram: A New Stoichiometric Approach for Compound Classification in Organisms. *Anal Chem* **2018**, *90* (10), 6152–6160. https://doi.org/10.1021/acs.analchem.8b00529.
(66) Smith, C. R.; Sleighter, R. L.; Hatcher, P. G.; Lee, J. W. Molecular Characterization of Inhibiting Biochar Water-Extractable Substances Using Electrospray Ionization Fourier Transform Ion Cyclotron Resonance Mass Spectrometry. *Environ Sci Technol* **2013**, *47* (23), 13294–13302. https://doi.org/10.1021/es4034777.

CHAPTER 3: FIRE SEVERITY INFLUENCES ORGANIC NITROGEN AND CARBON COMPOSITION IN HIGH-ELEVATION FOREST SOILS

1. INTRODUCTION

Wildfire activity in the western United States has increased in recent decades in terms of the size of area burned[1–3] and the frequency and severity of large fires,[4,5] and is projected to continue to increase[6]. Observed warming conditions have led to greater frequency of wildfire in high-elevation forest in recent years;[7] therefore, it is critical that we understand the impacts of changing fire regimes on ecosystem dynamics, biodiversity, and productivity at higher elevations.[8,9] The expected increase in burn severity (i.e., degree of consumption of organic soil layers and vegetation) [10,11] may have implications for carbon cycling, potentially shifting forests from C sinks to C sources.[12,13] The post-fire soil organic matter (SOM) composition provides a baseline for a forest's recovery; thus, molecular-level analysis of SOM from different burn severities improves our understanding of ecosystem response following wildfire.[14,15]

Wildfires influence biogeochemical[16] and hydrological[17] cycles through the combustion of biomass, which alters SOM properties (e.g., C:N:P stoichiometry, pH, major functional groups),[18–20] forms hydrophobic layers,[21] and increases C and N in postfire runoff.[22] The combination of heat from wildfires and changes in SOM properties have consequences for plant and microbiome diversity[23,24] which may persist for years after the fire.[25,26] Previous studies indicate that burn severity differentially impacts the first 5 cm below the duff/mineral soil interface[27] and local soil microbiomes by destabilizing soil aggregates and affecting microbial biomass and composition and associated enzyme activity.[28–34] SOM transformations that occur during heating can result in increased chemical heterogeneity, forming a substrate which is generally more resistant to

microbial decomposition.[35–37] SOM and soil microbiota are important for reestablishment of native plant species; therefore, fire-induced transformations may influence post-fire plant succession, plant species composition, and ecosystem processes.[38–41] Short-term (1-5 years post-fire) impacts include significant losses in SOM and total N, with forest floor layers more highly influenced than mineral soils.[42] Additional short-term observations include increased erosion[43] and decreased bacterial and fungal community richness in burned plots compared to unburned.[28,44,45] These negative impacts may persist for over a decade; ectomycorrhizal and saprobic richness were lower than unburned levels 11 years after fire in a ponderosa pine (*Pinus ponderosa*) forest,[28] total soil N depletion persisted at least 14 years following fire with subsequent reduction on tree and shrub colonization in a Scots pine (*P. sylvestris*) forest,[44] and DTN export was ~10x higher in a burned catchment compared to a unburned catchment 14 years after the Hayman Fire in northern Colorado.[22] Recovery of microbial communities requires bioavailable C and N,[46] therefore, understanding the role of burn severity on SOM C and N composition is important for developing effective post-fire management strategies.[30]

Organic N is a dynamic component of soils, derived primarily from amino acids and peptides and easily mineralized into plant-available inorganic N.[47,48] Organic N comprises 62-83% of the total N in Norway spruce stands,[49] and dissolved organic N is a primary pathway for N loss in forest soils while acting as a N source for mycorrhizal plants in boreal forests.[50,51] Direct analysis of organic N is facilitated by Fourier transform ion cyclotron resonance mass spectrometry (FT-ICR MS), which provides molecular-level insight that can be used to calculate oxidation state, aromaticity, and biolability.[52–54] Acidic N species in burned SOM detected by negative-ion electrospray ionization (-ESI) FT-ICR MS indicate that N incorporates into refractory, heterocyclic aromatic compounds that are more resistant to microbial degradation.[55–58] Bahureksa,

et al. reported that aromatic N heterocycles were formed in soil burned at higher temperatures in a laboratory microcosm;[59] however, these findings have not yet been verified across burn severities. Additionally, positive-ion mode ESI detected more than twice the number of N-species across a wider H/C and O/C range compared to -ESI in fire-impacted soils.[60] Thus, in this study we focus on +ESI to selectively ionize SOM species through protonation reactions to catalogue molecular transformations that occur during soil heating and the potential implications for N cycling.

Nuclear magnetic resonance (NMR) spectroscopy can be paired with FT-ICR MS to quantify shifts in functionality, which is required to link SOM compositional changes to microbial degradation pathways to improve C and N cycling predictions in response to high severity fires.[61,62] NMR has been used to demonstrate an increase in aromatic structures and decrease in alkylated organic molecules in severely burned pine forest soils.[20] NMR spectra showing decreased atomic H/C and O/C ratios across a burn severity gradient in soils from wildfire-affected forest and shrub ecosystems are the net result of greater dehydration, dealkylation, and decarboxylation reactions at higher severity wildfire.[15] The abundance of N-heterocyclic compounds also increased with burn severity in these sites,[15,59,60] but varied with fuel composition (e.g., grasses or coniferous litter) and heating conditions.[63–66] However, rigorous analysis of the specific compounds formed at different burn severities remains limited, especially in field studies.

N-heterocycles have been linked to increased toxicity in hydrothermal liquefication of biomass[67] and have been shown to modulate the toxicity of co-occuring metals in soils (i.e., cadmium, boron).[68,69] The release of toxic compounds (e.g., polycyclic aromatic hydrocarbons; PAHs, toxic heavy metals, nitrogenated species),[70] suggests that fire may increase soil toxicity, with associated short- and long-term implications for ecosystem recovery due to their environmental persistence and propensity to bioaccumulate.[71,72] The formation of ecotoxicants

may prompt shifts in microbial populations that adversely affect ecosystem processe, [73] or may be transported downstream by water leaching or soil erosion. Microtox® is an assay that is frequently used to evaluate chemical contamination in soils, waters, and biochars[74–78] and can be related to contaminant concentrations (e.g., metals, pesticides, PAHs) through bioluminescence inhibition of the bacterium *Aliivbrio fischeri (A. fischeri)*.[79] Limited studies exist on the eco-toxicological impacts of fire on water quality, despite evidence that postfire runoff is toxic across different trophic levels.[80] Indeed, Silva et al. found that the aqueous ash leachate concentrations were positively related to decreases in microbial activity in wildfire-affected mixed pine and eucalypt stands;[81] however, the impact of burn severity on soil toxicity is relatively unexplored.

Here, we characterize how fire severity influences SOM composition along soil burn severity gradients and discuss the implications of N-heterocycle formation for soil toxicity. Soil was collected from two recently burned lodgepole pine dominated forests along the Colorado-Wyoming border (**Figure 3.1**). We hypothesized that distinct soil C and N chemical profiles were formed in response to burn severity, which would yield microbially-recalcitrant organic matter, with more heterocyclic N compounds at higher burn severities. To test our hypotheses, we performed a suite of high-resolution analyses which included NMR, FT-ICR MS and Microtox ®. We report the composition of C and N indeed differed between the burn severity classifications, with potential implications for soil toxicity through the formation of highly nitrogenated species (i.e., N > 1). Indeed, Microtox® analysis indicated that soil toxicity increased at higher burn severities, with potential to further impact C and N cycling in fire-impacted forests.

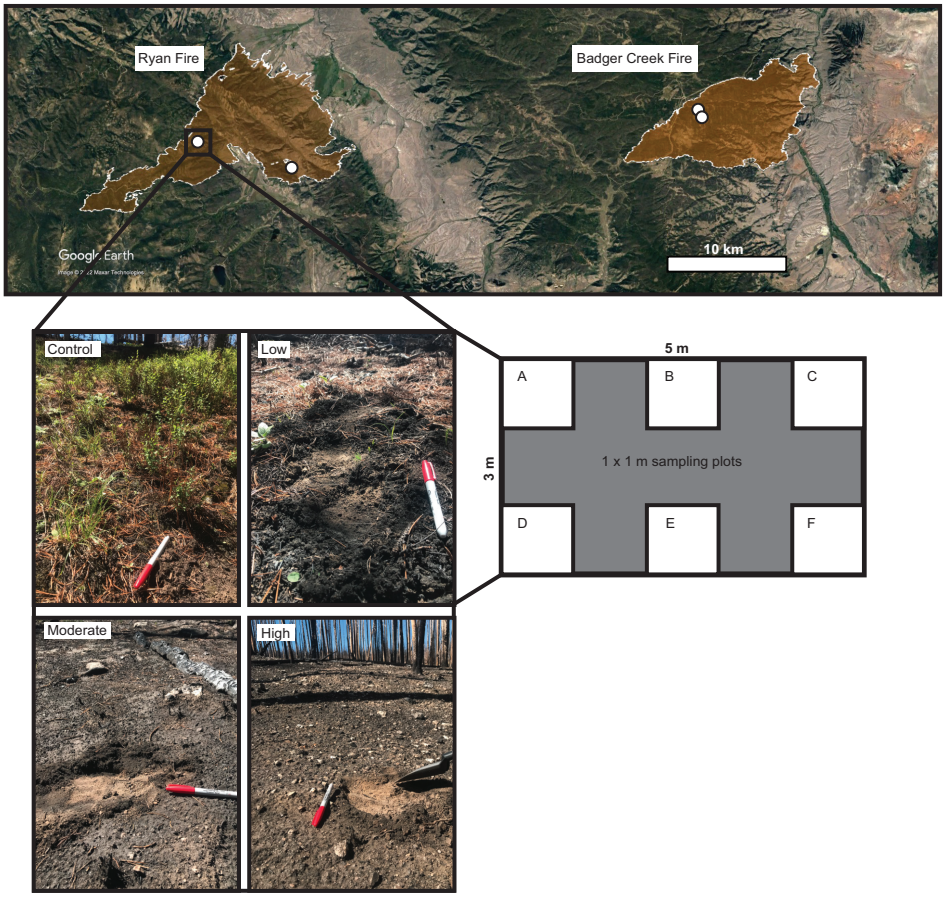

Figure 3.1: Map indicating sampling sites and strategy in the 2018 Ryan and Badger Creek Fire burn scars. Top: Google Earth image of the Ryan Fire and Badger Creek Fire burn scars. White dots indicate locations where burn severity transects were identified. Bottom left: photos representing each of the burn severity treatments (Control, Low, Moderate, High). Bottom right: visual representation of the 3x5 m sampling grid with subplots labeled A-F.

2. Materials and Methods

2.1 Soil Sampling and Preparation

Soil samples were collected in early August 2019, with full details available in Nelson, et al.[45] Briefly, soil sampling was conducted one year post-fire in lodgepole pine-dominated forests burned by the 2018 Badger Creek and Ryan fires in the Medicine Bow National Forest The most abundant soil types are loamy-skeletal Ustic Haplocryepts and fine-loamy Ustic Haplocryalfs. Four independent burn severity gradients comprised of low, moderate, and high severity burns and an unburned control were selected based on remotely sensed comparison of pre- and post-fire

greenness.[82] Severity was field-validated prior to sampling using US Forest Service soil burn severity indicators.[10,83] Low, moderate, and high severity sites had >85%, 20-85%, and <20% O-horizon cover, respectively.[10] Samples were collected on 16 and 19 August 2019, two days without precipitation events, approximately one year following containment of both fires. At each sampling site, a 3x5 m sampling grid with 6 m^2 subplots was laid out perpendicular to the dominant slope (**Figure 1**). Each treatment within the individual gradient transects was no more than 50 m from one another. A sterilized trowel was used to collect approximately 150 g of surface (0-5 cm depth) and near-surface soils (5-10 cm depth) by first sampling and collecting the surface soil, then collecting the near-surface soil from below that. The 0-5 cm depth was comprised primarily of mineral soil, though a thin layer (~5mm) of particulate O-horizon (i.e., undecomposed or partially decomposed litter such as leaves, needles, or twigs) occurred at the surface of both the unburned control and low severity soil samples and a similar thickness of charred organic material and ash was part of the moderate and high severity samples. The small amount of residual organic components allowed us determine the burn severity of the surface soil and the impacts of burn severity on soil molecular composition. A total of 48 samples were collected from four severity gradients (16 samples per gradient). Samples for chemical analyses were immediately placed on ice and stored at 4°C in the laboratory until processing. Prior to analysis, soils were air-dried and sieved through 2 mm mesh to remove large litter particles, roots, rocks, and other large debris.

2.1.1 Elemental Measurements

Dissolved organic carbon (DOC) and dissolved total nitrogen (DTN) concentrations were determined from warm water extracts for the soil samples. Measurements were performed with a TOC-VCPN total organic C/N analyzer (Shimadzu Corporation, Columbia, MD, USA). A subset of surface (n=16) and near-surface soil samples (n=25) were dried (48 h at 60°C), ground to a fine

powder, and analyzed for total C and N by dry combustion (LECO Corporation, St. Joseph, MI, USA). The results from the elemental measurements were used to identify trends that occurred within the soils and select a subset of six representative samples for further analyses based on differences in C and N content and pH.

2.1.2 Soil extractions

Based on trends identified from the elemental measurements (**Table C1, C2**), a subset of six samples from the 48 collected were selected for further analyses, including acute toxicity, 21 tesla FT-ICR MS, and solid-state ^{13}C NMR: a high severity surface soil (HS_S), moderate severity surface and near-surface soils (MS_S and MS_NS, respectively), a low severity surface soil (LS_S), and controls from the surface and near-surface soils (CNTL_S and CNTL_NS, respectively) (**Table C3**). Water extracts of the surface soils from this subset were also analyzed by solution-state ^{1}H NMR. For acute toxicity and FT-ICR MS, 50 g dry, sieved soil was weighed into a polystyrene weigh boat and transferred to a 250 mL Erlenmeyer flask. For solution-state ^{1}H NMR, we used the DOC concentrations to determine the amount of soil needed to extract 10 mg of DOC. For all samples, Millipore water was added to a final ratio of 1 g soil : 2 mL water in Erlenmeyer flasks (one flask for FT-ICR MS and acute toxicity, another for ^{1}H NMR), which were covered with parafilm and shaken (10 hours, 170 rpm) in the dark. Water and soil slurries were quantitatively transferred to pre-rinsed 50 mL centrifuge tubes with an additional 150 mL Millipore water. The samples were then centrifuged at 7500 rpm (756 xg) for 10 minutes, during which a vacuum filtration system was assembled using acid-washed, pre-combusted glassware. 0.2 μm polyethersulfone (PES) filters were pre-rinsed with 100-150 mL Millipore water prior to sample introduction. A 50 mL aliquot from the FT-ICR MS samples was stored in centrifuge tubes; the remaining filtrate was stored in amber bottles at 4°C until solid phase extractions. Solid soils

were analyzed by solid-state 13C NMR, and soil water extracts were analyzed by solution-state 1H NMR, 21 T FT-ICR MS, and Microtox ®.

2.1.3 Acute toxicity of water-soluble species

Microtox® acute toxicity analysis was used to determine the toxicity of soil water extracts in the control and burned samples.[84–86] During sample preparation for FT-ICR MS, 50 mL of each sample was subsampled and stored in centrifuge tubes. From these samples, 1 mL was transferred to amber HPLC vials (3 mL for RYN_126 only) for Microtox® analysis. Samples were carbon normalized to 9.29 ppm of C based on DOC values and stored at 4°C until analysis. The percent decrease in bioluminescence of *A. fischeri* bacteria after a 15-minute incubation period determines the toxicity of each sample based on the amount of light emitted by the bacteria.[87,88] The Microtox® 81.9% screening test protocol was used on the Microtox® model 500 analyzer (Modern Water, New Castle, DE, USA) as previously described [89].

2.1.4 Solid phase extractions

Solid phase extractions were performed prior to FT-ICR MS analysis according to Dittmar, et al.[90] Briefly, samples were brought to room temperature and acidifed to pH 2 with trace-metal free hydrochloric acid (Sigma-Aldrich Chemical Co., St. Louis, MO, USA). PPL cartridges (Bond Elut PPL (Priority Pollutant^{TM}), a styrene-divinylbenzene (SDVB) polymer modified with a proprietary nonpolar surface) were rinsed with 15 mL HPLC-grade methanol (Sigma Aldrich Chemical Co., St. Louis, MO, USA) and 15 mL pH 2 millipore water. Polar species in the water samples were retained on the sorbent, rinsed with 15 mL pH 2 water to remove salts, and allowed to dry overnight. Each sample was recovered from the cartridge by elution with 2 mL HPLC-grade methanol and transferred to 2 mL borosilicate vials prior to 21 tesla FT-ICR MS analysis.

2.2 FT-ICR MS Analyses

2.2.1 Sample preparation. All solvents were HPLC grade (Sigma-Aldrich Chemical Co., St. Louis, MO) and SPE extracts were analyzed after further dilution in methanol (1:10, by volume) prior to analysis by negative and positive ion electrospray ionization. See "Soil Extractions" for full details.

2.2.2 Instrumentation: ESI Source.

Sample solution was infused via a microelectrospray source[91] (50 μm i.d. fused silica emitter) at 500 nL/min by a syringe pump. Typical conditions for negative ion formation were: emitter voltage, -2.7-3.1 kV; S-lens RF: (45 %) and heated metal capillary temperature 350 °C. Positive-ion ESI spray conditions were opposite in polarity.

2.2.3 Instrumentation: 21 T FT-ICR MS.

DOM extracts were analyzed with a custom-built hybrid linear ion trap FT-ICR mass spectrometer equipped with a 21 T superconducting solenoid magnet[92,93] equipped with automatic gain control (AGC ion target: 1E6)[94,95] Ions were initially accumulated in an external multipole ion guide (1-5 ms) and released *m/z*-dependently by decrease of an auxiliary radio frequency potential between the multipole rods and the end-cap electrode.[96] Ions were excited to *m/z*-dependent radius to maximize the dynamic range and number of observed mass spectral peaks (32-64%),[96] and excitation and detection were performed on the same pair of electrodes.[97] The dynamically harmonized ICR cell in the 21 T FT-ICR is operated with 6 V trapping potential.[96,98] Time-domain transients of 3.1 seconds conditionally-coadded with the Predator data station that handled excitation and detection only, initiated by a TTL trigger from the commercial Thermo data station, with 100 time-domain acquisitions averaged for all experiment. [99] Mass spectra were phase-corrected[100] and internally calibrated with 10-15 highly abundant homologous series that span the entire molecular weight distribution based on the "walking" calibration method.[101]

Experimentally measured masses were converted from the International Union of Pure and Applied Chemistry (IUPAC) mass scale to the Kendrick mass scale[102] for rapid identification of homologous series for each heteroatom class (i.e., species with the same $C_cH_hN_nO_oS_s$ content, differing only by degree of alkylation).[103] For each elemental composition, $C_cH_hN_nO_oS_s$, the heteroatom class, type (double bond equivalents, DBE = number of rings plus double bonds to carbon, DBE = $C - h/2 + n/2 + 1$)[104] and carbon number, c, were tabulated for subsequent generation of heteroatom class relative abundance distributions and graphical relative-abundance weighted images and van Krevelen diagrams.[105]

Peaks with signal magnitude greater than 6 times the baseline root-mean-square (rms) noise at *m/z* 500 were exported to peak lists, and molecular formula assignments and data visualization were performed with PetroOrg © software[106] Molecular formula assignments with an error >0.2 parts-per-million were discarded, and only chemical classes with a combined relative abundance of ≥0.10% of the total were considered. . All FT-ICR mass spectra files and assigned elemental compositions are publicly available via the Open Science Framework at https://osf.io/758ux/ (DOI: DOI 10.17605/OSF.IO/758UX). Futher details can be found in Supporting Information.

2.3 MAG annotation for N heterocycle degradation genes

To investigate whether the soil microbiome were expressing genes for degrading N heterocycles, we utilized the metagenome-assembled genome (MAG) and metatranscriptomic dataset presented in Nelson et al (2022) (NCBI BioProject PRJNA682830). We analyzed a MAG dataset which was assembled from metagenomic sequencing done on 12 samples that consisted of a triplicate of high severity and low severity (3 from 0-5 cm and 3 from 5-10 cm for each treatment). We used HMMER[107] gainst hidden Markov models (HMMs) curated from UniProt[108] to search for the genes needed to constitute the multicomponent enzyme carbazole 1,9a-

dioxygenase (CARDO).[109,110] CARDO is made up of four parts: two terminal oxygenases (*carAa*; PF11723), a ferredoxin (*carAc*; PF00355), and a ferredoxin reductase (*carAd*; PF00970, PF00111, PF00175). Following the identification of the genes, we used the metatranscriptomics mapping data presented in Nelson et al (2022)[45] to identify whether the genes were being expressed within the given MAG.

2.4 NMR Analyses

2.4.1 Solid-state ^{13}C NMR analysis

Six soil samples were prepared for solid-state ^{13}C NMR: high, moderate, low, and control samples (surface), and moderate and control soils from the near surface. Soil samples were repeatedly extracted with hydrofluoric acid (10% w/w; ACS grade; Fisher Scientific, Hampton, NH, USA) to dissolve soil minerals and thus concentrate carbon.[111] Once enriched, samples were rinsed with deionized water to remove excess salts, freeze-dried, and ground in a mortar and pestle. Each sample was packed into a 4mm zirconium NMR rotor and closed with a Kel-F cap. Data acquisition was performed on a 500 MHz Bruker BioSpin Avance III spectrometer equipped with a 4 mm H-X magic angle spinning probe. Spectra were acquired using ramped amplitude cross polarization with a magic angle spinning rate of 11 kHz. The cross-polarization contact time was 1 ms with a 1 s recycle delay. All NMR spectra were processed using TopSpin (v. 3.6.2). NMR spectra were manually phased, baseline corrected and processed with a line broadening of 100 Hz. All NMR spectra were integrated into four main chemical shift regions: alkyl C (0-50 ppm), *O*-alkyl C (50-110 ppm), aromatic and phenolic C (110-165 ppm), and carboxyl and carbonyl C (165-215 ppm),[112,113] and normalized to the total signal intensity (expressed as percentage of the total signal, 100%).

2.4.2 Solution-state NMR analyses

Soil-derived DOM samples were filtered, freeze-dried and dried over phosphorus pentoxide in a vacuum desiccator to remove any residual water, then re-constituted in ~60 µL deuterium oxide (D_2O, 99.9% D) and 5 µL sodium deuteroxide (NaOD, 99.5% D, 30 wt. % in D_2O). Samples were centrifuged (10,000 x g at 4°C), transferred into 1.7 mm NMR tubes (Norell), and analyzed using a Bruker BioSpin Avance III 500 MHz NMR spectrometer (Karlsruhe, Germany) and a ^{1}H-^{15}N-^{13}C TXI 1.7 mm microprobe equipped with an actively shielded Z gradient. ^{1}H NMR spectra were collected using presaturation utilizing relaxation gradients and echoes water suppression.[114] Each ^{1}H NMR spectra contained 2,048 scans per sample with a recycle delay of 2 s, and 32K time domain points. Spectra were processed using a zero filling factor of 2 and apodized by multiplication with an exponential decay corresponding to 0.3 Hz line broadening.[115]

All ^{1}H NMR spectra were integrated based on typical chemical shift regions for DOM and included: materials derived from linear terpenoids (MDLT; 0.6−1.6 ppm); carboxyl-rich alicyclic molecules (CRAM; 1.6−3.2 ppm); carbohydrates and peptides (3.2−4.5 ppm); and aromatic and phenolic components (6.5−8.4 ppm).[115,116] NMR spectra were integrated using TopSpin (v. 3.6.2) software and expressed as percentage relative to the total ^{1}H signal which was normalized to 100%.

3. Results and Discussion

3.1 Burned soils are less labile than unburned soils

To evaluate the impacts of burn severity on the soil, we performed solid-state ^{13}C NMR spectroscopy on six samples (CNTL_S, CNTL_NS, LS_S, MS_S, MS_NS, HS_S) to visualize the differences in functionality across the burn severity gradient, with spectra reported in **Figure 3.2** and integration results in **Table 3.1**. We chose to analyze the ^{13}C isotope due to the low abundance of ^{15}N in natural samples. In the surface soils, there was a decrease in alkyl C and *O*-alkyl C from

the unburned control to the low severity soil, consistent with the results reported for *Pinus pinaster* duff, which indicated a dominance of alkyl C and *O*-alkyl C compounds in the unburned sample.[30] Conversely, aromatic and phenolic C was approximately 3x higher in the low severity soil, indicative of incomplete combustion.[63] The alkyl/*O*-alkyl C ratio, used as an indicator of SOM decomposition (a higher ratio indicates a higher relative stage of decomposition),[117–119] nearly doubled in the low severity soil compared to the control. From low to moderate severity, the relative proportion of alkyl C and *O*-alkyl C increased in the moderate severity surface soil, then decreased slightly from moderate to high. These shifts primarily resulted in decreases in the relative proportion of aromatic and phenolic C in the moderate and high severity samples; carboxylic + carbonyl C were slightly higher in the moderate and high severity surface soils compared to the control. Importantly, the alkyl/O-alkyl C ratio remained approximately double that of the control in all burned samples, which indicates that fire drives SOM chemistry towards more complex forms that are less preferred microbial substrates. This is also reflected in the aromatic C integration data (higher in burned soils), as aromatic C is generally considered to be less labile for microbial respiration than other C forms.[36,120,121] However, a separate study on the same samples presented here found that microbial genes from targeting aromatic compounds were present in the soils,[45] which indicates that aromatic substrates are utilized as C sources in the burned soils.

Table 3.1: Integration results for solid-state ^{13}C NMR spectroscopy for the burn severity gradient. Surface soils are denoted by (S) and near-surface soils are denoted by (NS). Chemical shift in reported in parts per million (ppm). This table lists the relative proportion of each SOM category to the total signal of ^{13}C across all regions.

	Relative Proportion of SOM categories to the total ^{13}C NMR signal				
Sample	Alkyl C (0-50 ppm)	*O*-alkyl C (50-100 ppm)	Aromatic & phenolic C (110-165 ppm)	Carboxylic + Carbonyl C (165-210 ppm)	Alkyl/*O*-alkyl carbon ratio
Control (S)	40	35	20	5	1.14
Low (S)	25	11	59	5	2.27

Moderate (S)	37	17	39	7	2.18
High (S)	35	13	46	6	2.69
Control (NS)	42	35	19	4	1.20
Moderate (NS)	41	25	31	3	1.64

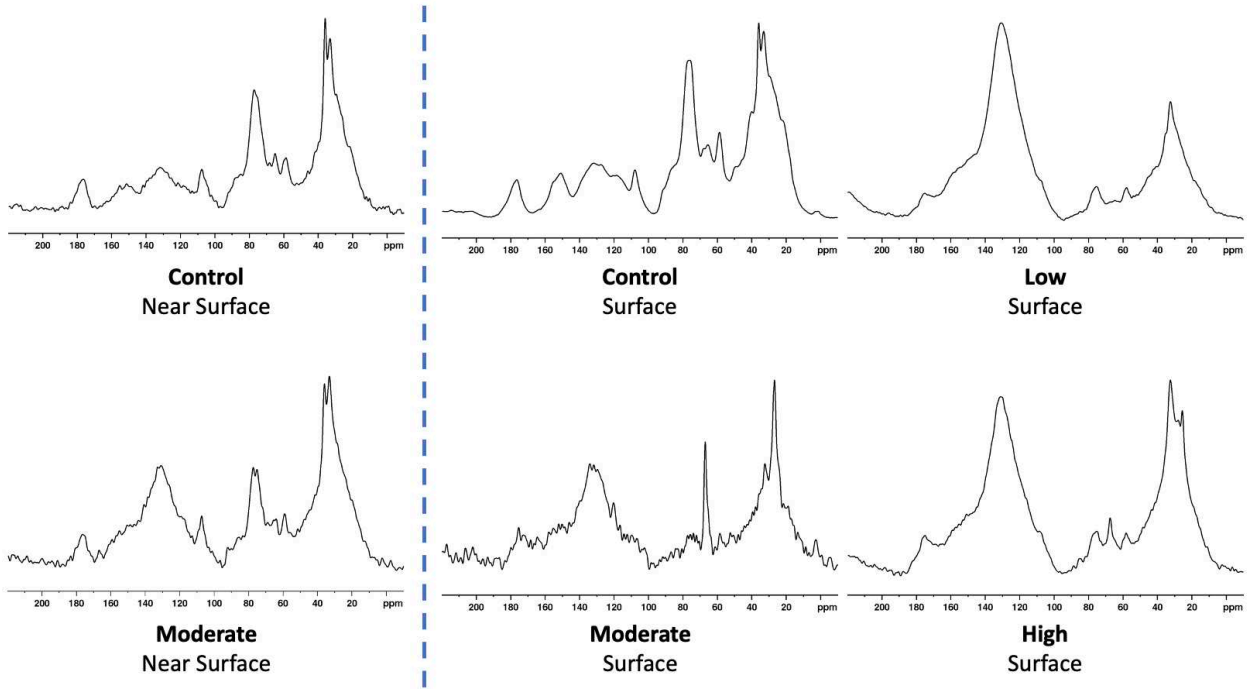

Figure 3.2: ^{13}C solid-state NMR spectra of the burn severity soil samples. Surface = 0-5 cm, Near Surface = 5-10 cm.

3.2 DOM displays burn severity-dependent trends in surface soils

We collected FT-ICR mass spectra for six soil water extracts along the burn severity gradient – four from surface soils (CNTL_S, LS_S, MS_S, HS_S) and two near-surface soils (CNTL_NS, MS_NS). To increase compositional coverage, we ionized samples in ESI negative and positive modes.[60] There were an average of 11320 assigned species in -ESI and 21377 in +ESI, and a substantial increase in the number of nitrogenated species in the burned soils relative to the unburned control, consistent with previously reported increases of CHNO in fire-impacted water extracts of Jeffrey pine (*P. jeffreyi*) needles and woody trunks in -ESI.[122] We plotted all elemental compositions identified in the analysis of the water-soluble soil extracts in van Krevelen diagrams

(H/C vs O/C) to provide rapid visualization of the data and highlight compositional differences between the samples in **Figure 3.3**.[105] Fire-impacted samples spanned a wide range of H/C ratios (0.2-1.9), with larger relative abundance of highly saturated compounds in the low and high severity burn samples. Maximum O/C ratios decreased with burn severity, as did average O/C (**Table C2**), consistent with carbonization and aromatization processes and a decrease in the lability of soil species reported for *P. pinaster* soils.[30] Within the N-containing species, we again observed an enrichment in highly saturated compounds in the low and high severity soils. O/C ratios in the nitrogenated species did not appear to be as dependent on burn severity as the total assignments, which demonstrates that O/C ratio is likely not a primary driver for biotic or abiotic transformations of these species.

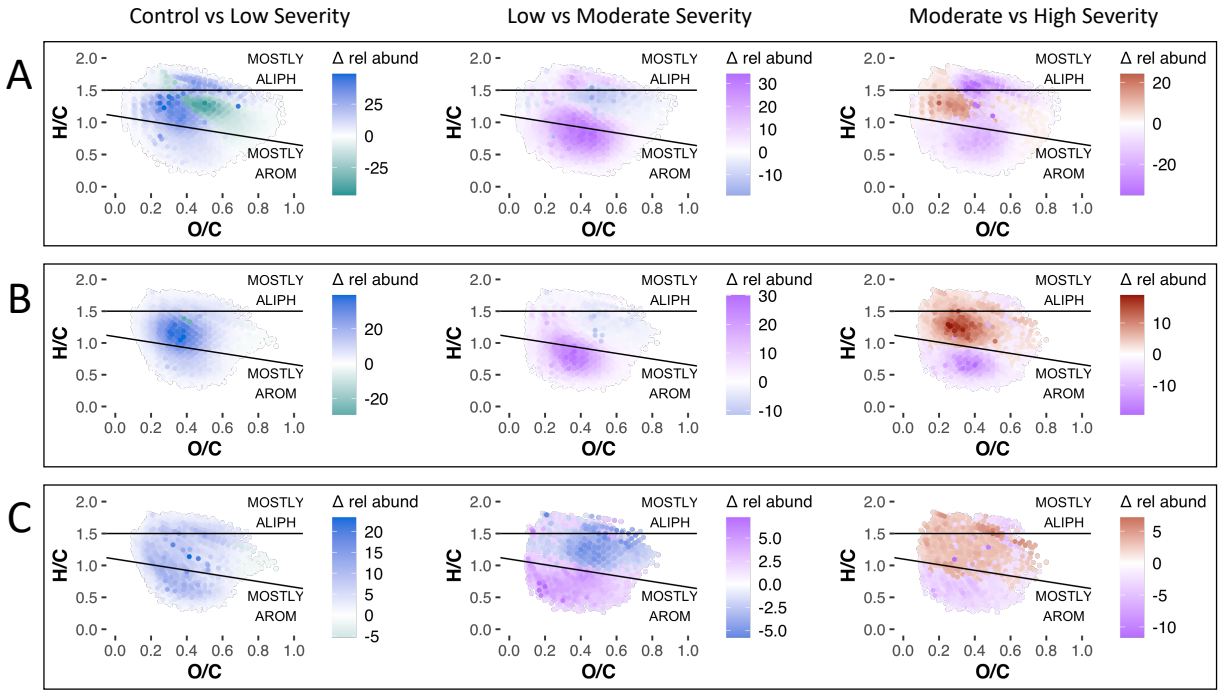

Figure 3.3: van Krevelen diagrams of the detected species of water-soluble soil extracts (0-5 cm) identified by +ESI FT-ICR MS. The top row (A) contains all formulas, the middle row (B) contains only CHNO molecular formulas, and (C) contains only the unique CHNO species. Each panel compares two samples, indicated by color. Larger changes in relative abundance (Δ rel abund) are indicated by more saturated colors. Formulas plotted below the line that intercepts at H/C 1.2 are

generally more aromatic in structure, while those plotting above the line that intercepts at H/C 1.5 are more aliphatic.[54]

Table 3.2: Integration results for solution-state ^{1}H NMR spectroscopy for the surface soil severity gradient. Chemical shift is reported in parts per million (ppm). This table lists the relative proportion of each DOM category to the total signal of ^{1}H across all regions.

	Relative proportion of soil-derived DOM categories to the total ^{1}H NMR signal			
Sample	MDLT (0.6-1.6 ppm)	CRAM (1.6-3.2 ppm)	Carbohydrates & peptides (3.2-4.5 ppm)	Aromatic & phenolic (6.5-8.4 ppm)
Control	34	37	22	7
Low	38	31	27	4
Moderate	34	32	25	9
High	36	31	26	7

To further analyze the alteration of DOM chemistry, we also performed solution-state ^{1}H NMR spectroscopy on DOM isolated from surface soils (CTNL_S, LS_S, MS_S, HS_S) in the burn severity gradient (**Table 3.2**). Relative to the control, there was little to no change in the relative proportion of materials derived from linear terpenoids (MDLT). Carboxyl-rich alicyclic molecules (CRAM) were lower in the burned samples, consistent with lower average O and O/C and lower average molecular weight in the FT-ICR mass spectra. Conversely, the relative contribution of soluble carbohydrates and peptides was higher in the burned samples, with a maximum intensity in the low severity soil extract, possibly indicative of cell lysis and residual necromass left behind after fire,[123] and compounded by the lightly combusted organic layer in the low severity soil. The relative contribution of aromatic and phenolic functional groups reached a maximum in the moderate severity soil extract, consistent with the calculated DBE and aromaticity index in the FT-ICR mass spectra (**Table 3.3**). These results are generally supported by previous studies across a wide range of environments, which reported increases in aromaticity following fire.[124] These results also indicate that the changes observed in the DOM chemistry are unique in

comparison to the SOM chemistry, as indicated by the ^{13}C NMR. It is likely that the changes in aromaticity observed in the bulk soils are larger than those reported in the solution-state due to solubility limitations of the aromatic compounds. Therefore, both the bulk soils and extractable DOM must be evaluated together in order to clearly identify changes to functionality which impact C and N cycling.

Table 3.3: Double bond equivalents (DBE) and modified aromaticity index (AI_{mod}) of the burned soil PPL extracts from the FT-ICR MS of ESI in both positive and negative ion modes.

Variable	Ionization Mode	Control	Low	Moderate	High
DBE	-ESI	14.3	15.0	16.3	13.8
DBE	+ESI	14.4	13.5	14.4	15.1
AI_{mod}	-ESI	0.311	0.367	0.434	0.380
AI_{mod}	+ESI	0.286	0.319	0.370	0.361

3.3 Nitrogen contents in surface soils were heavily influenced by fire activity

To further investigate the influence of fire on soil N species, we focused our analysis on the +ESI spectra, as this method has been reported to increase the compositional coverage of CHNO species compared to -ESI.[60] **Table 3.4** reports the average C, N and C:N of each of the surface soil samples determined by FT-ICR MS. We found that fire lowered the average C assigned, but this value was not dependent on burn severity. Average N was 3x higher than the control for the low and moderate severity soils and was highest for the high severity soil. This greatly influenced the C:N ratio of the samples, which was lowest for the low severity soil. Enrichment of N species in burned soils has been observed in controlled lab settings,[59] and may be attributed to increases in pyridine, benzonitrile, and pyrrole functionalities at higher burn temperatures which were identified in soils affected by the 2013 Rim Fire in California.[125] Additionally, the lysing of soil microorganisms during soil heating represents a potential source

of labile organic C and N associated with necromass, which may also contribute to increased dissolved N species in the high and moderate mineral soils.[126]

Table 3.4: Average (Avg) oxygen (O), carbon (C), nitrogen (N), calculated C:N ratios, O:C, and mass of the burn severity gradient shallow soils determined by +ESI FT-ICR MS.

Severity	Avg O	Avg C	Avg N	C:N	O:C	Avg Mass (m/z)
Control	113.0	37.1	0.454	**56.2**	0.423	635
Low	11.7	29.6	1.11	**18.6**	0.401	596
Moderate	11.3	29.4	1.10	**22.9**	0.389	584
High	11.1	29.4	1.18	**21.7**	0.387	579

Unique N species were compared across the burn severity gradient (Control vs Low, Low vs Moderate, and Moderate vs High) to determine the major changes which occur at each severity (**Table 3.5**). Because isotopes are not differentiated, there may be additional transformations that are unable to be resolved here. From the control to low burn severity, 99817 unique N species were formed, likely from incomplete combustion of SOM.[59] Only 297 of the 5632 N species assigned in the control were unique, which indicates that the unique CHNO in the low severity soil is likely newly formed. There is also a clear change in N speciation through the formation of molecules which are more N-dense (containing more N per molecule) which results in an expanded range of oxygenation and increased N in the low severity soil (**Figure C1A**). From low to moderate severity, 3592 formulas are lost from the low severity soil, and 2153 species are newly formed in the moderate severity sample. Transformations occur across all N classes, and do not appear to preferentially impact any one class over another (**Figure C1B**). From moderate to high severity, the largest losses are in the N_1 class (i.e., compound containing one N atom;

Moderate) and there are substantial increases in the N_3-N_5 class (High) compared to the other transitions. The loss of N_1 formulas was primarily accompanied by a shift towards lower oxygen in the high severity soil from N_{1-3}, and a non-preferential increase in species containing N_{4-5} (**Figure C1C**). N enrichment may be driven by a number of combustion-catalyzed processes, including the Maillard reaction pathway and the formation of covalent bonds between burned SOM and NH_3-N.[59,127,128] These results suggest that soils that burned at higher severities contain higher polyaromatic N and are potentially more resistant to microbial degradation. Therefore, the observed decrease in C:N ratios in FT-ICR MS data may indicate a higher proportion of immobilized N,[129] as observed in char derived from lignin, cellulose, grass, and wood produced at 350°C and 450°C[130] rather than a more preferential substrate as typically interpreted from bulk data. Additionally, these species may contribute to increased toxicity in water extracts, as N-containing species have been shown to increase in toxicity following photocatalysis.[131]

Table 3.5: Unique N species identified through +ESI FT-ICR MS. Unique formulas are determined only between the two samples compared, denoted in the top row. N1 includes only molecules containing exactly one N, which applies to all the other N numbers as well.

Unique N species	Control vs Low		Low vs Moderate		Moderate vs High	
	Control	Low	Low	Moderate	Moderate	High
All N	297	9817	3592	2153	1499	1932
N_1	295	3464	2091	891	981	358
N_2	2	2850	670	560	346	410
N_3	0	1602	378	504	121	532
N_4	N/A	1338	261	126	39	379
N_5	N/A	563	92	72	12	262

The m/z vs C:N of each CHNO species was plotted in **Figure 3.4** to visualize differences in molecular mass and N content along the burn severity gradient. We found that although the average mass of the formulas decreased as burn severity increased (**Table 3.4**), the relative abundance of nitrogenated high molecular weight species increased with burn severity. N-

heterocyclic structures are known to form during incomplete combustion of SOM,[20,130,132] which is thought to be less labile compared to unburned DON.[133] The shift in DON functionality from peptides in unburned soils[132] to polycyclic aromatic compounds (i.e., indoles and carbazoles)[134] likely transforms SOM into a less bioavailable form, of which the microbial genes required for processing may not be widespread in the soil microbiome. To investigate this, we used HMMER[107] against HMMs curated from UniProt[108] to identify genes that constitute the primary enzyme for degrading carbazole (carbazole 1,9a-dioxgenase)[109] within the metagenome-assembled genome (MAG) dataset curated from these soils in Nelson et al (2022)[45]. Of the total 637 MAGs, only 13 were actively expressing (via metatranscriptomics data) the majority of the genes required for the multicomponent enzyme (*carAd, carAa, carAc*), suggesting that these compounds are widely recalcitrant to bacterial degradation. Therefore, newly formed N species may represent an important N sink after fire in high severity burned lodgepole pine soils. Broad shifts in N speciation throughout the burn severity gradient, along with the loss of O-containing functional groups (**Table C2**), may be important for differences in soil structure after burn[135] and large alterations in microbial activity which have previously been reported[45].

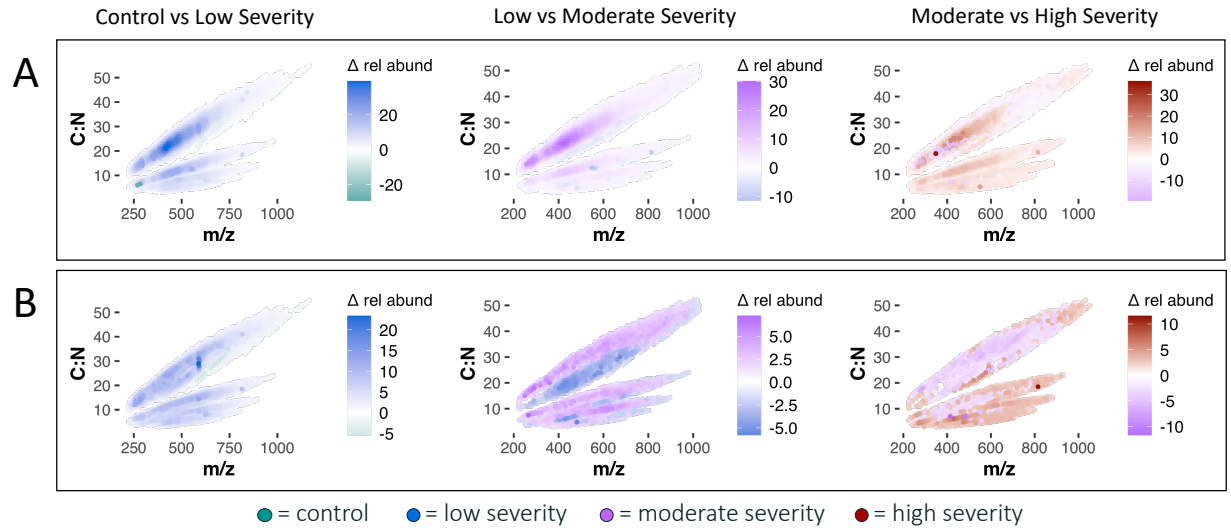

Figure 3.4: Plots of the mass to charge (m/z) and nitrogen to carbon (N/C) ratios of the N-containing (i.e., CHNO) fraction obtained via +ESI FT-ICR MS of PPL extracts of a Ryan fire soil burn severity gradient. A displays plots with all the assigned N species; B displays only the unique species between the two spectra. Changes in relative abundance (Δ rel abund) are indicated by darker colors. Green dots denote higher abundance in the control, and blue, purple, and red dots correspond to higher abundance in the low, moderate, and high severity extracts, respectively.

3.4 Surface soils are more influenced by fire than near-surface soils

To determine how sampling depth influenced speciation, we compared the control and moderate soils at surface (CNTL_S, MS_S) and near-surface (CNTL_NS, CNTL_NS) sampling depths. The near-surface control sample had 17653 formulas assigned, 5032 of which contained N. Of the 17870 formulas assigned to the near-surface moderate soil, 6212 were N-containing. The increase in N species for the near-surface soils is much smaller than the surface soils, which increased from 5632 in the control to 13813 in the moderate surface soil. To further investigate the influence of fire on N species in near-surface soils, we plotted the individual heteroatoms (N_xO_x) in a bar plot, with formula counts on the y-axis (**Figure C2**). Between the surface and near-surface samples in the control, little variation is noted aside that the surface soil was slightly shifted towards lower oxygenation compared to the near-surface soil. There is a clear difference in N content, where the surface samples are far more N-enriched than the near-surface samples. These results are supported by previous literature which indicates that fire generally impacts approximately the top 5 cm of mineral soils, with much less influence of heat further down the soil column.[124] However, we did note some important shifts between the control and moderate near-surface soils, as illustrated in **Figure 3.5**. Specifically, the moderate severity soil was shifted towards lower oxygen levels, consistent with our observations in the surface samples. We also found that in the more N-rich species (N_2-N_4), there were far more assignments in the moderate severity soil compared to the control. Therefore, our results indicate that even though the largest

effects are seen closer to the soil surface (i.e., surface soils), the effects of fire on N speciation persist at least 10 cm down the soil column.

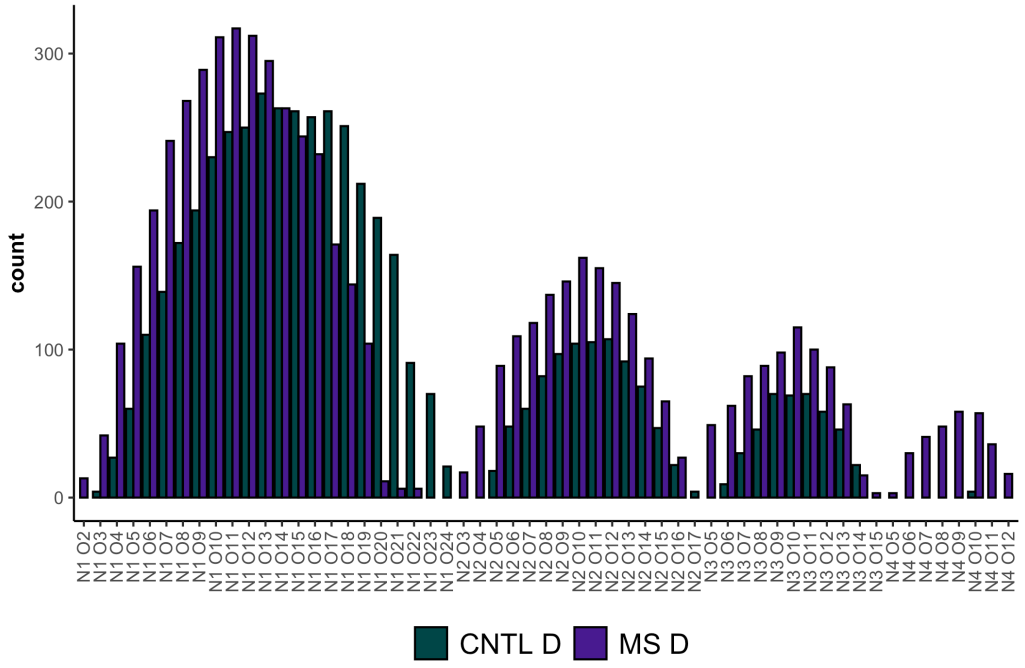

Figure 3.5: Bar plot of the nitrogen-containing classes from the +ESI FT-ICRMS of control and moderate severity near-surface samples. The x-axis is organized by heteroatoms, grouped first by the number of N atoms (1-4) assigned to the formulas and second by the number of oxygen atoms, increasing from left to right. The y-axis depicts the number of formulas assigned to each heteroatom class.

The relative contribution of all SOM categories determined by solid-state ^{13}C NMR was approximately the same for the surface and near-surface samples in the control soil (**Table 3.1**), consistent with the FT-ICR MS results and indicating that the organic horizon contributed minimally to the overall signal. However, there were notable differences between the near-surface control and moderate soils. The relative proportion of *O*-alkyl C decreased by 10, while the aromatic and phenolic C signal increased by 11 in the moderate near-surface soil compared to the control. Shifts in the relative proportion of SOM signal indicate that the functionality of the soils

was indeed affected by the burn, even at the lower sampling depths. The moderate surface soil was more aromatic and displayed a lower proportion of *O*-alkyl C than the near-surface sample, consistent with previous studies which reported that the degree of carbonization and aromatization is lower in *Pinus pinaster* mineral soils than in duff.[30] Because the near-surface soil is not as highly impacted as the surface soil, it likely contains more labile substrates for microbial degradation. The alkyl/*O*-alkyl C ratio supports this hypothesis, as the values are lower in the burned near-surface soil than the surface soil. Complementary metagenomics analyses indicated major shifts in microbial processing of substrates in surface soils which were not as prevalent in the near-surface soils,[45] suggesting that while there are some differences in soil chemistry of the control and moderate near-surface samples, these changes are not nearly as influential as those in the surface soils.

3.5 Acute toxicity of soil extract from fire-impacted soils as a function of burn severity

Carbon normalized burn severity water extracts of six soils were analyzed for acute toxicity by Microtox® to determine toxicity as a function of sample composition rather than concentration. Higher bioluminescence inhibition of *A. fischeri*, measured per unit C, corresponds to higher acute toxicity.[88] **Figure 3.6** shows the acute toxicity of water-soluble species per unit C extracted from burned soils. We observed an increase in toxicity with increasing burn severity in the surface soils, and no change in the near-surface soils. For surface soils, the high severity (HS_S) has the highest acute toxicity (43%) followed by moderate (MS_S, 17%) and low severity (LS_S 10%). The toxicity of the species extracted from the near-surface soils were approximately equal, with the unburned control (CNTL_NS) slightly higher than the moderate severity (MS_NS) (14.7% and 14.1%, respectively).

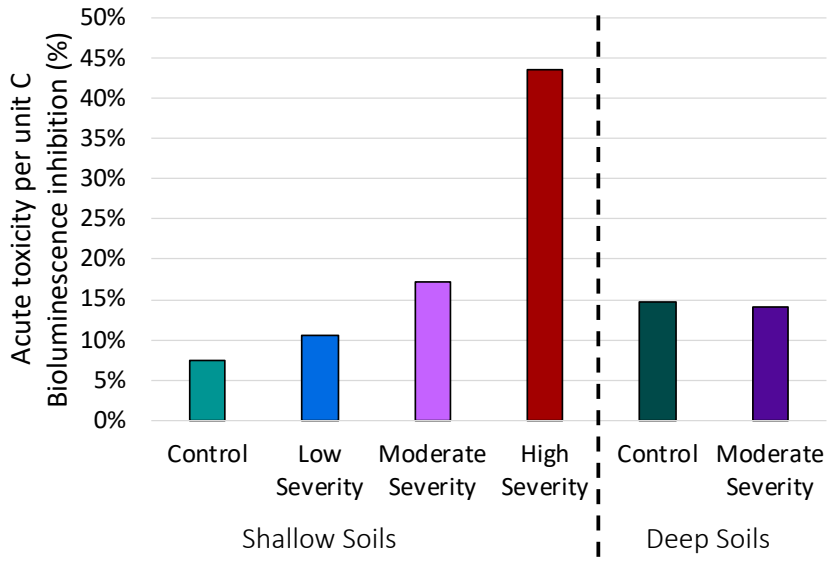

Figure 3.6: 15 minute % bioluminescence inhibition of burned soil water extracts (n = 1); higher % inhibition corresponds to higher toxicity. Surface soil samples are to the left of the dotted line; near-surface soil samples are to the right.

Microtox® bioassays have previously been applied to determine the acute toxicity of aqueous ash extracts and runoff following wildfires, both of which inhibited the luminescence of *A. fischeri*.[80,81] The highest inhibitory effects were reported for the highest ash concentrations [81]; more "complete" combustion in high severity soils may explain the increase in toxicity reported here. A toxicity study using *Daphnia magna* found pH to be a strong influence on toxicity; [136] however, pH cannot explain the increases in toxicity seen here, as maximum pH values were observed in the moderate severity surface soil (average pH = 8.00), while the near-surface samples did not appear to be affected (average pH ranging between 7.11 to 7.71) (**Table 3.6**). Previous studies have indicated that the formation of N-heterocycles may contribute to increased toxicity,[68,69,131] which likely contributes to the observed increases in toxicity here. However, further research is required to identify the specific drivers of toxicity increases in burned organic matter. The observed increase in surface soil extract toxicity emphasizes the role of wildfire as a potential source of diffuse contamination for downstream water bodies.

Table 3.6: Average pH for burned soils from Ryan and Badger Creek fires.

Severity	Soil depth (cm)	pH
Control	0-5	6.80
Low	"	7.64
Moderate	"	8.00
High	"	7.69
Control	5-10	7.34
Low	"	7.71
Moderate	"	7.43
High	"	7.11

4. CONCLUSION

Molecular-level analysis of C and N contained in soil organic matter across a burn severity gradient allowed us to make inferences regarding how organic N is altered by wildfire in high-elevation forests. Although high-resolution results for only gradient are reported here, trends identified from bulk data collected from four burn severity gradients indicate that these results are likely representative of all the soils we collected. Our results suggest that N-dense heterocycles (e.g., carbazoles, indoles) are formed at higher fire severities, which has implications for post-fire C and N cycling since evidence of processing of such compounds was not widespread in the soil microbiome. We noted a shift in N speciation in the 5-10 cm depth, which indicates that heating at that depth was sufficient to shift SOM chemistry. We also provide evidence that soil toxicity is dependent on burn severity, although further research is required to identify the specific drivers of soil toxicity increases and their potential downstream effects. Collectively, these results emphasize the importance of molecular-level characterization of SOM components to evaluate the impacts of

fire on C and N biogeochemistry and provides new insight into the impact of severe wildfire on soil chemistry in forest ecosystems.

5. AUTHOR CONTRIBUTIONS

According to CRediT criteria, my contributions to this work included conceptualization, data curation, formal analysis, investigation, methodology, visualization, writing – original draft, and writing – reviewing and editing. Contributions by A.M.M. included data curation, methodology, resources, validation, and writing – review and editing. Contributions by M.J.S. included data curation, methodology, funding acquisition, and writing – review and editing. Contributions by Huan Chen included data curation, methodology, and writing – review and editing. Contributions by N.S. included data curation and visualization. Contributions by T.S.F. included data curation and methodology. Contributions by A.R.N. included data curation, formal analysis, and writing – review and editing. Contributions by C.C.R. included data curation, investigation, resources, validation, writing – original draft, and writing – review and editing. Contributions by M.J.W. included data curation, funding acquisition, project administration, resources, and writing – review and editing. Contributions by T.B. included conceptualization, funding acquisition, project administration, resources, writing – original draft, and writing – review and editing.

REFERENCES

(1) Westerling, A. L.; Hidalgo, H. G.; Cayan, D. R.; Swetnam, T. W. Warming and Earlier Spring Increase Western U.S. Forest Wildfire Activity. *Science (1979)* **2006**, *313* (5789), 940–943. https://doi.org/10.1126/science.1128834.
(2) Lannom, K. O.; Tinkham, W. T.; Smith, A. M. S.; Abatzoglou, J.; Newingham, B. A.; Hall, T. E.; Morgan, P.; Strand, E. K.; Paveglio, T. B.; Anderson, J. W.; Sparks, A. M. Defining Extreme Wildland Fires Using Geospatial and Ancillary Metrics. *Int J Wildland Fire* **2014**, *23* (3), 322–337. https://doi.org/10.1071/WF13065.
(3) Williams, A. P.; Abatzoglou, J. T. Recent Advances and Remaining Uncertainties in Resolving Past and Future Climate Effects on Global Fire Activity. *Current Climate Change Reports*. Springer March 1, 2016. https://doi.org/10.1007/s40641-016-0031-0.
(4) Dennison, P. E.; Brewer, S. C.; Arnold, J. D.; Moritz, M. A. Large Wildfire Trends in the Western United States, 1984-2011. *Geophys Res Lett* **2014**, *41* (8), 2928–2933. https://doi.org/10.1002/2014GL059576.
(5) Abatzoglou, J. T.; Kolden, C. A.; Williams, A. P.; Lutz, J. A.; Smith, A. M. S. Climatic Influences on Interannual Variability in Regional Burn Severity across Western US Forests. *Int J Wildland Fire* **2017**, *26* (4), 269–275. https://doi.org/10.1071/WF16165.
(6) Westerling, A. L. R. Increasing Western US Forest Wildfire Activity: Sensitivity to Changes in the Timing of Spring. *Philosophical Transactions of the Royal Society B: Biological Sciences* **2016**, *371* (1696). https://doi.org/10.1098/rstb.2015.0178.
(7) Alizadeh, M. R.; Abatzoglou, J. T.; Luce, C. H.; Adamowski, J. F.; Farid, A.; Sadegh, M. Warming Enabled Upslope Advance in Western US Forest Fires. *PNAS* **2021**, *118*. https://doi.org/10.1073/pnas.2009717118/-/DCSupplemental.
(8) Pausas, J. G.; Keeley, J. E. Wildfires as an Ecosystem Service. *Front Ecol Environ* **2019**, *17* (5), 289–295. https://doi.org/10.1002/fee.2044.
(9) Doerr, S. H.; Santín, C. Global Trends in Wildfire and Its Impacts: Perceptions versus Realities in a Changing World. *Philosophical Transactions of the Royal Society B: Biological Sciences* **2016**, *371* (1696). https://doi.org/10.1098/rstb.2015.0345.
(10) Parsons, A.; Robichaud, P. R.; Lewis, S. A.; Napper, C.; Clark, J. T. Field Guide for Mapping Post-Fire Soil Burn Severity. *General Technical Report RMRS-GTR-243* **2010**.
(11) Keeley, J. E. Fire Intensity, Fire Severity and Burn Severity: A Brief Review and Suggested Usage. *Int J Wildland Fire* **2009**, *18* (1), 116–126. https://doi.org/10.1071/WF07049.
(12) Doerr, S. H.; Santín, C.; Merino, A.; Belcher, C. M.; Baxter, G. Fire as a Removal Mechanism of Pyrogenic Carbon From the Environment: Effects of Fire and Pyrogenic Carbon Characteristics. *Front Earth Sci (Lausanne)* **2018**, *6*. https://doi.org/10.3389/feart.2018.00127.
(13) Walker, X. J.; Baltzer, J. L.; Cumming, S. G.; Day, N. J.; Ebert, C.; Goetz, S.; Johnstone, J. F.; Potter, S.; Rogers, B. M.; Schuur, E. A. G.; Turetsky, M. R.; Mack, M. C. Increasing Wildfires Threaten Historic Carbon Sink of Boreal Forest Soils. *Nature* **2019**, *572* (7770), 520–523. https://doi.org/10.1038/s41586-019-1474-y.
(14) Jain, T. B.; Pilliod, D. S.; Graham, R. T.; Lentile, L. B.; Sandquist, J. E. Index for Characterizing Post-Fire Soil Environments in Temperate Coniferous Forests. *Forests* **2012**, *3* (3), 445–466. https://doi.org/10.3390/f3030445.
(15) Merino, A.; Chávez-Vergara, B.; Salgado, J.; Fonturbel, M. T.; García-Oliva, F.; Vega, J. A. Variability in the Composition of Charred Litter Generated by Wildfire in Different Ecosystems. *Catena (Amst)* **2015**, *133*, 52–63. https://doi.org/10.1016/j.catena.2015.04.016.

(16) Santín, C.; Doerr, S. H.; Kane, E. S.; Masiello, C. A.; Ohlson, M.; de la Rosa, J. M.; Preston, C. M.; Dittmar, T. Towards a Global Assessment of Pyrogenic Carbon from Vegetation Fires. *Glob Chang Biol* **2016**, *22* (1), 76–91. https://doi.org/10.1111/gcb.12985.
(17) Shakesby, R. A.; Doerr, S. H. Wildfire as a Hydrological and Geomorphological Agent. *Earth Sci Rev* **2006**, *74* (3–4), 269–307. https://doi.org/10.1016/j.earscirev.2005.10.006.
(18) Kong, J.; Xiang, X.; Yang, J. Wildfire Alters the Linkage between Total and Available Soil C:N:P Ratios and the Stoichiometric Effects on Fine Root Growth in a Chinese Boreal Larch Forest. *Plant Soil* **2021**. https://doi.org/10.1007/s11104-021-05215-1.
(19) Certini, G. Effects of Fire on Properties of Forest Soils: A Review. *Oecologia* **2005**, *143* (1), 1–10. https://doi.org/10.1007/s00442-004-1788-8.
(20) Knicker, H.; Hilscher, A.; González-Vila, F. J.; Almendros, G. A New Conceptual Model for the Structural Properties of Char Produced during Vegetation Fires. *Org Geochem* **2008**, *39* (8), 935–939. https://doi.org/10.1016/j.orggeochem.2008.03.021.
(21) Moody, J. A.; Ebel, B. A.; Nyman, P.; Martin, D. A.; Stoof, C.; Mckinley, R. Relations between Soil Hydraulic Properties and Burn Severity. *Int J Wildland Fire* **2016**, *25* (3), 279–293. https://doi.org/10.1071/WF14062.
(22) Rhoades, C. C.; Chow, A. T.; Covino, T. P.; Fegel, T. S.; Pierson, D. N.; Rhea, A. E. The Legacy of a Severe Wildfire on Stream Nitrogen and Carbon in Headwater Catchments. *Ecosystems* **2018**. https://doi.org/10.1007/s10021-018-0293-6.
(23) Arshad, M. A.; Martin, S. *Identifying Critical Limits for Soil Quality Indicators in Agro-Ecosystems*; 2002; Vol. 88.
(24) Roem, W. J.; Berendse, F. *Soil Acidity and Nutrient Supply Ratio as Possible Factors Determining Changes in Plant Species Diversity in Grassland and Heathland Communities*. www.elsevier.com/locate/biocon.
(25) Pellegrini, A. F. A.; Ahlström, A.; Hobbie, S. E.; Reich, P. B.; Nieradzik, L. P.; Staver, A. C.; Scharenbroch, B. C.; Jumpponen, A.; Anderegg, W. R. L.; Randerson, J. T.; Jackson, R. B. Fire Frequency Drives Decadal Changes in Soil Carbon and Nitrogen and Ecosystem Productivity. *Nature* **2018**, *553* (7687), 194–198. https://doi.org/10.1038/nature24668.
(26) Dove, N. C.; Safford, H. D.; Bohlman, G. N.; Estes, B. L.; Hart, S. C. High-Severity Wildfire Leads to Multi-Decadal Impacts on Soil Biogeochemistry in Mixed-Conifer Forests. *Ecological Applications* **2020**, *0* (0), 1–18. https://doi.org/10.1002/eap.2072.
(27) Hartford, R. A.; Frandsen, W. H. *When It's Hot, It's Hot ... or Maybe It's Not! (Surface Flaming May Not Portend Extensive Soil Heating)*; 1992; Vol. 2.
(28) Pulido-Chavez, M. F.; Alvarado, E. C.; DeLuca, T. H.; Edmonds, R. L.; Glassman, S. I. High-Severity Wildfire Reduces Richness and Alters Composition of Ectomycorrhizal Fungi in Low-Severity Adapted Ponderosa Pine Forests. *For Ecol Manage* **2021**, *485*. https://doi.org/10.1016/j.foreco.2021.118923.
(29) Fernández-García, V.; Marcos, E.; Fernández-Guisuraga, J. M.; Taboada, A.; Suárez-Seoane, S.; Calvo, L. Impact of Burn Severity on Soil Properties in a Pinus Pinaster Ecosystem Immediately after Fire. *Int J Wildland Fire* **2019**, *28* (5), 354–364. https://doi.org/10.1071/WF18103.
(30) Merino, A.; Fonturbel, M. T.; Fernández, C.; Chávez-Vergara, B.; García-Oliva, F.; Vega, J. A. Inferring Changes in Soil Organic Matter in Post-Wildfire Soil Burn Severity Levels in a Temperate Climate. *Science of the Total Environment* **2018**, *627*, 622–632. https://doi.org/10.1016/j.scitotenv.2018.01.189.

(31) Lagomarsino, A.; Moscatelli, M. C.; di Tizio, A.; Mancinelli, R.; Grego, S.; Marinari, S. Soil Biochemical Indicators as a Tool to Assess the Short-Term Impact of Agricultural Management on Changes in Organic C in a Mediterranean Environment. *Ecol Indic* **2009**, *9* (3), 518–527. https://doi.org/10.1016/j.ecolind.2008.07.003.
(32) Adetunji, A. T.; Lewu, F. B.; Mulidzi, R.; Ncube, B. *The Biological Activities of β-Glucosidase, Phosphatase and Urease as Soil Quality Indicators: A Review*; 2017; Vol. 17.
(33) Li, Y. T.; Rouland, C.; Benedetti, M.; Li, F. bai; Pando, A.; Lavelle, P.; Dai, J. Microbial Biomass, Enzyme and Mineralization Activity in Relation to Soil Organic C, N and P Turnover Influenced by Acid Metal Stress. *Soil Biol Biochem* **2009**, *41* (5), 969–977. https://doi.org/10.1016/j.soilbio.2009.01.021.
(34) Santín, C.; Doerr, S. H. Fire Effects on Soils: The Human Dimension. *Philosophical Transactions of the Royal Society B: Biological Sciences*. Royal Society of London June 5, 2016. https://doi.org/10.1098/rstb.2015.0171.
(35) Singh, N.; Abiven, S.; Torn, M. S.; Schmidt, M. W. I. Fire-Derived Organic Carbon in Soil Turns over on a Centennial Scale. *Biogeosciences* **2012**, *9* (8), 2847–2857. https://doi.org/10.5194/bg-9-2847-2012.
(36) Schmidt, M. W. I.; Noack, A. G. Black Carbon in Soils and Sediments: Analysis, Distribution, Implications, and Current Challenges. *Global Biogeochemical Cycles*. Blackwell Publishing Ltd September 1, 2000, pp 777–793. https://doi.org/10.1029/1999GB001208.
(37) Knicker, H. How Does Fire Affect the Nature and Stability of Soil Organic Nitrogen and Carbon? A Review. *Biogeochemistry* **2007**, *85* (1), 91–118. https://doi.org/10.1007/s10533-007-9104-4.
(38) Turner, M. G. *Disturbance and Landscape Dynamics in a Changing World*; 2010; Vol. 91.
(39) Liu, S.; Bond-Lamberty, B.; Hicke, J. A.; Vargas, R.; Zhao, S.; Chen, J.; Edburg, S. L.; Hu, Y.; Liu, J.; McGuire, A. D.; Xiao, J.; Keane, R.; Yuan, W.; Tang, J.; Luo, Y.; Potter, C.; Oeding, J. Simulating the Impacts of Disturbances on Forest Carbon Cycling in North America: Processes, Data, Models, and Challenges. *Journal of Geophysical Research: Biogeosciences*. Blackwell Publishing Ltd December 1, 2011. https://doi.org/10.1029/2010JG001585.
(40) Franklin, J.; Syphard, A. D.; He, H. S.; Mladenoff, D. J. Altered Fire Regimes Affect Landscape Patterns of Plant Succession in the Foothills and Mountains of Southern California. *Ecosystems* **2005**, *8* (8), 885–898. https://doi.org/10.1007/s10021-005-0017-6.
(41) Bond-Lamberty, B.; Peckham, S. D.; Ahl, D. E.; Gower, S. T. Fire as the Dominant Driver of Central Canadian Boreal Forest Carbon Balance. *Nature* **2007**, *450* (7166), 89–92. https://doi.org/10.1038/nature06272.
(42) Nave, L. E.; Vance, E. D.; Swanston, C. W.; Curtis, P. S. Fire Effects on Temperate Forest Soil C and N Storage. *Ecological Applications* **2011**, *21* (4), 1189–1201. https://doi.org/10.1890/10-0660.1.
(43) Moody, J. A.; Shakesby, R. A.; Robichaud, P. R.; Cannon, S. H.; Martin, D. A. Current Research Issues Related to Post-Wildfire Runoff and Erosion Processes. *Earth Sci Rev* **2013**, *122*, 10–37. https://doi.org/10.1016/j.earscirev.2013.03.004.
(44) Dzwonko, Z.; Loster, S.; Gawroński, S. Impact of Fire Severity on Soil Properties and the Development of Tree and Shrub Species in a Scots Pine Moist Forest Site in Southern Poland. *For Ecol Manage* **2015**, *342*, 56–63. https://doi.org/10.1016/j.foreco.2015.01.013.
(45) Nelson, A. R.; Narrowe, A. B.; Rhoades, C. C.; Fegel, T. S.; Daly, R. A.; Roth, H. K.; Chu, R. K.; Amundson, K. K.; Young, R. B.; Steindorff, A. S.; Mondo, S. J.; Grigoriev, I. v.;

Salamov, A.; Borch, T.; Wilkins, M. J. Wildfire-Dependent Changes in Soil Microbiome Diversity and Function. *Nat Microbiol* **2022**. https://doi.org/10.1038/s41564-022-01203-y.
(46) Hernández, T.; García, · C; Reinhardt, · I. *Short-Term Effect of Wildfire on the Chemical, Biochemical and Microbiological Properties of Mediterranean Pine Forest Soils*; 1997; Vol. 25.
(47) Zhong, Z.; Makeschin, F. Soluble Organic Nitrogen in Temperate Forest Soils. *Soil Biology & Biogeochemistry* **2003**, *35*, 333–338.
(48) Mengel, K.; Schneider, B.; Kosegarten, H. Nitrogen Compounds Extracted by Electroultrafiltration (EUF) or CaCl2 Solution and Their Relationships to Nitrogen Mineralization in Soils. *Journal of Plant Nutrition and Soil Science* **1999**, *162* (2), 139–148. https://doi.org/10.1002/(SICI)1522-2624(199903)162:2<139::AID-JPLN139>3.0.CO;2-6.
(49) Smolander, A.; Kitunen, V.; Mälkönen, E.; Smolander, A.; Kitunen, V.; Mälkönen, E. *Dissolved Soil Organic Nitrogen and Carbon in a Norway Spruce Stand and an Adjacent Clear-Cut*; Springer-Verlag, 2001; Vol. 33.
(50) Andersson, S.; Nilsson, S. I.; Saetre, P. Leaching of Dissolved Organic Carbon (DOC) and Dissolved Organic Nitrogen (DON) in Mor Humus as Affected by Temperature and PH. *Soil Biology & Biogeochemistry* **2000**, *32*, 1–10.
(51) Nasholm, T.; Ekbald, A.; Nordin, A.; Giesler, R.; Hogberg, M.; Hogberg, P. Boreal Forest Plants Take up Organic Nitrogen. *Nature* **1998**, *392*, 914–916.
(52) Nebbioso, A.; Piccolo, A. Molecular Characterization of Dissolved Organic Matter (DOM): A Critical Review. *Anal Bioanal Chem* **2013**, *405* (1), 109–124. https://doi.org/10.1007/s00216-012-6363-2.
(53) D'Andrilli, J.; Cooper, W. T.; Foreman, C. M.; Marshall, A. G. An Ultrahigh-Resolution Mass Spectrometry Index to Estimate Natural Organic Matter Lability. *Rapid Communications in Mass Spectrometry* **2015**, *29* (24), 2385–2401. https://doi.org/10.1002/rcm.7400.
(54) Koch, B. P.; Dittmar, T. From Mass to Structure: An Aromaticity Index for High-Resolution Mass Data of Natural Organic Matter. *Rapid Communications in Mass Spectrometry* **2006**, *20* (5), 926–932. https://doi.org/10.1002/rcm.2386.
(55) Luo, L.; Chen, Z.; Lv, J.; Cheng, Y.; Wu, T.; Huang, R. Molecular Understanding of Dissolved Black Carbon Sorption in Soil-Water Environment. *Water Res* **2019**, *154*, 210–216. https://doi.org/10.1016/j.watres.2019.01.060.
(56) de la Rosa, J. M.; Knicker, H. Bioavailability of N Released from N-Rich Pyrogenic Organic Matter: An Incubation Study. *Soil Biol Biochem* **2011**, *43* (12), 2368–2373. https://doi.org/10.1016/j.soilbio.2011.08.008.
(57) Jiménez-Morillo, N. T.; de la Rosa, J. M.; Waggoner, D.; Almendros, G.; González-Vila, F. J.; González-Pérez, J. A. Fire Effects in the Molecular Structure of Soil Organic Matter Fractions under Quercus Suber Cover. *Catena (Amst)* **2016**, *145*, 266–273. https://doi.org/10.1016/j.catena.2016.06.022.
(58) Roth, H. K.; Nelson, A. R.; McKenna, A. M.; Fegel, T. S.; Young, R. B.; Rhoades, C. C.; Wilkins, M. J.; Borch, T. Impact of Beaver Ponds on Biogeochemistry of Organic Carbon and Nitrogen along a Fire-Impacted Stream. *Environ Sci Process Impacts* **2022**, *24* (10), 1661–1677. https://doi.org/10.1039/D2EM00184E.
(59) Bahureksa, W.; Young, R. B.; McKenna, A. M.; Chen, H.; Thorn, K. A.; Rosario-Ortiz, F. L.; Borch, T. Nitrogen Enrichment during Soil Organic Matter Burning and Molecular Evidence of Maillard Reactions. *Environ Sci Technol* **2022**, acs.est.1c06745. https://doi.org/10.1021/acs.est.1c06745.

(60) Roth, H. K.; Borch, T.; Young, R. B.; Bahureksa, W.; Blakney, G. T.; Nelson, A. R.; Wilkins, M. J.; McKenna, A. M. Enhanced Speciation of Pyrogenic Organic Matter from Wildfires Enabled by 21 T FT-ICR Mass Spectrometry. *Anal Chem* **2022**, acs.analchem.1c05018. https://doi.org/10.1021/acs.analchem.1c05018.
(61) Schmidt, M. W. I.; Torn, M. S.; Abiven, S.; Dittmar, T.; Guggenberger, G.; Janssens, I. A.; Kleber, M.; Kögel-Knabner, I.; Lehmann, J.; Manning, D. A. C.; Nannipieri, P.; Rasse, D. P.; Weiner, S.; Trumbore, S. E. Persistence of Soil Organic Matter as an Ecosystem Property. *Nature* **2011**, *478* (7367), 49–56. https://doi.org/10.1038/nature10386.
(62) Ping, X.; Chang, Y.; Liu, M.; Hu, Y.; Huang, W.; Shi, S.; Jia, Y.; Li, D. Carbon Emission and Redistribution among Forest Carbon Pools, and Change in Soil Nutrient Content after Different Severities of Forest Fires in Northeast China. *Forests* **2022**, *13* (1). https://doi.org/10.3390/f13010110.
(63) Bodí, M. B.; Martin, D. A.; Balfour, V. N.; Santín, C.; Doerr, S. H.; Pereira, P.; Cerdà, A.; Mataix-Solera, J. Wildland Fire Ash: Production, Composition and Eco-Hydro-Geomorphic Effects. *Earth Sci Rev* **2014**, *130*, 103–127. https://doi.org/10.1016/j.earscirev.2013.12.007.
(64) Mastrolonardo, G.; Certini, G.; Krebs, R.; Forte, C.; Egli, M. Effects of Fire on Soil Organic Matter Quality along an Altitudinal Sequence on Mt. Etna, Sicily. *Catena (Amst)* **2013**, *110*, 133–145. https://doi.org/10.1016/j.catena.2013.05.017.
(65) Hilscher, A.; Heister, K.; Siewert, C.; Knicker, H. Mineralisation and Structural Changes during the Initial Phase of Microbial Degradation of Pyrogenic Plant Residues in Soil. *Org Geochem* **2009**, *40* (3), 332–342. https://doi.org/10.1016/j.orggeochem.2008.12.004.
(66) Leifeld, J. Thermal Stability of Black Carbon Characterised by Oxidative Differential Scanning Calorimetry. *Org Geochem* **2007**, *38* (1), 112–127. https://doi.org/10.1016/j.orggeochem.2006.08.004.
(67) Alimoradi, S.; Stohr, H.; Stagg-Williams, S.; Sturm, B. Effect of Temperature on Toxicity and Biodegradability of Dissolved Organic Nitrogen Formed during Hydrothermal Liquefaction of Biomass. *Chemosphere* **2020**, *238*. https://doi.org/10.1016/j.chemosphere.2019.124573.
(68) Dresler, S.; Hawrylak-Nowak, B.; Kovacik, J.; Wozniak, M.; Galazka, A.; Staniak, M.; Wojciak, M.; Sowa, I. Organic Nitrogen Modulates Not Only Cadmium Toxicity but Also Microbial Activity in Plants. *J Hazard Mater* **2021**, 123887.
(69) Cervilla, L. M.; Blasco, B.; Ríos, J. J.; Rosales, M. A.; Rubio-Wilhelmi, M. M.; Sánchez-Rodríguez, E.; Romero, L.; Ruiz, J. M. Response of Nitrogen Metabolism to Boron Toxicity in Tomato Plants. *Plant Biol (Stuttg)* **2009**, *11* (5), 671–677. https://doi.org/10.1111/j.1438-8677.2008.00167.x.
(70) Campos, I.; Abrantes, N. Forest Fires as Drivers of Contamination of Polycyclic Aromatic Hydrocarbons to the Terrestrial and Aquatic Ecosystems. *Current Opinion in Environmental Science and Health*. Elsevier B.V. December 1, 2021. https://doi.org/10.1016/j.coesh.2021.100293.
(71) Vila-Escalé, M.; Vegas-Vilarrúbia, T.; Prat, N. Release of Polycyclic Aromatic Compounds into a Mediterranean Creek (Catalonia, NE Spain) after a Forest Fire. *Water Res* **2007**, *41* (10), 2171–2179. https://doi.org/10.1016/j.watres.2006.07.029.
(72) Manoli, E.; Samara, C. Polycyclic Aromatic Hydrocarbons in Natural Waters: Sources, Occurrence and Analysis. *Trends in Analytical Chemistry* **1999**, *18* (6), 417–428.

(73) Whitacre, D. M. *Reviews of Environmental Contamination and Toxicology Volume 211*; Whitacre, D. M., Ed.; Reviews of Environmental Contamination and Toxicology; Springer New York: New York, NY, 2011; Vol. 211. https://doi.org/10.1007/978-1-4419-8011-3.
(74) Gavrić, S.; Flanagan, K.; Österlund, H.; Blecken, G. T.; Viklander, M. Facilitating Maintenance of Stormwater Ponds: Comparison of Analytical Methods for Determination of Metal Pollution. *Environmental Science and Pollution Research* **2022**, *29* (49), 74877–74893. https://doi.org/10.1007/s11356-022-20694-0.
(75) Lara-Moreno, A.; Morillo, E.; Merchán, F.; Villaverde, J. A Comprehensive Feasibility Study of Effectiveness and Environmental Impact of PAH Bioremediation Using an Indigenous Microbial Degrader Consortium and a Novel Strain Stenotrophomonas Maltophilia CPHE1 Isolated from an Industrial Polluted Soil. *J Environ Manage* **2021**, *289*. https://doi.org/10.1016/j.jenvman.2021.112512.
(76) Szopka, K.; Gruss, I.; Gruszka, D.; Karczewska, A.; Gediga, K.; Gałka, B.; Dradrach, A. The Effects of Forest Litter and Waterlogging on the Ecotoxicity of Soils Strongly Enriched in Arsenic in a Historical Mining Site. *Forests* **2021**, *12* (3). https://doi.org/10.3390/f12030355.
(77) Telesiński, A.; Pawłowska, B.; Biczak, R.; Śnieg, M.; Wróbel, J.; Dunikowska, D.; Meller, E. Enzymatic Activity and Its Relationship with Organic Matter Characterization and Ecotoxicity to Aliivibrio Fischeri of Soil Samples Exposed to Tetrabutylphosphonium Bromide. *Sensors* **2021**, *21* (5), 1–19. https://doi.org/10.3390/s21051565.
(78) Bastos, A. C.; Prodana, M.; Abrantes, N.; Keizer, J. J.; Soares, A. M. V. M.; Loureiro, S. Potential Risk of Biochar-Amended Soil to Aquatic Systems: An Evaluation Based on Aquatic Bioassays. *Ecotoxicology* **2014**, *23* (9), 1784–1793. https://doi.org/10.1007/s10646-014-1344-1.
(79) Doherty, F. G. *A Review of the Microtox ® Toxicity Test System for Assessing the Toxicity of Sediments and Soils*; 2001; Vol. 36. http://iwaponline.com/wqrj/article-pdf/36/3/475/229261/wqrjc0360475.pdf.
(80) Campos, I.; Abrantes, N.; Vidal, T.; Bastos, A. C.; Gonçalves, F.; Keizer, J. J. Assessment of the Toxicity of Ash-Loaded Runoff from a Recently Burnt Eucalypt Plantation. *Eur J For Res* **2012**, *131* (6), 1889–1903. https://doi.org/10.1007/s10342-012-0640-7.
(81) Silva, V.; Pereira, J. L.; Campos, I.; Keizer, J. J.; Gonçalves, F.; Abrantes, N. Toxicity Assessment of Aqueous Extracts of Ash from Forest Fires. *Catena (Amst)* **2015**, *135*, 401–408. https://doi.org/10.1016/j.catena.2014.06.021.
(82) Key, C. H.; Benson, N. C. Landscape Assessment (LA) Sampling and Analysis Methods. *USDA Forest Service Gen Tech. Rep RMRS-GTR-164-CD* **2006**.
(83) Miesel, J. R.; Hockaday, W. C.; Kolka, R. K.; Townsend, P. A. Soil Organic Matter Composition and Quality across Fire Severity Gradients in Coniferous and Deciduous Forests of the Southern Boreal Region. *Journal of Geophysical Research G: Biogeosciences* **2015**, *120* (6), 1124–1141. https://doi.org/10.1002/2015JG002959.
(84) Brohon, B.; Delolme, C.; Gourdon, R. *Complementarity of Bioassays and Microbial Activity Measurements for the Evaluation of Hydrocarbon-Contaminated Soils Quality*. www.elsevier.com/locate/soilbio.
(85) Morales-Caselles, C.; Kalman, J.; Riba, I.; DelValls, T. A. Comparing Sediment Quality in Spanish Littoral Areas Affected by Acute (Prestige, 2002) and Chronic (Bay of Algeciras) Oil Spills. *Environmental Pollution* **2007**, *146* (1), 233–240. https://doi.org/10.1016/j.envpol.2006.04.042.

(86) Pelletier, E.; Delille, D.; Delille, B. Crude Oil Bioremediation in Sub-Antarctic Intertidal Sediments: Chemistry and Toxicity of Oiled Residues. *Mar Environ Res* **2004**, *57* (4), 311–327. https://doi.org/10.1016/j.marenvres.2003.07.001.
(87) Adams, R. H.; Domínguez-Rodríguez, V. I.; Zavala-Cruz, J. *Vibrio Fischeri Bioassay for Determination of Toxicity in Petroleum Contaminated Soils from Tropical Southeast Mexico (Bioasai Vibrio Fischeri Untuk Menentukan Ketoksikan Dalam Tanah Terlumus Petroleum Dari Tenggara Tropika Mexico)*; 2015; Vol. 44.
(88) Domínguez-Rodríguez, V. I.; Adams, R. H.; Sánchez-Madrigal, F.; Pascual-Chablé, J. de los S.; Gómez-Cruz, R. Soil Contact Bioassay for Rapid Determination of Acute Toxicity with Eisenia Foetida. *Heliyon*. Elsevier Ltd January 1, 2020. https://doi.org/10.1016/j.heliyon.2019.e03131.
(89) Chen, H.; McKenna, A. M.; Niles, S. F.; Frye, J. W.; Glattke, T. J.; Rodgers, R. P. Time-Dependent Molecular Progression and Acute Toxicity of Oil-Soluble, Interfacially-Active, and Water-Soluble Species Reveals Their Rapid Formation in the Photodegradation of Macondo Well Oil. *Science of the Total Environment* **2022**, *813*. https://doi.org/10.1016/j.scitotenv.2021.151884.
(90) Dittmar, T.; Koch, B.; Hertkorn, N.; Kattner, G. A Simple and Efficient Method for the Solid-Phase Extraction of Dissolved Organic Matter (SPE-DOM) from Seawater. *Limnol Oceanogr Methods* **2008**, *6*, 230–235.
(91) Emmett, M. R.; White, F. M.; Hendrickson, C. L.; Shi, D. H.; Marshall, A. G. Application of Micro-Electrospray Liquid Chromatography Techniques to FT-ICR MS to Enable High-Sensitivity Biological Analysis. *J Am Soc Mass Spectrom* **1998**, *9* (4), 333–340. https://doi.org/10.1016/S1044-0305(97)00287-0.
(92) Hendrickson, C. L.; Quinn, J. P.; Kaiser, N. K.; Smith, D. F.; Blakney, G. T.; Chen, T.; Marshall, A. G.; Weisbrod, C. R.; Beu, S. C. 21 Tesla Fourier Transform Ion Cyclotron Resonance Mass Spectrometer: A National Resource for Ultrahigh Resolution Mass Analysis. *J Am Soc Mass Spectrom* **2015**, *26* (9), 1626–1632. https://doi.org/10.1007/s13361-015-1182-2.
(93) Smith, D. F.; Podgorski, D. C.; Rodgers, R. P.; Blakney, G. T.; Hendrickson, C. L. 21 Tesla FT-ICR Mass Spectrometer for Ultrahigh-Resolution Analysis of Complex Organic Mixtures. *Anal Chem* **2018**, *90* (3), 2041–2047. https://doi.org/10.1021/acs.analchem.7b04159.
(94) Belov, M. E.; Rakov, V. S.; Nikolaev, E. N.; Goshe, M. B.; Anderson, G. A.; Smith, R. D. Initial Implementation of External Accumulation Liquid Chromatography/Electrospray Ionization Fourier Transform Ion Cyclotron Resonance with Automated Gain Control. *Rapid Communications in Mass Spectrometry* **2003**, *17* (7), 627–636. https://doi.org/10.1002/rcm.955.
(95) Page, J. S.; Bogdanov, B.; Vilkov, A. N.; Prior, D. C.; Buschbach, M. A.; Tang, K.; Smith, R. D. Automatic Gain Control in Mass Spectrometry Using a Jet Disrupter Electrode in an Electrodynamic Ion Funnel. *J Am Soc Mass Spectrom* **2005**, *16* (2), 244–253. https://doi.org/10.1016/j.jasms.2004.11.003.
(96) Kaiser, N. K.; McKenna, A. M.; Savory, J. J.; Hendrickson, C. L.; Marshall, A. G. Tailored Ion Radius Distribution for Increased Dynamic Range in FT-ICR Mass Analysis of Complex Mixtures. *Anal Chem* **2013**, *85* (1), 265–272. https://doi.org/10.1021/ac302678v.
(97) Chen, T.; Beu, S. C.; Kaiser, N. K.; Hendrickson, C. L. Note: Optimized Circuit for Excitation and Detection with One Pair of Electrodes for Improved Fourier Transform Ion Cyclotron Resonance Mass Spectrometry. *Review of Scientific Instruments* **2014**, *85* (6). https://doi.org/10.1063/1.4883179.

(98) Boldin, I. A.; Nikolaev, E. N. Fourier Transform Ion Cyclotron Resonance Cell with Dynamic Harmonization of the Electric Field in the Whole Volume by Shaping of the Excitation and Detection Electrode Assembly. *Rapid Communications in Mass Spectrometry* **2011**, *25* (1), 122–126. https://doi.org/10.1002/rcm.4838.
(99) Blakney, G. T.; Hendrickson, C. L.; Marshall, A. G. Predator Data Station: A Fast Data Acquisition System for Advanced FT-ICR MS Experiments. *Int J Mass Spectrom* **2011**, *306* (2–3), 246–252. https://doi.org/10.1016/j.ijms.2011.03.009.
(100) Xian, F.; Hendrickson, C. L.; Blakney, G. T.; Beu, S. C.; Marshall, A. G. Automated Broadband Phase Correction of Fourier Transform Ion Cyclotron Resonance Mass Spectra. *Anal Chem* **2010**, *82* (21), 8807–8812. https://doi.org/10.1021/ac101091w.
(101) Savory, J. J.; Kaiser, N. K.; McKenna, A. M.; Xian, F.; Blakney, G. T.; Rodgers, R. P.; Hendrickson, C. L.; Marshall, A. G. Parts-per-Billion Fourier Transform Ion Cyclotron Resonance Mass Measurement Accuracy with a Walking Calibration Equation. *Anal Chem* **2011**, *83* (5), 1732–1736. https://doi.org/10.1021/ac102943z.
(102) Kendrick, E. A Mass Scale Based Resolution Mass Spectrometry of Organic Compounds. *Anal Chem* **1963**, *35* (13), 2146–2154.
(103) Hughey, C. A.; Hendrickson, C. L.; Rodgers, R. P.; Marshall, A. G.; Qian, K. Kendrick Mass Defect Spectrum: A Compact Visual Analysis for Ultrahigh-Resolution Broadband Mass Spectra. *Anal Chem* **2001**, *73* (19), 4676–4681. https://doi.org/10.1021/ac010560w.
(104) McLafferty, F. W.; Turecek, F. *Interpretation of Mass Spectra*, 4th ed.; University Science Books: Mill Valley, CA, 1993.
(105) Kim, S.; Kramer, R. W.; Hatcher, P. G. Graphical Method for Analysis of Ultrahigh-Resolution Broadband Mass Spectra of Natural Organic Matter, the Van Krevelen Diagram. *Anal Chem* **2003**, *75* (20), 5336–5344. https://doi.org/10.1021/ac034415p.
(106) Corilo, Y. E. PetroOrg Software. Florida State University, Omics LLC: Tallahassee, FL 2014.
(107) Eddy, S. R. Accelerated Profile HMM Searches. *PLoS Comput Biol* **2011**, *7* (10). https://doi.org/10.1371/journal.pcbi.1002195.
(108) Bateman, A.; Martin, M. J.; O'Donovan, C.; Magrane, M.; Apweiler, R.; Alpi, E.; Antunes, R.; Arganiska, J.; Bely, B.; Bingley, M.; Bonilla, C.; Britto, R.; Bursteinas, B.; Chavali, G.; Cibrian-Uhalte, E.; da Silva, A.; de Giorgi, M.; Dogan, T.; Fazzini, F.; Gane, P.; Castro, L. G.; Garmiri, P.; Hatton-Ellis, E.; Hieta, R.; Huntley, R.; Legge, D.; Liu, W.; Luo, J.; Macdougall, A.; Mutowo, P.; Nightingale, A.; Orchard, S.; Pichler, K.; Poggioli, D.; Pundir, S.; Pureza, L.; Qi, G.; Rosanoff, S.; Saidi, R.; Sawford, T.; Shypitsyna, A.; Turner, E.; Volynkin, V.; Wardell, T.; Watkins, X.; Zellner, H.; Cowley, A.; Figueira, L.; Li, W.; McWilliam, H.; Lopez, R.; Xenarios, I.; Bougueleret, L.; Bridge, A.; Poux, S.; Redaschi, N.; Aimo, L.; Argoud-Puy, G.; Auchincloss, A.; Axelsen, K.; Bansal, P.; Baratin, D.; Blatter, M. C.; Boeckmann, B.; Bolleman, J.; Boutet, E.; Breuza, L.; Casal-Casas, C.; de Castro, E.; Coudert, E.; Cuche, B.; Doche, M.; Dornevil, D.; Duvaud, S.; Estreicher, A.; Famiglietti, L.; Feuermann, M.; Gasteiger, E.; Gehant, S.; Gerritsen, V.; Gos, A.; Gruaz-Gumowski, N.; Hinz, U.; Hulo, C.; Jungo, F.; Keller, G.; Lara, V.; Lemercier, P.; Lieberherr, D.; Lombardot, T.; Martin, X.; Masson, P.; Morgat, A.; Neto, T.; Nouspikel, N.; Paesano, S.; Pedruzzi, I.; Pilbout, S.; Pozzato, M.; Pruess, M.; Rivoire, C.; Roechert, B.; Schneider, M.; Sigrist, C.; Sonesson, K.; Staehli, S.; Stutz, A.; Sundaram, S.; Tognolli, M.; Verbregue, L.; Veuthey, A. L.; Wu, C. H.; Arighi, C. N.; Arminski, L.; Chen, C.; Chen, Y.; Garavelli, J. S.; Huang, H.; Laiho, K.; McGarvey, P.; Natale, D. A.; Suzek, B. E.; Vinayaka, C. R.; Wang, Q.; Wang, Y.; Yeh, L. S.; Yerramalla, M. S.; Zhang, J. UniProt: A Hub

for Protein Information. *Nucleic Acids Res* **2015**, *43* (D1), D204–D212. https://doi.org/10.1093/nar/gku989.
(109) Nojiri, H.; Ashikawa, Y.; Noguchi, H.; Nam, J. W.; Urata, M.; Fujimoto, Z.; Uchimura, H.; Terada, T.; Nakamura, S.; Shimizu, K.; Yoshida, T.; Habe, H.; Omori, T. Structure of the Terminal Oxygenase Component of Angular Dioxygenase, Carbazole 1,9a-Dioxygenase. *J Mol Biol* **2005**, *351* (2), 355–370. https://doi.org/10.1016/j.jmb.2005.05.059.
(110) Xu, P.; Yu, B.; Li, F. L.; Cai, X. F.; Ma, C. Q. Microbial Degradation of Sulfur, Nitrogen and Oxygen Heterocycles. *Trends in Microbiology*. September 2006, pp 398–405. https://doi.org/10.1016/j.tim.2006.07.002.
(111) Schmidt, M. W. I.; Knicker, H.; Hatcher, P. G.; Kogel-Knabner, I. Improvement of 13C and 15N CPMAS NMR Spectra of Bulk Soils, Particle Size Ftactions and Organic Material by Treatment with 10% Hydrofluoric Acid. *Eur J Soil Sci* **1997**, *48*, 319–328.
(112) Baldock, J. A.; Oades, J. M.; Waters, A. G.; Peng, X.; Vassallo, A. M.; Wilson, M. A. Aspects of the Chemical Structure of Soil Organic Materials as Revealed by Solid-State 13C NMR Spectroscopy. *Biogeochemistry* **1992**, *16*, 1–42.
(113) Simpson, M. J.; Simpson, A. J. The Chemical Ecology of Soil Organic Matter Molecular Constituents. *J Chem Ecol* **2012**, *38* (6), 768–784. https://doi.org/10.1007/s10886-012-0122-x.
(114) Simpson, A. J.; Brown, S. A. Purge NMR: Effective and Easy Solvent Suppression. *Journal of Magnetic Resonance* **2005**, *175* (2), 340–346. https://doi.org/10.1016/j.jmr.2005.05.008.
(115) Mitchell, P.; Simpson, A.; Soong, R.; Simpson, M. Nuclear Magnetic Resonance Analysis of Changes in Dissolved Organic Matter Composition with Successive Layering on Clay Mineral Surfaces. *Soil Syst* **2018**, *2* (1), 8. https://doi.org/10.3390/soils2010008.
(116) Woods, G. C.; Simpson, M. J.; Koerner, P. J.; Napoli, A.; Simpson, A. J. HILIC-NMR: Toward the Identification of Individual Molecular Components in Dissolved Organic Matter. *Environ Sci Technol* **2011**, *45* (9). https://doi.org/10.1021/es103425s.
(117) Simpson, M. J.; Otto, A.; Feng, X. Comparison of Solid-State Carbon-13 Nuclear Magnetic Resonance and Organic Matter Biomarkers for Assessing Soil Organic Matter Degradation. *Soil Science Society of America Journal* **2008**, *72* (1), 268–276. https://doi.org/10.2136/sssaj2007.0045.
(118) Baldock, J. A.; Preston, C. M. Chemistry of Carbon Decomposition Processes in Forests as Revealed by Solid-State Carbon-13 Nuclear Magnetic Resonance. In *Carbon Forms and Functions in Forest Soils*; Soil Science Society of America: Madison, WI, USA, 2006; pp 89–117. https://doi.org/10.2136/1995.carbonforms.c6.
(119) Clemente, J. S.; Gregorich, E. G.; Simpson, A. J.; Kumar, R.; Courtier-Murias, D.; Simpson, M. J. Comparison of Nuclear Magnetic Resonance Methods for the Analysis of Organic Matter Composition from Soil Density and Particle Fractions. *Environmental Chemistry* **2012**, *9* (1), 97. https://doi.org/10.1071/EN11096.
(120) Kopecký, M.; Kolář, L.; Váchalová, R.; Konvalina, P.; Batt, J.; Mráz, P.; Menšík, L.; Hoang, T. N.; Dumbrovský, M. Black Carbon and Its Effect on Carbon Sequestration in Soil. *Agronomy* **2021**, *11* (11). https://doi.org/10.3390/agronomy11112261.
(121) Wagner, S.; Coppola, A. I.; Stubbins, A.; Dittmar, T.; Niggemann, J.; Drake, T. W.; Seidel, M.; Spencer, R. G. M.; Bao, H. Questions Remain about the Biolability of Dissolved Black Carbon along the Combustion Continuum. *Nat Commun* **2021**, *12* (4281). https://doi.org/10.1038/s41467-020-18808-8.

(122) Chen, H.; Ersan, M. S.; Tolić, N.; Chu, R. K.; Karanfil, T.; Chow, A. T. Chemical Characterization of Dissolved Organic Matter as Disinfection Byproduct Precursors by UV/Fluorescence and ESI FT-ICR MS after Smoldering Combustion of Leaf Needles and Woody Trunks of Pine (Pinus Jeffreyi). *Water Res* **2022**, *209*. https://doi.org/10.1016/j.watres.2021.117962.
(123) Donhauser, J.; Qi, W.; Bergk-Pinto, B.; Frey, B. High Temperatures Enhance the Microbial Genetic Potential to Recycle C and N from Necromass in High-Mountain Soils. *Glob Chang Biol* **2021**, *27* (7), 1365–1386. https://doi.org/10.1111/gcb.15492.
(124) González-Pérez, J. A.; González-Vila, F. J.; Almendros, G.; Knicker, H. The Effect of Fire on Soil Organic Matter - A Review. *Environ Int* **2004**, *30* (6), 855–870. https://doi.org/10.1016/j.envint.2004.02.003.
(125) Chen, H.; Wang, J.-J.; Ku, P.-J.; Tsui, M. T.-K.; Abney, R. B.; Berhe, A. A.; Zhang, Q.; Burton, S. D.; Dahlgren, R. A.; Chow, A. T. Burn Intensity Drives the Alteration of Phenolic Lignin to (Poly) Aromatic Hydrocarbons as Revealed by Pyrolysis Gas Chromatography–Mass Spectrometry (Py-GC/MS). *Environ Sci Technol* **2022**. https://doi.org/10.1021/acs.est.2c00426.
(126) Mooshammer, M.; Hofhansl, F.; Frank, A. H.; Wanek, W.; Hämmerle, I.; Leitner, S.; Schnecker, J.; Wild, B.; Watzka, M.; Keiblinger, K. M.; Zechmeister-Boltenstern, S.; Richter, A. *Decoupling of Microbial Carbon, Nitrogen, and Phosphorus Cycling in Response to Extreme Temperature Events*. https://www.science.org.
(127) Hemmler, D.; Roullier-Gall, C.; Marshall, J. W.; Rychlik, M.; Taylor, A. J.; Schmitt-Kopplin, P. Evolution of Complex Maillard Chemical Reactions, Resolved in Time. *Sci Rep* **2017**, *7* (1), 3–8. https://doi.org/10.1038/s41598-017-03691-z.
(128) Hestrin, R.; Torres-Rojas, D.; Dynes, J. J.; Hook, J. M.; Regier, T. Z.; Gillespie, A. W.; Smernik, R. J.; Lehmann, J. Fire-Derived Organic Matter Retains Ammonia through Covalent Bond Formation. *Nat Commun* **2019**, *10* (1), 1–8. https://doi.org/10.1038/s41467-019-08401-z.
(129) Whitman, T.; Enders, A.; Lehmann, J. Pyrogenic Carbon Additions to Soil Counteract Positive Priming of Soil Carbon Mineralization by Plants. *Soil Biol Biochem* **2014**, *73*, 33–41. https://doi.org/10.1016/j.soilbio.2014.02.009.
(130) Knicker, H. "Black Nitrogen" - an Important Fraction in Determining the Recalcitrance of Charcoal. *Org Geochem* **2010**, *41* (9), 947–950. https://doi.org/10.1016/j.orggeochem.2010.04.007.
(131) Bamba, D.; Coulibaly, M.; Robert, D. Nitrogen-Containing Organic Compounds: Origins, Toxicity and Conditions of Their Photocatalytic Mineralization over TiO2. *Science of the Total Environment*. Elsevier B.V. February 15, 2017, pp 1489–1504. https://doi.org/10.1016/j.scitotenv.2016.12.130.
(132) Knicker, H. Soil Organic N - An under-Rated Player for C Sequestration in Soils? *Soil Biology and Biochemistry*. June 2011, pp 1118–1129. https://doi.org/10.1016/j.soilbio.2011.02.020.
(133) Czimczik, C. I.; Masiello, C. A. Controls on Black Carbon Storage in Soils. *Global Biogeochem Cycles* **2007**, *21* (3), 1–8. https://doi.org/10.1029/2006GB002798.
(134) Sharma, R. K.; Chan, W. G.; Seeman, J. I.; Hajaligol, M. R. *Formation of Low Molecular Weight Heterocycles and Polycyclic Aromatic Compounds (PACs) in the Pyrolysis of a-Amino Acids*; 2003; Vol. 66. www.elsevier.com/locate/jaap.
(135) Merino, A.; Ferreiro, A.; Salgado, J.; Fontúrbel, M. T.; Barros, N.; Fernández, C.; Vega, J. A. Use of Thermal Analysis and Solid-State 13C CP-MAS NMR Spectroscopy to Diagnose

Organic Matter Quality in Relation to Burn Severity in Atlantic Soils. *Geoderma* **2014**, *226–227* (1), 376–386. https://doi.org/10.1016/j.geoderma.2014.03.009.
(136) Harper, A. R.; Santin, C.; Doerr, S. H.; Froyd, C. A.; Albini, D.; Otero, X. L.; Viñas, L.; Pérez-Fernández, B. Chemical Composition of Wildfire Ash Produced in Contrasting Ecosystems and Its Toxicity to Daphnia Magna. *Int J Wildland Fire* **2019**, *28* (10), 726–737. https://doi.org/10.1071/WF18200.

CHAPTER 4: IMPACT OF BEAVER PONDS ON BIOGEOCHEMISTRY OF ORGANIC CARBON AND NITROGEN ALONG A FIRE-IMPACTED STREAM [2]

1 INTRODUCTION

Forests provide ecosystem services valued at ~$5 trillion annually[1–3] and are critical global sources of high-quality drinking water.[4,5] Wetlands contribute to these services, as they filter water, influence biogeochemical cycling, and support local flora and fauna.[5] Such services are susceptible to natural or anthropogenic disturbances (e.g., wildfire, insect infestation, development, etc.), especially as such disruptions may threaten downstream water quality.[6] Wildfires are of particular concern in the western U.S., as their frequency, intensity, and duration have increased in recent years and are projected to increase further.[7,8] This underscores the need to better understand the consequences of severe fire on the ecosystem processes that regulate clean water supply.

Heating and combustion of organic matter during severe wildfires creates pyrogenic organic matter (pyOM),[9] comprised of char, soot, and condensed polycyclic aromatic molecules, and accounts for ~5-15% of soil carbon.[10] The higher hydrophobicity and aromaticity, lower C:N ratios, and longer mean residence times of C in pyOM alters biogeochemical processes compared to unburned soils.[11–13] pyOM may be introduced to fluvial systems in post-fire runoff, which can be enriched in dissolved organic carbon (DOC), nitrogen (N), heavy metals, nutrients, and polycyclic aromatic hydrocarbons.[14–16] Indeed, stream DOC concentrations often increase following fire,[17–19] though its reactivity and impacts on either river microbial communities or water

[2] Reproduced with permissions from Roth, H., Nelson, A., McKenna, A., Fegel, T., Young, R., Rhoades, C., Wilkins, M., Borch, T. Impact of beaver ponds on biogeochemistry of organic carbon and nitrogen along a fire-impacted stream. Environmental Science: Processes & Impacts 2022, 24 (10): 1661-1677. Copyright 2022, The Royal Society of Chemistry.

treatment is less certain. Recent studies document elevated post-fire DOC with increased aromaticity and aromatic carboxylic acid concentrations,[20,21] though a comprehensive molecular-level characterization of these compounds is lacking. Shifts to more recalcitrant functional groups may inhibit microbial metabolism of DOC[22,23] and preserve pyOM within aquatic ecosystems. Further, exported pyOM from burned catchments is known to have costly short- and long-term impacts on downstream drinking water treatment and aquatic ecosystems.[6,24] Wildfire effects on water quality can persist for years,[15] and therefore represent important financial and functional challenges for water treatment.[10]

Concurrent to increases in fire activity, North American beaver (*Castor canadensis*) populations have steadily increased since their near eradication in the northern U.S. in the early 1900s.[25] These "ecosystem engineers" build dams and create channels which influence hydrologic and biogeochemical processes with relevance to downstream water quality.[26,27] The structure of beaver dams and associated physical features are known to influence post-fire stream channel and floodplain geomorphology,[32] but their impact on microbial communities and biogeochemical processes remains poorly studied.[30] Beaver dams and the floodplain complexity they create trap particulate carbon (C) and nutrients and create reduced zones that are depleted in dissolved oxygen,[27] where microbes must rely on alternate electron acceptors for respiration (e.g., NO_3^-, Fe^{3+}).[28] Tied to these biogeochemical changes, beaver ponds influence the availability of nutrients, solubility of metals, and quality of C in surface waters and sediments,[25,29,30] likely affecting C and N dynamics.[31,32] In contrast to free-flowing stream reaches that favor aerobic respiration, the reducing conditions within beaver ponds favor anaerobic metabolisms. Microbes are known to metabolize pyOM in well-oxygenated soils,[33,34] but the potential for microbial processing of pyOM under saturated beaver pond anoxic conditions is less well understood. With beaver populations

reaching approximately 30 million in North America[35] and over 1 million in Eurasia,[36] understanding the influence of beaver ponds on pyOM processing is critical to predict C and N cycling in impacted areas.

Nitrogen is a limiting reactant for microbial and plant productivity,[37,38] and its lability and bioavailability are sensitive to both heating and postfire ecosystem characteristics.[39,40] Although dissolved nitrogen can remain elevated in streams for years following fire,[41–43] little is known about the biotic (e.g., nitrification, dissimilatory nitrate reduction to ammonium) or abiotic (e.g., sorption, aggregation) processes that regulate soil N cycling and release to surface water.[44] Fourier transform ion cyclotron resonance mass spectrometry (FT-ICR MS) coupled with electrospray ionization analysis shows that combustion during wildfire creates thermodynamically recalcitrant organic matter that resists microbial degradation and alters C and N cycling.[45–47] FT-ICR MS permits direct measurement of DON and has shown that the N contained in pyOM is incorporated into refractory, heterocyclic aromatic compounds.[44,46,48,49] However, molecular transformations which may occur to nitrogenated pyOM in anoxic conditions are not not-well known, despite the implications they may have for N cycling.[50,51]

This work investigates potential post-fire changes to surface water C and N chemistry and sediment microbiome composition and function within beaver ponds. Work was conducted in a subalpine forest watershed within the Medicine Bow-Routt National Forest, Wyoming, USA, that burned during the 2018 Ryan Fire. We collected surface water and sediment samples along a series of beaver ponds within a severely burned portion of the watershed (**Figure 4.1**). We expected to find higher N concentrations and DOM with higher aromaticity and larger molecular sizes in the beaver ponds compared to free-flowing stream reaches. We hypothesized that changes in surface water molecular speciation would influence microbial communities in beaver pond sediments.

Finally, we examined whether microbially mediated biogeochemical processes influence C and N composition or export from fire-affected beaver ponds.

2. Materials and Methods

2.1 Site Description, Sample Collection and Processing

Surface water was collected at six locations along a burned stream affected by the 2018 Ryan Fire (Middle Fork of Big Creek) starting above a series of four beaver ponds and from an adjacent unburned tributary of McAnulty Creek (**Figure 4.1**). Three neighboring ponds were combined and analyzed as a complex, whereas Pond 4 was 3.5 km downstream and was analyzed separately. Surface grab samples (one per sampling location) were collected monthly starting near peak runoff throughout the summer (mid-June through October) one and two years postfire. Stream water samples were collected from the thalweg of the stream and pond samples were collected near the outlet at the sediment-water interface.

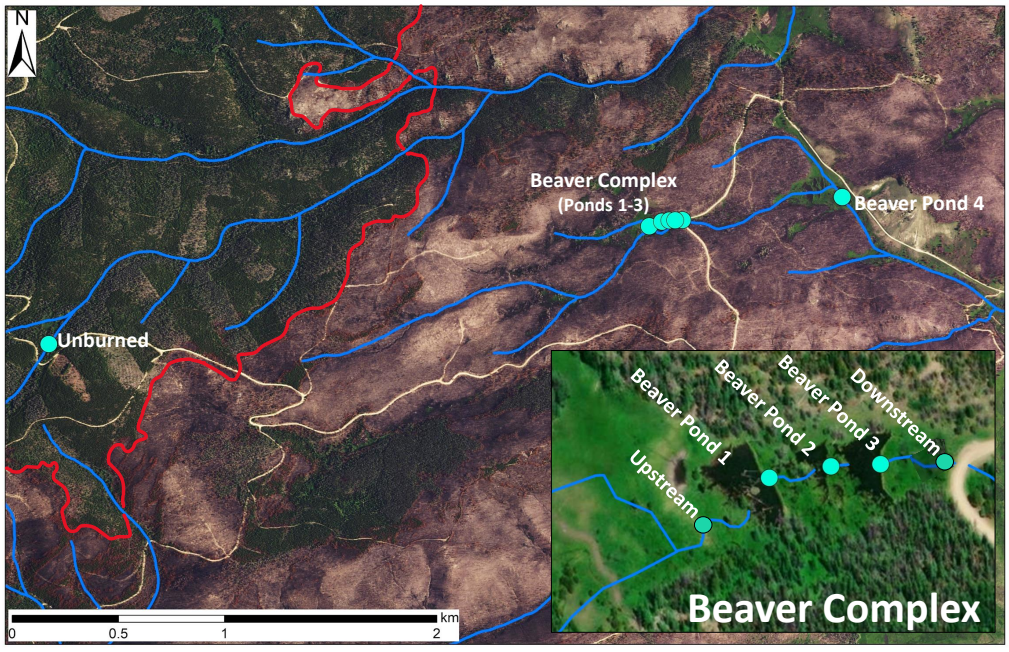

Figure 4.1. Sampling locations along Middle Fork of Big Creek within the Ryan Fire near the Colorado-Wyoming border and unburned subalpine forest along a tributary of McAnulty Creek.

Because water chemistry and the environmental microbiome are intimately connected, we used DNA-based methods to characterize the beaver pond microbiome within our sampling sites and adjacent wetlands outside of the Ryan Fire (**Figure 4.2**). Based on year 1 observations, we sampled bulk surficial sediments and associated pore water from Beaver Ponds 1, 2, and 4, along with 4 other beaver ponds in adjacent watersheds in the fall of 2020, for a total of seven samples. We additionally attempted to collect only porewater samples from the ponds, but the sediment in the ponds was very fine and all attempts to use porewater "sippers" resulted in them clogging without yielding sufficient sample for analysis. Therefore, surficial sediment and pore water samples (approximately 5 cm depth) were collected from the sediment-water interface using an ethanol-sterilized plastic cup and stored in a cooler for transport. One sediment sample was collected per sampling location.

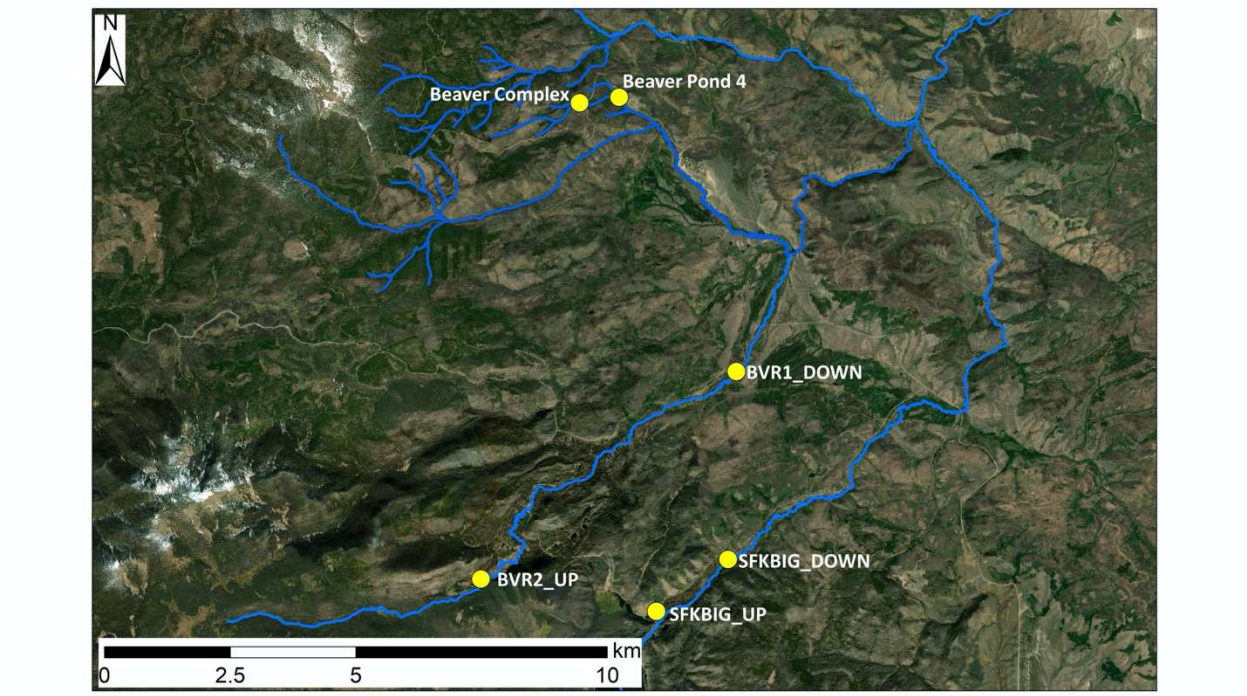

Figure 4.2. Sampling locations of adjacent beaver ponds outside the Ryan Fire burn scar near the Colorado-Wyoming border. Ponds were used as control ponds for chemical and microbial analyses. BVR1_DOWN = Control Pond 1, SFKBIG_DOWN = Control Pond 2, SFKBIG_UP = Control Pond 3.

2.3 Carbon, Nitrogen, and UV-Vis Fluorescence

Water samples analyzed for DOC, DTN, and UV-Vis fluorescence spectroscopy were collected in pre-combusted (heated for 3 hours at 500 ºC) glass amber bottles and filtered through 0.7 μm pore-size glass fiber filters (Millipore Corp, Burlington, MA) within 24 hours of collection. Samples for anion and cation analyses were collected in opaque high-density polyethylene (HDPE) plastic bottles after triple washing with de-ionized water (EC < 1.0 μS cm^{-1}).

DOC and DTN measurements were performed via high-temperature combustion catalytic oxidation on a Shimadzu TOC-VCPN total organic C/N analyzer with 2 M HCl addition before analysis to remove mineral C (Shimadzu Corporation, Columbia, MD). Inorganic nutrient concentrations were determined by ion chromatography via electrical conductivity detection, using an AS19A Anion-Exchange column for anions and a CS12A Cation-Exchange column for cations (Dionex Corp, Sunnyvale, CA, APHA, 1998a). Detection limits for NO_3^- and NH_4^+ were 10 μg/L. DON is estimated as the difference between DTN and the sum of dissolved inorganic N forms (NO_3^-N + NH_4^+-N).

Optical parameters, such as fluorescence index (FI), and freshness index (β/α) approximate DOM characteristics, (e.g., aromaticity, degree of microbial processing) to measure shifts in DOM composition.[50] Although these parameters only reflect the fluorophores in the sample, they can be used to determine variations in DOM source and biogeochemical processes.[51,52] FI is widely applied in stream water and wildfire studies, as it appears to be particularly sensitive for wildfire-impacted DOM due to increases in oxidized functional groups (increased by ~0.13 in fire-impacted sediment leachates).[53] Samples were analyzed using a Horiba Scientific Aqualog (Horiba-Jobin Yvon Scientific Edison, New Jersey, US) with excitation and emission wavelengths from 200-800 nm at 3 nm intervals and scan times of 2 seconds. Filtered samples were diluted to 5 mg C L^{-1} prior

to analysis to reduce inner-filter effects and normalize their concentrations. A sealed cuvette of deionized water was used as a blank and analyzed between every ten samples to correct for instrument drift. The samples were corrected for inner-filter effects and Rayleigh scatter was masked using first and second grating orders after spectral analysis. Finally, each spectrum was normalized by the area of the deionized water Raman scattering peak, as determined by the blank.[54] From this, fluorescence index (FI, Equation 4.1),[50] and freshness index were calculated (β/α, Equation 4.2).[55]

$$FI = excitation{:}\,370\ nm, emission\,\frac{470nm}{520nm} \quad \text{(EQ 4.1)}$$

$$\beta/\alpha = \frac{beta\ (excitation{:}310\ nm, emission\ 380\ nm)}{alpha(excitation{:}310\ nm, emission\ \max intensity\ between\ 420{-}435\ nm)} \quad \text{(EQ 4.2)}$$

2.4 Fourier Transform Ion Cyclotron Resonance Mass Spectrometry

2.4.1 Sample Preparation

Compositional analysis of the water samples was conducted using 21 tesla FT-ICR MS, used to further explore the differences in DOM composition which cannot be determined by concentration alone. The 21T FT-ICR mass spectrometer achieves high resolving power ($m/\Delta m_{50\%}$=3,000,000 at m/z 200), sub-ppm mass accuracy (20−80 ppb), and high dynamic ranges that allows the assignment of tens of thousands of species per mass spectrum.[56–58] To extend compositional coverage, we applied both positive-ion (+ESI) and negative-ion electrospray ionization (-ESI) to selectively ionize basic/acidic polar species through protonation/deprotonation.[46,59]

Water samples collected in June 2019 were extracted for FT-ICR MS analysis, with each beaver pond in the beaver complex analyzed separately to evaluate the effect of different retention times on chemical composition. Samples for FT-ICR MS analysis were collected in pre-combusted (heated for 6 hours at 400 ºC) glass amber bottles, filtered through 0.2 μm polyether sulfone filters

and stored at 4°C to minimize microbial activity. Prior to FT-ICR MS analysis, samples were prepared via solid phase extraction according to Dittmar et al., 2008.[61] Briefly, 500 mL of each sample was acidified to pH 2 using trace metal-grade HCl (Sigma-Aldrich Chemical Co.). Agilent Bond Elut PPL cartridges (3 mL, 200 mg) were prepared by rinsing first with 15 mL methanol followed by 15 mL pH 2 water. PPL cartridges are a common SPE sorbent, as they are selective for polar compounds that are prevalent in OM.[62] PPL selectivity and high extraction efficiency (approximately 40-65% DOC recovery) made them an appropriate sorbent for this analysis.[63] Each water sample was passed through a PPL cartridge that was subsequently rinsed with 15 mL pH 2 water to remove salts. Finally, each sample was eluted with 2 mL HPLC grade methanol (Sigma-Aldrich Chemical Co., St. Louis, MO). SPE extracts were ran without further dilution prior to analysis by negative and positive ion electrospray ionization (ESI).[46]

2.4.2 Instrumentation: ESI Source

The sample solution was infused via a micro electrospray source[64] (50 μm i.d. fused silica emitter) at 500 nL/min by a syringe pump. Typical conditions for negative ion formation were: emitter voltage, -2.7-3.2 kV; S-lens RF (45 %) and heated metal capillary temperature 350 °C. Positive-ion ESI spray conditions were opposite in polarity.

2.4.3 Instrumentation: 21 T FT-ICR MS

SPE extracts were analyzed with a custom-built hybrid linear ion trap FT-ICR mass spectrometer equipped with a 21 T superconducting solenoid magnet.[58,65] Ions were initially accumulated in an external multipole ion guide (1-5 ms) and released *m/z*-dependently by decrease of an auxiliary radio frequency potential between the multipole rods and the end-cap electrode.[66] Ions were excited to *m/z* dependent radius to maximize the dynamic range and number of observed mass spectral peaks (32-64%),[66] and excitation and detection were performed on the same pair of electrodes.[67] The dynamically harmonized ICR cell in the 21 T FT-ICR is operated with 6 V

trapping potential.[66,68] Time-domain transients of 3.1 seconds were acquired with the Predator data station that handled excitation and detection only, initiated by a TTL trigger from the commercial Thermo data station, with 100 time-domain acquisitions conditionally-coadded for all experiments.[69] Mass spectra were phase-corrected[70] and internally calibrated with 10-15 highly abundant homologous series that span the entire molecular weight distribution based on the "walking" calibration method.[71] Mass spectral peaks with signal magnitude greater than six-times the baseline root-mean-square noise level at m/z 500 were exported to a peak list. Experimentally measured masses were converted from the International Union of Pure and Applied Chemistry (IUPAC) mass scale to the Kendrick mass scale[72] for rapid identification of homologous series for each heteroatom class (i.e., species with the same $C_cH_hN_nO_oS_s$ content, differing only by degree of alkylation).[73] For each elemental composition, $C_cH_hN_nO_oS_s$, heteroatom class, double bond equivalents (DBE = number of rings plus double bonds to C, DBE = $C - h/2 + n/2 + 1$)[74] and C number, c, were tabulated for subsequent generation of heteroatom class relative abundance distributions and graphical relative-abundance weighted images and van Krevelen diagrams. Molecular formula assignments and data visualization were performed with PetroOrg © software.[75] Molecular formula assignments with an error >0.25 parts-per-million were discarded, and only chemical classes with a combined relative abundance of ≥0.15% of the total were considered. All FT-ICR MS spectra are publicly available through the Open Science Framework (https://osf.io/t4eqx/) (DOI 10.17605/OSF.IO/T4EQX).

2.4.4 Molecular Formula Calculations

Assigned elemental compositions from neutral species were used to calculate O/C and C/N ratios, modified aromaticity index (AI_{mod}; Equation 4.3),[76,77] and nominal oxidation state of carbon (NOSC; Equation 4.4).[78] NOSC values are related to the change in Gibbs free energy for the

oxidation of organic matter ($\Delta G°_{ox}$; Equation 4.5).[78] Van Krevelen diagrams were also constructed from the FT-ICR MS results, in which the elemental ratio of O/C is plotted on the x-axis and the H/C ratio is plotted on the y-axis to visualize the spread of the assigned formulas and major compositional shifts.[79]

$$AI_{mod} = \frac{1+C-\frac{1}{2}O-S-\frac{1}{2}(N+P+H)}{C-\frac{1}{2}O-N-S-P} \quad \text{(EQ 4.3)}$$

$$NOSC = 4 - \frac{4C+H-2O-3N-2S}{C} \quad \text{(EQ 4.4)}$$

$$\Delta G°ox = 60.3 - 28.5 * NOSC \quad \text{(EQ 4.5)}$$

C = carbon, H = hydrogen, O = oxygen, N = nitrogen, S = sulfur, P = phosphorus

2.5 MICROBIAL ANALYSES

2.5.1 DNA extraction and 16S rRNA gene sequencing

To extract pore fluids and corresponding microbial communities, sediment-pore water slurries were centrifuged at 7000 rpm for 10 minutes and the supernatant was then pulled off and filtered through a 0.22 μm filter. DNA was extracted from the filters using the Zymobiomics Quick-DNA Fecal Soil Microbe Kits (Zymo Research, Ca, USA). For community composition analysis, 16S rRNA genes in the extracted DNA were amplified and sequenced at Argonne National Laboratory (primer set 515F/806R). Raw sequencing data was processed using the QIIME2 pipeline (QIIME2-2019.10), reads were clustered into amplicon sequence variant (ASV) classifications at 99% similarities, and taxonomy was assigned using the QIIME2 scikit-learn classifier trained on the SILVA[80] (release 132) database.[81] All 16S rRNA gene sequencing data is available at NCBI and can be accessed under accession number PRJNA792827. Mean species diversity of each sample (alpha diversity) was calculated based on species abundance and evenness using Shannon's Diversity Index (H), Pielou's Evenness (J), and species richness (R vegan package).

2.5.2 Metagenomic sequencing and binning

A subset of seven beaver pond sediment samples were selected for metagenomic sequencing to analyze metabolic functional potential within these sediments. Three of these samples were recovered from BP1, 2, and 4, while four other samples were collected from additional beaver wetlands outside the Ryan Fire burn scar (**Figure D1**). Libraries were prepared using the Tecan Ovation Ultralow System V2 and were sequenced on the NovaSEQ6000 platform on a S4 flow cell at Genomics Shared Resource, Colorado Cancer Center, Denver, CO, USA. Sequencing adapters were removed from reads using Bbduk (https://jgi.doe.gov/data-and-tools/bbtools/bb-tools-user-guide/bbduk-guide/)), and Sickle (v1.33)[82] was used to trim reads. FastQC (v0.11.2) was used before and after trimming reads to ensure high-quality reads were used for downstream processing. Trimmed metagenomic reads are available on NCBI and can be accessed under accession number PRJNA792827. Reads were assembled into contiguous sequences (contigs) using MEGAHIT (v1.2.9)[83] with a minimum kmer of 27, maximum kmer of 127, and step of 10 bp. Assembled contigs greater than 2500 bp were binned using Metabat with default parameters (v2.12.1).[84] We additionally used co-assembly techniques to maximize the number of bins from this dataset. The final metagenome-assembled genomes (MAGs) were assessed for completion and contamination using checkM v1.1.2[85] and taxonomy was assigned using GTDB-Tk v1.3.0.[86] The final MAG dataset was combined and dereplicated using dRep v3.0.0[87] to create the complete non-redundant database. MAG relative abundance across each sample was calculated using coverM genome v0.6.0 (https://github.com/wwood/CoverM). All quality metrics and taxonomy for the 33 medium- and high-quality MAGs discussed here are deposited on Zenodo (DOI: 10.5281/zenodo.5806541). MAGs were annotated using DRAM v1.2.[88] To identify multiheme c-type cytochromes (MHCs), we used the Geneious Prime (version

2020.0.3) 'Search for motifs' tool to identify protein sequences with at least 3 CXXCH motifs. To remove MHCs not involved with metal reduction, we used the DRAM annotations to remove any sequences annotated as a function likely unassociated with metals. We then analyzed these sequences using PSORTb (v3.0.2)[89] to remove any proteins that were predicted to remain within the cytoplasm.

2.6 Iron Analyses

Water samples for ICP-MS were filtered through ashless Whatman paper filters (GE Healthcare) and acidified to 2% HNO_3 prior to analysis. Elemental concentrations of iron (Fe) were measured via a NexION 250D mass spectrometer (PerkinElmer, Waltham, MA) connected to a PFA-ST nebulizer (Elemental Scientific, Omaha, Nebraska) and Peltier controlled (PC3x, Elemental Scientific) quartz cyclonic spray chamber (Elemental Scientific) set at 4°C. Samples were introduced using a prepFAST SC-2 autosampler (Elemental Scientific). The nebulizer gas flow was optimized for maximum Indium signal intensity (58380 counts per second, 0.82 L/min). To minimize interferences, these measurements were made in dynamic reaction cell mode using ammonia as the reactive gas. Iron (Fe) concentrations reported represent the sum of the detected concentrations of ^{54}Fe and ^{56}Fe. The detection limits for ^{54}Fe and ^{56}Fe were 7.24 and 6.46 ppb, respectively.

2.7 Statistical Analyses

DOC, DTN, %DON, and C:N were evaluated for statistical significance using student's t-test. All burned samples were compared to the unburned sample for these analyses. First, an F test was performed to assess the equality of variances between samples. If $F_{calculated}$ (Equations 4.6 & 4.7) is greater than F Critical one-tail (determined by degrees of freedom), the difference in variability between measurements is significant, and the variances are unequal; a lower $F_{calculated}$

indicates equal variances.[90] The results of the F test were used to inform the appropriate t-Test (Two-Sample Assuming Equal or Unequal Variances) to determine if the difference in sample means was significant. If t Stat (Equations 4.8 & 4.9) is less than t Critical two-tail (determined by degrees of freedom at 95% confidence interval), the difference is not significant; a higher t Stat indicates a significant difference.[90] A significance level of 0.05 was used for statistical significance in all analyses, and all results are reported in **Table D1**.

$$F_{calculated} = \frac{s_1^2}{s_2^2} \quad \text{(EQ 4.6)}$$

$$\text{Where } s = \sqrt{\frac{\sum_i (x_i - x_{avg})^2}{n-1}} \quad \text{(EQ 4.7)}$$

$$t = \frac{|x_{1avg} - x_{2avg}|}{s_{pooled}} \sqrt{\frac{n_1 n_2}{n_1 + n_2}} \quad \text{(EQ 4.8)}$$

$$\text{Where } s_{pooled} = \sqrt{\frac{s_1^2(n_1-1) + s_2^2(n_2-1)}{n_2 + n_2 - 2}} \quad \text{(EQ 4.9)}$$

3. Results and Discussion

3.1 DOC and DTN increase within beaver ponds

DOC concentrations in the surface grab samples throughout the fire-impacted stream varied on both spatial (**Figure 4.3a**) and temporal scales (**Figure D1**). Average DOC concentrations were highest in June 2019 (6.42 ppm, one year after fire, immediately following snow melt) and decreased from June to October (averaging 6.42 ppm to 3.60 ppm, respectively). Such seasonal changes to DOC concentrations have been documented in other high-elevation ecosystems[91] as well as in fire-impacted streams.[15] While DTN averages also varied throughout the summer, the highest average was reported in August 2019 (0.33 ppm) and the lowest in October (0.21 ppm). Seasonal variations in N export agree with changes observed following the 2012 Hayman Fire in Colorado, in which DTN export varied by month.[15]

There was no difference in DOC concentrations between the unburned stream and the burned stream above the beaver ponds (**Figure 4.3a**). DOC roughly doubled and increased steadily as water passed through the sequence of beaver ponds; however, this difference was not significant (**Table D1**). Average DTN exhibited a similar trend; the unburned and upstream sites were roughly the same concentrations, and the concentrations in beaver ponds were nearly twice those of the sites preceding them (**Table 4.1**). In contrast with DOC, DTN increases within the ponds were statistically significant (**Table D1**). Importantly, the beaver ponds typically contained higher concentrations of DOC and DTN than the site upstream of them (**Figure 4.3b**), in agreement with previous studies conducted on beaver ponds which have shown that these features influence organic C storage by trapping large quantities of sediment and organic material,[92,93] therefore affecting C and N dynamics within those sites.[31] Further evidence of a shift in C and N dynamics is provided by the C:N ratio, which was 32 in the unburned stream and fluctuated between 16-20 in the burned stream (**Table 4.2**). While these differences are not significant (**Table D1**), they do represent a shift below the commonly accepted threshold in which microbes are no longer N limited (C:N ratio of 24).[94]

Table 4.1. Average dissolved organic carbon (DOC), dissolved total nitrogen (DTN), and % dissolved organic nitrogen (%DON) for the monthly Ryan Fire water samples collected one-year post-fire (n = 5). Sampling locations located within the burned area are highlighted in gray.

Year 1 averages	**Unburned**	**Upstream**	**Beaver Complex 1**	**Down-stream**	**Beaver Pond 4**
DOC (ppm)	4.27 ± 2.27	3.60 ± 0.100	5.59 ± 1.65	6.45 ± 1.84	7.01 ± 1.66
DTN (ppm)	0.16 ± 0.055	0.20 ± 0.076	0.34 ± 0.093	0.35 ± 0.098	0.370 ± 0.049
%DON	53 ± 30.	42 ± 19	70 ± 16	73 ± 17	75 ± 11
C:N	32 ± 22	20. ± 11	16 ± 3.7	18 ± 6.6	21 ± 7.0

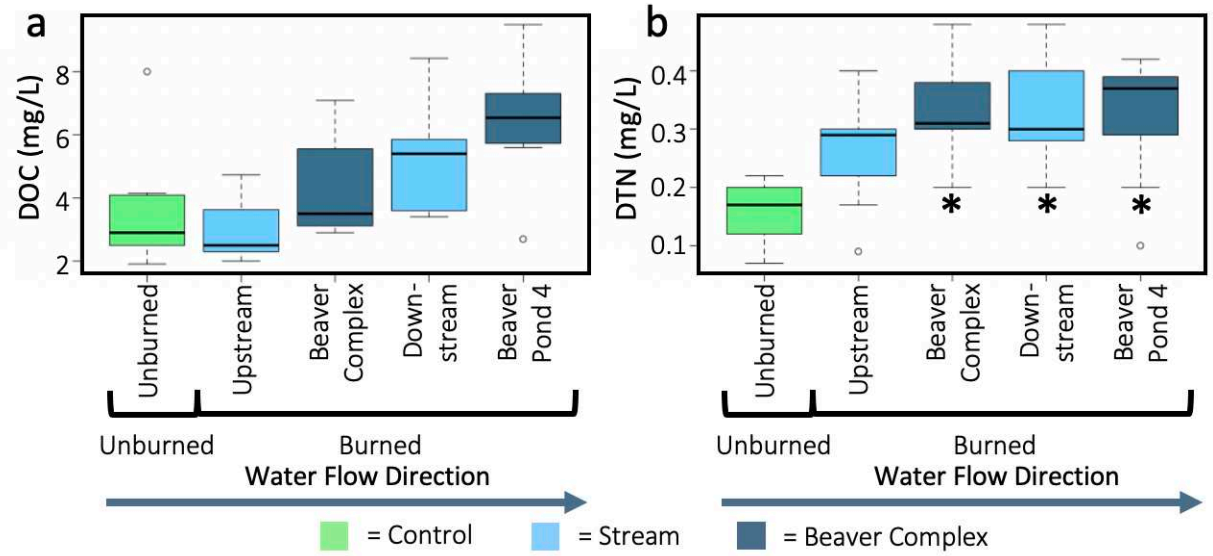

Figure 4.3. Dissolved organic carbon (DOC; a) and dissolved total nitrogen (DTN; b) concentrations along a stream impacted by the 2018 Ryan fire and an adjacent unburned stream (**Fig S1**). The lower and upper hinges of the boxplots represent the 25th and 75th percentile and the middle line is the median. The upper whisker extends to the median plus 1.5x interquartile range and the lower whisker extends to the median minus 1.5x interquartile range and are comprised of the data from five months of sampling one-year post-fire. Outliers are identified by open circles, and asterisks identify statistical significance.

DON constitutes a large percentage of DTN in unburned free-flowing rivers (62-99%).[44] Soil and stream nitrate commonly increase following fire due to decrease of plant uptake, leaching losses and increased nitrification.[95,96] Stream nitrate and DTN were both elevated in watersheds affected by extensive, severe wildfire in ponderosa pine forests in Colorado, but increases in nitrate caused the fraction of DTN comprised by DON to decline from 35% in unburned catchments to 6% in burned catchments.[15] Both nitrate and DTN roughly doubled within the Ryan fire, which indicates minimal wildfire effect on the proportion of DTN comprised by DON. Nitrate decreased by about 40% downstream of the Beaver Complex, consistent with denitrification in the anoxic beaver pond soils (**Figure D2**). The nitrate decline resulted in substantial increases in %DON within the ponds, constituting 60% of DTN in the Beaver Complex and 75% of DTN in BP4 (**Table 4.1**). Although increases in ammonium (NH_4^+) concentrations in rivers following fires have

been reported, they were primarily attributed to stormwater events[42], which were not included in this study. NH_4^+ concentrations reported here showed no appreciable changes on a spatial or temporal scale, remaining very low across the entire sampling gradient, often below 0.01 ppm (**Figure D3**). While only DTN values differed significantly (**Table D1**), the observed patten demonstrates N enrichment within the beaver pond relative to unburned and upstream sites (**Table 4.1**). Local changes in DOC and DTN trends through the stream and beaver ponds may indicate that the influx of pyDOM, among other watershed-derived inputs, into anoxic waters may be less favorable for microbial respiration,[97] leading to localized increases in %DON.

3.2 Nitrogen-containing compounds are enriched within beaver ponds

The elemental class distribution of the surface grab samples for both ionization modes is listed in **Figure 4.4** (formula counts) and **Table 4.2** (% relative abundances). Within the -ESI spectra, there is an overall decrease in the %CHO and increase in %CHNO between the burned and unburned stream (**Table 4.2**), although the CHO fraction still constitutes most formulas assigned (6,922 to 9,065 formulas and represents 82.2-89.7% of the spectrum). The smallest number of CHO formulas and lowest %CHO were assigned for Beaver Pond 1 (BP1), accompanied by an increase in %CHNO at the site, consistent with the observed increase in DTN in that pond (**Figure 4.3**). The other beaver ponds (BP2, BP3, BP4) also display fewer CHO formulas than the non-beaurever pond sites (Unburned, Upstream, Downstream). CHNO variability through the stream resulted in the lowest number of formulas assigned for BP2 (**Figure 4.4**). Importantly, this site also has lower DTN concentrations and a lower %DON than the other beaver ponds (**Table 4.1**). Contrary to other wetland studies, calculated O/C ratios do not appear to be substantially affected by the presence of beaver ponds. Within the sites analyzed here, assigned O/C ratios varied by 0.03 throughout the entire stream (**Table 4.3**), a magnitude of change

smaller than that observed in Florida wetlands, where O/C increased by ~0.2.[45] Thus, the observed changes in O/C ratios at the Ryan Fire site are likely not large enough to fundamentally alter the ability of the microbial community to process the pyDOM inputs. To further investigate this, we calculated the nominal oxidative state of carbon (NOSC), which describes a molecule's lability through its direct relationship to the Gibbs free energy (DG°) of the reduction half-reaction between organic matter (electron donor) and a terminal electron acceptor (e.g., O_2, NO_3^-, Fe^{3+}, SO_2^{2-}) (**EQ 4.5**).[78] NOSC values showed little variation between sampling locations and remained above the thermodynamic limits for standard state (NOSC < -0.6) and sulfidic reduction (NOSC < -0.3)[97] (**Table 4.3**), indicating that thermodynamic limitations associated with oxygen and sulfate reduction (representing the highest and lowest energy yields, respectively) do not apply with respect to NOSC in these samples. Therefore, compositional changes identified through FT-ICR MS are likely not a limiting factor for microbial respiration. However, it is important to note that this value can only be used to predict whether respiration is thermodynamically favorable, and not whether a microbial community is actively transcribing the genes necessary for the breakdown of these compounds.

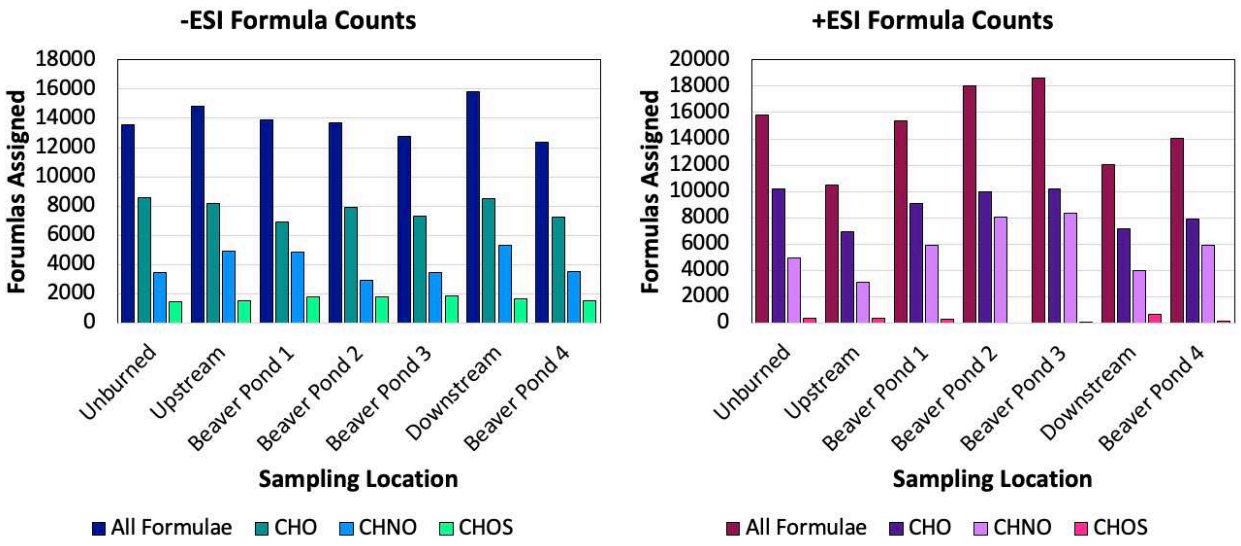

Figure 4.4. Elemental composition assignments derived from +/- ESI FT-ICR MS at 21 T mass spectra for the Ryan Fire PPL water extracts. Bar charts include the assigned formula counts for each heteroatom class assigned. -ESI bar chart on the left and +ESI bar chart on the right. C = carbon, H = hydrogen, N = nitrogen, O = oxygen, S = sulfur.

Table 4.2. FT-ICR MS data collected via electrospray ionization in negative and positive mode for the Ryan Fire water PPL extracts. % abundance data for -ESI reported on top, +ESI results on the bottom.

ESI Negative Mode	**Unburned**	**Up-stream**	**Beaver Pond 1**	**Beaver Pond 2**	**Beaver Pond 3**	**Down-stream**	**Beaver Pond 4**
CHO	89.7	84.8	82.2	84.6	84.7	84.2	86
CHNO	6.41	10.3	11.7	10.3	9.5	11.3	9.55
CHOS	3.74	4.69	5.75	4.95	5.68	4.09	4.39
ESI Positive Mode	**Unburned**	**Up-stream**	**Beaver Pond 1**	**Beaver Pond 2**	**Beaver Pond 3**	**Down-stream**	**Beaver Pond 4**
CHO	84.6	78.8	75.7	70.6	68.9	66.4	70.9
CHNO	14.8	9.72	17.5	29.4	30.5	14.2	26.9
CHOS	0.385	11.1	6.61	0	0.612	18.7	2.09

Table 4.3. Abundance-weighted O/C ratios, modified aromaticity indices (AI_{mod}),[76,77] and Nominal Oxidative State of Carbon (NOSC)[78] for Ryan Fire formulas detected by -ESI FT-ICR MS.

-ESI	Unburned	Upstream	BP1	BP2	BP3	Downstream	BP4
O/C	0.494	0.514	0.526	0.512	0.509	0.517	0.501
AI_{mod}	0.35	0.38	0.40	0.38	0.37	0.35	0.37
NOSC	-0.058	-0.057	-0.019	-0.057	-0.056	-0.057	-0.095

Complementary +ESI data also displays class element variability throughout the stream (**Table 4.2**). The site with the least CHO formulas assigned was Upstream, while the site with the lowest %CHO (66.4%) was Downstream. %CHO steadily declined through each of the successive ponds (BP1, BP2, BP3). This was accompanied by changes in the CHNO fraction, which increased from 3,069 formulas Upstream to 8,336 in BP 3 (**Figure 4.4**), accompanied by substantial increases in %CHNO. In general, both positive and negative ESI displayed an increase in the number of nitrogenated formulas assigned within the beaver ponds, in conjunction with the increased %DON within those sites (**Table 4.1**). Here, we report more N-containing compounds (**Table 4.2**), lower C/N ratios, and higher average N per formula assigned within the beaver ponds compared to the free-flowing sites (**Table 4.4**), evidence for a shift in DOM processing. Previous studies have observed that heterocyclic N-compounds and aromatic N structures are formed and enriched during the heating of soil OM and plant biomass[98–101] that may describe the CHNO species we detected within the beaver ponds.

Table 4.4. Average molecular weight (MW; in daltons) and calculated C/N ratios and average N per formula for the Ryan Fire +ESI FT-ICR MS data.

+ESI	Unburned	Upstream	BP1	BP2	BP3	Downstream	BP4
MW	644	677	664	616	618	646	621
C/N	58.8	54.9	44.6	33.9	36.8	44.64	35.7
Average N	0.489	0.527	0.635	0.784	0.720	0.593	0.749

We compared the tens of thousands of individual elemental compositions identified by FT-ICR MS with van Krevelen diagrams to visualize major shifts in the molecular composition and biological precursor.[56,79,102] For each plot, the mass spectrum was compared to the unburned control, and we subtracted all common formulas between the two spectra. We further refined our analysis to only those formulas that contained N, using only the +ESI data as this method has been

demonstrated to increase the compositional coverage of CHNO species compared to -ESI.[46] We present van Krevelen diagrams that display only these unique nitrogenated species (**Figure 4.5**), which show that CHNO type and quantity differs as the water travels through the stream. Upstream (**Figure 4.5a**), the unique CHNO is centered in the mid-aromatic region. Through the beaver complex, unique CHNO increases in number and expands within the van Krevelen diagram space, first in the aromatic region in BP1 (**Figure 4.5b**), and later covering both the aromatic and aliphatic regions of the van Krevelen diagram (**Figure 4.5b-d, f**). This expansion mirrors the observed increase in in DTN and %DON (**Table 4.1**) and indicates that there is regional preservation of CHNO compounds within these ponds, likely due to lower oxygen levels which in turn promote anaerobic metabolism within the microbial community. Indeed, microbial analyses indicate a diversity of putative anaerobic metabolisms within these locations (**Figure 4.8**). Downstream of BP3 the unique CHNO rapidly decreases (**Figure 4.5e**) before increasing again in BP4 (**Figure 4.5f**), further indicating that CHNO type and quantity is heavily reliant on its environment and its preservation is indeed highly localized.

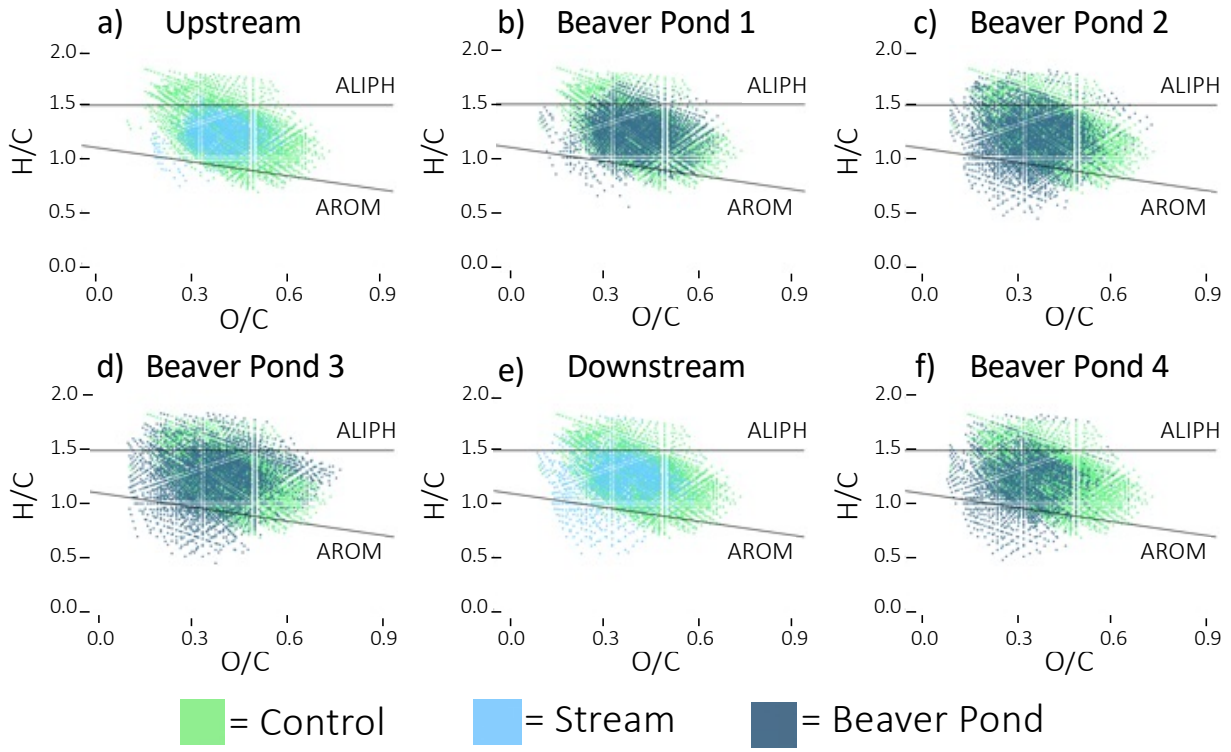

Figure 4.5. van Krevelen diagrams plotting the H/C and O/C ratios of the N-containing fraction (i.e., CHNO) obtained via +ESI FT-ICR MS of Ryan Fire stream and beaver pond PPL extracts of the unburned control (green) and burned sampling site (blue, see plot title for specific site). Sites are labeled alphabetically through the stream (a-f). Darker blue denotes beaver ponds. Formulas in common are subtracted out, so that only the formulas unique to each sample are plotted. Formulas plotted below the line that intercepts at H/C 1.2 are generally more aromatic in nature, while those plotting above the line that intercepts at 1.5 are more aliphatic.[76]

3.3 FI AND β/α ARE INFLUENCED BY FIRE AND WETLAND PRESENCE

FI is commonly used to infer the source of OM (i.e., microbial or terrestrial), where FI = 1.8 indicates microbially-derived DOM and FI = 1.2 indicates terrestrially-derived.[103] While this does not directly measure fire inputs, shifts in FI may represent important differences in microbial processing requirements. We observed an increase in FI values in the surface grab samples through the burned portion of the stream (**Figure D4**) which indicates that fire-influenced DOM more closely resembles microbially-derived DOM, in agreement with previous studies,[53] and is consistent with decreased molecular weight (MW) during the combustion of DOM.[104] This is supported by FT-ICR MS data which indicated that beaver ponds had lower average MW than

free-flowing streams (**Table 4.4**). While our FI values for the beaver ponds fall within previously reported ranges for wetlands (approx. 1.3-1.5),[92] there was no appreciable difference between the beaver ponds and the Upstream or Downstream sampling location.

Additionally, β/α is used to infer the proportion of recently produced DOM, in which the beta peak represents recently produced (likely microbial) DOM and the alpha peak represents older, more decomposed DOM.[105] β/α follows a similar trend to FI, increasing with burn activity and remaining elevated throughout the beaver ponds (**Figure D5**). Increases in β/α have been reported following fire[106] and within wetlands,[92] attributed to more simple structures with lower molecular weight and lower dissolved oxygen, respectively.

3.4 Microbial communities drive diverse anaerobic metabolisms in beaver ponds

Fire can have indirect effects on wetland microbes through broad changes in biogeochemistry (e.g., C, N availability). A combination of marker gene (16S rRNA gene) and metagenomic sequencing was used to investigate how the observed changes in aqueous chemistry impacted the microbiomes associated with the beaver pond sediments. 16S rRNA gene sequencing of sediment samples showed that the microbial communities within BP1, 2, and 4 were dominated by the phylum *Proteobacteria* (average relative abundance of ~35%; **Figure 4.6a)**. Within the *Proteobacteria*, the class *Deltaproteobacteria*, which is widely known for anaerobic metabolisms[107,108] and frequently identified as one of the most common taxa in wetlands,[109] was the most prevalent throughout the complexes (~20% average relative abundance). Notable orders within the *Deltaproteobacteria* included *Desulforomonadales*, *Syntrophobacterales*, and *Desulfobacterales* (average relative abundances of 4.4%, 6.5%, and 2%, respectively; **Figure 4.6b**), which include known sulfate reducers and are therefore well-suited for low-oxygen environments, such as beaver ponds.[110]

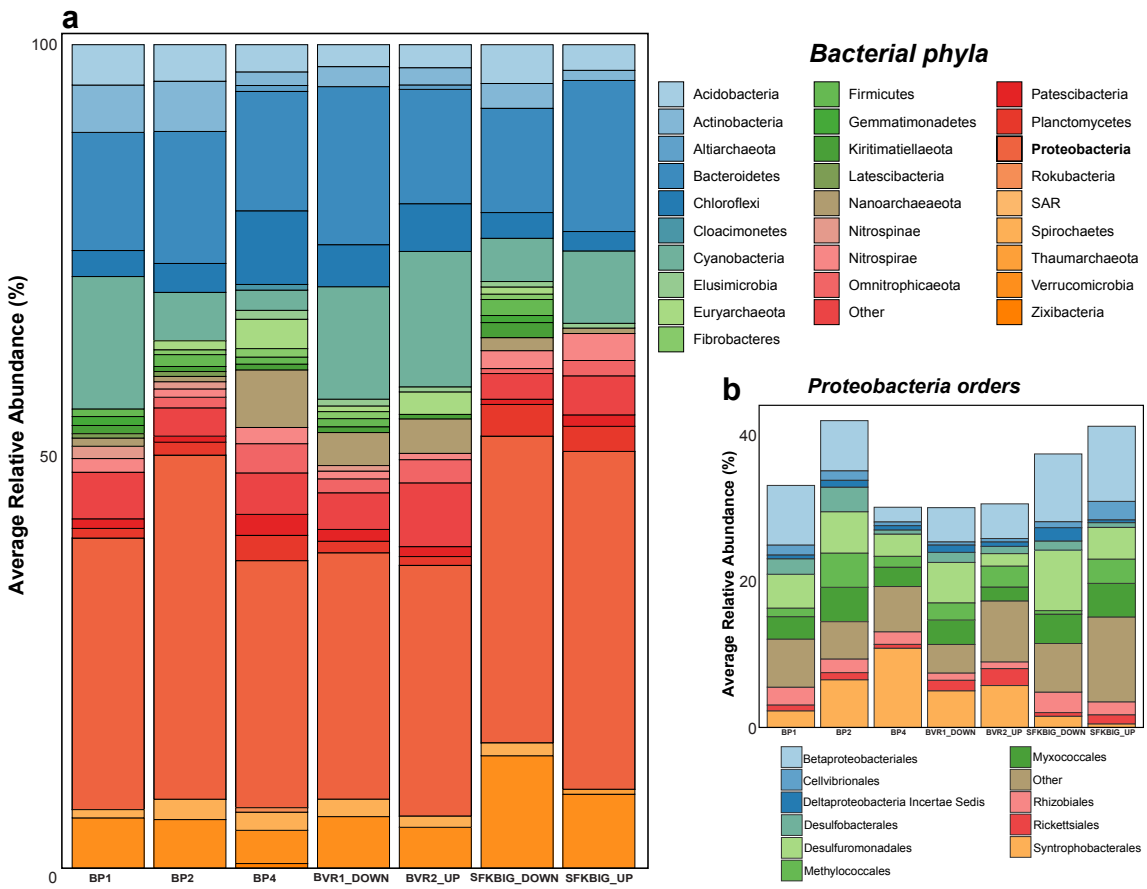

Figure 4.6. (a) Bacterial community composition (from 16S rRNA gene sequencing) showing bacterial phyla from beaver pond sediment samples affected by the Ryan fire (2018; BP1, 2, 4) and Beaver Creek fire (2016) (BVR1_DOWN, BVR2_UP, SFKBIG_UP, SFKBIG_DOWN) shown with the relative abundance of dominant bacterial phyla. Community composition is generally consistent across sample sites. (b) The relative abundance of orders within the dominant bacterial phyla, *Proteobacteria*, across samples. For both a and b, all phyla and orders with average relative abundance <0.005 (0.5%) added to 'Other'.

The microbial communities observed within the Ryan Fire beaver ponds were consistent across additional beaver ponds burned by the Beaver Creek Fire (2016). These nearby wetlands were also dominated by *Deltaproteobacteria* (~15% average relative abundance) and *Desulforomonadales*, *Syntrophobacterales*, and *Desulfobacterales* orders (4.4%, 3.2% and 1.5% respectively) (**Figure 4.6**), indicating that fresh pyDOM input did not significantly impact the dominant phyla within the beaver ponds. However, the more recently burned (Ryan fire) beaver

pond sediment microbiome was more compositionally diverse than nearby burned soils which were also affected by the same fire and reported elsewhere.[111] Average species richness (number of unique microbial taxa in a sample) within the beaver complexes was approximately double that in nearby burned soils (995 and 503 total species, respectively),[34] likely explained by a combination of factors including significant reductions in soil microbial diversity driven by wildfire events[112,113] and increased DOC and DON complexity within the ponds driven by possible pyDOM inputs.[112,113]

From the metagenomic sequencing of the seven sediment samples, including BP1, 2, and 4, we reconstructed 33 medium and high-quality (>50% complete, <10% contaminated)[114] metagenome-assembled genomes (MAGs), representing the majority of the dominant community members in the corresponding 16S rRNA gene dataset. The MAGs encompassed 12 different phyla, including 14 MAGs from the *Desulfobacterota*, 7 from the *Proteobacteria*, and 3 from the *Acidobacteria*. We linked *Deltaproteobacteria* amplicon sequence variants (ASVs) with two *Desulfobacterota* MAGs (with BLAST matches between 16S rRNA gene ASVs and MAG contigs containing 16S rRNA genes of > 95% identity over at least 150 bp). We infer that due to known taxonomic inconsistencies between the SILVA and GTDB-TK databases, MAGs classified as *Desulfobacterota* are taxonomically equivalent to the *Deltaproteobacteria* ASVs. The *Desulfobacterota* taxa was dominant in the MAG dataset, accounting for 14 of the 33 MAGs and ~35% of the relative abundance across the three main samples.

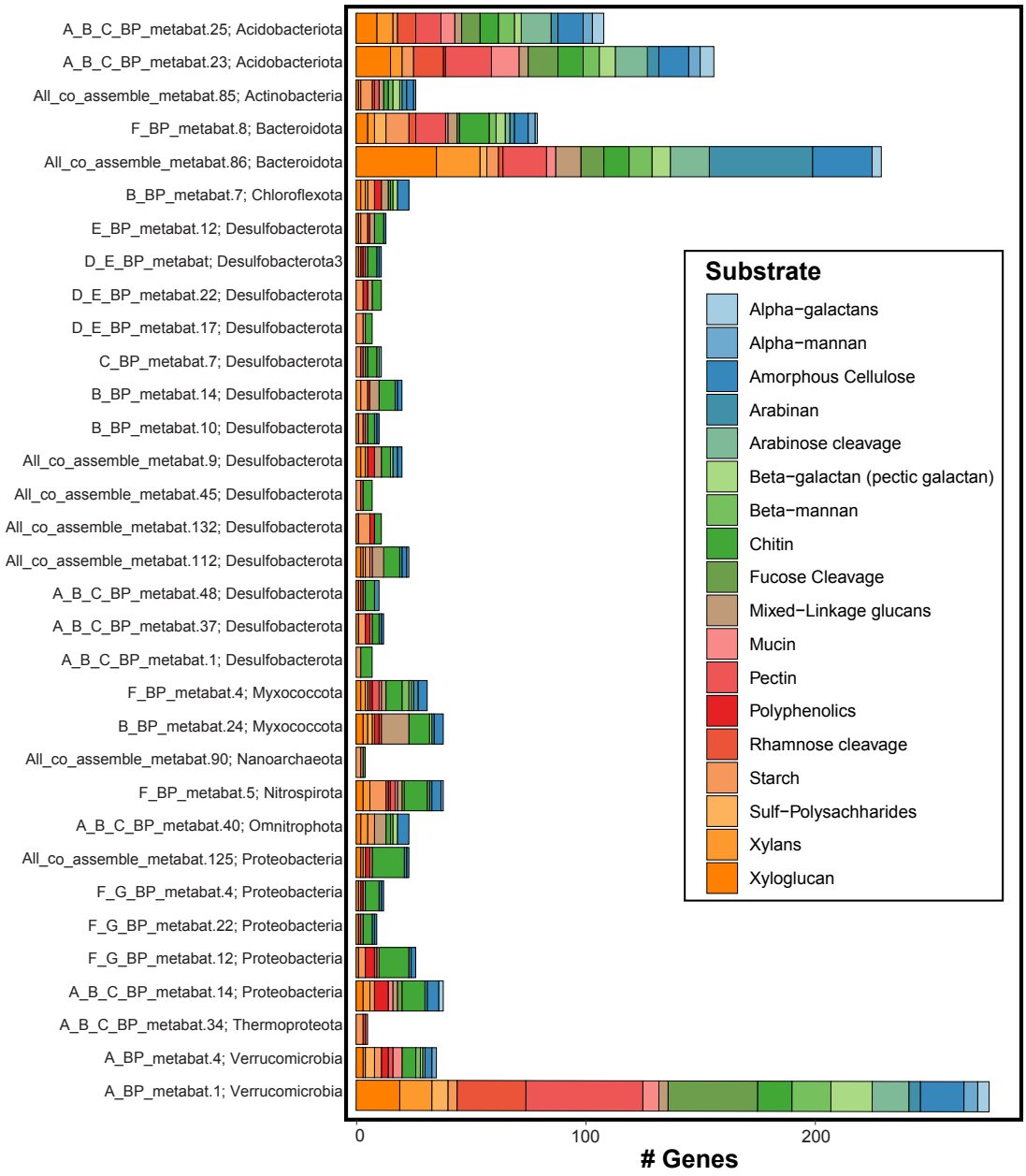

Figure 4.7. Metagenomics data collected from Ryan Fire-affected beaver pond sediments. The number of CAZymes encoded by each MAG (MAG name and phyla listed along y-axis), colored by the carbohydrate substrate upon which they act.

Highlighting the distinct chemical conditions found within beaver ponds, we identified a range of putative microbial metabolisms that, in contrast, are generally not observed in fire-impacted soils.[34] We inferred a fermentative lifestyle for several MAGs (i.e., A_BP_metabat.1,

All_co_assemble_metabat.86) that encoded a diverse suite of carbohydrate-active enzymes (CAZymes) (**Figure 4.7**), but which lacked a complete TCA cycle and electron transport chain components (e.g., NADH dehydrogenase, cytochrome C oxidase) (**Figure 4.8a**). Furthermore, these MAGs likely yield fermentation waste products (e.g., short-chain fatty acids) that can be utilized as both C and electron sources by many of the other MAGs (e.g., *Desulfobacterota*) that perform respiratory metabolisms (**Figure 4.8d**). Indeed, the 14 *Desulfobacterota* MAGs encoded widespread genomic potential for anaerobic respiratory metabolisms, including metal reduction (i.e., Fe^{3+}, Mn^{4+}), which could drive increased aqueous Fe concentrations in the beaver complexes (**Figure D6**), and potentially cause the observed increases in DOC and DON in the beaver ponds (**Figure 4.3**) and increased number of formulas assigned in the +ESI spectra (**Figure 4.5**) through the dissolution of DOM-metal complexes.[115] This functionality was inferred from the presence of genes encoding multi-heme c-type cytochromes (MHCs), which are used to transfer electrons to extracellular electron acceptors[116] Of the 33 recovered MAGs, 29 encoded MHCs, including all 14 of the *Desulfobacterota* MAGs (**Figure 4.8c**). Eleven of these 14 MAGs had MHCs that could be localized to the periplasm or extracellular space (average of 31 cytochromes per MAG; **Figure 4.8c**), with an average of ~7 CXXCH motifs per cytochrome (range of 3-16), which is similar to iron reducing microorganisms in other systems.[108] Another prevalent anaerobic metabolism is sulfate reduction, identified here through the presence of reductive *dsrAB* genes. Fourteen MAGs – including 10 *Desulfobacterota* MAGs – encoded these enzymes, further revealing the capacity for diverse metabolisms within the beaver ponds (**Figure 4.6c**). Importantly, our calculated NOSC values indicate that the DOM in the beaver ponds is not energetically constrained from reduction by these alternate electron acceptors (**Table 4.3**)[97] and is a suitable substrate for the wide range of metabolisms identified in the ponds.

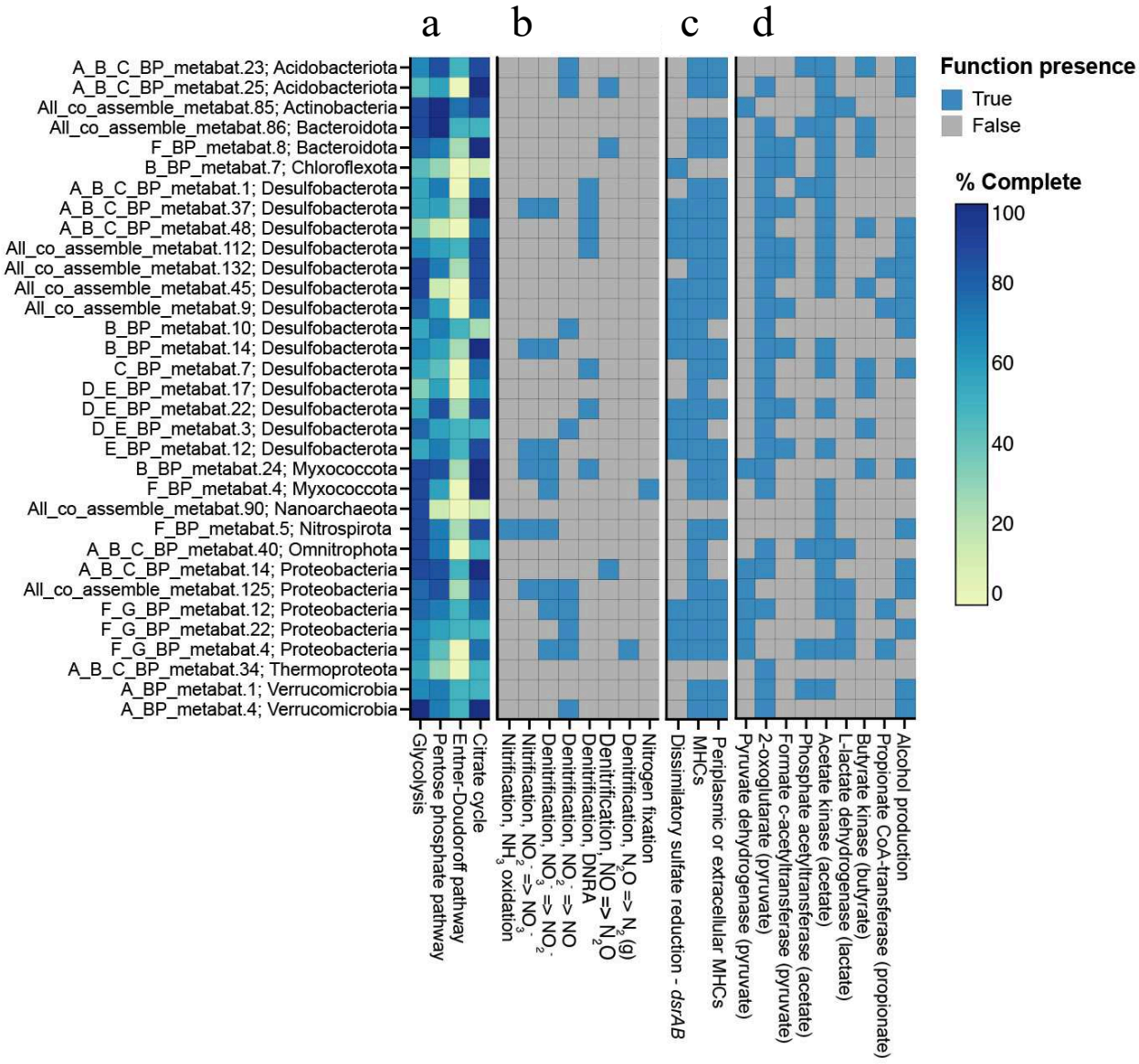

Figure 4.8. Broad overview of the (a) completeness or (b, c, d) presence/absence of functions of interest in the 33 MAGs (listed on the left). Panels overview (a) central metabolism pathways, (b) inorganic N metabolisms, (c) alternate electron acceptors, and (d) SCFA and alcohol conversions. In d, the compound that the enzyme acts upon is in parentheses. Figure adapted from DRAM product.[88]

Although there is clear evidence for accumulation of unique aromatic compounds within the beaver ponds (**Figure 4.6**), none of the MAGs in this study encoded the enzymatic machinery for anaerobic degradation of aromatic C, which is often formed during soil heating. For example, the enzyme benzylsuccinate synthase (EC:4.1.99.11) that catalyzes fumarate addition as the first

step of anaerobic toluene catabolism was absent from all the reconstructed MAGs.[117] Only one MAG (B_BP_metabat.7; phyla *Chloroflexota*) encoded a benzylsuccinate CoA-transferase subunit (EC:2.8.3.15), which catalyzes the next step of the degradation reaction. Therefore, we infer that the anaerobic degradation of aromatic compounds is likely not a widespread metabolism in the beaver pond microbiome. Because pyDOM is rich in aromatic structures,[118] these results could explain why these molecules appear to be enriched in the low-oxygen beaver ponds (**Figure 4.5**).

Conversely, there is evidence for the potential utilization of other, likely more labile, compounds generated indirectly following wildfire through microbial degradation of necromass-derived C via the utilization of peptidases; all 33 of the MAGs encoded peptidases, with an average of ~116 per genome. Peptidases in the families S33 and C26 were among the most encoded (298 and 219 encoded genes, respectively), similar to other freshwater studies (Wilkins, unpublished data). Peptidases within the S33 family release the N-terminal residue from a peptide, and C26 peptides cleave gamma-linked glutamate bonds. Another top represented family is the M23B family, which contains endopeptidases which lyse bacterial cell wall peptidoglycans. Previous studies have discussed the potential lysing of heat-sensitive cells during fire, which may lead to the release of microbially-derived C after wildfire.[119,120] The encoding of peptidases within our MAG database adds to the hypothesis that post-fire taxa may use this necromass-derived C, which is more labile than aromatic C, following wildfire. From these observations, we infer that the beaver pond microbiome is likely degrading necromass derived from heat-sensitive microbial or invertebrate soil fauna from the surrounding burned watershed,[121] rather than relying on pyDOM or limited vegetation inputs as the primary source of C. Although this has been shown in soils,[34] it

has yet to be shown in wetlands within burn scars. These observations also further explain the enrichment of aromatic DOM in the beaver ponds, which is often associated with pyDOM.

The microbial taxa discussed here (e.g., Desulfobacterota) are not typically found in free-flowing freshwater systems[122,123] or fire-impacted soils,[124] demonstrating that microbiomes within beaver pond sediments have the potential to perform unique biogeochemical reactions within the watershed, thus enhancing the ability of these features to act as ecosystem control points. The functional potential of the dominant community members in these burned beaver complex systems may contribute to Fe mobilization through the stream (**Figure D6**) and highly reducing metabolisms might also facilitate the local sequestration of DOC and DON seen through the complex (**Figure 4.5**). Thus, the implications of potential microbially-mediated heavy metal transformations are a key area for future research in fire-impacted wetlands. While we recognize the relatively small number of samples in our analysis, this study emphasizes the importance of beaver ponds on the biogeochemical processing of burned areas and represents an important step towards understanding how pyDOM is cycled in low-oxygen wetland environments.

4. Conclusion

Water chemistry and microbiology indeed change as water flows through a fire-impacted region, due to the combined influence of fire-impacted organic matter and the presence of beaver ponds along the stream channel. These burned beaver ponds had higher DOC, DTN, and nitrate compared to an upstream reach or an adjacent unburned stream. There was a pattern of increased DOC and DTN within the ponds compared to free-flowing streams and nitrate appeared to decline as water moved through the sequence of beaver ponds. There were more N-containing formulas detected in the ponds and lower C:N ratios, which would be consistent with increased DTN retention. Additionally, surface water in the beaver ponds had lower C:N ratios and higher

aromaticity than burned stream water. Impoundment within beaver ponds may enhance post-fire sediment and C and N storage compared to free-flowing streams, which may minimize the downstream formation of carcinogenic disinfection by-products during chlorination at water treatment plants.[101,125] Microbial analyses indicated that the input of fresh pyDOM did not significantly impact the dominant phyla in the beaver ponds. Rather than using aromatic pyDOM as the primary source of C for respiration, microbes in these sites likely degrade biomass and other more labile sources of organic C. The preservation of pyDOM appeared to be localized within the ponds themselves as changes in elemental composition and unique formulas were limited to the ponds and not observed downstream; therefore, fire-impacted beaver ponds appear to function as biogeochemical "hotspots" due to their unique biogeochemistry.

5. Author Contributions

According to CRediT criteria, my contributions to this work included conceptualization, data curation, formal analysis, investigation, methodology, visualization, writing – original draft, and writing – reviewing and editing. Contributions by A.R.N. included data curation, formal analysis, methodology, writing – original draft, and writing – reviewing and editing. Contributions by A.M.M. included data curation, resources, validation, and writing – review and editing. Contributions by T.S.F. included data curation, methodology, and writing – review and editing. Contributions by R.B.Y. included software and writing – review and editing. Contributions by C.C.R. included conceptualization, data curation, validation, and writing – review and editing. Contributions by M.J.W. and T.B. included conceptualization, funding acquisition, project administration, resources, writing – original draft, and writing – review and editing.

REFERENCES

(1) McDonald, R.; Shemie, D. *Urban Water Blueprint: Mapping Conservation Solutions to the Global Water Challenge.*; Washington, D.C., 2014.

(2) de Groot, R.; D'Arge, R.; Sutton, P.; Grasso, M.; Limburg, K.; Farber, S.; Raskin, R.; van den Belt, M.; Costanza, R.; Hannon, B.; Paruelo, J.; O'Neill, R.; Naeem, S. The Value of the the World's Ecosystem Services and Natural Capital. *Nature* **2003**, No. 387, 253–260.

(3) Stein, S. M.; Butler, B. Private Forests and Public Resources. *Wildland Waters* **2004**, *Summer* (FS 790), 1–24. https://doi.org/10.1034/j.1399-3038.2001.012004179-.x.

(4) Bladon, K. D.; Emelko, M. B.; Silins, U.; Stone, M. Wildfire and the Future of Water Supply. *Environ Sci Technol* **2014**, *48* (16), 8936–8943. https://doi.org/10.1021/es500130g.

(5) Ramchander, M.; Rahul, K. Microbial Diversity of Wetlands of India. *Res J Chem Environ* **2021**, *25* (3), 153–163.

(6) Emelko, M. B.; Silins, U.; Bladon, K. D.; Stone, M. Implications of Land Disturbance on Drinking Water Treatability in a Changing Climate: Demonstrating the Need for " Source Water Supply and Protection" Strategies. *Water Res* **2011**, *45* (2), 461–472. https://doi.org/10.1016/j.watres.2010.08.051.

(7) Alizadeh, M. R.; Abatzoglou, J. T.; Luce, C. H.; Adamowski, J. F.; Farid, A.; Sadegh, M. Warming Enabled Upslope Advance in Western US Forest Fires. *PNAS* **2021**, *118*. https://doi.org/10.1073/pnas.2009717118/-/DCSupplemental.

(8) Abatzoglou, J. T.; Kolden, C. A.; Williams, A. P.; Lutz, J. A.; Smith, A. M. S. Climatic Influences on Interannual Variability in Regional Burn Severity across Western US Forests. *Int J Wildland Fire* **2017**, *26* (4), 269–275. https://doi.org/10.1071/WF16165.

(9) Knicker, H. How Does Fire Affect the Nature and Stability of Soil Organic Nitrogen and Carbon? A Review. *Biogeochemistry* **2007**, *85* (1), 91–118. https://doi.org/10.1007/s10533-007-9104-4.

(10) Bird, M. I.; Wynn, J. G.; Saiz, G.; Wurster, C. M.; McBeath, A. The Pyrogenic Carbon Cycle. *Annu Rev Earth Planet Sci* **2015**, *43*, 273–298. https://doi.org/10.1146/annurev-earth-060614-105038.

(11) Viedma, O.; Quesada, J.; Torres, I.; de Santis, A.; Moreno, J. M. Fire Severity in a Large Fire in a Pinus Pinaster Forest Is Highly Predictable from Burning Conditions, Stand Structure, and Topography. *Ecosystems* **2015**, *18* (2), 237–250. https://doi.org/10.1007/s10021-014-9824-y.

(12) Doerr, S. H.; Santín, C. Global Trends in Wildfire and Its Impacts: Perceptions versus Realities in a Changing World. *Philosophical Transactions of the Royal Society B: Biological Sciences* **2016**, *371* (1696). https://doi.org/10.1098/rstb.2015.0345.

(13) Schmidt, M. W. I.; Noack, A. G. Black Carbon in Soils and Sediments: Analysis, Distribution, Implications, and Current Challenges. *Global Biogeochemical Cycles*. Blackwell Publishing Ltd September 1, 2000, pp 777–793. https://doi.org/10.1029/1999GB001208.

(14) Olivella, M. A.; Ribalta, T. G.; de Febrer, A. R.; Mollet, J. M.; de Las Heras, F. X. C. Distribution of Polycyclic Aromatic Hydrocarbons in Riverine Waters after Mediterranean Forest Fires. *Science of the Total Environment* **2006**, *355* (1–3), 156–166. https://doi.org/10.1016/j.scitotenv.2005.02.033.

(15) Rhoades, C. C.; Chow, A. T.; Covino, T. P.; Fegel, T. S.; Pierson, D. N.; Rhea, A. E. The Legacy of a Severe Wildfire on Stream Nitrogen and Carbon in Headwater Catchments. *Ecosystems* **2018**. https://doi.org/10.1007/s10021-018-0293-6.

(16) Rhoades, C. C.; Nunes, J. P.; Silins, U.; Doerr, S. H. The Influence of Wildfire on Water Quality and Watershed Processes: New Insights and Remaining Challenges. *Int J Wildland Fire* **2019**, *28* (10), 721–725. https://doi.org/10.1071/WFv28n10_FO.
(17) Minshall, G. W.; Brock, J. T.; Andrews, D. A.; Robinson, C. T. Water Quality, Substratum and Biotic Responses of Five Central Idaho (USA) Streams during the First Year Following the Mortar Creek Fire. *Int J Wildland Fire* **2001**, *10* (2), 185–199. https://doi.org/10.1071/WF01017.
(18) Murphy, S. F.; Writer, J. H.; McCleskey, R. B.; Martin, D. A. The Role of Precipitation Type, Intensity, and Spatial Distribution in Source Water Quality after Wildfire. *Environmental Research Letters* **2015**, *10* (8). https://doi.org/10.1088/1748-9326/11/7/079501.
(19) Hohner, A. K.; Cawley, K.; Oropeza, J.; Summers, R. S.; Rosario-Ortiz, F. L. Drinking Water Treatment Response Following a Colorado Wildfire. *Water Res* **2016**, *105*, 187–198. https://doi.org/10.1016/j.watres.2016.08.034.
(20) Ferrer, I.; Thurman, E. M.; Zweigenbaum, J. A.; Murphy, S. F.; Webster, J. P.; Rosario-Ortiz, F. L. Wildfires: Identification of a New Suite of Aromatic Polycarboxylic Acids in Ash and Surface Water. *Science of the Total Environment* **2021**, *770*. https://doi.org/10.1016/j.scitotenv.2020.144661.
(21) Smith, H. G.; Sheridan, G. J.; Lane, P. N. J.; Nyman, P.; Haydon, S. Wildfire Effects on Water Quality in Forest Catchments: A Review with Implications for Water Supply. *Journal of Hydrology*. January 5, 2011, pp 170–192. https://doi.org/10.1016/j.jhydrol.2010.10.043.
(22) Kleber, M. What Is Recalcitrant Soil Organic Matter? *Environmental Chemistry* **2010**, *7* (4), 320–332. https://doi.org/10.1071/EN10006.
(23) Lehmann, J.; Kleber, M. The Contentious Nature of Soil Organic Matter. *Nature* **2015**, *528* (7580), 60–68. https://doi.org/10.1038/nature16069.
(24) Robinne, F. N.; Bladon, K. D.; Miller, C.; Parisien, M. A.; Mathieu, J.; Flannigan, M. D. A Spatial Evaluation of Global Wildfire-Water Risks to Human and Natural Systems. *Science of the Total Environment* **2018**, *610–611*, 1193–1206. https://doi.org/10.1016/j.scitotenv.2017.08.112.
(25) Naiman, R. J.; Johnston, C. A.; Kelley, J. C. Alteration of North American Streams by Beaver. *Bioscience* **1988**, *38* (11), 753–762. https://doi.org/10.2307/1310784.
(26) Rosell, F.; Bozsér, O.; Collen, P.; Parker, H. Ecological Impact of Beavers Castor Fiber and Castor Canadensis and Their Ability to Modify Ecosystems. *Mamm Rev* **2005**, *35* (3–4), 248–276. https://doi.org/10.1111/j.1365-2907.2005.00067.x.
(27) Briggs, M. A.; Wang, C.; Day-Lewis, F. D.; Williams, K. H.; Dong, W.; Lane, J. W. Return Flows from Beaver Ponds Enhance Floodplain-to-River Metals Exchange in Alluvial Mountain Catchments. *Science of the Total Environment* **2019**, *685*, 357–369. https://doi.org/10.1016/j.scitotenv.2019.05.371.
(28) Boye, K.; Herrmann, A. M.; Schaefer, M. v.; Tfaily, M. M.; Fendorf, S. Discerning Microbially Mediated Processes during Redox Transitions in Flooded Soils Using Carbon and Energy Balances. *Front Environ Sci* **2018**, *6* (MAY). https://doi.org/10.3389/fenvs.2018.00015.
(29) Larsen, A.; Larsen, J. R.; Lane, S. N. Dam Builders and Their Works: Beaver Influences on the Structure and Function of River Corridor Hydrology, Geomorphology, Biogeochemistry and Ecosystems. *Earth-Science Reviews*. Elsevier B.V. July 1, 2021. https://doi.org/10.1016/j.earscirev.2021.103623.
(30) Missik, J. E. C.; Liu, H.; Gao, Z.; Huang, M.; Chen, X.; Arntzen, E.; Mcfarland, D. P.; Ren, H.; Titzler, P. S.; Thomle, J. N.; Goldman, A. Groundwater-River Water Exchange

Enhances Growing Season Evapotranspiration and Carbon Uptake in a Semiarid Riparian Ecosystem. *J Geophys Res Biogeosci* **2019**, *124* (1), 99–114. https://doi.org/10.1029/2018JG004666.
(31) Lynch, L. M.; Covino, T. P.; Boot, C. M.; Wallenstein, M. D.; Sutfin, N. A.; Fegel, T. S. River Channel Connectivity Shifts Metabolite Composition and Dissolved Organic Matter Chemistry. *Nat Commun* **2019**, *10* (1). https://doi.org/10.1038/s41467-019-08406-8.
(32) Wegener, P.; Covino, T.; Rhoades, C. Evaluating Controls on Nutrient Retention and Export in Wide and Narrow Valley Segments of a Mountain River Corridor. *J Geophys Res Biogeosci* **2018**, *123* (6), 1817–1826. https://doi.org/10.1029/2017JG004109.
(33) Fischer, M. S.; Stark, F. G.; Berry, T. D.; Zeba, N.; Whitman, T.; Traxler, M. F. Pyrolyzed Substrates Induce Aromatic Compound Metabolism in the Post-Fire Fungus, Pyronema Domesticum. *Front Microbiol* **2021**, *12*. https://doi.org/10.3389/fmicb.2021.729289.
(34) Nelson, A. R.; Narrowe, A. B.; Rhoades, C. C.; Fegel, T. S.; Roth, H. K.; Chu, R. K.; Amundson, K. K.; Geonczy, S. E.; Young, R. B.; Steindorff, A. S.; Mondo, S. J.; Grigoriev, I. v; Salamov, A.; Borch, T.; Wilkins, M. J.; author, C. Playing with FiRE: A Genome Resolved View of the Soil Microbiome Responses to High Severity Forest Wildfire. *bioRxiv* **2021**. https://doi.org/10.1101/2021.08.17.456416.
(35) Whitfield, C. J.; Baulch, H. M.; Chun, K. P.; Westbrook, C. J. Beaver-Mediated Methane Emission: The Effects of Population Growth in Eurasia and the Americas. *Ambio* **2015**, *44* (1), 7–15. https://doi.org/10.1007/s13280-014-0575-y.
(36) Halley, D. J.; Saveljev, A. P.; Rosell, F. Population and Distribution of Beavers Castor Fiber and Castor Canadensis in Eurasia. *Mammal Review*. Blackwell Publishing Ltd January 1, 2021, pp 1–24. https://doi.org/10.1111/mam.12216.
(37) Geisseler, D.; Horwath, W. R.; Joergensen, R. G.; Ludwig, B. Pathways of Nitrogen Utilization by Soil Microorganisms - A Review. *Soil Biology and Biochemistry*. December 2010, pp 2058–2067. https://doi.org/10.1016/j.soilbio.2010.08.021.
(38) Acquisti, C.; Elser, J. J.; Kumar, S. Ecological Nitrogen Limitation Shapes the DNA Composition of Plant Genomes. *Mol Biol Evol* **2009**, *26* (5), 953–956. https://doi.org/10.1093/molbev/msp038.
(39) Adkins, J.; Sanderman, J.; Miesel, J. Soil Carbon Pools and Fluxes Vary across a Burn Severity Gradient Three Years after Wildfire in Sierra Nevada Mixed-Conifer Forest. *Geoderma* **2019**, *333*, 10–22. https://doi.org/10.1016/j.geoderma.2018.07.009.
(40) Miesel, J. R.; Hockaday, W. C.; Kolka, R. K.; Townsend, P. A. Soil Organic Matter Composition and Quality across Fire Severity Gradients in Coniferous and Deciduous Forests of the Southern Boreal Region. *Journal of Geophysical Research G: Biogeosciences* **2015**, *120* (6), 1124–1141. https://doi.org/10.1002/2015JG002959.
(41) Rhoades, C. C.; Entwistle, D.; Butler, D. The Influence of Wildfire Extent and Severity on Streamwater Chemistry, Sediment and Temperature Following the Hayman Fire, Colorado. *Int J Wildland Fire* **2011**, *20* (3), 430–442. https://doi.org/10.1071/WF09086.
(42) Bladon, K. D.; Silins, U.; Wagner, M. J.; Stone, M.; Emelko, M. B.; Mendoza, C. A.; Devito, K. J.; Boon, S. Wildfire Impacts on Nitrogen Concentration and Production from Headwater Streams in Southern Alberta's Rocky Mountains. *Canadian Journal of Forest Research* **2008**, *38* (9), 2359–2371. https://doi.org/10.1139/X08-071.
(43) Robinne, F. N.; Bladon, K. D.; Silins, U.; Emelko, M. B.; Flannigan, M. D.; Parisien, M. A.; Wang, X.; Kienzle, S. W.; Dupont, D. P. A Regional-Scale Index for Assessing the Exposure

of Drinking-Water Sources to Wildfires. *Forests* **2019**, *10* (5), 1–21. https://doi.org/10.3390/f10050384.
(44) Pisani, O.; Boyer, J. N.; Podgorski, D. C.; Thomas, C. R.; Coley, T.; Jaffé, R. Molecular Composition and Bioavailability of Dissolved Organic Nitrogen in a Lake Flow-Influenced River in South Florida, USA. *Aquat Sci* **2017**, *79* (4), 891–908. https://doi.org/10.1007/s00027-017-0540-5.
(45) Hertkorn, N.; Harir, M.; Cawley, K. M.; Schmitt-Kopplin, P.; Jaffé, R. Molecular Characterization of Dissolved Organic Matter from Subtropical Wetlands: A Comparative Study through the Analysis of Optical Properties, NMR and FTICR/MS. *Biogeosciences* **2016**, *13* (8), 2257–2277. https://doi.org/10.5194/bg-13-2257-2016.
(46) Roth, H. K.; Borch, T.; Young, R. B.; Bahureksa, W.; Blakney, G. T.; Nelson, A. R.; Wilkins, M. J.; McKenna, A. M. Enhanced Speciation of Pyrogenic Organic Matter from Wildfires Enabled by 21 T FT-ICR Mass Spectrometry. *Anal Chem* **2022**, acs.analchem.1c05018. https://doi.org/10.1021/acs.analchem.1c05018.
(47) Jiménez-Morillo, N. T.; de la Rosa, J. M.; Waggoner, D.; Almendros, G.; González-Vila, F. J.; González-Pérez, J. A. Fire Effects in the Molecular Structure of Soil Organic Matter Fractions under Quercus Suber Cover. *Catena (Amst)* **2016**, *145*, 266–273. https://doi.org/10.1016/j.catena.2016.06.022.
(48) Luo, L.; Chen, Z.; Lv, J.; Cheng, Y.; Wu, T.; Huang, R. Molecular Understanding of Dissolved Black Carbon Sorption in Soil-Water Environment. *Water Res* **2019**, *154*, 210–216. https://doi.org/10.1016/j.watres.2019.01.060.
(49) de la Rosa, J. M.; Knicker, H. Bioavailability of N Released from N-Rich Pyrogenic Organic Matter: An Incubation Study. *Soil Biol Biochem* **2011**, *43* (12), 2368–2373. https://doi.org/10.1016/j.soilbio.2011.08.008.
(50) Mcknight, D. M.; Boyer, E. W.; Westerhoff, P. K.; Doran, P. T.; Kulbe, T.; Andersen, D. T. *Spectrofluorometric Characterization of Dissolved Organic Matter for Indication of Precursor Organic Material and Aromaticity*; 2001; Vol. 46.
(51) Jaffé, R.; McKnight, D.; Maie, N.; Cory, R.; McDowell, W. H.; Campbell, J. L. Spatial and Temporal Variations in DOM Composition in Ecosystems: The Importance of Long-Term Monitoring of Optical Properties. *J Geophys Res Biogeosci* **2008**, *113* (4), 1–15. https://doi.org/10.1029/2008JG000683.
(52) Rosario-Ortiz, F. L.; Korak, J. A. Oversimplification of Dissolved Organic Matter Fluorescence Analysis: Potential Pitfalls of Current Methods. *Environ Sci Technol* **2017**, *51* (2), 759–761. https://doi.org/10.1021/acs.est.6b06133.
(53) Cawley, K. M.; Hohner, A. K.; McKee, G. A.; Borch, T.; Omur-Ozbek, P.; Oropeza, J.; Rosario-Ortiz, F. L. Characterization and Spatial Distribution of Particulate and Soluble Carbon and Nitrogen from Wildfire-Impacted Sediments. *J Soils Sediments* **2018**, *18* (4), 1314–1326. https://doi.org/10.1007/s11368-016-1604-1.
(54) Cory, R. M.; McKnight, D. M. Fluorescence Spectroscopy Reveals Ubiquitous Presence of Oxidized and Reduced Quinones in Dissolved Organic Matter. *Environ Sci Technol* **2005**, *39* (21), 8142–8149. https://doi.org/10.1021/es0506962.
(55) Parlanti, E.; Woè Rz, K.; Geo€roy, L.; Lamotte, M. Dissolved Organic Matter Fluorescence Spectroscopy as a Tool to Estimate Biological Activity in a Coastal Zone Submitted to Anthropogenic Inputs. *Org Geochem* **2000**, 1765–1781. https://doi.org/10.1016/S0146-6380(00)00124-8.

(56) Bahureksa, W.; Tfaily, M. M.; Boiteau, R. M.; Young, R. B.; Logan, M. N.; McKenna, A. M.; Borch, T. Soil Organic Matter Characterization by Fourier Transform Ion Cyclotron Resonance Mass Spectrometry (FTICR MS): A Critical Review of Sample Preparation, Analysis, and Data Interpretation. *Environmental Science and Technology*. American Chemical Society July 20, 2021, pp 9637–9656. https://doi.org/10.1021/acs.est.1c01135.
(57) Hertkorn, N.; Frommberger, M.; Witt, M.; Koch, B. P.; Schmitt-Kopplin, P.; Perdue, E. M. Natural Organic Matter and the Event Horizon of Mass Spectrometry. *Anal Chem* **2008**, *80* (23), 8908–8919. https://doi.org/10.1021/ac800464g.
(58) Hendrickson, C. L.; Quinn, J. P.; Kaiser, N. K.; Smith, D. F.; Blakney, G. T.; Chen, T.; Marshall, A. G.; Weisbrod, C. R.; Beu, S. C. 21 Tesla Fourier Transform Ion Cyclotron Resonance Mass Spectrometer: A National Resource for Ultrahigh Resolution Mass Analysis. *J Am Soc Mass Spectrom* **2015**, *26* (9), 1626–1632. https://doi.org/10.1007/s13361-015-1182-2.
(59) Ohno, T.; Sleighter, R. L.; Hatcher, P. G. Comparative Study of Organic Matter Chemical Characterization Using Negative and Positive Mode Electrospray Ionization Ultrahigh-Resolution Mass Spectrometry. *Anal Bioanal Chem* **2016**, *408* (10), 2497–2504. https://doi.org/10.1007/s00216-016-9346-x.
(60) Dittmar, T.; Koch, B.; Hertkorn, N.; Kattner, G. A Simple and Efficient Method for the Solid-Phase Extraction of Dissolved Organic Matter (SPE-DOM) from Seawater. *Limnol Oceanogr Methods* **2008**, *6* (6), 230–235. https://doi.org/10.4319/lom.2008.6.230.
(61) Dittmar, T.; Koch, B.; Hertkorn, N.; Kattner, G. A Simple and Efficient Method for the Solid-Phase Extraction of Dissolved Organic Matter (SPE-DOM) from Seawater. *Limnol Oceanogr Methods* **2008**, *6*, 230–235.
(62) Lam, B.; Baer, A.; Alaee, M.; Lefebvre, B.; Moser, A.; Williams, A.; Simpson, A. J. Major Structural Components in Freshwater Dissolved Organic Matter. *Environ Sci Technol* **2007**, *41* (24), 8240–8247. https://doi.org/10.1021/es0713072.
(63) Li, Y.; Harir, M.; Uhl, J.; Kanawati, B.; Lucio, M.; Smirnov, K. S.; Koch, B. P.; Schmitt-Kopplin, P.; Hertkorn, N. How Representative Are Dissolved Organic Matter (DOM) Extracts? A Comprehensive Study of Sorbent Selectivity for DOM Isolation. *Water Res* **2017**, *116*, 316–323. https://doi.org/10.1016/j.watres.2017.03.038.
(64) Emmett, M. R.; White, F. M.; Hendrickson, C. L.; Shi, D. H.; Marshall, A. G. Application of Micro-Electrospray Liquid Chromatography Techniques to FT-ICR MS to Enable High-Sensitivity Biological Analysis. *J Am Soc Mass Spectrom* **1998**, *9* (4), 333–340. https://doi.org/10.1016/S1044-0305(97)00287-0.
(65) Smith, D. F.; Podgorski, D. C.; Rodgers, R. P.; Blakney, G. T.; Hendrickson, C. L. 21 Tesla FT-ICR Mass Spectrometer for Ultrahigh-Resolution Analysis of Complex Organic Mixtures. *Anal Chem* **2018**, *90* (3), 2041–2047. https://doi.org/10.1021/acs.analchem.7b04159.
(66) Kaiser, N. K.; McKenna, A. M.; Savory, J. J.; Hendrickson, C. L.; Marshall, A. G. Tailored Ion Radius Distribution for Increased Dynamic Range in FT-ICR Mass Analysis of Complex Mixtures. *Anal Chem* **2013**, *85* (1), 265–272. https://doi.org/10.1021/ac302678v.
(67) Chen, T.; Beu, S. C.; Kaiser, N. K.; Hendrickson, C. L. Note: Optimized Circuit for Excitation and Detection with One Pair of Electrodes for Improved Fourier Transform Ion Cyclotron Resonance Mass Spectrometry. *Review of Scientific Instruments* **2014**, *85* (6). https://doi.org/10.1063/1.4883179.
(68) Boldin, I. A.; Nikolaev, E. N. Fourier Transform Ion Cyclotron Resonance Cell with Dynamic Harmonization of the Electric Field in the Whole Volume by Shaping of the Excitation

and Detection Electrode Assembly. *Rapid Communications in Mass Spectrometry* **2011**, *25* (1), 122–126. https://doi.org/10.1002/rcm.4838.
(69) Blakney, G. T.; Hendrickson, C. L.; Marshall, A. G. Predator Data Station: A Fast Data Acquisition System for Advanced FT-ICR MS Experiments. *Int J Mass Spectrom* **2011**, *306* (2–3), 246–252. https://doi.org/10.1016/j.ijms.2011.03.009.
(70) Xian, F.; Hendrickson, C. L.; Blakney, G. T.; Beu, S. C.; Marshall, A. G. Automated Broadband Phase Correction of Fourier Transform Ion Cyclotron Resonance Mass Spectra. *Anal Chem* **2010**, *82* (21), 8807–8812. https://doi.org/10.1021/ac101091w.
(71) Savory, J. J.; Kaiser, N. K.; Mckenna, A. M.; Xian, F.; Blakney, G. T.; Rodgers, R. P.; Hendrickson, C. L.; Marshall, A. G. Measurement Accuracy with a "Walking" Calibration Equation. *Anal Chem* **2011**, *83*, 1732–1736.
(72) Kendrick, E. A Mass Scale Based Resolution Mass Spectrometry of Organic Compounds. *Anal Chem* **1963**, *35* (13), 2146–2154.
(73) Hughey, C. A.; Hendrickson, C. L.; Rodgers, R. P.; Marshall, A. G.; Qian, K. Kendrick Mass Defect Spectrum: A Compact Visual Analysis for Ultrahigh-Resolution Broadband Mass Spectra. *Anal Chem* **2001**, *73* (19), 4676–4681. https://doi.org/10.1021/ac010560w.
(74) McLafferty, F. W.; Turecek, F. *Interpretation of Mass Spectra*, 4th ed.; University Science Books: Mill Valley, CA, 1993.
(75) Corilo, Y. E. PetroOrg Software. Florida State University, Omics LLC: Tallahassee, FL 2014.
(76) Koch, B. P.; Dittmar, T. From Mass to Structure: An Aromaticity Index for High-Resolution Mass Data of Natural Organic Matter. *Rapid Communications in Mass Spectrometry* **2006**, *20* (5), 926–932. https://doi.org/10.1002/rcm.2386.
(77) Koch, B. P.; Dittmar, T. Erratum: From Mass to Structure: An Aromaticity Index for High-Resolution Mass Data of Natural Organic Matter (Rapid Communications in Mass Spectrometry (2006) 20 (926-932) DOI: 10.1002/Rcm.2386). *Rapid Communications in Mass Spectrometry* **2016**, *30* (1), 250. https://doi.org/10.1002/rcm.7433.
(78) LaRowe, D. E.; van Cappellen, P. Degradation of Natural Organic Matter: A Thermodynamic Analysis. *Geochim Cosmochim Acta* **2011**, *75* (8), 2030–2042. https://doi.org/10.1016/j.gca.2011.01.020.
(79) Kim, S.; Kramer, R. W.; Hatcher, P. G. Graphical Method for Analysis of Ultrahigh-Resolution Broadband Mass Spectra of Natural Organic Matter, the Van Krevelen Diagram. *Anal Chem* **2003**, *75* (20), 5336–5344. https://doi.org/10.1021/ac034415p.
(80) Quast, C.; Pruesse, E.; Yilmaz, P.; Gerken, J.; Schweer, T.; Yarza, P.; Peplies, J.; Glöckner, F. O. The SILVA Ribosomal RNA Gene Database Project: Improved Data Processing and Web-Based Tools. *Nucleic Acids Res* **2012**, *41* (D1), D590–D596. https://doi.org/10.1093/nar/gks1219.
(81) Quast, C.; Pruesse, E.; Yilmaz, P.; Gerken, J.; Schweer, T.; Yarza, P.; Peplies, J.; Glöckner, F. O. The SILVA Ribosomal RNA Gene Database Project: Improved Data Processing and Web-Based Tools. *Nucleic Acids Res* **2013**, *41* (D1). https://doi.org/10.1093/nar/gks1219.
(82) Joshi, N.; Fass, J. Sickle: A Sliding-Window, Adaptive, Quality-Based Trimming Tool for FastQ Files. 2011.
(83) Li, D.; Liu, C. M.; Luo, R.; Sadakane, K.; Lam, T. W. MEGAHIT: An Ultra-Fast Single-Node Solution for Large and Complex Metagenomics Assembly via Succinct de Bruijn Graph. *Bioinformatics* **2015**, *31* (10), 1674–1676. https://doi.org/10.1093/bioinformatics/btv033.

(84) Kang, D. D.; Li, F.; Kirton, E.; Thomas, A.; Egan, R.; An, H.; Wang, Z. MetaBAT 2: An Adaptive Binning Algorithm for Robust and Efficient Genome Reconstruction from Metagenome Assemblies. *PeerJ* **2019**, *2019* (7). https://doi.org/10.7717/peerj.7359.
(85) Parks, D. H.; Imelfort, M.; Skennerton, C. T.; Hugenholtz, P.; Tyson, G. W. CheckM: Assessing the Quality of Microbial Genomes Recovered from Isolates, Single Cells, and Metagenomes. *Genome Res* **2015**, *25* (7), 1043–1055. https://doi.org/10.1101/gr.186072.114.
(86) Chaumeil, P. A.; Mussig, A. J.; Hugenholtz, P.; Parks, D. H. GTDB-Tk: A Toolkit to Classify Genomes with the Genome Taxonomy Database. *Bioinformatics* **2020**, *36* (6), 1925–1927. https://doi.org/10.1093/bioinformatics/btz848.
(87) Olm, M. R.; Brown, C. T.; Brooks, B.; Banfield, J. F. DRep: A Tool for Fast and Accurate Genomic Comparisons That Enables Improved Genome Recovery from Metagenomes through de-Replication. *ISME Journal* **2017**, *11* (12), 2864–2868. https://doi.org/10.1038/ismej.2017.126.
(88) Shaffer, M.; Borton, M. A.; McGivern, B. B.; Zayed, A. A.; la Rosa, S. L. 0003 3527 8101; Solden, L. M.; Liu, P.; Narrowe, A. B.; Rodríguez-Ramos, J.; Bolduc, B.; Gazitúa, M. C.; Daly, R. A.; Smith, G. J.; Vik, D. R.; Pope, P. B.; Sullivan, M. B.; Roux, S.; Wrighton, K. C. DRAM for Distilling Microbial Metabolism to Automate the Curation of Microbiome Function. *Nucleic Acids Res* **2020**, *48* (16), 8883–8900. https://doi.org/10.1093/nar/gkaa621.
(89) Yu, N. Y.; Wagner, J. R.; Laird, M. R.; Melli, G.; Rey, S.; Lo, R.; Dao, P.; Cenk Sahinalp, S.; Ester, M.; Foster, L. J.; Brinkman, F. S. L. PSORTb 3.0: Improved Protein Subcellular Localization Prediction with Refined Localization Subcategories and Predictive Capabilities for All Prokaryotes. *Bioinformatics* **2010**, *26* (13), 1608–1615. https://doi.org/10.1093/bioinformatics/btq249.
(90) Harris, D. C. *Exploring Chemical Analysis*, Fifth Edition.; Fiorillo, J., Murphy, B., Hadler, G. L., Simpson, J., Szczepanski, T., Eds.; W.H. Freeman and Company: New York, 2013.
(91) Wagner, S.; Jaffé, R.; Cawley, K.; Dittmar, T.; Stubbins, A. Associations between the Molecular and Optical Properties of Dissolved Organic Matter in the Florida Everglades, a Model Coastal Wetland System. *Front Chem* **2015**, *3* (NOV), 1–14. https://doi.org/10.3389/fchem.2015.00066.
(92) Catalán, N.; Herrero Ortega, S.; Gröntoft, H.; Hilmarsson, T. G.; Bertilsson, S.; Wu, P.; Levanoni, O.; Bishop, K.; Bravo, A. G. Effects of Beaver Impoundments on Dissolved Organic Matter Quality and Biodegradability in Boreal Riverine Systems. *Hydrobiologia* **2017**, *793* (1), 135–148. https://doi.org/10.1007/s10750-016-2766-y.
(93) Nummi, P.; Vehkaoja, M.; Pumpanen, J.; Ojala, A. Beavers Affect Carbon Biogeochemistry: Both Short-Term and Long-Term Processes Are Involved. *Mamm Rev* **2018**, *48* (4), 298–311. https://doi.org/10.1111/mam.12134.
(94) Brust, G. E. Management Strategies for Organic Vegetable Fertility. In *Safety and Practice for Organic Food*; Elsevier, 2019; pp 193–212. https://doi.org/10.1016/B978-0-12-812060-6.00009-X.
(95) Certini, G. Effects of Fire on Properties of Forest Soils: A Review. *Oecologia* **2005**, *143* (1), 1–10. https://doi.org/10.1007/s00442-004-1788-8.
(96) Wan, S.; Hui, D.; Luo, Y. *FIRE EFFECTS ON NITROGEN POOLS AND DYNAMICS IN TERRESTRIAL ECOSYSTEMS: A META-ANALYSIS*; 2001; Vol. 11.

(97) Noël, V.; Tfaily, M. M.; Fendorf, S.; Bone, S. E.; Boye, K.; Williams, K. H.; Bargar, J. R. Thermodynamically Controlled Preservation of Organic Carbon in Floodplains. *Nat Geosci* **2017**, *10* (6), 415–419. https://doi.org/10.1038/ngeo2940.
(98) de La Rosa, J. M.; Miller, A. Z.; Knicker, H. Soil-Borne Fungi Challenge the Concept of Long-Term Biochemical Recalcitrance of Pyrochar. *Sci Rep* **2018**, *8* (1), 1–9. https://doi.org/10.1038/s41598-018-21257-5.
(99) Faria, S. R.; de la Rosa, J. M.; Knicker, H.; González-Pérez, J. A.; Keizer, J. J. Molecular Characterization of Wildfire Impacts on Organic Matter in Eroded Sediments and Topsoil in Mediterranean Eucalypt Stands. *Catena (Amst)* **2015**, *135*, 29–37. https://doi.org/10.1016/j.catena.2015.07.007.
(100) Knicker, H.; González-Vila, F. J.; Polvillo, O.; González, J. A.; Almendros, G. Fire-Induced Transformation of C- and N- Forms in Different Organic Soil Fractions from a Dystric Cambisol under a Mediterranean Pine Forest (Pinus Pinaster). *Soil Biol Biochem* **2005**, *37* (4), 701–718. https://doi.org/10.1016/j.soilbio.2004.09.008.
(101) Bahureksa, W.; Young, R. B.; McKenna, A. M.; Chen, H.; Thorn, K. A.; Rosario-Ortiz, F. L.; Borch, T. Nitrogen Enrichment during Soil Organic Matter Burning and Molecular Evidence of Maillard Reactions. *Environ Sci Technol* **2022**, acs.est.1c06745. https://doi.org/10.1021/acs.est.1c06745.
(102) Rivas-Ubach, A.; Liu, Y.; Bianchi, T. S.; Tolić, N.; Jansson, C.; Paša-Tolić, L. Moving beyond the van Krevelen Diagram: A New Stoichiometric Approach for Compound Classification in Organisms. *Anal Chem* **2018**, *90* (10), 6152–6160. https://doi.org/10.1021/acs.analchem.8b00529.
(103) Wang, L.; Chen, Y.; Chen, S.; Long, L.; Bu, Y.; Xu, H.; Chen, B.; Krasner, S. A One-Year Long Survey of Temporal Disinfection Byproducts Variations in a Consumer's Tap and Their Removals by a Point-of-Use Facility. *Water Res* **2019**, *159*, 203–213. https://doi.org/10.1016/j.watres.2019.04.062.
(104) Romera-Castillo, C.; Chen, M.; Yamashita, Y.; Jaffé, R. Fluorescence Characteristics of Size-Fractionated Dissolved Organic Matter: Implications for a Molecular Assembly Based Structure? *Water Res* **2014**, *55*, 40–51. https://doi.org/10.1016/j.watres.2014.02.017.
(105) Hansen, A. M.; Kraus, T. E. C.; Pellerin, B. A.; Fleck, J. A.; Downing, B. D.; Bergamaschi, B. A. Optical Properties of Dissolved Organic Matter (DOM): Effects of Biological and Photolytic Degradation. *Limnol Oceanogr* **2016**, *61* (3), 1015–1032. https://doi.org/10.1002/lno.10270.
(106) Wang, J. J.; Dahlgren, R. A.; Erşan, M. S.; Karanfil, T.; Chow, A. T. Wildfire Altering Terrestrial Precursors of Disinfection Byproducts in Forest Detritus. *Environ Sci Technol* **2015**, *49* (10), 5921–5929. https://doi.org/10.1021/es505836m.
(107) Jochum, L. M.; Schreiber, L.; Marshall, I. P. G.; Jørgensen, B. B.; Schramm, A.; Kjeldsen, K. U. Single-Cell Genomics Reveals a Diverse Metabolic Potential of Uncultivated Desulfatiglans-Related Deltaproteobacteria Widely Distributed in Marine Sediment. *Front Microbiol* **2018**, *9* (SEP). https://doi.org/10.3389/fmicb.2018.02038.
(108) Danczak, R. E.; Johnston, M. D.; Kenah, C.; Slattery, M.; Wilkins, M. J. Capability for Arsenic Mobilization in Groundwater Is Distributed across Broad Phylogenetic Lineages. *PLoS One* **2019**, *14* (9). https://doi.org/10.1371/journal.pone.0221694.
(109) Abraham, B. S.; Caglayan, D.; Carrillo, N. v.; Chapman, M. C.; Hagan, C. T.; Hansen, S. T.; Jeanty, R. O.; Klimczak, A. A.; Klingler, M. J.; Kutcher, T. P.; Levy, S. H.; Millard-Bruzos, A. A.; Moore, T. B.; Prentice, D. J.; Prescott, M. E.; Roehm, R.; Rose, J. A.; Yin, M.; Hyodo, A.;

Lail, K.; Daum, C.; Clum, A.; Copeland, A.; Seshadri, R.; del Rio, T. G.; Eloe-Fadrosh, E. A.; Benskin, J. B. Shotgun Metagenomic Analysis of Microbial Communities from the Loxahatchee Nature Preserve in the Florida Everglades. *Environmental Microbiomes* **2020**, *15* (1). https://doi.org/10.1186/s40793-019-0352-4.

(110) Pester, M.; Knorr, K. H.; Friedrich, M. W.; Wagner, M.; Loy, A. Sulfate-Reducing Microorganisms in Wetlands - Fameless Actors in Carbon Cycling and Climate Change. *Front Microbiol* **2012**, *3* (FEB). https://doi.org/10.3389/fmicb.2012.00072.

(111) Nelson, A. R.; Narrowe, A. B.; Rhoades, C. C.; Fegel, T. S.; Daly, R. A.; Roth, H. K.; Chu, R. K.; Amundson, K. K.; Young, R. B.; Steindorff, A. S.; Mondo, S. J.; Grigoriev, I. v.; Salamov, A.; Borch, T.; Wilkins, M. J. Wildfire-Dependent Changes in Soil Microbiome Diversity and Function. *Nat Microbiol* **2022**. https://doi.org/10.1038/s41564-022-01203-y.

(112) Sáenz de Miera, L. E.; Pinto, R.; Gutierrez-Gonzalez, J. J.; Calvo, L.; Ansola, G. Wildfire Effects on Diversity and Composition in Soil Bacterial Communities. *Science of the Total Environment* **2020**, *726*. https://doi.org/10.1016/j.scitotenv.2020.138636.

(113) Whitman, T.; Whitman, E.; Woolet, J.; Flannigan, M. D.; Thompson, D. K.; Parisien, M. A. Soil Bacterial and Fungal Response to Wildfires in the Canadian Boreal Forest across a Burn Severity Gradient. *Soil Biol Biochem* **2019**, *138*. https://doi.org/10.1016/j.soilbio.2019.107571.

(114) Bowers, R. M.; Kyrpides, N. C.; Stepanauskas, R.; Harmon-Smith, M.; Doud, D.; Reddy, T. B. K.; Schulz, F.; Jarett, J.; Rivers, A. R.; Eloe-Fadrosh, E. A.; Tringe, S. G.; Ivanova, N. N.; Copeland, A.; Clum, A.; Becraft, E. D.; Malmstrom, R. R.; Birren, B.; Podar, M.; Bork, P.; Weinstock, G. M.; Garrity, G. M.; Dodsworth, J. A.; Yooseph, S.; Sutton, G.; Glöckner, F. O.; Gilbert, J. A.; Nelson, W. C.; Hallam, S. J.; Jungbluth, S. P.; Ettema, T. J. G.; Tighe, S.; Konstantinidis, K. T.; Liu, W. T.; Baker, B. J.; Rattei, T.; Eisen, J. A.; Hedlund, B.; McMahon, K. D.; Fierer, N.; Knight, R.; Finn, R.; Cochrane, G.; Karsch-Mizrachi, I.; Tyson, G. W.; Rinke, C.; Lapidus, A.; Meyer, F.; Yilmaz, P.; Parks, D. H.; Eren, A. M.; Schriml, L.; Banfield, J. F.; Hugenholtz, P.; Woyke, T. Minimum Information about a Single Amplified Genome (MISAG) and a Metagenome-Assembled Genome (MIMAG) of Bacteria and Archaea. *Nature Biotechnology*. Nature Publishing Group August 8, 2017, pp 725–731. https://doi.org/10.1038/nbt.3893.

(115) Patzner, M. S.; Mueller, C. W.; Malusova, M.; Baur, M.; Nikeleit, V.; Scholten, T.; Hoeschen, C.; Byrne, J. M.; Borch, T.; Kappler, A.; Bryce, C. Iron Mineral Dissolution Releases Iron and Associated Organic Carbon during Permafrost Thaw. *Nat Commun* **2020**, *11* (1). https://doi.org/10.1038/s41467-020-20102-6.

(116) Sharma, S.; Cavallaro, G.; Rosato, A. A Systematic Investigation of Multiheme C-Type Cytochromes in Prokaryotes. *Journal of Biological Inorganic Chemistry* **2010**, *15* (4), 559–571. https://doi.org/10.1007/s00775-010-0623-4.

(117) Fuchs, G.; Boll, M.; Heider, J. Microbial Degradation of Aromatic Compounds- From One Strategy to Four. *Nat Rev Microbiol* **2011**, *9* (11), 803–816. https://doi.org/10.1038/nrmicro2652.

(118) Knicker, H.; Hilscher, A.; de la Rosa, J. M.; González-Pérez, J. A.; González-Vila, F. J. Modification of Biomarkers in Pyrogenic Organic Matter during the Initial Phase of Charcoal Biodegradation in Soils. *Geoderma* **2013**, *197–198*, 43–50. https://doi.org/10.1016/j.geoderma.2012.12.021.

(119) Donhauser, J.; Niklaus, P. A.; Rousk, J.; Larose, C.; Frey, B. Temperatures beyond the Community Optimum Promote the Dominance of Heat-Adapted, Fast Growing and Stress

Resistant Bacteria in Alpine Soils. *Soil Biol Biochem* **2020**, *148*. https://doi.org/10.1016/j.soilbio.2020.107873.
(120) Donhauser, J.; Qi, W.; Bergk-Pinto, B.; Frey, B. High Temperatures Enhance the Microbial Genetic Potential to Recycle C and N from Necromass in High-Mountain Soils. *Glob Chang Biol* **2021**, *27* (7), 1365–1386. https://doi.org/10.1111/gcb.15492.
(121) Bruns, T. D.; Chung, J. A.; Carver, A. A.; Glassman, S. I. A Simple Pyrocosm for Studying Soil Microbial Response to Fire Reveals a Rapid, Massive Response by Pyronema Species. *PLoS One* **2020**, *15* (3), 1–20. https://doi.org/10.1371/journal.pone.0222691.
(122) Nelson, A. R.; Sawyer, A. H.; Gabor, R. S.; Saup, C. M.; Bryant, S. R.; Harris, K. D.; Briggs, M. A.; Williams, K. H.; Wilkins, M. J. Heterogeneity in Hyporheic Flow, Pore Water Chemistry, and Microbial Community Composition in an Alpine Streambed. *J Geophys Res Biogeosci* **2019**, *124* (11), 3465–3478. https://doi.org/10.1029/2019JG005226.
(123) Saup, C. M.; Bryant, S. R.; Nelson, A. R.; Harris, K. D.; Sawyer, A. H.; Christensen, J. N.; Tfaily, M. M.; Williams, K. H.; Wilkins, M. J. Hyporheic Zone Microbiome Assembly Is Linked to Dynamic Water Mixing Patterns in Snowmelt-Dominated Headwater Catchments. *J Geophys Res Biogeosci* **2019**, *124* (11), 3269–3280. https://doi.org/10.1029/2019JG005189.
(124) Weber, C. F.; Lockhart, J. S.; Charaska, E.; Aho, K.; Lohse, K. A. Bacterial Composition of Soils in Ponderosa Pine and Mixed Conifer Forests Exposed to Different Wildfire Burn Severity. *Soil Biol Biochem* **2014**, *69*, 242–250. https://doi.org/10.1016/j.soilbio.2013.11.010.
(125) Wang, J. J.; Dahlgren, R. A.; Erşan, M. S.; Karanfil, T.; Chow, A. T. Temporal Variations of Disinfection Byproduct Precursors in Wildfire Detritus. *Water Res* **2016**, *99*, 66–73. https://doi.org/10.1016/j.watres.2016.04.030.

CHAPTER 6: SUMMARY

The purpose of the work presented in this dissertation is to develop and apply methods to better understand the composition of SOM and DOM after wildfires. The research described here achieves this by: (I) developing analytical methodology to improve organic nitrogen analysis, (II) measuring the compositional differences in SOM as a function of burn severity and depth, and (III) identifying the effects of reducing conditions (i.e., low redox potential) on SOM composition in fire-impacted watersheds.

First, water extracts from a high severity burned soil were analyzed by negative- and positive- ion mode ESI to investigate the influence of ionization mode on detectable nitrogenated species (Chapter 2). We quantified the differences in assigned elemental compositions and found that -ESI substantially underestimates the amount of nitrogen in burned soil samples, preferentially ionizing $N_{1\text{-}2}$ species. However, +ESI increases the compositional coverage of N and allows for the detection of N-rich species (i.e., $N_{3\text{-}5}$). Many chemical parameters are calculated based on the elemental composition determined by FT-ICR MS; therefore, the biases associated with a given method must be fully understood to provide necessary context for C and N models. Comparisons of other ionization modes (i.e., atmospheric pressure photoionization) for burned soils are needed to continue to constrain predictions of C and N cycling in fire-affected landscapes.

Second, soils collected along four burn severity gradients were sampled and analyzed to determine differences in SOM composition in each of the three burn severity categories: low, moderate, and high (Chapter 3). We found that soils in the mineral horizon were increasingly impacted by soil burn severity, with important implications for microbial cycling and soil toxicity. As burn severity increased, the number of N-containing species increased and became more N-

dense (shifted from N_{1-2} to N_{3-5}). Importantly, the soil microbiome did not contain widespread abilities to transform the newly formed N species, indicating that N-dense compounds likely represent a SOM fraction with a relatively long mean residence time. Soil toxicity also increased with burn severity, as determined by Microtox®. While increases in toxicity may be attributed to many pyrogenic constituents, N-dense species are typically more toxic than their non-nitrogenated counterparts and likely represent a substantial contribution to increased soil toxicity. To better understand the specific N species formed in burned soils, future analyses could include collision-induced dissociation to elucidate structural characteristics from FT-ICR MS spectra.

Next, surface water and sediment samples from a severely burned portion of a fire-impacted watershed were examined for shifts in surface water molecular speciation due to reducing conditions caused by beaver ponds (Chapter 4). Our analysis revealed that surface water chemistry and sediment microbiomes in beaver ponds were influenced by fire. DOC and DTN increased in the ponds, with concurrent decreases in stream nitrate. DOM chemistry shifted towards higher aromaticity and more N-containing species, which resulted in a lower C:N ratio in the beaver ponds than in the free-flowing surface water. The input of pyrogenic organic matter on microbial communities was small but important. Instead of using pyrogenic organic matter as a primary C source, microbial communities likely relied on necromass and other sources of labile C which could be eroded into the ponds during snowmelt or precipitation events. The observed differences were localized to the beaver ponds and did not proliferate downstream, supporting the function of beaver ponds as biogeochemical "hotspots" governed by unique conditions. This work would benefit from small molecule analysis to identify the specific metabolites used for microbial respiration in fire-affected beaver ponds.

Mechanistic understandings of N transformations are confounded by environmental variability, which will address using open-air pyrocosms, which allow for control over fuel load, fuel type, temperature, and amount of time soils burn for. For this study, soils were collected from adjacent pine and aspen stands and burned with their respective fuel types to evaluate how overstory vegetation could influence C and N storage in burned soils (Appendix A). DOM was analyzed for differences in dissolved carbon and nitrogen, as well as NH_4-N and NO_3-N. Differences in C and N concentrations, as well as expected shifts in functionality, lead to different microbial processing requirements in the burned soils and may have larger impacts on C and N cycling in fire-impacted soils under deciduous versus coniferous stands. However, full characterization of the changes in major functional groups are required to understand the potential changes to C and N cycling in burned systems. Future analyses will include metagenomics and metatranscriptomics to evaluate how microbiome composition and activity differ between the two soil types and between burned and unburned soils. FT-ICR MS will be performed to determine shifts in elemental composition of molecules with high molecular weight, while gas chromatography-mass spectrometry (GC-MS) will be used to analyze the small molecules. Together, this additional information will be utilized to understand the dynamics of C and N preservation more comprehensively in soils with different inputs.

Collectively, the work in this dissertation contributes to our understanding of C and N transformations in fire-affected soils and the implications for water quality and microbial activity. Increased aromaticity and decreased SOM quality were observed in the solid fraction, with implications for nutrient cycling and recovery of fire-impacted watersheds. In the dissolved fraction, we identified increasingly N-dense species which were previously only observed in

laboratory-based muffle furnace experiments. Future studies aiming to refine our mechanistic understanding of SOM processing and sequestration could incorporate small-scale laboratory studies to characterize organo-mineral interactions. Additionally, small-molecule analyses could be performed to link the presence of small molecules in microbial degradation pathways to the community and activity information determined from metagenomics and metatranscriptomics analyses.

APPENDICES

APPENDIX A: IMPACTS OF BURNING ON PINE AND ASPEN SOIL ORGANIC MATTER

1. INTRODUCTION

Future climate change may lead to shifts in the habitat of different forest types, with deciduous species such as aspen expected to move into higher elevations.[1] This may lead to larger effects on soils, with aspen promoting greater C stabilization through physicochemical protection owing to the enrichment of species with a higher affinity for mineral adsorption (i.e., aromatic compounds, carboxylates, polysaccharides) in aspen litter.[2–5] Aspen soils have a higher sorption affinity for new C input than conifer soils, which is hypothesized to be due to root-microbe-soil interactions in the rhizosphere and confers a positive feedback for C storage[6] and higher C stocks in aspen stands than pine stands.[7,8] Currently, little is known about how increased wildfire activity, due to a changing climate, affects the capacity of soils to store C.[9] However, direct comparisons of C and N composition between aspen and pine soils are limited despite the importance of vegetation cover on physical soil characteristics.

Soils under coniferous and deciduous trees differ in SOM quantity and composition. Mineral SOM in unburned coniferous soils is generally dominated by carbohydrates and lignin, while carbohydrates and lipids contribute the greatest proportion of SOM in deciduous mineral soils.[10] At high fire severity, molecular mixing models of solid-state ^{13}C NMR spectra indicate that coniferous mineral SOM shifts towards more carbonyl and protein, and deciduous mineral soils increase in pyrogenic organic carbon (e.g., polyaromatic structures produced during charring) and lignin.[10] There are also large increases in the relative proportion of proteins in both soil types,[10]

likely originating from biomass,[11] which indicates that soil nitrogen (N) is also highly impacted by fire. Differences in composition influence how SOM interacts with biotic and abiotic factors in the soil, which may lead to differences in the stabilization and storage of C and N pools between dominant vegetation overstory.[12] By evaluating the differences in SOM between pine and aspen soils, we can better understand the heterogeneity of burned soils to constrain future predictions of C and nutrient cycling in fire-affected soils.

Some frameworks suggest that C persistence can more accurately be predicted if SOM is divided into two major pools: particulate organic matter (POM) and mineral-associated organic matter (MAOM).[13–16] POM is primarily of plant origin and contains a low N content; its persistence in soil is linked to chemical recalcitrance, physical protection in aggregates, or microbial inhibition.[17] On the other hand, MAOM is mostly made up of microbial products which are richer in N, and persists due to chemical bonds with minerals and physical protection in small aggregates.[18] POM is generally considered to be more vulnerable to environmental disturbance and displays faster turnover times than MAOM, although the specific mechanisms controlling soil C storage are still under debate.[19–22] Soil C:N typically decreases with increasing proportion of MAOM due to N enrichment in that fraction compared to POM.[23] Because organic matter typically contributes less than 5% of soil by weight,[24,25] the interactions between organic matter and minerals are important for biogeochemical activity within a system.[26]

Organo-mineral interactions are generally thought to stabilize more easily degradable compounds, such as carbohydrates and amino acids.[27] Therefore, fire-driven changes in organo-mineral interactions may represent an equally important stabilization mechanism as black C formation. Increased stabilization of SOM under aspen stands may partially be attributed to a higher abundance of microbially recalcitrant compounds (i.e., cutin, suberin, waxes),[12,28,29]

although the accumulation of such compounds has not been observed in the forest floor or A horizon of aspen soils.[30,31] However, aspen litter compositionally differs from pine litter, which may generate compounds that are more susceptible to stabilization through organo-mineral interactions despite being seemingly more degradable.[32–35] Links between aspen SOM chemistry and stabilization may be controlled by the chemistry of root exudates, mycorrhizal associations, N availability, and mineral associations,[23,36] all of which may be affected by fire.

In addition to vegetation overstory, other site factors (i.e., microbial community, soil parent material, soil nutrient availability) may influence SOM composition and stabilization[23,36] and may additionally be impacted by fire activity. Therefore, we designed a study to investigate the differences in C and N storage between lodgepole pine (*Pinus contorta*) and quaking aspen (*Populus tremuloides*) and how the storage would be influenced by fire. We hypothesized that aspen soils would store more C and N in MAOM which would improve C storage, and that MAOM would be more protected from heat-induced transformations than POM. To investigate our hypothesis, we collected pine and aspen soils from the Arapaho and Roosevelt National Forests and burned them in open-air pyrocosms, first employed by Bruns, et al.[37] We determined differences in C and N storage between the dissolved and solid fraction of the soils (whole soil, MAOM, and POM) before and after fire to evaluate how SOM storage differed between the two soils and determine the implications for C and N cycling in deciduous versus coniferous soils.

2. Materials and Methods

Pyrocosm assembly

Soils were collected from lodgepole pine and quaking aspen stands in the Arapaho and Roosevelt National Forests, Colorado, USA, near Cameron Pass. Pine and aspen litter were collected from the soil surface along with pine and aspen woods from the surrounding area. The O horizon was

removed from the mineral surface, and mineral soils were collected from 0-10 cm depths and sieved to 0.5 inches (12.7 mm).

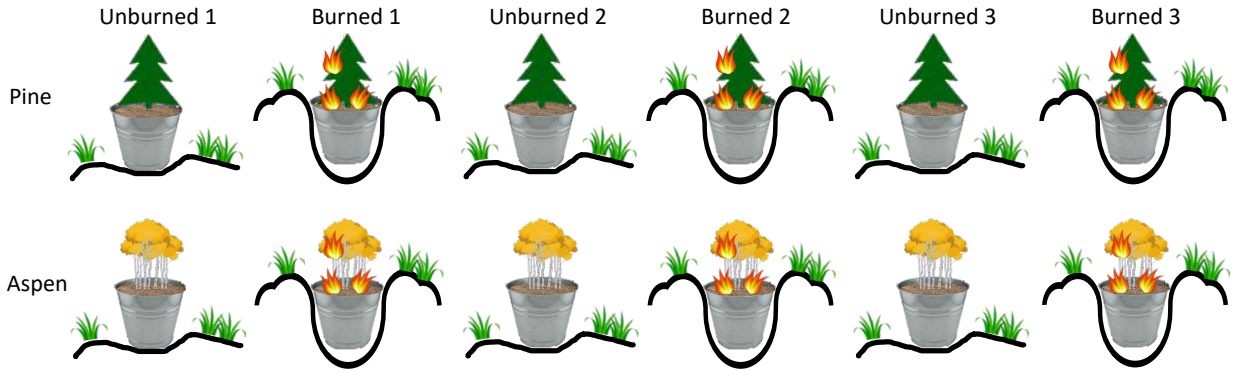

Figure A1. Schematic illustrating the pyrocosm experimental design. Galvanized steel buckets were filled with the corresponding mineral soil. Burned pyrocosms were placed in holes in the ground while unburned pyrocosms were placed on the soil surface.

Twelve pyrocosms total were assembled – six with aspen soils and six with pine soils (**Figure A1**). Three of each soil were burned and three were unburned, which were assembled according to Bruns et al.[37] Briefly, 12-quart galvanized steel buckets were marked at 0.5 cm, 5 cm and 10 cm depths and holes were drilled to accommodate thermocouple leads (two at 0.5 cm, one each at 5 and 10 cm). Stainless steel screens (20 mesh, Valchoose) were cut to fit inside the buckets, and the screens and the buckets were washed with HPLC-grade toluene (Sigma-Aldrich, St. Louis, MO, USA). The buckets were filled with the appropriate soil to a bulk density of 1 g cm^{-1}. The stainless-steel screens were inserted at the 5 cm mark to facilitate consistent soil sampling depths.

The assembled pyrocosms were transported to Colorado State University's Agricultural Research, Development and Education Center in field 100A, which was cleared of all vegetation prior to burning. Holes were dug for each of the "burn" buckets to insulate the pyrocosms during the burn, while control buckets were placed on the soil surface. Approximately 1 inch of the respective litter was placed on top of the soil in each bucket, and small twigs were added on top.

About 9 kg of wood was weighed for each bucket, which was slowly added once the fires were started. Fuels were periodically shifted throughout the burn to ensure equal combustion across the pyrocosms.

Pyrocosm soil sampling

Prior to sampling soils, cardboard was cut to fit the diameter of the galvanized steel buckets in order to sample half of the soil in the bucket without disturbing the structure of the remaining half. The cardboard pieces were wrapped in aluminum foil and wiped with methanol prior to sampling the day after the burns (Day 1). During sampling, a small trowel was wiped with methanol and used to break up the soil across the diameter of the pyrocosms, and then the aluminum-wrapped cardboard was placed in the center and pushed down to the 5 cm mark. The ash or vegetation (burned and unburned pyrocosms, respectively) plus mineral soil on one side of the divider was collected in gallon storage bags and stored at 4 °C after transport to the lab.

After sampling, approximately 400 mL of millipore water was added to each bucket to simulate a 0.5 inch precipitation event and stimulate microbial activity. A galvanized steel bucket was prepared by drilling small holes in the bottom and was rinsed with methanol immediately before use. The water was added to the bucket and allowed to slowly percolate through. The buckets were sampled again one week after wetting (Day 8), and the remaining soil from 0-5 cm was collected. Upon returning to the lab, soils were air-dried and sieved to 2 mm. Soil texture was determined by the particle size analysis hydrometer method.[38]

Carbon and nitrogen analyses

To measure dissolved organic carbon (DOC) and dissolved total nitrogen (DTN), 20 g soil and 100 mL Millipore water were combined in an Erlenmeyer flask and shaken for 1 hour at 200 rpm. The soil and water slurries were vacuum filtered to 0.45 um using glass fiber filters

(Advantec, Japan). Measurements were performed with a TOC-VCPN total organic C/N analyzer (Shimadzu Corporation, Columbia, MD, USA).

To determine the supply of inorganic forms of soil N (NO_3-N and NH_4-N), 10 g soil was mixed with 50 mL 2 M potassium chloride and shaken for 1 hour. Samples were filtered (Q5 filter papers, Fisher Scientific) and the filtrate was analyzed for NO_3-N and NH_4-N by colorimetric spectrophotometry (Lachat Company, Loveland, CO).

pH and EC measurements

To determine changes in pH across the soils, 20 g dried soil and 40 mL millipore water were added to Erlenmeyer flasks and shaken for 1 hour at 200 rpm before pH measurements were recorded. Samples were stirred and final pH was recorded. For electrical conductivity (EC), a 2.5:1 ratio of Millipore water and soil was shaken for 24 hours, and electrical conductivity was recorded.

3. Results and Discussion

Soil physical properties are influenced by fire

Soil texture was determined using the particle size analysis hydrometer method,[38] with results reported in **Table D1**. Compared to the aspen soils, pine soils contained less sand and clay, but more silt. Although both the pine and aspen pyrocosms were loaded with approximately the same mass of fuel, the temperature profiles varied considerably between the soils (**Table A2**). The pine soils reached higher temperatures than the aspen soils at the 0.5 and 5 cm depths, and the soils were the same temperature at 10 cm. pH increased by 2-3 in the burned soils compared to the unburned soils, with the highest increase in the burned pine soils (**Figure A2**). Increases in pH are commonly observed in post-fire soils, attributed to the denaturation of organic acids and release of bases (i.e., ammonium) during combustion.[39] Large changes in pH, such as those observed, can affect soil organo-mineral interactions, as lower pH generally results in a higher surface charge for

metal oxides and phyllosilicates and encourages rapid ligand exchange.[40,41] The basic pH values observed in the burned soils here may also result in modifications of functional group ionization and disruption of hydrogen bonding, which impact protein folding and thus may negatively affect microbial activity. Electrical conductivity (EC) also increased in the burned soils (**Figure A3**) due to the release of inorganic ions from combusted organic matter.[42] Increased ion concentrations in the soil can affect sorption kinetics,[43,44] as the competition between organic compounds and inorganic ions for sorptive sites increases.[45] Collectively, changes to soil physical properties with burn influence many of the variables which control the magnitude and rate of sorption in soils (i.e., size, charge, OM concentration, pH, ionic strength, etc).[46,47] Rapid adsorption of organic matter to minerals occurs at low pH values, high OM concentration, and in the presence of cations,[46–49] all of which are influenced by fire and the interactions of which are highly complex.

Table A1. Soil texture analysis results of the pine and aspen pyrocosms (n = 4).

Soil texture	Pine	Aspen
Sand %	65-70	73-79
Clay %	4-6	9-12
Silte %	25-29	12-15

Table A2. Average temperatures of the pine and aspen pyrocosms (n = 3; * denotes n = 6).

Depth (cm)	**Pine Max T (°C)**	**Aspen Max T (°C)**
0.5	682*	591*
5	251	187
10	149	153

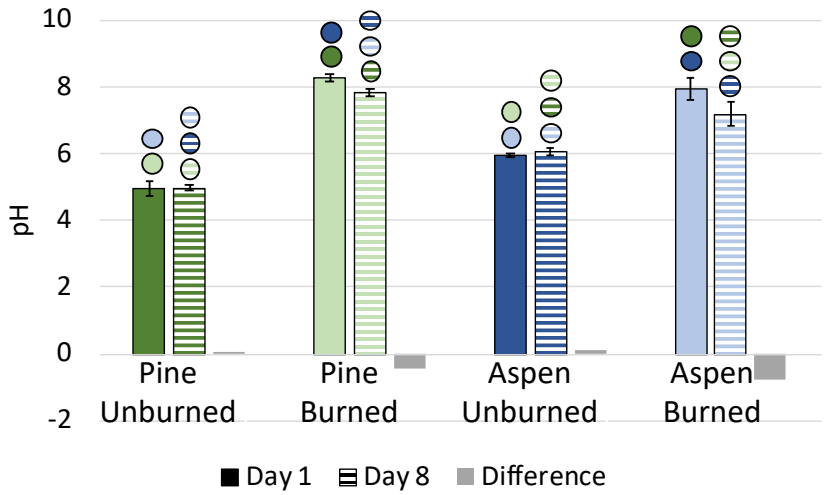

Figure A2. pH measurements of the burned and unburned pine and aspen soils. Solid bars represent soils collected one day after fire (Day 1) and striped bars indicate soils that were collected eight days after fire (Day 8). Error bars indicate standard deviation. Circles indicate statistically significant differences ($P < 0.05$) between conditions ($n = 3$).

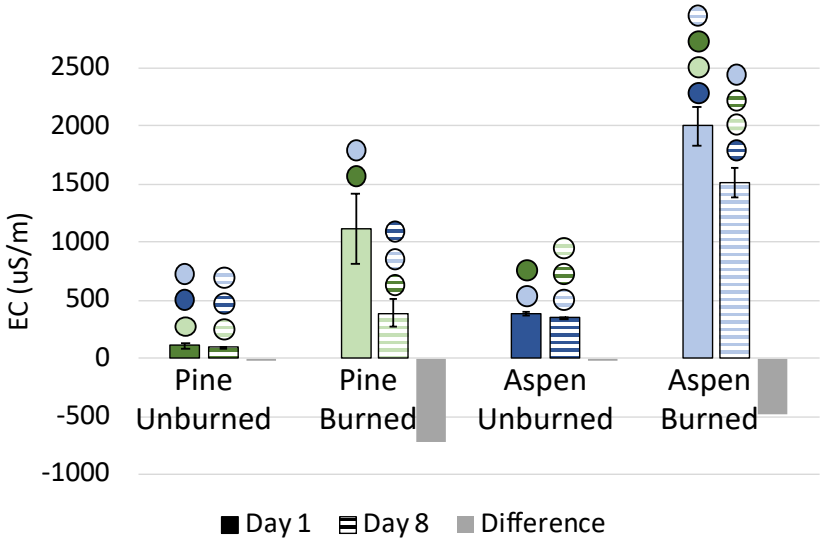

Figure A3. Electrical conductivity (EC) measurements of the burned and unburned pine and aspen soils. Solid bars represent soils collected one day after fire (Day 1) and striped bars indicate soils that were collected eight days after fire (Day 8). Error bars indicate standard deviation. Circles indicate statistically significant differences ($P < 0.05$) between conditions ($n = 3$).

DOC and DTN released from aspen soils increases after burning

Figure A4 shows dissolved organic carbon ([DOC], A4a) and dissolved total nitrogen ([DTN], A4b) concentrations for the burned and unburned pyrocosm soils. The DOC in the burned pine soils was significantly lower than both aspen conditions but did not significantly differ from

the unburned pine soils on Day 1. Lower DOC concentrations in unburned pine soils can be attributed to differences in litter chemistry, microbial community, and soil properties between the tree species.[12] DOC in the aspen soils increased with burn, approximately 2x higher in the burned soils compared to the unburned. Soils across all conditions significantly decreased from Day 1 to Day 8, potentially due to microbial processing or leachate losses after the simulated rain event. Higher DOC concentrations have previously been reported in deciduous soils,[50–52] in agreement with the results reported here. DTN concentrations in burned pine soils were the same as the unburned pine soil on Day 1, but larger DTN losses in the pine controls resulted in their being significantly lower by Day 8. The burned aspen soils contained a higher DTN concentration than any other soils and were over 2x higher than the unburned aspen soils on both sampling dates. The burned aspen soils experienced the greatest DTN losses during the week (12.76 mg/L), although the concentration remained the highest of the conditions on Day 8. A study in European forest systems found that dissolved organic matter composition was primarily influenced by main tree species,[53] which supports the findings for the unburned soils. DTN is often elevated in streams draining fire-impacted watersheds,[54–56] although DTN concentrations in burned soils is highly variable.[57–59]

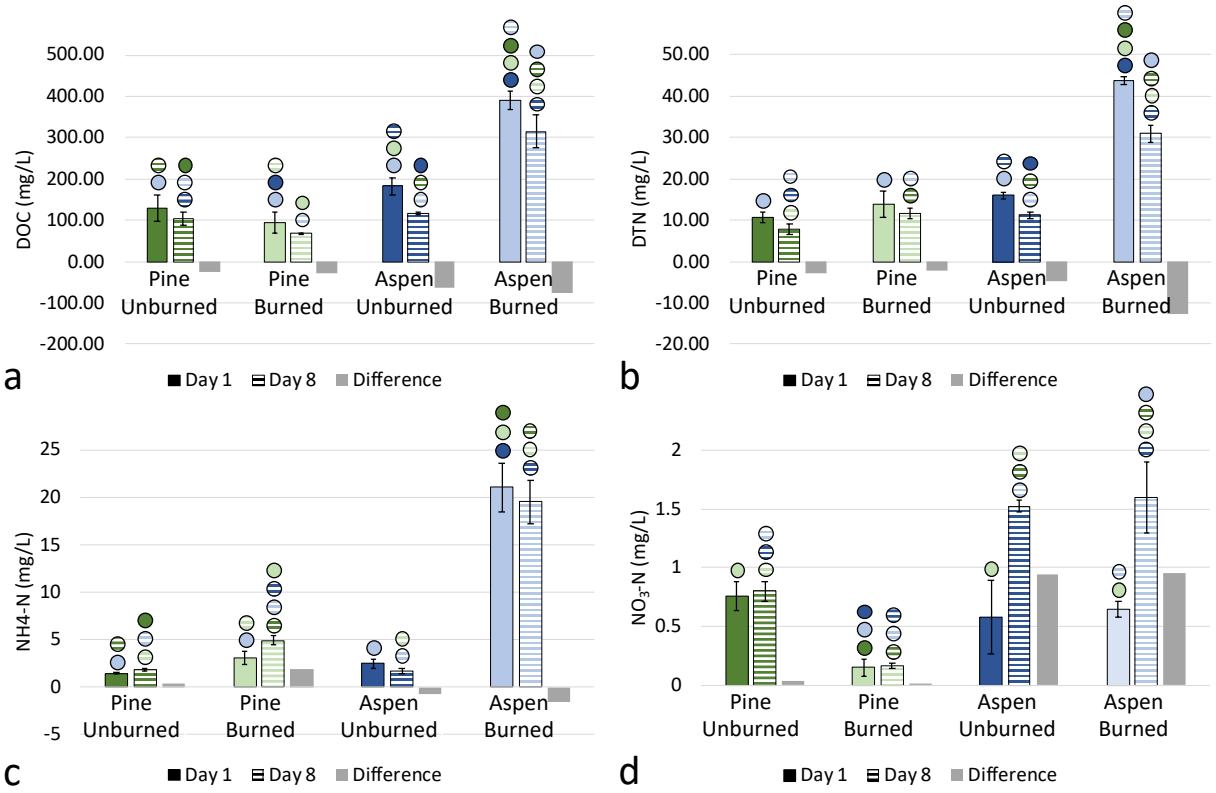

Figure A4. Average dissolved organic carbon (DOC; a), dissolved total nitrogen (DTN; b), ammonium-N (NH_4-N; c) and nitrate-N (NO_3-N; d) concentrations of burned and unburned pine and aspen soils. Solid bars represent soils collected one day after fire (Day 1) and striped bars indicate soils that were collected eight days after fire (Day 8). Error bars indicate standard deviation. Circles indicate statistically significant differences ($P < 0.05$) between conditions ($n = 3$).

Plant-available N was also variable across soil types. The concentration of NH_4-N in aspen soils was highly influenced by burn, while the effect on pine soils was relatively minor in comparison (**Figure A4**). Pine and aspen soils were differentially affected over the week, with pine soils increasing in NH_4-N and aspen soils decreasing. While NH_4-N concentrations in pine soils were initially not influenced by the burn, an increase in NH_4-N in burned pine soils during the week resulted in a significant increase compared to the unburned soils on Day 8. Ammonium is a direct product of combustion, which is often associated with higher ash contents.[60] Over time, ammonium can be converted to nitrate through microbial denitrification.[61] NO_3-N (**Figure A4**) in the pine soils decreased significantly with burn and was much lower than all other soil types, while

aspen soil NO_3-N was not affected by burn. NO_3-N in all soils increased from Day 1 to Day 8, but the change was nearly an order of magnitude higher in aspen soils compared to the pine. Differences in NO_3^- processing may be driven by differences in microbial communities, which likely differ between the two soils. The fates of NH_4-N and NO_3-N pools are typically opposite: free nitrate in the soil generally leaches downwards, while ammonium is adsorbed onto negatively charged surfaces of minerals and organics.[62] Differences in inorganic N fates may partially explain the different trends in NH_4-N and NO_3-N observed here during the first week postfire, along with differences in starting material.

4. Summary and Future Directions

The results presented here summarize the differences in dissolved C and N in burned pine and aspen soils. Fire is expected to additionally affect the solid fraction of the soils, which we will investigate by determining the %C and %N in the dried and sieved soils, as well as in the individual MAOM and POM fractions. MAOM and POM will allow us to evaluate the potential for C and N sequestration in the soils. However, molecular-level information about the specific species stored in each soil is required to fully understand the potential for mineralization or sequestration in pine-affected soils and extrapolate their potential for greenhouse gas emissions. Differences in C and N composition likely lead to different microbial processing requirements, which will be evaluated with a combination of 16S rRNA sequencing, metagenomics sequencing, and metatranscriptomics.

REFERENCES

(1) Hanewinkel, M.; Cullmann, D. A.; Schelhaas, M. J.; Nabuurs, G. J.; Zimmermann, N. E. Climate Change May Cause Severe Loss in the Economic Value of European Forest Land. *Nat Clim Chang* **2013**, *3* (3), 203–207. https://doi.org/10.1038/nclimate1687.
(2) Yeasmin, S.; Singh, B.; Johnston, C. T.; Sparks, D. L. Organic Carbon Characteristics in Density Fractions of Soils with Contrasting Mineralogies. *Geochim Cosmochim Acta* **2017**, *218*, 215–236. https://doi.org/10.1016/j.gca.2017.09.007.
(3) Spielvogel, S.; Prietzel, J.; Kögel-Knabner, I. Soil Organic Matter Stabilization in Acidic Forest Soils Is Preferential and Soil Type-Specific. *Eur J Soil Sci* **2008**, *59* (4), 674–692. https://doi.org/10.1111/j.1365-2389.2008.01030.x.
(4) Wattel-Koekkoek, E. J. W.; van Genuchten, P. P. L.; Buurman, P.; van Lagen, B. *Amount and Composition of Clay-Associated Soil Organic Matter in a Range of Kaolinitic and Smectitic Soils*; 2001; Vol. 99. www.elsevier.nlrlocatergeoderma.
(5) Rumpel, C.; Eusterhues, K.; Kögel-Knabner, I. Location and Chemical Composition of Stabilized Organic Carbon in Topsoil and Subsoil Horizons of Two Acid Forest Soils. *Soil Biol Biochem* **2004**, *36* (1), 177–190. https://doi.org/10.1016/j.soilbio.2003.09.005.
(6) Boča, A.; Miegroet, H. van. Can Carbon Fluxes Explain Differences in Soil Organic Carbon Storage under Aspen and Conifer Forest Overstories? *Forests* **2017**, *8* (4). https://doi.org/10.3390/f8040118.
(7) Buck, J. R.; st. Clair, S. B. Aspen Increase Soil Moisture, Nutrients, Organic Matter and Respiration in Rocky Mountain Forest Communities. *PLoS One* **2012**, *7* (12). https://doi.org/10.1371/journal.pone.0052369.
(8) Dobarco, M. R.; van Miegroet, H. Soil Organic Carbon Storage and Stability in the Aspen-Conifer Ecotone in Montane Forests in Utah, USA. *Forests* **2014**, *5* (4), 666–688. https://doi.org/10.3390/f5040666.
(9) Jones, A.; Stolbovoy, V.; Rusco, E.; Gentile, A. R.; Gardi, C.; Marechal, B.; Montanarella, L. Climate Change in Europe. 2. Impact on Soil. A Review. *Agronomy for Sustainable Development*. July 2009, pp 423–432. https://doi.org/10.1051/agro:2008067.
(10) Miesel, J. R.; Hockaday, W. C.; Kolka, R. K.; Townsend, P. A. Soil Organic Matter Composition and Quality across Fire Severity Gradients in Coniferous and Deciduous Forests of the Southern Boreal Region. *Journal of Geophysical Research G: Biogeosciences* **2015**, *120* (6), 1124–1141. https://doi.org/10.1002/2015JG002959.
(11) Knicker, H. Soil Organic N - An under-Rated Player for C Sequestration in Soils? *Soil Biology and Biochemistry*. June 2011, pp 1118–1129. https://doi.org/10.1016/j.soilbio.2011.02.020.
(12) Román Dobarco, M.; Jacobson, A. R.; van Miegroet, H. Chemical Composition of Soil Organic Carbon from Mixed Aspen-Conifer Forests Characterized with Fourier Transform Infrared Spectroscopy. *Eur J Soil Sci* **2021**, *72* (3), 1410–1430. https://doi.org/10.1111/ejss.13065.
(13) Lavallee, J. M.; Soong, J. L.; Cotrufo, M. F. Conceptualizing Soil Organic Matter into Particulate and Mineral-Associated Forms to Address Global Change in the 21st Century. *Glob Chang Biol* **2020**, *26* (1), 261–273. https://doi.org/10.1111/gcb.14859.
(14) Averill, C.; Waring, B. Nitrogen Limitation of Decomposition and Decay: How Can It Occur? *Global Change Biology*. Blackwell Publishing Ltd April 1, 2018, pp 1417–1427. https://doi.org/10.1111/gcb.13980.

(15) Cotrufo, M. F.; Soong, J. L.; Horton, A. J.; Campbell, E. E.; Haddix, M. L.; Wall, D. H.; Parton, W. J. Formation of Soil Organic Matter via Biochemical and Physical Pathways of Litter Mass Loss. *Nat Geosci* **2015**, *8* (10), 776–779. https://doi.org/10.1038/ngeo2520.
(16) Castellano, M. J.; Mueller, K. E.; Olk, D. C.; Sawyer, J. E.; Six, J. Integrating Plant Litter Quality, Soil Organic Matter Stabilization, and the Carbon Saturation Concept. *Glob Chang Biol* **2015**, *21* (9), 3200–3209. https://doi.org/10.1111/gcb.12982.
(17) Golchin, A.; Oades, J. M.; Skjemstad, J. O.; Clarke, P. Study of Free and Occluded Particulate Organic Matter in Soils by Solid State 13c CP/MAS NMR Spectroscopy and Scanning Electron Microscopy. *Aust. J. Soil Res* **1994**, *32*, 285–309.
(18) Kögel-Knabner, I.; Guggenberger, G.; Kleber, M.; Kandeler, E.; Kalbitz, K.; Scheu, S.; Eusterhues, K.; Leinweber, P. Organo-Mineral Associations in Temperate Soils: Integrating Biology, Mineralogy, and Organic Matter Chemistry. *Journal of Plant Nutrition and Soil Science*. February 2008, pp 61–82. https://doi.org/10.1002/jpln.200700048.
(19) Cambardella, C. A.; Elliott, E. T. Particulate Soil Organic-Matter Changes across a Grassland Cultivation Sequence. *Soil Science Society of America Journal* **1992**, *56* (3), 777–783. https://doi.org/10.2136/sssaj1992.03615995005600030017x.
(20) Poeplau, C.; Don, A.; Six, J.; Kaiser, M.; Benbi, D.; Chenu, C.; Cotrufo, M. F.; Derrien, D.; Gioacchini, P.; Grand, S.; Gregorich, E.; Griepentrog, M.; Gunina, A.; Haddix, M.; Kuzyakov, Y.; Kühnel, A.; Macdonald, L. M.; Soong, J.; Trigalet, S.; Vermeire, M. L.; Rovira, P.; van Wesemael, B.; Wiesmeier, M.; Yeasmin, S.; Yevdokimov, I.; Nieder, R. Isolating Organic Carbon Fractions with Varying Turnover Rates in Temperate Agricultural Soils – A Comprehensive Method Comparison. *Soil Biol Biochem* **2018**, *125*, 10–26. https://doi.org/10.1016/j.soilbio.2018.06.025.
(21) Kalbitz, K.; Schwesig, D.; Rethemeyer, J.; Matzner, E. Stabilization of Dissolved Organic Matter by Sorption to the Mineral Soil. *Soil Biol Biochem* **2005**, *37* (7), 1319–1331. https://doi.org/10.1016/j.soilbio.2004.11.028.
(22) Derrien, D.; Barré, P.; Basile-Doelsch, I.; Cécillon, L.; Chabbi, A.; Crème, A.; Fontaine, S.; Henneron, L.; Janot, N.; Lashermes, G.; Quénéa, K.; Rees, F.; Dignac, M. F. Current Controversies on Mechanisms Controlling Soil Carbon Storage: Implications for Interactions with Practitioners and Policy-Makers. A Review. *Agronomy for Sustainable Development*. Springer-Verlag Italia s.r.l. February 1, 2023. https://doi.org/10.1007/s13593-023-00876-x.
(23) Cotrufo, M. F.; Ranalli, M. G.; Haddix, M. L.; Six, J.; Lugato, E. Soil Carbon Storage Informed by Particulate and Mineral-Associated Organic Matter. *Nat Geosci* **2019**, *12* (12), 989–994. https://doi.org/10.1038/s41561-019-0484-6.
(24) Jobbágy, E. G.; Jackson, R. B. The Vertical Distribution of Soil Organic Carbon and Its Relation to Climate and Vegetation. *Ecological Applications* **2000**, *10* (2), 423–436. https://doi.org/10.1890/1051-0761(2000)010[0423:TVDOSO]2.0.CO;2.
(25) Batjes, N. H. Batjes, N. H. 1996. Total Carbon and Nitrogen in the Soils of the World: European Journal of Soil Science, 47, 151-163. Reflections by N.H. Batjes. *European Journal of Soil Science*. January 2014, pp 2–3. https://doi.org/10.1111/ejss.12115.
(26) Meysman, F. J. R.; Middelburg, J. J.; Heip, C. H. R. Bioturbation: A Fresh Look at Darwin's Last Idea. *Trends in Ecology and Evolution*. December 2006, pp 688–695. https://doi.org/10.1016/j.tree.2006.08.002.
(27) Schmidt, M. W. I.; Torn, M. S.; Abiven, S.; Dittmar, T.; Guggenberger, G.; Janssens, I. A.; Kleber, M.; Kögel-Knabner, I.; Lehmann, J.; Manning, D. A. C.; Nannipieri, P.; Rasse, D. P.;

Weiner, S.; Trumbore, S. E. Persistence of Soil Organic Matter as an Ecosystem Property. *Nature* **2011**, *478* (7367), 49–56. https://doi.org/10.1038/nature10386.
(28) Lorenz, K.; Lal, R.; Preston, C. M.; Nierop, K. G. J. Strengthening the Soil Organic Carbon Pool by Increasing Contributions from Recalcitrant Aliphatic Bio(Macro)Molecules. *Geoderma*. November 15, 2007, pp 1–10. https://doi.org/10.1016/j.geoderma.2007.07.013.
(29) Sollins, P.; Homann, P.; Caldwell, B. A. *Stabilization and Destabilization of Soil Organic Matter: Mechanisms and Controls*; 1996; Vol. 74.
(30) Otto, A.; Simpson, M. J. Sources and Composition of Hydrolysable Aliphatic Lipids and Phenols in Soils from Western Canada. *Org Geochem* **2006**, *37* (4), 385–407. https://doi.org/10.1016/j.orggeochem.2005.12.011.
(31) Strukelj, M.; Brais, S.; Quideau, S. A.; Oh, S. W. Chemical Transformations of Deadwood and Foliar Litter of Mixed Boreal Species during Decomposition. *Canadian Journal of Forest Research* **2012**, *42* (4), 772–788. https://doi.org/10.1139/X2012-027.
(32) Relationships between Litterquality and Nitrogen Availability in Rocky Mountain Forests.
(33) Ayres, E.; Steltzer, H.; Berg, S.; Wallenstein, M. D.; Simmons, B. L.; Wall, D. H. Tree Species Traits Influence Soil Physical, Chemical, and Biological Properties in High Elevation Forests. *PLoS One* **2009**, *4* (6). https://doi.org/10.1371/journal.pone.0005964.
(34) Miltner, A.; Bombach, P.; Schmidt-Brücken, B.; Kästner, M. SOM Genesis: Microbial Biomass as a Significant Source. *Biogeochemistry* **2012**, *111* (1–3), 41–55. https://doi.org/10.1007/s10533-011-9658-z.
(35) Cotrufo, M. F.; Wallenstein, M. D.; Boot, C. M.; Denef, K.; Paul, E. The Microbial Efficiency-Matrix Stabilization (MEMS) Framework Integrates Plant Litter Decomposition with Soil Organic Matter Stabilization: Do Labile Plant Inputs Form Stable Soil Organic Matter? *Glob Chang Biol* **2013**, *19* (4), 988–995. https://doi.org/10.1111/gcb.12113.
(36) Adamczyk, B.; Sietiö, O. M.; Straková, P.; Prommer, J.; Wild, B.; Hagner, M.; Pihlatie, M.; Fritze, H.; Richter, A.; Heinonsalo, J. Plant Roots Increase Both Decomposition and Stable Organic Matter Formation in Boreal Forest Soil. *Nat Commun* **2019**, *10* (1). https://doi.org/10.1038/s41467-019-11993-1.
(37) Bruns, T. D.; Chung, J. A.; Carver, A. A.; Glassman, S. I. A Simple Pyrocosm for Studying Soil Microbial Response to Fire Reveals a Rapid, Massive Response by Pyronema Species. *PLoS One* **2020**, *15* (3), 1–20. https://doi.org/10.1371/journal.pone.0222691.
(38) Day, P. R. *Methods of Soil Analysis Part 1*, Brown.; American Society of Agronomy: Madison, WI, 1965.
(39) Arocena, J. M.; Opio, C. Prescribed Fire-Induced Changes in Properties of Sub-Boreal Forest Soils. *Geoderma* **2003**, *113* (1–2), 1–16. https://doi.org/10.1016/S0016-7061(02)00312-9.
(40) Ni, J.; Pignatello, J. J. Charge-Assisted Hydrogen Bonding as a Cohesive Force in Soil Organic Matter: Water Solubility Enhancement by Addition of Simple Carboxylic Acids. *Environ Sci Process Impacts* **2018**, *20* (9), 1225–1233. https://doi.org/10.1039/c8em00255j.
(41) Shaker, A. M.; Komy, Z. R.; Heggy, S. E. M.; El-Sayed, M. E. A. Kinetic Study for Adsorption Humic Acid on Soil Minerals. *Journal of Physical Chemistry A* **2012**, *116* (45), 10889–10896. https://doi.org/10.1021/jp3078826.
(42) Hernández, T.; García, · C; Reinhardt, · I. *Short-Term Effect of Wildfire on the Chemical, Biochemical and Microbiological Properties of Mediterranean Pine Forest Soils*; 1997; Vol. 25.
(43) Bowden, J. W.; Posnera, A. A. M.; Quirkac, J. P. *Ionic Adsorption on Variable Charge Mineral Surfaces. Theoretical-Charge Development and Titration Curves*; 1977; Vol. 15.

(44) Riedel, T.; Biester, H.; Dittmar, T. Molecular Fractionation of Dissolved Organic Matter with Metal Salts. *Environ Sci Technol* **2012**, *46* (8), 4419–4426. https://doi.org/10.1021/es203901u.
(45) Ohno, T.; Kubicki, J. D. Adsorption of Organic Acids and Phosphate to an Iron (Oxyhydr)Oxide Mineral: A Combined Experimental and Density Functional Theory Study. *Journal of Physical Chemistry A* **2020**, *124* (16), 3249–3260. https://doi.org/10.1021/acs.jpca.9b12044.
(46) Li, W.; Liao, P.; Oldham, T.; Jiang, Y.; Pan, C.; Yuan, S.; Fortner, J. D. Real-Time Evaluation of Natural Organic Matter Deposition Processes onto Model Environmental Surfaces. *Water Res* **2018**, *129*, 231–239. https://doi.org/10.1016/j.watres.2017.11.024.
(47) Avena, M. J.; Wilkinson, K. J. Disaggregation Kinetics of a Peat Humic Acid: Mechanism and PH Effects. *Environ Sci Technol* **2002**, *36* (23), 5100–5105. https://doi.org/10.1021/es025582u.
(48) Lee, S. S.; Fenter, P.; Park, C.; Nagy, K. L. Fulvic Acid Sorption on Muscovite Mica as a Function of PH and Time Using in Situ X-Ray Reflectivity. *Langmuir* **2008**, *24* (15), 7817–7829. https://doi.org/10.1021/la703456t.
(49) Avena, M. J.; Koopal, L. K. Kinetics of Humic Acid Adsorption at Solid-Water Interfaces. *Environ Sci Technol* **1999**, *33* (16), 2739–2744. https://doi.org/10.1021/es981236u.
(50) Wickland, K. P.; Neff, J. C.; Aiken, G. R. Dissolved Organic Carbon in Alaskan Boreal Forest: Sources, Chemical Characteristics, and Biodegradability. *Ecosystems* **2007**, *10* (8), 1323–1340. https://doi.org/10.1007/s10021-007-9101-4.
(51) Hagedorn, F.; Machwitz, M. Controls on Dissolved Organic Matter Leaching from Forest Litter Grown under Elevated Atmospheric CO2. *Soil Biol Biochem* **2007**, *39* (7), 1759–1769. https://doi.org/10.1016/j.soilbio.2007.01.038.
(52) Don, A.; Kalbitz, K. Amounts and Degradability of Dissolved Organic Carbon from Foliar Litter at Different Decomposition Stages. *Soil Biol Biochem* **2005**, *37* (12), 2171–2179. https://doi.org/10.1016/j.soilbio.2005.03.019.
(53) Thieme, L.; Graeber, D.; Hofmann, D.; Bischoff, S.; Schwarz, M. T.; Steffen, B.; Meyer, U. N.; Kaupenjohann, M.; Wilcke, W.; Michalzik, B.; Siemens, J. Dissolved Organic Matter Characteristics of Deciduous and Coniferous Forests with Variable Management: Different at the Source, Aligned in the Soil. *Biogeosciences* **2019**, *16* (7), 1411–1432. https://doi.org/10.5194/bg-16-1411-2019.
(54) Sham, C. H.; Tuccillo, M. E.; Rooke, J. *Report on the Effects of Wildfire on Drinking Water Utilities and Effective Practices for Wildfire Risk Reduction and Mitigation*; 2013.
(55) Emelko, M. B.; Silins, U.; Bladon, K. D.; Stone, M. Implications of Land Disturbance on Drinking Water Treatability in a Changing Climate: Demonstrating the Need for " Source Water Supply and Protection" Strategies. *Water Res* **2011**, *45* (2), 461–472. https://doi.org/10.1016/j.watres.2010.08.051.
(56) Rhoades, C. C.; Chow, A. T.; Covino, T. P.; Fegel, T. S.; Pierson, D. N.; Rhea, A. E. The Legacy of a Severe Wildfire on Stream Nitrogen and Carbon in Headwater Catchments. *Ecosystems* **2018**. https://doi.org/10.1007/s10021-018-0293-6.
(57) Hanan, E. J.; Tague, C. N.; Schimel, J. P. Nitrogen Cycling and Export in California Chaparral: The Role of Climate in Shaping Ecosystem Responses to Fire. *Ecol Monogr* **2017**, *87* (1), 76–90. https://doi.org/10.1002/ecm.1234.
(58) Rozendaal, D. M. A.; Chazdon, R. L.; Arreola-Villa, F.; Balvanera, P.; Bentos, T. v.; Dupuy, J. M.; Hernández-Stefanoni, J. L.; Jakovac, C. C.; Lebrija-Trejos, E. E.; Lohbeck, M.;

Martínez-Ramos, M.; Massoca, P. E. S.; Meave, J. A.; Mesquita, R. C. G.; Mora, F.; Pérez-García, E. A.; Romero-Pérez, I. E.; Saenz-Pedroza, I.; van Breugel, M.; Williamson, G. B.; Bongers, F. Demographic Drivers of Aboveground Biomass Dynamics During Secondary Succession in Neotropical Dry and Wet Forests. *Ecosystems* **2017**, *20* (2), 340–353. https://doi.org/10.1007/s10021-016-0029-4.
(59) Gustine, R. N.; Hanan, E. J.; Robichaud, P. R.; Elliot, W. J. From Burned Slopes to Streams: How Wildfire Affects Nitrogen Cycling and Retention in Forests and Fire-Prone Watersheds. *Biogeochemistry*. Springer Science and Business Media Deutschland GmbH January 1, 2022, pp 51–68. https://doi.org/10.1007/s10533-021-00861-0.
(60) Post, W. M.; Paster, J.; Zinke, P. J.; Stangenberger, A. G. Global Patterns of Soil Nitrogen Storage. *Nature* **1985**, *317*, 613–616.
(61) Covington, W. W.; Sackett, S. S.; Covington, W. W.; Box, P. O. *Soil Mineral Nitrogen Changes Following Prescribed Burning in Ponderosa Pine*; 1992; Vol. 54.
(62) Mroz, G. D.; Jurgensen, M. F.; Harvey, A. E.; Larsen, M. J. Effects of Fire on Nitrogen in Forest Floor Horizons. *Soil Science Society of America Journal* **1980**, *44* (2), 395–400. https://doi.org/10.2136/sssaj1980.03615995004400020038x.

APPENDIX B: SUPPLEMENTARY INFORMATION FOR CHAPTER 2

Table A1: pK_a's of common soil functional groups, adapted from Wade, 2021.[1]

Functional Group	**pK_a (approximate)**
Carboxylic acids	4-5
Thiols	10-11
Phenols	10
Alcohols	16-18
Pyrroles	17.5
Pyridines	5-11
Ketones	20-25
Amines/amines	30-35

Table B2a. Mass-to-charge ratio, mass error, resolving power, S/N, DBE and elemental composition for neutral species assigned from mass spectral peaks with signal magnitude greater than six-times the baseline RMS noise level between **m/z 611.03 – 611.38** derived from **positive-ion ESI 21 tesla FT-ICR MS** of a pyOM extract. Peaks denoted with (*) correspond to unknown species. Nitrogen-containing formulas highlighted in bold.

Peak #	**Exp. m/z**	**Theor. Mass**	**Error (ppm)**	**$m/\Delta m_{50\%}$**	**S/N**	**DBE**	**[M+H]+**
1	611.03038	611.0303754	-0.007	1400000	6	21	$C_{27}H_{14}O_{17}$
2	611.04564	611.0456320	0.01	780000	9	25	$C_{31}H_{14}O_{14}$
3	611.06434	611.0643553	0.02	1300000	16	17	$C_{26}H_{19}O_{16}Na$
4	611.06677	611.0667609	-0.01	1300000	39	20	$C_{28}H_{18}O_{16}$
5	611.07082	611.0708440	-0.04	700000	6	16	**$C_{23}H_{19}N_1O_{18}{}^{13}C$**
6	611.07795	611.0779943	0.07	1300000	8	20	**$C_{27}H_{18}N_2O_{15}$**
7	611.07970	611.0796114	-0.1	1200000	7	21	$C_{30}H_{20}O_{13}Na$
8	611.08202	611.0820171	-0.005	1000000	17	24	$C_{32}H_{18}O_{13}$
*	611.08464			1400000	5		
9	611.08542	611.0853880	0.05	1600000	6	19	$C_{29}H_{22}O_{13}S_1$
10	611.08611	611.0861000	0.02	1700000	6	20	**$C_{27}H_{19}N_1O_{15}{}^{13}C_1$**
11	611.08787	611.0878903	0.03	1300000	20	15	$C_{25}H_{22}O_{18}$
12	611.09326	611.0932505	-0.02	1000000	8	24	**$C_{31}H_{18}N_2O_{12}$**
13	611.10072	611.1007408	0.03	1300000	29	16	$C_{27}H_{23}O_{15}Na$
14	611.10314	611.1031465	0.01	1300000	87	19	$C_{29}H_{22}O_{15}$
*	611.10569			1100000	6		*
15	611.10719	611.1072300	-0.07	1000000	7	15	**$C_{24}H_{23}N_1O_{17}{}^{13}C_1$**
16	611.11436	611.1143798	0.03	1300000	29	19	**$C_{28}H_{22}N_2O_{14}$**

17	611.11605	611.1159969	-0.09	1400000	8	20	$C_{31}H_{23}O_{12}Na$
18	611.11841	611.1184026	-0.01	1200000	27	23	$C_{33}H_{22}O_{12}$
*	611.12100			1500000	6		
19	611.12185	611.1218701	0.03	1600000	8	11	$C_{24}H_{27}O_{17}Na$
20	611.12251	611.1224860	0.04	1700000	13	19	**$C_{28}H_{23}N_1O_{14}{}^{13}C$**
21	611.12428	611.1242758	-0.007	1290000	33	14	$C_{26}H_{26}O_{17}$
22	611.12562	611.1258570	0.01	1200000	8	19	**$C_{27}H_{22}N_4O_{13}$**
23	611.12819	611.1280720	-0.04	1300000	5	16	$C_{26}H_{25}O_{14}{}^{13}C_2Na$
24	611.12963	611.1296360	-0.01	1200000	12	23	**$C_{32}H_{22}N_2O_{11}$**
25	611.13057	611.1305920	-0.04	1400000	6	19	$C_{28}H_{24}O_{14}{}^{13}C_2$
26	611.13384	611.1337190	0.2	1300000	8	27	$C_{37}H_{22}O_9$
27	611.13551	611.1355090	0.002	1300000	6	14	**$C_{25}H_{26}N_2O_{16}$**
28	611.13711	611.1371263	0.03	1300000	42	15	$C_{28}H_{27}O_{14}Na$
29	611.13953	611.1395320	0.003	1300000	119	18	$C_{30}H_{26}O_{14}$
30	611.14360	611.1436150	-0.02	1900000	7	14	$C_{30}H_{25}O_{11}{}^{13}C_2Na$
31	611.14674	611.1467430	-0.005	1100000	6	14	**$C_{24}H_{26}N_4O_{15}$**
32	611.15076	611.1507653	0.009	1300000	57	18	**$C_{29}H_{26}N_2O_{13}$**
33	611.15238	611.1523824	0.004	1200000	12	19	$C_{32}H_{27}O_{11}Na$
34	611.15480	611.1547881	-0.02	1200000	32	22	$C_{34}H_{26}O_{11}$
35	611.15821	611.1582556	0.07	1500000	13	10	$C_{31}H_{30}O_{11}S_1$
36	611.15890	611.1588710	0.05	1700000	20	18	**$C_{29}H_{27}N_1O_{13}{}^{13}C_1$**
37	611.16065	611.1606613	0.02	1200000	44	13	$C_{27}H_{30}O_{16}$
38	611.16200	611.1619990	0.002	1200000	17	18	**$C_{28}H_{27}N_4O_{12}$**
39	611.16461	611.1646020	0.01	1200000	8	15	$C_{27}H_{29}O_{13}{}^{13}C_2Na$
40	611.16602	611.1660215	0.002	1300000	17	22	$C_{33}H_{26}N_2O_{10}$
41	611.16700	611.1669770	0.04	1300000	6	18	$C_{29}H_{28}O_{13}{}^{13}C_2$
42	611.17011	611.1700440	0.1	1400000	9	26	**$C_{28}H_{27}N_3O_{12}{}^{13}C_1$**
43	611.17189	611.1718947	0.008	1300000	19	13	**$C_{26}H_{30}N_2O_{15}$**
44	611.17350	611.1735118	0.02	1200000	70	14	$C_{29}H_{31}O_{13}Na$
45	611.17591	611.1759175	0.01	1300000	132	17	$C_{31}H_{30}O_{13}$
46	611.17936	611.1792880	0.1	1900000	8	12	$C_{28}H_{34}O_{13}S_1$
47	611.18001	611.1800010	0.01	1700000	8	13	**$C_{26}H_{31}N_1O_{15}{}^{13}C_1$**
48	611.18177	611.1817910	-0.03	870000	10	8	$C_{24}H_{34}O_{18}$
49	611.18313	611.1831280	0.003	1400000	8	13	**$C_{25}H_{30}N_4O_{14}$**
50	611.18470	611.1846485	-0.08	1300000	6	21	**$C_{28}H_{31}N_2O_{12}Na$**
51	611.18715	611.1871509	0.001	1300000	72	17	**$C_{30}H_{30}N_2O_{12}$**
52	611.18877	611.1887679	-0.003	1000000	11	18	$C_{33}H_{31}O_{10}Na$
53	611.19118	611.1911736	-0.01	1200000	34	21	$C_{35}H_{30}O_{10}$
54	611.19460	611.1946411	0.07	1700000	16	9	$C_{26}H_{35}O_{15}Na$
55	611.19526	611.1952567	-0.005	1800000	25	17	**$C_{30}H_{31}N_1O_{12}{}^{13}C_1$**
56	611.19704	611.1970468	0.01	1300000	47	12	$C_{28}H_{34}O_{15}$
57	611.19839	611.1983842	-0.01	1300000	22	17	**$C_{29}H_{30}N_4O_{11}$**
58	611.20102	611.2009870	0.05	1100000	10	14	$C_{28}H_{33}O_{12}{}^{13}C_2Na$

59	611.20238	611.2024070	0.04	1200000	20	21	**$C_{34}H_{30}N_2O_9$**
60	611.20425	611.2042580	-0.01	1400000	6	8	**$C_{22}H_{34}N_4O_{16}$**
61	611.20653	611.2064901	-0.07	1400000	11	17	**$C_{29}H_{31}N_3O_{11}{}^{13}C_1$**
62	611.20987	611.2098973	0.04	1300000	28	13	$C_{30}H_{35}O_{12}Na$
63	611.21229	611.2123030	0.02	1200000	140	16	$C_{32}H_{34}O_{12}$
64	611.21570	611.2156740	0.04	1800000	6	11	$C_{29}H_{38}O_{12}S_1$
65	611.21637	611.2163860	-0.03	1600000	13	12	**$C_{27}H_{35}N_1O_{14}{}^{13}C_1$**
66	611.21777	611.2176630	0.2	680000	5	25	**$C_{38}H_{31}N_2O_6$**
67	611.21953	611.2195140	0.03	1400000	13	12	**$C_{26}H_{34}N_4O_{13}$**
68	611.22113	611.2210340	-0.2	1400000	8	20	**$C_{29}H_{35}N_2O_{11}Na$**
69	611.22353	611.2235364	0.01	1300000	6	16	**$C_{31}H_{34}N_2O_{11}$**
70	611.22519	611.2251534	-0.06	1400000	10	17	$C_{34}H_{35}O_9Na$
71	611.22757	611.2275591	-0.02	1300000	32	20	$C_{36}H_{34}O_9$
72	611.23099	611.2310267	0.06	870000	44	8	$C_{27}H_{39}O_{14}N_a$
73	611.23164	611.2316420	-0.003	520000	39	16	**$C_{30}H_{35}N_1O_{11}{}^{13}C_1$**
74	611.23342	611.2334323	0.02	1200000	55	11	$C_{29}H_{38}O_{14}$
75	611.23477	611.2347698	-0.0004	1200000	23	16	**$C_{30}H_{34}N_4O_{10}$**
76	611.23878	611.2387925	0.02	1200000	17	20	**$C_{35}H_{34}N_2O_8$**
77	611.23971	611.2397480	-0.06	1500000	7	16	$C_{31}H_{36}O_{11}{}^{13}C_2$
*	611.24210			15052696	6		
78	611.24287	611.2427460	0.2	1300000	12	20	**$C_{30}H_{35}N_3O_{10}{}^{13}C_1$**
79	611.24465	611.2446657	0.03	1300000	28	11	**$C_{28}H_{38}N_2O_{13}$**
80	611.24625	611.2462828	0.05	1200000	89	12	$C_{31}H_{39}O_{11}Na$
81	611.24867	611.2486885	0.03	1300000	138	15	$C_{33}H_{38}O_{11}Na$
82	611.25277	611.2527716	0.003	1400000	13	11	**$C_{28}H_{39}N_1O_{13}{}^{13}C_1$**
83	611.25593	611.2558990	0.05	1400000	15	11	**$C_{27}H_{38}N_4O_{12}$**
84	611.25991	611.2599219	0.02	1300000	58	15	**$C_{32}H_{38}N_2O_{10}$**
85	611.26396	611.2639446	-0.03	1100000	22	19	$C_{37}H_{38}O_8$
86	611.26573	611.2657950	-0.1	1000000	12	6	**$C_{25}H_{42}N_2O_{15}$**
87	611.26731	611.2674122	0.2	950000	43	7	$C_{28}H_{43}O_{13}Na$
88	611.26802	611.2680280	-0.01	450000	31	15	**$C_{32}H_{39}N_1O_{10}{}^{13}C_1$**
89	611.26981	611.2698179	0.01	1300000	47	10	$C_{30}H_{42}O_{13}$
90	611.27113	611.2711553	0.04	1300000	17	15	**$C_{31}H_{38}N_4O_9$**
91	611.27370	611.2737580	-0.09	1200000	6	12	$C_{30}H_{41}O_{10}{}^{13}C_2$
92	611.27519	611.2751780	0.02	1300000	8	37	**$C_{36}H_{38}N_2O_7$**
93	611.27609	611.2761340	-0.07	1400000	7	15	$C_{32}H_{40}O_{10}{}^{13}C_2$
94	611.27928	611.2792010	0.1	1400000	7	23	$C_{41}H_{38}O_5$
95	611.28105	611.2810510	-0.002	1300000	21	10	**$C_{29}H_{42}N_2O_{12}$**
96	611.28264	611.2826683	-0.05	1200000	72	11	$C_{32}H_{43}O_{10}Na$
97	611.28506	611.2850740	-0.02	1300005	109	14	$C_{34}H_{42}O_{10}$
98	611.28916	611.2891570	0.005	1300000	12	10	**$C_{29}H_{43}N_1O_{12}{}^{13}C_1$**
99	611.29228	611.2922850	-0.008	1100000	11	10	**$C_{28}H_{42}N_4O_{11}$**
100	611.29384	611.2939320	-0.2	1300000	5	11	**$C_{31}H_{43}N_2O_9Na$**

101	611.29630	611.2963074	0.01	1300000	35	14	**$C_{33}H_{42}N_2O_9$**
102	611.30034	611.3003301	-0.02	1200000	14	18	$C_{38}H_{42}O_7$
103	611.30208	611.3021806	0.2	1000000	6	5	**$C_{26}H_{46}N_2O_{14}$**
104	611.30366	611.3037977	0.2	1200000	23	6	$C_{29}H_{47}O_{12}Na$
105	611.30444	611.3044132	-0.04	2000000	9	14	**$C_{33}H_{43}N_1O_9{}^{13}C_1$**
106	611.30619	611.3062034	0.02	1300000	32	9	$C_{31}H_{46}O_{12}$
107	611.30752	611.3075410	-0.03	1200000	7	14	$C_{32}H_{42}H_4O_8$
108	611.31154	611.3115635	0.04	1300000	6	18	**$C_{37}H_{42}N_2O_6$**
109	611.31742	611.3174368	0.03	1200000	13	9	**$C_{30}H_{46}N_2O_{11}$**
110	611.31901	611.3190538	0.07	1100000	33	10	$C_{33}H_{47}O_9Na$
111	611.32145	611.3214595	0.02	1200000	67	13	$C_{35}H_{46}O_9$
112	611.33268	611.3326930	-0.02	1200000	13	13	**$C_{34}H_{46}N_2O_8$**
113	611.33675	611.3367160	0.06	1000000	8	17	$C_{39}H_{46}O_6$
114	611.34001	611.3400860	-0.1	1200000	8	12	$C_{36}H_{50}O_6S_1$
115	611.34083	611.3407990	0.05	1600000	6	13	**$C_{34}H_{47}N_1O_8{}^{13}C_1$**
116	611.34258	611.3425889	0.01	1300000	14	8	$C_{32}H_{50}O_{11}$
117	611.35381	611.3538223	0.02	1300000	7	8	**$C_{31}H_{50}N_2O_{10}$**
118	611.35540	611.3554700	-0.1	1500000	6	9	$C_{34}H_{51}O_8Na$
119	611.35611	611.3561150	-0.008	1700000	7	9	**$C_{28}H_{48}N_4O_9{}^{13}C_2$**
120	611.35784	611.357845	0.008	1200000	24	12	$C_{36}H_{50}O_8$
121	611.36192	611.361928	-0.01	1600000	6	8	**$C_{31}H_{51}N_1O_{10}{}^{13}C_1$**
122	611.37629	611.376472	-0.3	1200000	6	11	$C_{37}H_{54}O_5S_1$
123	611.37896	611.378974	-0.02	1400000	6	7	$C_{33}H_{54}O_{10}$
		Average:		**1400000**			
		RMS error:	**19 ppb**				

Table B2b. Mass-to-charge ratio, mass error, resolving power, S/N, DBE and elemental composition for neutral species assigned from mass spectral peaks with signal magnitude greater than six-times the baseline RMS noise level between **m/z 612.06 – 612.38** derived from **positive-ion ESI 21 tesla FT-ICR MS** of a pyOM extract. Peaks denoted with (*) correspond to unknown species. Nitrogen-containing formulas highlighted in bold.

Peak #	**Exp. m/z**	**Theor. Mass**	**Error (ppm)**	**$m/\Delta m_{50\%}$**	**S/N**	**DBE**	**[M+H]+**
1	612.06204	612.0620099	-0.05	1000000	13	20	**$C_{27}H_{17}N_1O_{16}$**
2	612.07012	612.0701158	-0.007	1200000	13	20	$C_{27}H_{18}O_{16}{}^{13}C_1$
3	612.07727	612.0772661	-0.006	1100000	13	24	**$C_{31}H_{17}N_1O_{13}$**
*	612.08871	612.08887	-0.3	800000	8	12	$C_{22}H_{23}O_{18}{}^{13}C_1Na$
4	612.09129	612.091245	0.07	1300000	6	15	$C_{24}H_{22}O_{18}{}^{13}C_1$
5	612.09839	612.0983954	0.009	1200000	39	19	**$C_{28}H_{21}N_1O_{15}$**
6	612.10412	612.1040956	-0.04	1000000	12	16	$C_{26}H_{23}O_{15}{}^{13}C_1Na$
7	612.10648	612.1065013	0.03	1200000	26	19	$C_{28}H_{22}O_{15}{}^{13}C_1$
8	612.10962	612.1096288	0.01	1200000	12	19	**$C_{27}H_{21}N_3O_{14}$**
9	612.11363	612.1136516	0.04	1200000	24	23	**$C_{32}H_{21}N_1O_{12}$**

10	612.11775	612.1177347	-0.03	1600000	7	19	**$C_{27}H_{22}N_2O_{14}{}^{13}C_1$**
11	612.11950	612.1195248	0.04	1200000	14	14	**$C_{25}H_{25}N_1O_{17}$**
12	612.12175	612.1217574	0.01	1400000	7	23	$C_{32}H_{22}O_{12}{}^{13}C_1$
13	612.12502	612.124885	0.2	970000	10	23	**$C_{31}H_{21}N_3O_{11}$**
14	612.12759	612.1276307	0.07	1300000	9	14	$C_{25}H_{26}O_{17}{}^{13}C_1$
15	612.13478	612.1347809	0.002	1200000	72	18	**$C_{29}H_{25}N_1O_{14}$**
16	612.14045	612.1404811	0.05	1300000	16	15	$C_{27}H_{27}O_{14}{}^{13}C_1Na$
17	612.14289	612.1428868	-0.005	1300000	39	18	$C_{29}H_{26}O_{14}{}^{13}C_1$
18	612.14600	612.1460143	0.02	1200000	24	18	**$C_{28}H_{25}N_3O_{13}$**
19	612.15003	612.1500371	0.01	1200000	30	22	**$C_{33}H_{25}N_1O_{11}$**
20	612.15413	612.1541202	-0.02	1400000	14	18	**$C_{28}H_{26}N_2O_{13}{}^{13}C_1$**
21	612.15587	612.1559103	0.07	1100000	27	13	**$C_{26}H_{29}N_1O_{16}$**
22	612.15723	612.157248	-0.03	1200000	9	18	**$C_{27}H_{25}N_5O_{12}$**
23	612.15816	612.1581429	-0.03	1400000	11	22	$C_{33}H_{26}O_{11}{}^{13}C_1$
24	612.16135	612.1612705	-0.1	860000	15	22	**$C_{32}H_{25}N_3O_{10}$**
25	612.16402	612.1640162	-0.006	1100000	14	13	$C_{26}H_{30}O_{16}{}^{13}C_1$
26	612.16710	612.1671437	0.07	1200000	10	13	**$C_{25}H_{29}N_3O_{15}$**
27	612.16873	612.168791	-0.1	1400000	12	14	**$C_{28}H_{30}N_1O_{13}Na$**
28	612.17116	612.1711664	0.01	1300000	110	17	**$C_{30}H_{29}N_1O_{13}$**
29	612.17521	612.17525	-0.07	1300000	6	13	**$C_{25}H_{30}N_2O_{15}{}^{13}C_1$**
30	612.17689	612.1768666	-0.04	1200000	24	14	$C_{28}H_{31}O_{13}{}^{13}C_1$
31	612.17926	612.1792723	0.02	1400000	43	17	$C_{30}H_{30}O_{13}{}^{13}C_1$
32	612.18239	612.1823998	0.02	1200000	41	17	**$C_{29}H_{29}N_3O_{12}$**
33	612.18411	612.184047	0.1	1200000	8	18	**$C_{32}H_{30}N_1O_{10}$**
34	612.18643	612.1864226	-0.01	1300000	36	21	**$C_{34}H_{29}N_1O_{10}$**
35	612.19053	612.1905057	-0.04	1600000	15	17	**$C_{29}H_{30}N_2O_{12}{}^{13}C_1$**
36	612.19228	612.1922958	0.03	1300000	39	12	**$C_{27}H_{33}N_1O_{15}$**
37	612.19364	612.193633	0.01	1300000	14	17	**$C_{28}H_{29}N_5O_{11}$**
38	612.19455	612.1945284	-0.04	1500000	8	21	$C_{34}H_{30}O_{10}{}^{13}C_1$
39	612.19778	612.197656	-0.2	950000	14	21	**$C_{33}H_{29}N_3O_9$**
40	612.20039	612.2004017	0.02	1200000	18	12	$C_{27}H_{34}O_{15}{}^{13}C_1$
41	612.20177	612.201679	0.1	1400000	9	25	**$C_{38}H_{29}N_1O_7$**
42	612.20351	612.2035292	0.03	1200000	16	12	**$C_{26}H_{33}N_3O_{14}$**
43	612.20514	612.205177	-0.06	1300000	17	13	**$C_{29}H_{34}N_1O_{12}Na$**
44	612.20754	612.2075519	0.02	1300000	120	16	**$C_{31}H_{33}N_1O_{12}$**
45	612.21160	612.2116351	0.06	1400000	9	12	**$C_{26}H_{34}N_2O_{14}{}^{13}C_1$**
46	612.21328	612.2132521	-0.05	1100000	35	13	$C_{29}H_{35}O_{12}{}^{13}C_1Na$
47	612.21567	612.2156578	-0.02	1300000	10	16	$C_{31}H_{34}O_{12}{}^{13}C_1$
48	612.21879	612.2187853	-0.008	1300000	44	16	**$C_{30}H_{33}N_3O_{11}$**
49	612.22283	612.2228081	-0.04	1400000	33	20	**$C_{35}H_{33}N_1O_9$**
50	612.22611	612.226179	-0.1	1300000	7	15	**$C_{32}H_{37}N_1O_9S_1$**
51	612.22689	612.2268912	0.002	1600000	19	16	**$C_{30}H_{34}N_2O_{11}{}^{13}C_1$**
52	612.22867	612.2286813	0.02	1300000	41	11	**$C_{28}H_{37}N_1O_{14}$**

53	612.23001	612.230019	-0.0147	1300000	16	16	**$C_{29}H_{33}N_5O_{10}$**
54	612.23090	612.230914	0.02	1400000	6	20	$C_{35}H_{34}O_9{}^{13}C_1$
55	612.23418	612.2340415	-0.2	1000000	14	20	**$C_{34}H_{33}N_3O_8$**
56	612.23680	612.2367872	-0.02	1200000	17	11	$C_{28}H_{38}O_{14}{}^{13}C_1$
57	612.23817	612.238064	0.2	1100000	8	24	**$C_{39}H_{33}N_1O_6$**
58	612.23992	612.2399147	-0.009	1300000	19	11	**$C_{27}H_{37}N_3O_{13}$**
59	612.24150	612.241562	-0.1	1200000	14	19	**$C_{30}H_{38}N_1O_{11}Na$**
60	612.24394	612.2439375	-0.004	1300000	124	15	**$C_{32}H_{37}N_1O_{11}$**
61	612.24799	612.2480206	0.05	1300000	8	11	**$C_{27}H_{38}N_2O_{13}{}^{13}C_1$**
62	612.24966	612.2496376	-0.04	1200000	38	12	$C_{30}H_{39}O_{11}{}^{13}C_1Na$
63	612.25114	612.251148	-0.01	1600000	11	11	**$C_{26}H_{37}N_5O_{12}$**
64	612.25205	612.2520433	-0.01	1400000	43	15	$C_{32}H_{38}O_{11}{}^{13}C_1$
65	612.25516	612.2551708	0.02	1300000	36	15	**$C_{31}H_{37}N_3O_{10}$**
66	612.25918	612.2591936	0.02	1100000	27	19	**$C_{36}H_{37}N_1O_8$**
67	612.26246	612.262564	-0.2	1600000	6	14	**$C_{33}H_{41}N_1O_8S_1$**
68	612.26327	612.2632767	0.01	1300000	18	15	**$C_{31}H_{38}N_2O_{10}{}^{13}C_1$**
69	612.26506	612.2650668	0.01	1300000	37	10	**$C_{29}H_{41}N_1O_{13}$**
70	612.26641	612.266404	0.01	1400000	16	15	**$C_{30}H_{37}N_5O_9$**
71	612.27065	612.2706703	0.03	700000	16	14	$C_{33}H_{42}O_8S_1{}^{13}C_1$
72	612.27319	612.2731727	-0.03	1300000	14	10	$C_{29}H_{42}O_{13}{}^{13}C_1$
73	612.27626	612.2763002	0.07	1300000	14	10	**$C_{28}H_{41}N_3O_{12}$**
74	612.27782	612.277948	-0.2	1200000	12	11	**$C_{31}H_{42}N_1O_{10}Na$**
75	612.28031	612.280323	0.02	1300000	90	14	**$C_{33}H_{41}N_1O_{10}$**
76	612.28444	612.2844061	-0.06	1400000	8	10	**$C_{28}H_{42}N_2O_{12}{}^{13}C_1$**
77	612.28603	612.2860231	-0.01	1200000	30	11	$C_{31}H_{43}O_{10}{}^{13}C_1Na$
78	612.28753	612.287534	-0.007	1300000	13	10	**$C_{27}H_{41}N_5O_{11}$**
79	612.28844	612.2884288	-0.02	1300000	36	14	$C_{33}H_{42}O_{10}{}^{13}C_1$
80	612.29157	612.2915564	-0.02	1200000	23	14	**$C_{32}H_{41}N_3O_9$**
81	612.29560	612.2955791	-0.03	1200000	12	18	**$C_{37}H_{41}N_1O_7$**
*	612.29876			1300000	9		
82	612.29968	612.2996622	-0.03	1400000	11	14	**$C_{32}H_{42}N_2O_9{}^{13}C_1$**
83	612.30144	612.3014523	0.02	1200000	27	9	**$C_{30}H_{45}N_1O_{12}$**
84	612.30284	612.30279	0.08	1200000	8	14	**$C_{31}H_{41}N_5O_8$**
85	612.30703	612.307183	-0.2	1200000	9	6	$C_{28}H_{47}O_{12}{}^{13}C_1Na$
86	612.30955	612.3095582	0.01	1400000	7	9	$C_{30}H_{46}O_{12}{}^{13}C_1$
87	612.31269	612.3126857	-0.007	1200000	8	9	**$C_{29}H_{45}N_3O_{11}$**
88	612.31671	612.3167085	-0.002	1200000	51	13	**$C_{34}H_{45}N_1O_9$**
89	612.32237	612.3224087	0.06	1300000	13	10	$C_{32}H_{47}O_9{}^{13}C_1Na$
*	612.32396			1200000	10		
90	612.32483	612.3248143	-0.03	1300000	23	13	$C_{34}H_{46}O_9{}^{13}C_1$
91	612.32796	612.3279419	-0.03	1300000	9	13	**$C_{33}H_{45}N_3O_8$**
92	612.33782	612.3378378	0.03	1200000	15	8	**$C_{31}H_{49}N_1O_{11}$**
93	612.34905	612.349071	-0.03	700000	7	8	**$C_{30}H_{49}N_3O_{10}$**

94	612.35310	612.353094	-0.01	1300000	17	12	**$C_{35}H_{49}N_1O_8$**
95	612.36122	612.3611998	-0.03	1000000	8	12	$C_{35}H_{50}O_8{}^{13}C_1$
96	612.37420	612.3742234	0.04	1200000	8	7	**$C_{32}H_{53}N_1O_{10}$**
		Average		**1300000**			
		RMS error:	**24 ppb**				

Table B3a. Mass-to-charge ratio, mass error, resolving power, S/N, DBE and molecular formula for mass spectral peaks with signal magnitude greater than six-times the baseline RMS noise level between m/z **611.01 – 611.32** derived from **negative-ion ESI 21 tesla FT-ICR MS** of a pyOM extract. Peaks denoted with (*) correspond to unknown species. Nitrogen-containing formulas shown in bold.

Peak #	Exp. m/z	Theor. Mass	Error (ppm)	$m/\Delta m_{50\%}$	S/N	DBE	$[M-H]^-$
1	611.01037	611.0103432	-0.04	1200000	9	25	$C_{30}H_{10}O_{15}$
2	611.01625	611.0162165	-0.05	1000000	8	16	$C_{23}H_{16}O_{20}$
3	611.03151	611.0314726	-0.06	1200000	108	20	$C_{27}H_{14}O_{17}$
4	611.04273	611.042706	-0.04	1000000	14	20	**$C_{26}H_{16}N_2O_{16}$**
5	611.04676	611.0467287	-0.05	1100000	33	24	$C_{31}H_{16}O_{14}$
6	611.05085	611.0508118	-0.06	1200000	12	20	**$C_{26}H_{17}N_1O_{16}{}^{13}C_1$**
7	611.05265	611.052602	-0.08	1200000	45	15	$C_{24}H_{20}O_{19}$
8	611.05798	611.0579621	-0.03	1300000	12	24	**$C_{30}H_{16}N_2O_{13}$**
9	611.05899	611.0589177	-0.1	1200000	6	20	$C_{26}H_{18}O_{16}{}^{13}C_2$
10	611.06789	611.0678581	-0.05	1200000	217	19	$C_{28}H_{20}O_{16}$
11	611.07126	611.0712289	-0.05	1000000	12	14	$C_{25}H_{24}O_{16}S_1$
12	611.07195	611.0719412	-0.01	400000	6	15	**$C_{23}H_{21}N_1O_{18}{}^{13}C_1$**
*	611.07759	611.0776835		1200000	7		
13	611.07913	611.0790915	-0.06	1200000	30	19	**$C_{27}H_{20}N_2O_{15}$**
14	611.08314	611.0831142	-0.04	1000000	41	23	$C_{32}H_{20}O_{13}$
15	611.08724	611.0871974	-0.07	1200000	23	19	**$C_{27}H_{21}N_1O_{15}{}^{13}C_1$**
16	611.08904	611.0871974	-0.09	1200000	107	14	$C_{25}H_{24}O_{18}$
17	611.09439	611.0889875	-0.07	1400000	12	23	**$C_{31}H_{20}N_2O_{12}$**
18	611.09533	611.0943476	-0.04	1300000	8	19	$C_{36}H_{20}O_{15}{}^{13}C_2$
19	611.09852	611.0953032	-0.2	700000	9	27	$C_{36}H_{20}O_{10}$
20	611.10030	611.0983704	-0.1	1200000	8	14	**$C_{24}H_{24}N_2O_{17}$**
21	611.10429	611.1002209	-0.08	1200000	260	18	$C_{29}H_{24}O_{15}$
22	611.10763	611.1042436	-0.03	1400000	9	13	$C_{26}H_{28}O_{15}S_1$
23	611.11552	611.1076144	-0.07	1200000	40	18	**$C_{28}H_{24}N_2O_{14}$**
24	611.11954	611.115477	-0.07	1000000	35	22	$C_{33}H_{24}O_{12}$
25	611.12362	611.1194998	-0.06	1300000	24	18	**$C_{28}H_{25}N_1O_{14}{}^{13}C_1$**
26	611.12542	611.1235829	-0.08	1200000	134	13	$C_{26}H_{28}O_{17}$
27	611.12677	611.125373	-0.1	1200000	9	18	**$C_{27}H_{24}N_4O_{13}$**
28	611.13079	611.1267104	-0.09	1300000	9	22	**$C_{32}H_{24}N_2O_{11}$**
29	611.13178	611.1307331	-0.1	1000000	11	18	$C_{28}H_{26}O_{14}{}^{13}C_2$
30	611.13664	611.1316887	-0.05	1200000	11	13	**$C_{25}H_{28}N_2O_{16}$**

31	611.14068	611.1366064	-0.08	1200000	225	17	$C_{30}H_{28}O_{14}$
32	611.14402	611.1406291	-0.03	1600000	8	12	$C_{27}H_{32}O_{14}S_1$
33	611.14478	611.1439999	-0.1	1000000	6	13	**$C_{25}H_{29}N_1O_{16}{}^{13}C_1$**
34	611.14653	611.1447122	-0.04	990000	11	8	$C_{23}H_{32}O_{19}$
35	611.15188	611.1465023	-0.03	1200000	34	17	**$C_{29}H_{28}N_2O_{13}$**
36	611.15592	611.1518625	-0.06	1000000	28	21	$C_{34}H_{28}O_{11}$
37	611.16000	611.1558853	-0.05	1200000	22	17	**$C_{29}H_{29}N_1O_{13}{}^{13}C_1$**
38	611.16180	611.1599684	-0.07	1200000	123	12	$C_{27}H_{32}O_{16}$
39	611.16314	611.1617585	-0.07	1200000	9	17	**$C_{28}H_{28}N_4O_{12}$**
40	611.16726	611.1630959	-0.2	780000	6	21	**$C_{33}H_{28}N_2O_{10}$**
41	611.16808	611.1671187	-0.009	1100000	8	17	$C_{29}H_{30}O_{13}{}^{13}C_2$
42	611.17304	611.1680742	-0.08	1400000	11	12	**$C_{26}H_{32}N_2O_{15}$**
43	611.17706	611.1729919	-0.07	1200000	165	16	$C_{31}H_{32}O_{13}$
44	611.18047	611.1770146	0.09	900000	11	11	$C_{28}H_{36}O_{13}S_1$
45	611.18111	611.1805243	-0.02	500000	8	12	**$C_{26}H_{33}N_1O_{15}{}^{13}C_1$**
46	611.18292	611.1810977	-0.05	1100000	12	7	$C_{24}H_{36}O_{18}$
47	611.18829	611.1828879	-0.07	1200000	18	16	**$C_{30}H_{32}N_2O_{12}$**
48	611.19229	611.188248	-0.03	980000	17	20	$C_{35}H_{32}O_{10}$
49	611.19639	611.1922708	-0.06	1300000	8	16	**$C_{30}H_{33}N_1O_{12}{}^{13}C_1$**
50	611.19818	611.1963539	-0.06	1200000	104	11	$C_{28}H_{36}O_{15}$
51	611.20451	611.198144	-0.08	1300000	7	16	$C_{30}H_{34}O_{12}{}^{13}C_2$
52	611.20942	611.2044597	-0.07	1200000	7	11	**$C_{27}H_{36}N_2O_{14}$**
53	611.21345	611.2093774	-0.08	1200000	114	15	$C_{32}H_{36}O_{12}$
54	611.21682	611.2134001	-0.08	1300000	9	10	$C_{29}H_{40}O_{12}S_1$
55	611.22059	611.216771	0.03	1200000	8	11	**$C_{26}H_{36}N_4O_{13}$**
56	611.22468	611.2206108	-0.07	1300000	11	15	**$C_{31}H_{36}N_2O_{11}$**
57	611.22869	611.2246335	-0.06	1200000	7	19	$C_{36}H_{36}O_9$
58	611.23457	611.2286563	-0.07	1200000	80	10	$C_{29}H_{40}O_{14}$
59	611.24984	611.2345295	-0.09	1200000	57	14	$C_{33}H_{40}O_{11}$
60	611.25317	611.2497856	-0.02	1200000	18	9	$C_{30}H_{44}O_{11}S_1$
61	611.26503	611.2531565	0.02	520000	6	18	$C_{37}H_{40}O_8$
62	611.27095	611.2650418	-0.06	1200000	40	9	$C_{30}H_{44}O_{13}$
63	611.28621	611.270915	-0.06	1200000	23	13	$C_{34}H_{44}O_{10}$
64	611.28958	611.2861712	-0.06	1300000	12	8	$C_{31}H_{48}O_{10}S_1$
65	611.30732	611.289542	-0.03	1100000	15	8	$C_{31}H_{48}O_{12}$
66	611.32264	611.3073005	-0.1	1300000	8	12	$C_{35}H_{48}O_9$
		Average		**1200000**			
		RMS Error	**-0.06**				

Table B3b. Mass-to-charge ratio, mass error, resolving power, S/N, DBE and molecular formula for mass spectral peaks with signal magnitude greater than six-times the baseline RMS noise level

between m/z **612.02 – 612.32** derived from **negative-ion ESI 21 tesla FT-ICR MS**. Peaks denoted with (*) correspond to unknown species. Nitrogen-containing formulas are shown in bold.

Peak #	Exp. m/z	Theor. Mass	Error (ppm)	$m/\Delta m_{50}$ %	S/N	DBE	$[M-H]^-$
1	612.02678	612.0267216	-0.1	1100000	20	20	**$C_{26}H_{15}N_1O_{17}$**
2	612.03488	612.0348274	-0.09	1200000	32	20	$C_{26}H_{16}O_{17}{}^{13}C_1$
3	612.04202	612.0419777	-0.07	1200000	26	24	**$C_{30}H_{15}N_1O_{14}$**
4	612.04539	612.0454874	0.2	1400000	6	19	**$C_{27}H_{19}N_1O_{14}S_1$**
5	612.05011	612.0500836	-0.04	1100000	8	24	$C_{30}H_{16}O_{14}{}^{13}C_1$
6	612.05329	612.0532111	-0.1	1300000	6	24	**$C_{29}H_{16}N_3O_{13}$**
7	612.05601	612.0559568	-0.09	1300000	10	15	$C_{23}H_{21}O_{19}{}^{13}C_1$
8	612.06315	612.0631071	-0.07	1200000	62	19	**$C_{27}H_{19}N_1O_{16}$**
9	612.07125	612.0712129	-0.06	1200000	64	19	$C_{27}H_{20}O_{16}{}^{13}C_1$
10	612.07441	612.0743405	-0.1	980000	11	19	**$C_{26}H_{19}N_3O_{15}$**
11	612.07841	612.0783632	-0.08	1200000	25	23	**$C_{31}H_{19}N_1O_{13}$**
12	612.08248	612.0824463	-0.06	1600000	6	19	**$C_{26}H_{20}N_2O_{15}{}^{13}C_1$**
13	612.08431	612.0842364	-0.1	1200000	11	14	**$C_{24}H_{23}N_1O_{18}$**
14	612.08648	612.0864691	-0.02	940000	10	23	$C_{31}H_{20}O_{13}{}^{13}C_1$
15	612.08965	612.0895966	-0.09	900000	8	23	**$C_{30}H_{19}N_3O_{12}$**
16	612.09240	612.0923423	-0.09	1200000	28	14	$C_{24}H_{24}O_{18}{}^{13}C_1$
17	612.09954	612.0994926	-0.08	1200000	91	18	**$C_{28}H_{23}N_1O_{15}$**
18	612.10765	612.1075984	-0.08	1200000	83	18	$C_{28}H_{24}O_{15}{}^{13}C_1$
19	612.11081	612.110726	-0.1	1100000	19	18	**$C_{27}H_{23}N_3O_{14}$**
20	612.11478	612.1147487	-0.05	1100000	26	22	**$C_{32}H_{23}N_1O_{12}$**
21	612.11891	612.1188318	-0.1	1300000	10	18	**$C_{27}H_{24}N_2O_{14}{}^{13}C_1$**
22	612.12068	612.120622	-0.09	1200000	20	13	$C_{32}H_{24}O_{12}{}^{13}C_1$
23	612.12286	612.1228546	-0.009	1200000	13	22	$C_{32}H_{24}O_{12}{}^{13}C_1$
24	612.12610	612.1259821	-0.2	1400000	7	22	**$C_{31}H_{23}N_3O_{11}$**
25	612.12877	612.1287278	-0.07	1200000	39	13	$C_{25}H_{28}O_{17}{}^{13}C_1$
26	612.13592	612.1358781	-0.07	1200000	86	17	**$C_{29}H_{27}N_1O_{14}$**
27	612.14403	612.143984	-0.08	1200000	70	17	$C_{29}H_{28}O_{14}{}^{13}C_1$
28	612.14719	612.1471115	-0.1	1000000	21	17	**$C_{28}H_{27}N_3O_{13}$**
29	612.15119	612.1511342	-0.09	1100000	15	21	**$C_{33}H_{27}N_1O_{11}$**
30	612.15529	612.1552173	-0.1	1400000	9	17	**$C_{28}H_{28}N_2O_{13}{}^{13}C_1$**
31	612.15706	612.1570075	-0.08	1200000	20	12	**$C_{26}H_{31}N_1O_{16}$**
32	612.15929	612.1592401	-0.08	1400000	7	21	$C_{33}H_{28}O_{11}{}^{13}C_1$
33	612.16515	612.1651133	-0.06	1100000	36	12	$C_{26}H_{32}O_{16}{}^{13}C_1$
34	612.16833	612.1682408	-0.1	1000000	6	12	**$C_{25}H_{31}N_3O_{15}$**
35	612.17232	612.1722636	-0.09	1200000	64	16	**$C_{30}H_{31}N_1O_{13}$**
36	612.18041	612.1803695	-0.07	1200000	51	16	$C_{30}H_{32}O_{13}{}^{13}C_1$
37	612.18360	612.183497	-0.2	1000000	18	16	**$C_{29}H_{31}N_3O_{12}$**
38	612.18753	612.1875197	-0.02	1200000	10	20	**$C_{34}H_{31}N_1O_{10}$**
39	612.19161	612.1916029	-0.01	1100000	8	16	**$C_{29}H_{32}N_2O_{12}{}^{13}C_1$**
40	612.19345	612.193393	-0.09	1300000	15	11	**$C_{27}H_{35}N_1O_{15}$**

41	612.20155	612.2014988	-0.08	1300000	30	11	$C_{27}H_{36}O_{15}{}^{13}C_1$
42	612.20465	612.2046264	-0.04	1200000	8	11	**$C_{26}H_{35}N_3O_{14}$**
43	612.2087	612.2086491	-0.08	1200000	36	15	**$C_{31}H_{35}N_1O_{12}$**
44	612.21682	612.216755	-0.1	1200000	34	15	$C_{31}H_{36}O_{12}{}^{13}C_1$
45	612.21999	612.2198825	-0.2	1300000	8	15	**$C_{30}H_{35}N_3O_{11}$**
46	612.22981	612.2297785	-0.05	1100000	11	10	**$C_{28}H_{39}N_1O_{14}$**
47	612.23793	612.2378843	-0.07	1100000	25	10	$C_{28}H_{40}O_{14}{}^{13}C_1$
48	612.24511	612.2450346	-0.1	1100000	19	14	**$C_{32}H_{39}N_1O_{11}$**
49	612.25321	612.2531405	-0.1	1200000	17	14	$C_{32}H_{40}O_{11}{}^{13}C_1$
50	612.27433	612.2742699	-0.1	1100000	7	9	$C_{29}H_{44}O_{13}{}^{13}C_1$
51	612.28149	612.2814201	-0.1	1200000	13	13	**$C_{33}H_{43}N_1O_{10}$**
52	612.28955	612.289526	-0.04	1200000	7	13	$C_{33}H_{44}O_{10}{}^{13}C_1$
53	612.29290	612.2928968	-0.005	590000	9	8	$C_{30}H_{48}O_{10}S_1{}^{13}C_1$
54	612.31069	612.3106554	-0.06	1200000	7	8	$C_{30}H_{48}O_{12}{}^{13}C_1$
		Average:		**1200000**			
		RMS error	**-0.081**				

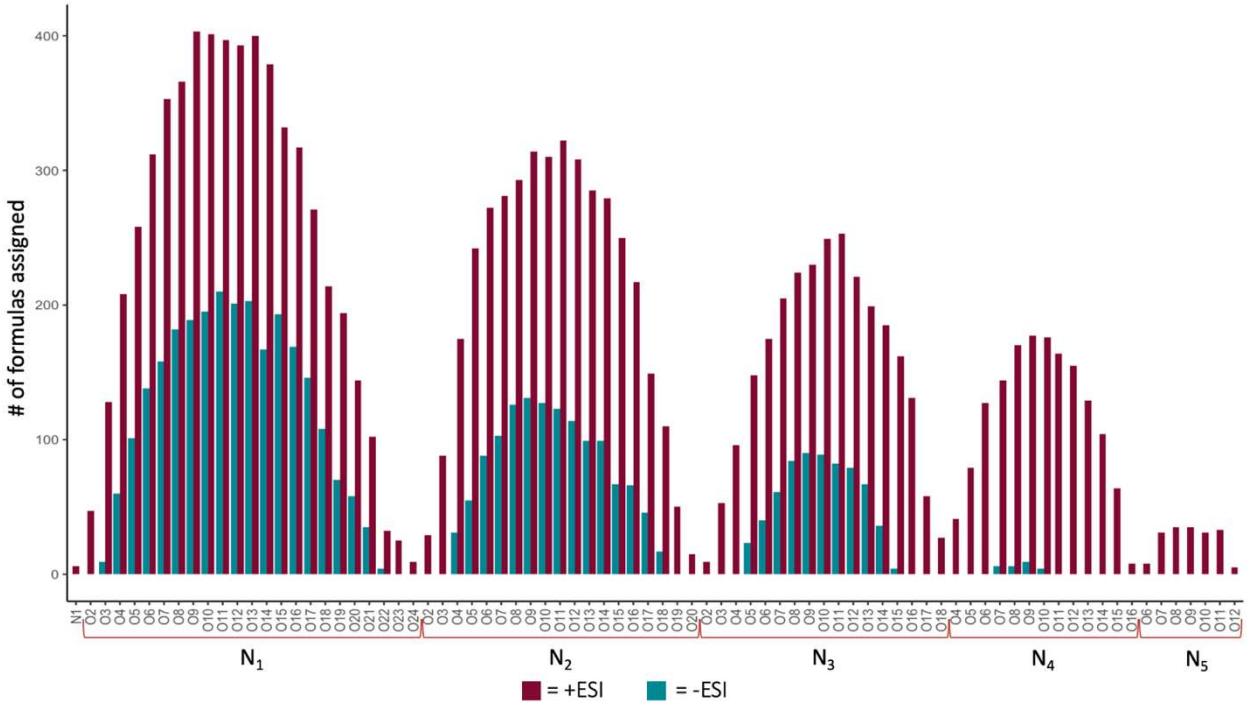

Figure B1. Bar plot of the nitrogen-containing classes from the FT-ICR MS of ESI in both positive and negative ion modes of a pyOM extract. The x-axis is organized by heteroatoms, grouped first by the number of N atoms (1 – 5) assigned to the formulas and second by the number of oxygen atoms, with each increasing from left to right. The y-axis depicts the number of formulas assigned to each heteroatom class.

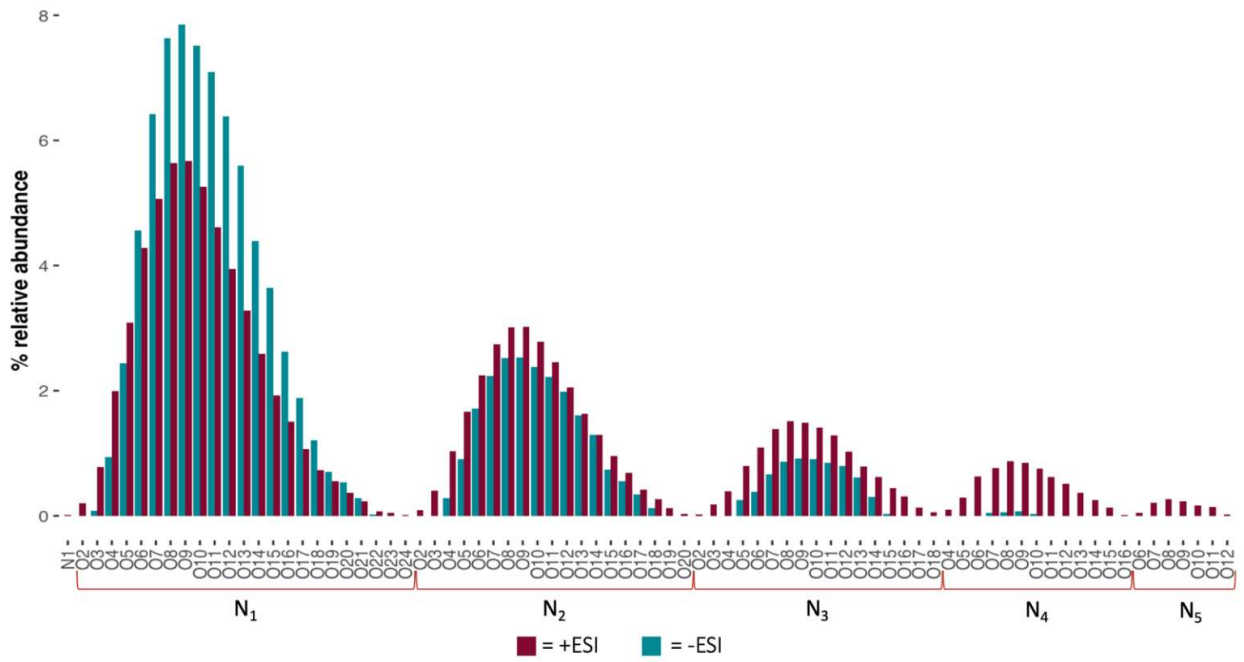

Figure B2. Bar plot of the nitrogen-containing classes from the FT-ICR MS of ESI in both positive and negative ion modes for a pyOM extract. The x-axis is organized by heteroatoms, grouped first by the number of nitrogen (1 – 5) assigned to the formulas and second by the number of oxygen, with each increasing from left to right. The y-axis depicts the percent relative abundance of each heteroatom class.

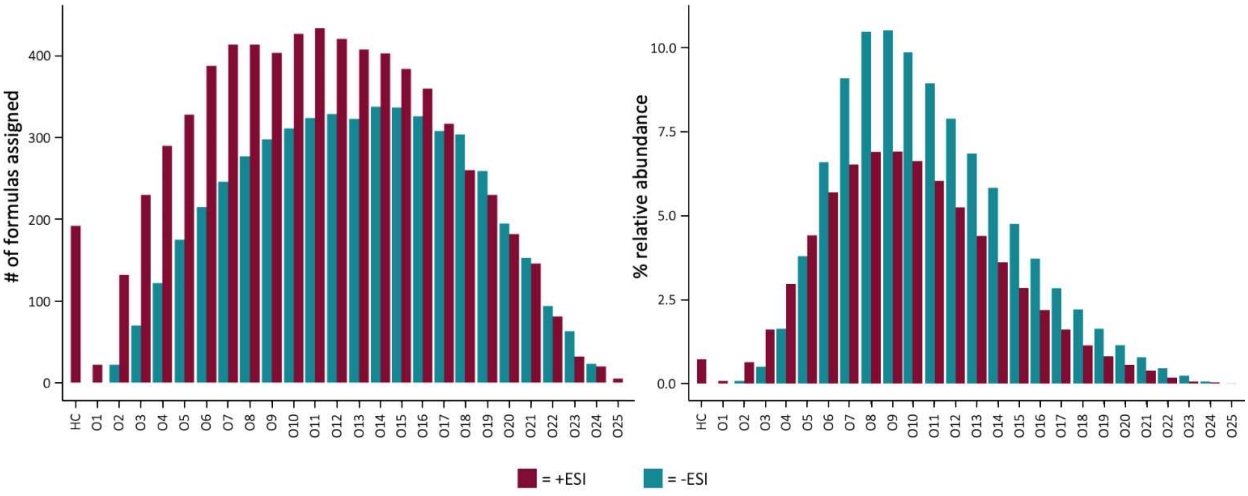

Figure B3. Number of formulas assigned (left) and percent relative abundance (right) for positive and negative ESI (red and blue, respectively).

REFERENCES

(1) Wade Jr., L. G. *Organic Chemistry*, 8th Edition.; Pearson, 2012.

APPENDIX C: SUPPLEMENTARY INFORMATION FOR CHAPTER 3

Table C1: Average dissolved organic carbon (DOC), dissolved total nitrogen (TDN), C:N, and pH of Ryan Fire and Badger Creek Fire soil extracts. Shallow and deep soils are reported separately. Asterisks (*) denote values which are statistically different from the control (* = alpha 0.1: ** = alpha 0.05).

Severity	Soil depth	Average DOC (ppm)	Average DTN (ppm)	Average C:N	pH
Control	0-5	184.83	12.8	14.4	6.80
Low	0-5	131.1	9.7	13.5	7.64**
Moderate	0-5	58.0*	6.2*	9.3	8.00**
High	0-5	42.9**	5.7**	7.6	7.69**
Control	5-10	42.3	3.4	12.5	7.34
Low	5-10	45.6	3.4	13.4	7.71
Moderate	5-10	37.7	2.6	14.1	7.43
High	5-10	39.9	2.7	14.6	7.11

Table C2: Total soil average %C and %N for burned soils. Asterisk (*) denotes values which are statistically different from the control.

Severity	Soil depth (cm)	%N	%C	C:N
Control	0-5	0.73	13.69	26.38
Low	0-5	0.85	13.39	16.50
Moderate	0-5	0.12**	2.38**	21.78
High	0-5	0.17**	4.20**	24.52
Control	5-10	0.06	2.13	39.85
Low	5-10	0.04	1.94	56.99
Moderate	5-10	0.03	1.56	69.12
High	5-10	0.01	1.08	86.98

Table C3: Selected samples for FT-ICR MS, NMR, and Microtox analyses. Transect selected corresponds with site "1" in Figure B1. All soils were collected from the Ryan fire burn scar.

Bag #	**89**	**101**	**102**	**113**	**125**	**126**
Burn type	High	Moderate	Moderate	Low	Control	Control
Soil depth (cm)	0-5	0-5	5-10	0-5	0-5	5-10

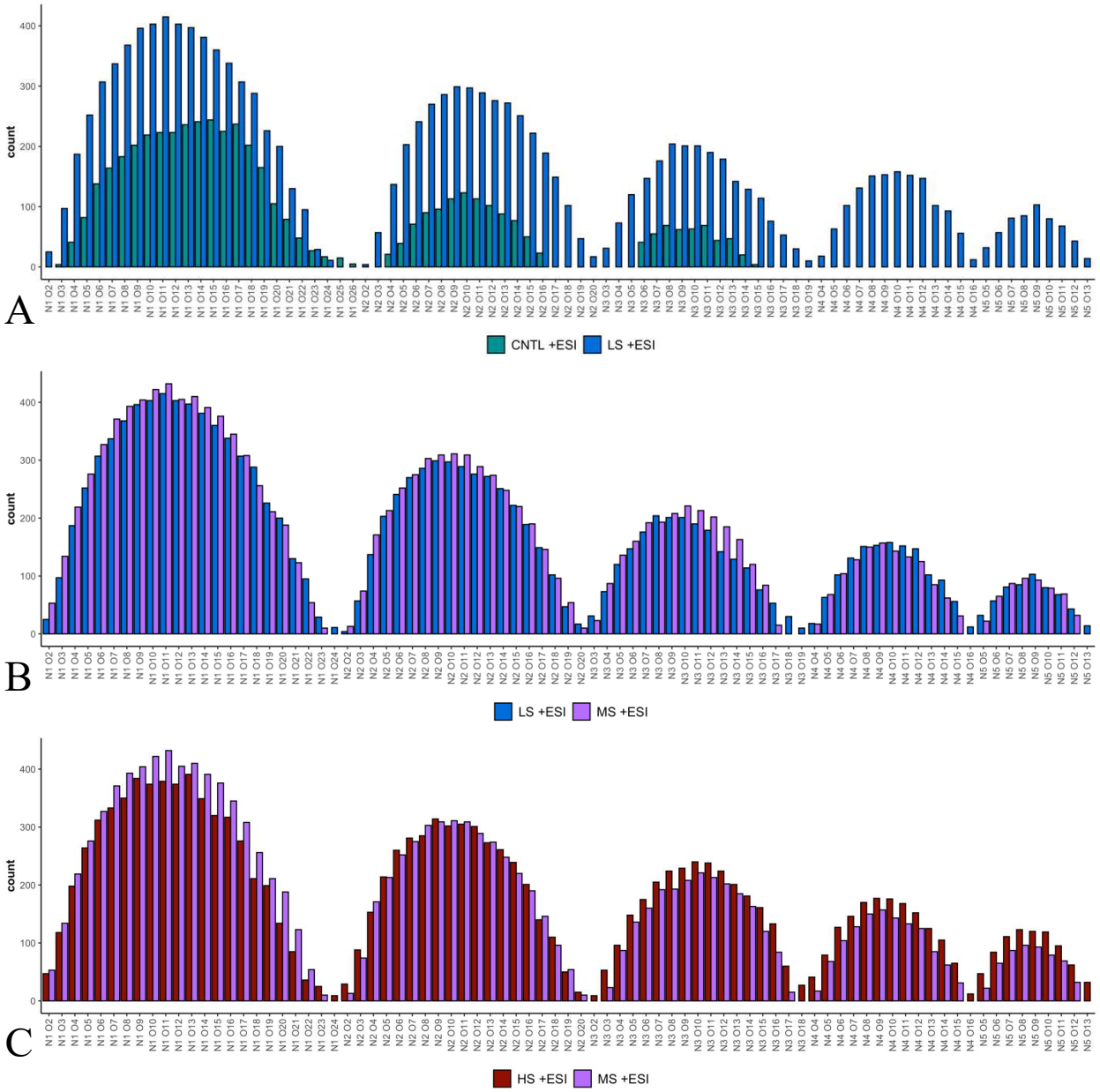

Figure C1: Bar plot of the nitrogen-containing classes from the +ESI FT-ICR MS extracts of control and low (A), low and moderate (B), and moderate and high severity (C) surface 0-5 cm soils. The x-axis is organized by heteroatoms, grouped first by the number of N atoms (1-5) and second by the number of oxygen atoms, increasing from left to right. The y-axis depicts the number of formulas assigned to each heteroatom class.

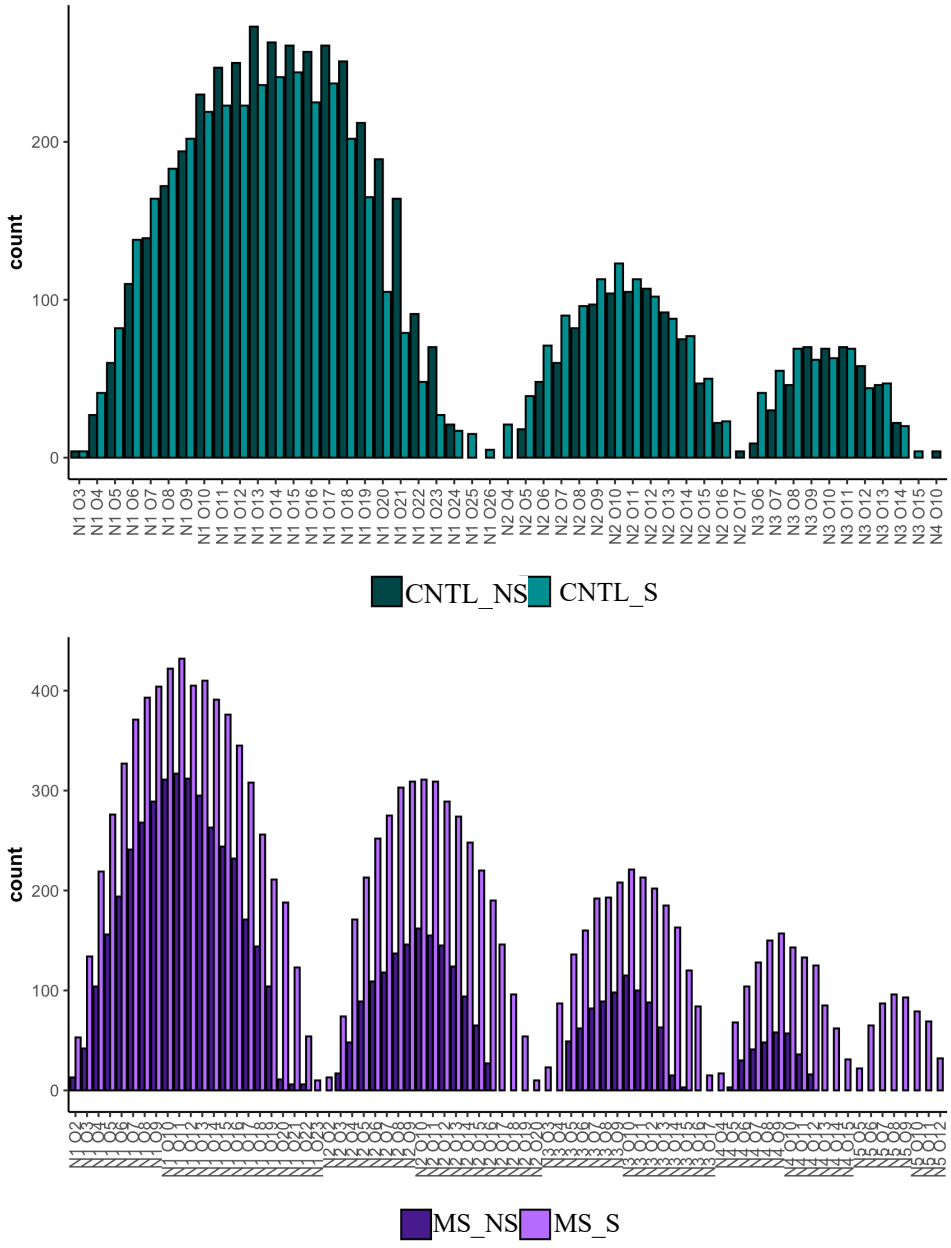

Figure C2: Bar plot of the nitrogen-containing classes from the +ESI FT-ICR MS extracts of control 0-5 and 5-15 cm (top) and moderate severity 0-5 and 5-10 cm (bottom) soils. The x-axis is organized by heteroatoms, grouped first by the number of N atoms (1-5) and second by the number of oxygen atoms, increasing from left to right. The y-axis depicts the number of formulas assigned to each heteroatom class. NS = near surface, S = surface.

APPENDIX D: SUPPLEMENTARY INFORMATION FOR CHAPTER 4

Table D1: Results of F test and student's t test calculated to determine significance between sample means of DOC, DTN, %DON, and C:N.[1] All calculations at 95% confidence interval. Results of each test highlighted in blue.

Variables	**F test**	**Upstream**	**Beaver Complex 1**	**Downstream**	**Beaver Pond 4**
DOC (ppm)	$F_{calculated}$	1.9	1.9	1.5	1.9
	F Critical one-tail	6.4	6.4	6.4	6.4
	Result	Equal	Equal	Equal	Equal
DTN (ppm)	$F_{calculated}$	1.9	2.8	2.3	1.8
	F Critical one-tail	6.4	6.4	6.4	6.4
	Result	Equal	Equal	Equal	Equal
%DON	$F_{calculated}$	2.5	3.5	3.1	7.1
	F Critical one-tail	6.4	6.4	6.4	6.4
	Result	Equal	Equal	Equal	Unequal
C:N	$F_{calculated}$	4.1	36	12	10.
	F Critical one-tail	6.4	6.4	6.4	6.4
	Result	Equal	Unequal	Unequal	Unequal
Variables	**T test**	**Upstream**	**Beaver Complex 1**	**Downstream**	**Beaver Pond 4**
DOC (ppm)	t Stat	0.60	1.1	1.7	2.2
	t Critical two-tail	2.3	2.3	2.3	2.3
	Result	Not significant	Not significant	Not significant	Not significant
DTN (ppm)	t Stat	1.0	3.8	4.7	4.4
	t Critical two-tail	2.3	2.3	2.3	2.3
	Result	Not significant	Significant	Significant	Significant
%DON	T Stat	0.68	1.1	1.3	1.5
	t Critical two-tail	2.3	2.3	2.3	2.3
	Result	Not significant	Not significant	Not significant	Not significant
	t Stat	1.1	1.6	1.3	1.0

C:N	t Critical two-tail	2.3	2.8	2.8	2.8
	Result	Not significant	Not significant	Not significant	Not significant

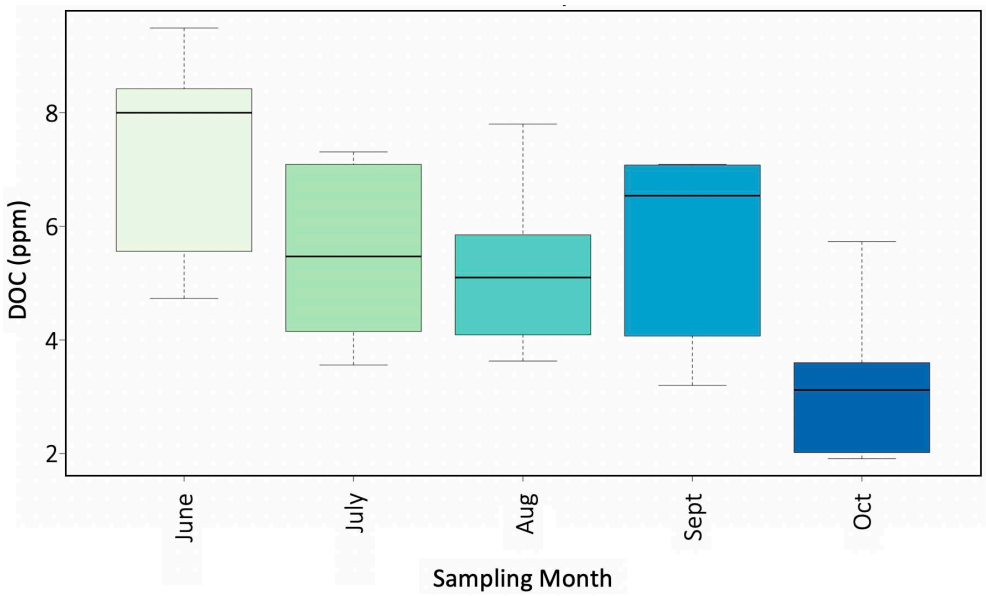

Figure D1: Monthly dissolved organic carbon (DOC) concentrations through the Ryan fire watershed. Each box plot displays the minimum, first quartile, median, third quartile, and maximum values for the dataset, consisting of data from five months of sampling one-year post-fire.

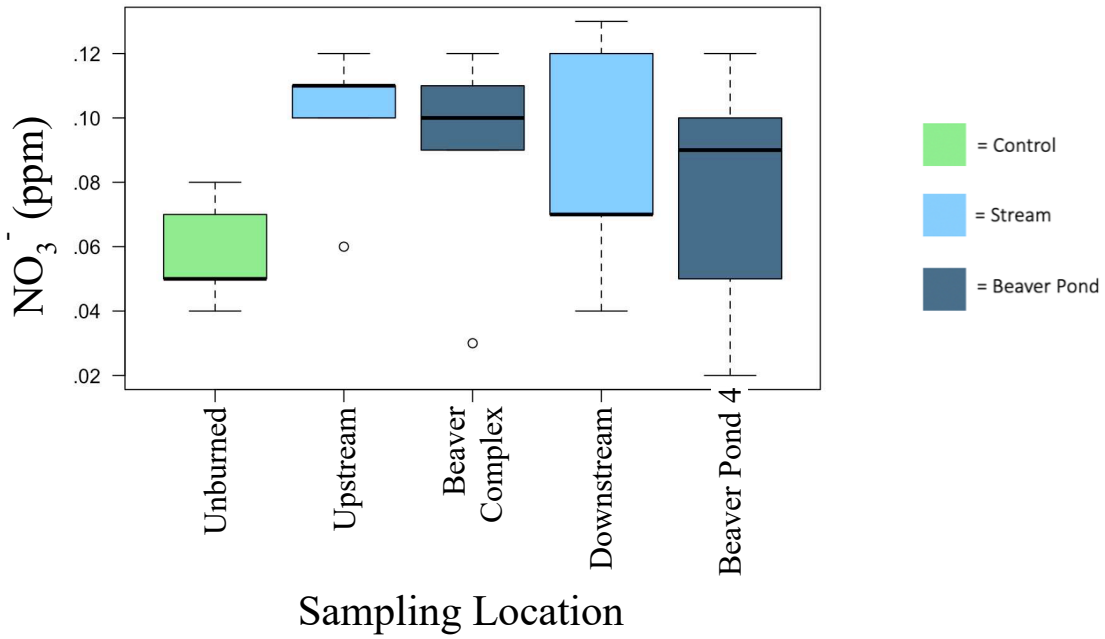

Figure D2: Nitrate (NO_3^-) concentrations through the Ryan fire watershed. Location is plotted on x-axis going from upstream to downstream (left to right) and concentration is plotted on the y-axis. Each box plot displays the minimum, first quartile, median, third quartile, and maximum values for the dataset, consisting of data from five months of sampling one-year post-fire.

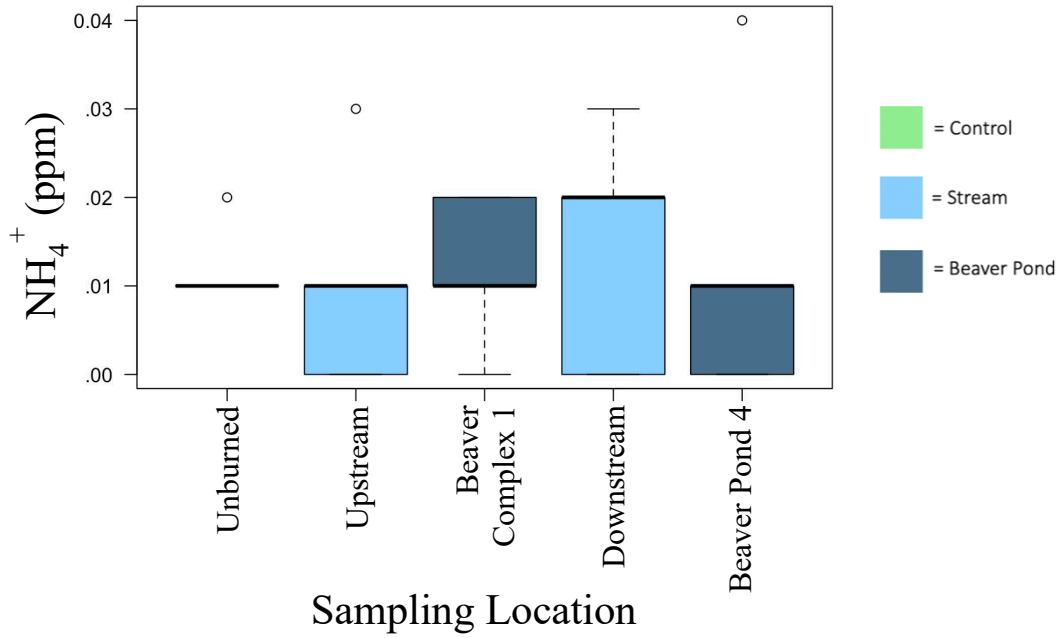

Figure D3: Ammonium (NH_4^+) concentrations through the Ryan fire watershed. Location is plotted on x-axis going from upstream to downstream (left to right) and concentration is plotted on the y-axis. Each box plot displays the minimum, first quartile, median, third quartile, and maximum values for the dataset, consisting of data from five months of sampling one-year post-fire.

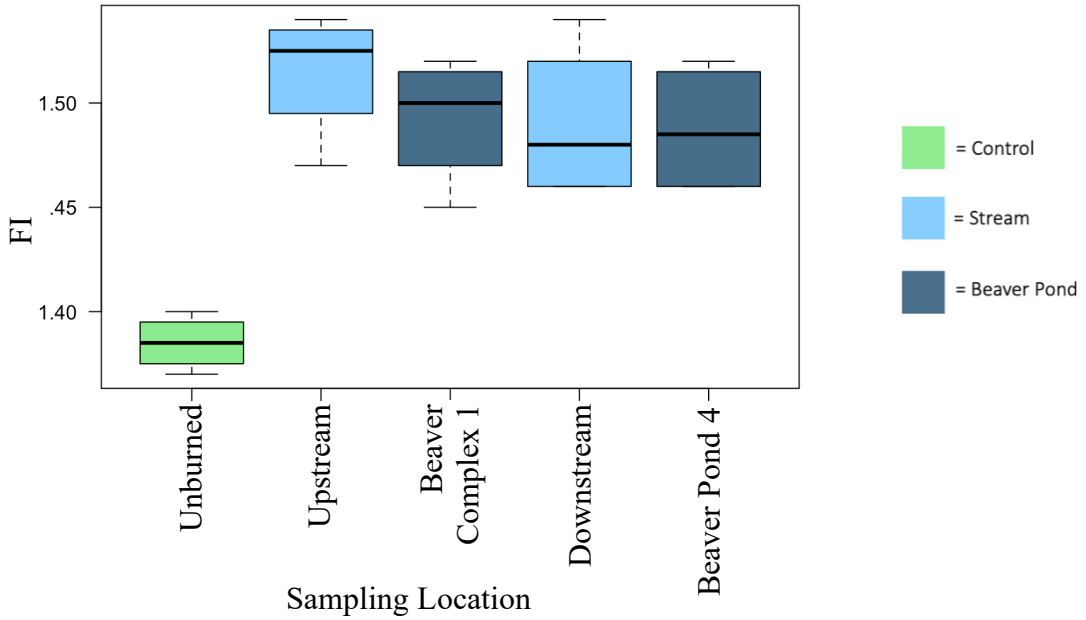

Figure D4: Fluorescence index[2] through the Ryan fire watershed. Location is plotted on x-axis going from upstream to downstream (left to right) and concentration is plotted on the y-axis. Each box plot displays the minimum, first quartile, median, third quartile, and maximum values for the dataset, consisting of data from five months of sampling one-year post-fire.

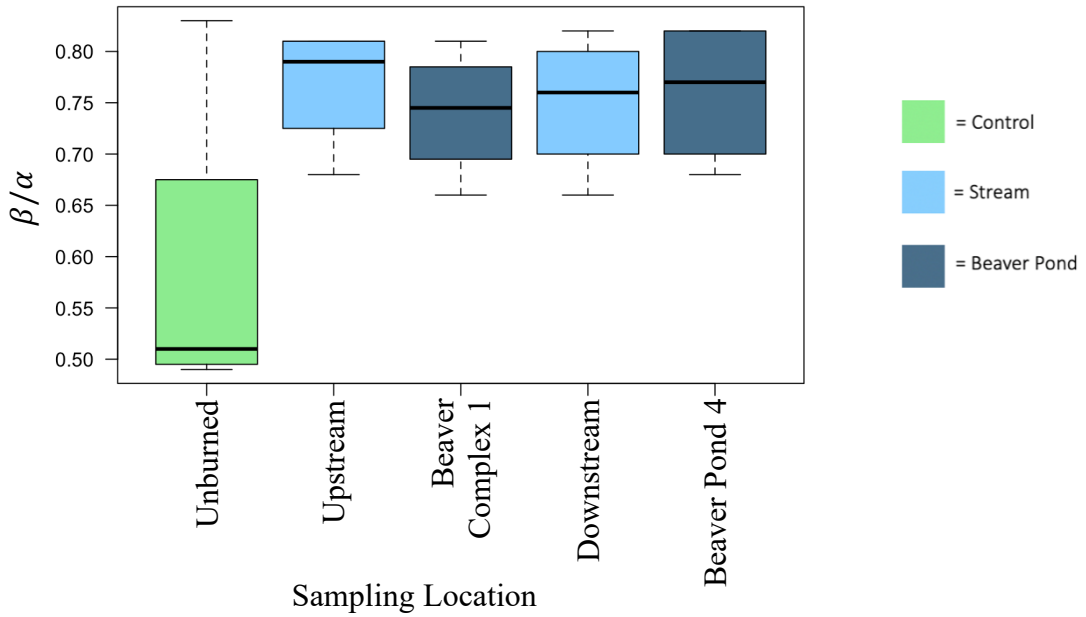

Figure D5: Freshness index[3] through the Ryan Fire watershed. Location is plotted on x-axis going from upstream to downstream (left to right) and concentration is plotted on the y-axis. Each box plot displays the minimum, first quartile, median, third quartile, and maximum values for the dataset, consisting of data from five months of sampling one-year post-fire.

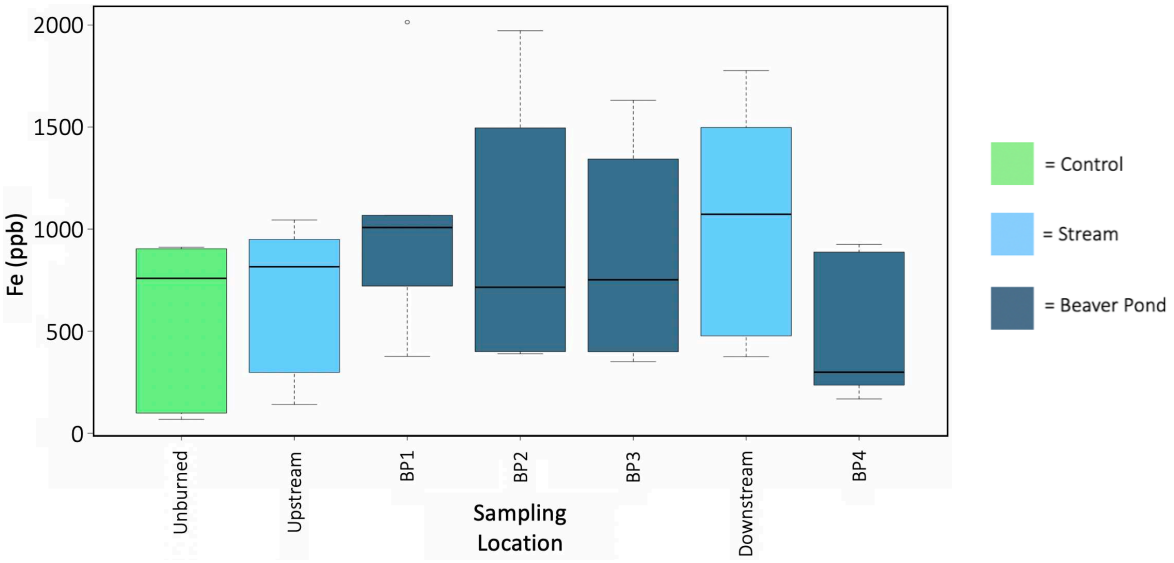

Figure D6: Iron (Fe) concentrations through the Ryan Fire watershed. Location is plotted on x-axis going from upstream to downstream (left to right) and concentration is plotted on the y-axis. Each box plot displays the minimum, first quartile, median, third quartile, and maximum values for the dataset, consisting of data from five months of sampling one-year post-fire.

REFERENCES

(1) Harris, D. C. *Exploring Chemical Analysis*, Fifth Edition.; Fiorillo, J., Murphy, B., Hadler, G. L., Simpson, J., Szczepanski, T., Eds.; W.H. Freeman and Company: New York, 2013.
(2) McKnight, D. M.; Boyer, E. W.; Westerhoff, P. K.; Doran, P. T.; Kulbe, T.; Andersen, D. T. Spectrofluorometric Characterization of Dissolved Organic Matter for Indication of Precursor Organic Material and Aromaticity. *Limnol Oceanogr* **2001**, *46* (1), 38–48. https://doi.org/10.4319/lo.2001.46.1.0038.
(3) Parlanti, E.; Woè Rz, K.; Geo€roy, L.; Lamotte, M. Dissolved Organic Matter Fluorescence Spectroscopy as a Tool to Estimate Biological Activity in a Coastal Zone Submitted to Anthropogenic Inputs. *Org Geochem* **2000**, 1765–1781. https://doi.org/10.1016/S0146-6380(00)00124-8.

APPENDIX E: CO-AUTHOR CONTRIBUTIONS TO PER- AND POLYFLUOROALKYL SUBSTANCES (PFASS) PAPER

Reprinted from Young, R. B.; Pica, N. E.; Sharifan, H.; Chen, H.; Roth, H. K.; Blakney, G. T.; Borch, T.; Higgins, C. P.; Kornuc, J. J.; McKenna, A. M.; Blotevogel, J. PFAS Analysis with Ultrahigh Resolution 21T FT-ICR MS: Suspect and Nontargeted Screening with Unrivaled Mass Resolving Power and Accuracy. *Environmental Science & Technology*. **2022**, 56 (4), 2455–2465.

According to CRediT criteria, my co-author contributions to this work included data curation and writing/reviewing/editing.

Environmental Science & Technology

pubs.acs.org/est

Article

PFAS Analysis with Ultrahigh Resolution 21T FT-ICR MS: Suspect and Nontargeted Screening with Unrivaled Mass Resolving Power and Accuracy

Robert B. Young,[#] Nasim E. Pica,[#] Hamidreza Sharifan, Huan Chen, Holly K. Roth, Greg T. Blakney, Thomas Borch, Christopher P. Higgins, John J. Kornuc, Amy M. McKenna, and Jens Blotevogel*

Cite This: *Environ. Sci. Technol.* 2022, 56, 2455−2465

Read Online

ACCESS | Metrics & More | Article Recommendations | Supporting Information

ABSTRACT: Per- and polyfluoroalkyl substances (PFASs) are a large family of thousands of chemicals, many of which have been identified using nontargeted time-of-flight and Orbitrap mass spectrometry methods. Comprehensive characterization of complex PFAS mixtures is critical to assess their environmental transport, transformation, exposure, and uptake. Because 21 tesla (T) Fourier-transform ion cyclotron resonance mass spectrometry (FT-ICR MS) offers the highest available mass resolving power and sub-ppm mass errors across a wide molecular weight range, we developed a nontargeted 21 T FT-ICR MS method to screen for PFASs in an aqueous film-forming foam (AFFF) using suspect screening, a targeted formula database (C, H, Cl, F, N, O, P, S; ≤865 Da), isotopologues, and Kendrick-analogous mass difference networks (KAMDNs). False-positive PFAS identifications in a natural organic matter (NOM) sample, which served as the negative control, suggested that a minimum length of 3 should be imposed when annotating CF_2-homologous series with positive mass defects. We putatively identified 163 known PFASs during suspect screening, as well as 134 novel PFASs during nontargeted screening, including a suspected polyethoxylated perfluoroalkane sulfonamide series. This study shows that 21 T FT-ICR MS analysis can provide unique insights into complex PFAS composition and expand our understanding of PFAS chemistries in impacted matrices.

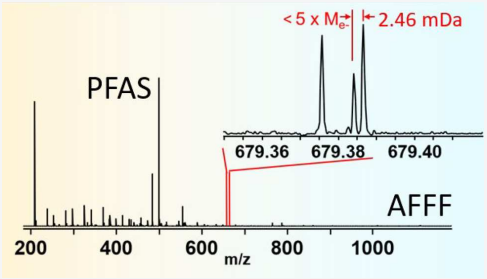

KEYWORDS: *perfluoroalkyl, polyfluoroalkyl, AFFF, ion cyclotron resonance, mass spectrometry, Kendrick mass defect, KMD, network analysis*

INTRODUCTION

Per- and polyfluoroalkyl substances (PFASs) are a complex chemical family comprising thousands of individual species. Because of highly valued water-, oil-, and heat-resistant properties, PFASs have been used in an endless number of industrial applications and consumer products.[1,2] The pervasive use of PFASs has led to their widespread environmental release from many sources such as manufacturing, wastewater treatment plants, landfills, and the application of aqueous film-forming foams (AFFFs) for firefighting.[3−9]

Currently, targeted quantitative mass spectrometry methods for PFAS regulatory compliance are limited by reference standard availability to dozens of PFASs out of thousands possibly present. These methods, while valuable, require an *a priori* determination of what to target and quantify, which is sensible for regulatory compliance but unsuitable for comprehensive sample characterization. A more holistic approach to PFAS speciation in AFFFs, natural waters, and other complex mixtures is needed to more thoroughly assess environmental transport and transformation, source attribution, additive or synergistic health effects, and other issues associated with PFAS contamination.[10−14] Consequently, many previous and ongoing research efforts have employed nontargeted analytical techniques using high-resolution time-of-flight (TOF), Orbitrap, and ion mobility mass spectrometers to discover novel PFASs.[4,10,15−20]

Nontargeted techniques are facilitated by accurate mass measurements, which can be used to screen detected ions against lists of known contaminants.[21,22] Accurate mass measurements from high-resolution mass spectrometry (HRMS) can be combined with MS/MS spectra collected in the same analysis using data-dependent or data-independent fragmentation techniques[23−25] or used to generate suspects for

Received: November 29, 2021
Revised: January 17, 2022
Accepted: January 18, 2022
Published: January 31, 2022

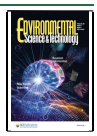

https://doi.org/10.1021/acs.est.1c08143
Environ. Sci. Technol. 2022, 56, 2455−2465

subsequent, targeted analyses. The latter is particularly helpful for detecting low-abundance ions in complex mixtures, when data-dependent acquisitions may not be triggered and data-independent acquisitions may struggle to collect unconvoluted MS/MS spectra.

Accurate mass measurements can also be used to assign molecular formulas to detected ions.[26] Elemental compositions do not distinguish among structural isomers (e.g., branched versus linear PFASs),[27,28] but they are sufficient to identify highly fluorinated species when screening for known or novel PFAS classes.[29] Molecular formula assignment poses its own challenges because, within the analytical error window of the measured mass, the number of potential formula assignments increases dramatically with molecular weight and the number of assignable elements.[22,30,31] Isotopologues (e.g., the presence or absence of a ^{34}S or ^{37}Cl isotope) help to constrain the number of possible elemental compositions,[32] but the isotopologues of low-abundance ions can be difficult to detect above the signal-to-noise threshold. Fortunately, PFASs often occur in homologous series, where the series members differ from one another by a characteristic repeating unit such as a difluoromethylene group ($-CF_2-$). In this case, isotopologues can help to establish unequivocal formula assignments for the more abundant homologues, and their formulas can help to identify low-abundance ions from the same homologous series.

In recent years, Fourier-transform ion cyclotron resonance mass spectrometry (FT-ICR MS)[33] has become the method of choice for analyzing complex hydrocarbon and natural organic matter mixtures[34] because of its unsurpassed mass resolving power, mass accuracy, and high dynamic range,[35] and these metrics improve with magnetic field strength.[33] These features also make FT-ICR MS a powerful mass analyzer to screen for PFASs in AFFF, environmental samples, and other complex matrices. Because direct-infusion FT-ICR MS does not isolate structural isomers, their signals combine to increase the signal-to-noise ratios of the isomers and their isotopologues.[36] However, the associated isotope ratio tolerances do need to account for biases in the relative abundances of ions from closely spaced cyclotron frequencies.[30] D'Agostino and Mabury previously applied FT-ICR MS to PFASs and demonstrated that a 9.4 T FT-ICR MS could resolve two mass spectral peaks in AFFF samples that differed by 0.059 Da when the same peaks could not be resolved with a TOF mass spectrometer.[10] Once a list of PFAS suspects has been identified, subsequent, targeted analyses can be conducted using liquid chromatography (LC) and MS/MS fragmentation detected by FT-ICR MS[37,38] or another mass analyzer to confirm their molecular structures.

Kendrick mass defect (KMD) analysis is commonly used to group and assign formulas to homologous series in petroleum hydrocarbon and natural organic matter samples,[39,40] and has been successfully used to identify homologous PFAS series.[4,41] KMD analysis produces a mass scale that is normalized by the ratio of the characteristic repeating unit's nominal and accurate masses (e.g., CH_2: 14.0000 Da/14.01565 Da).[42] As a result, the KMD of the repeating unit is zero, and the KMDs of homologous compounds, which have identical core structures and various numbers of repeating units, are approximately identical (within the mass spectrometer's level of precision when computed with measured masses[43]). Because compounds from different homologous series can have very similar KMDs, it can be difficult to distinguish homologous series in complex samples using only KMD values. For this reason, KMDs are often combined with z^* values, which group compounds by the nominal mass of the repeating unit and allow for rapid visualization.[44,45] Table S1 contains 13 experimental m/z values with identical KMDs using CF_2 as the repeating unit and demonstrates how the z^* values separate the identical KMDs into two CF_2 series and 3 individual m/z values.

Kendrick-analogous mass difference networks (KAMDNs) extend the KMD approach by creating network graphs that connect detected ions to each other by one or more characteristic mass differences.[40,46,47] For example, in Figure 1, the black nodes (or vertices) represent known PFASs

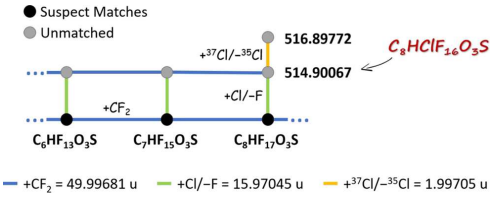

Figure 1. Conceptual diagram of a Kendrick-analogous mass difference network (KAMDN) for identified and unidentified PFASs. The legend at the bottom shows characteristic mass differences for a difluoromethylene repeating unit ($-CF_2-$), a chlorine-for-fluorine substitution ($+Cl/-F$), and a ^{37}Cl isotopologue ($+^{37}Cl/-^{35}Cl$).

identified during suspect screening, the gray nodes represent detected ions that remain unidentified, and the links (or edges) between them represent certain characteristic mass differences: a CF_2 repeating unit (blue), a chlorine-for-fluorine substitution (green),[48] and the presence of a ^{37}Cl isotopologue (orange). In this example, the relationships among the detected ions are easy to visualize, and the identified PFASs and ^{37}Cl isotopologue can be used to assign formulas to the unmatched ions (e.g., $C_8HClF_{16}O_3S$, red). KAMDNs have been successfully used to assign molecular formulas to natural organic matter (NOM) after FT-ICR MS analysis[46] but have not been employed for nontargeted PFAS screening. Recently, molecular networks have also been used to predict PFAS reaction pathways[49] via the enviPath database and prediction system.[50]

The 21 T FT-ICR MS instrument at the National High Magnetic Field Laboratory (NHMFL) in Tallahassee, Florida, achieves the highest resolving power in the world for complex mixture analysis,[34,51] with unrivaled mass accuracy (sub-ppm mass errors) for tens of thousands of peaks across a wide molecular weight range. Here, we combine the NHMFL's 21 T FT-ICR MS with suspect screening, molecular formula assignment, and KAMDNs to screen AFFF and NOM samples for PFASs (Figure 2). The NOM sample is highly complex (>27 000 detected ions), presumed to be largely free of PFAS contamination, and therefore intended to serve as a negative control for PFAS formula assignment. This study demonstrates the power of using direct-infusion FT-ICR MS to screen for PFASs and their isotopologues in complex mixtures, and especially to earmark suspected new PFAS classes or series for further analysis. This study also shows that targeted formula databases, isotopologue analysis, and KAMDNs can facilitate this process, distinguishing mere formula assignments from the most likely PFAS suspects.

https://doi.org/10.1021/acs.est.1c08143
Environ. Sci. Technol. 2022, 56, 2455−2465

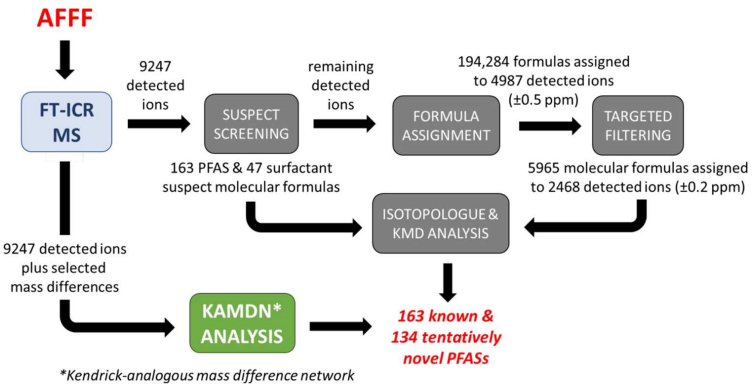

Figure 2. Summary of the data analysis workflow for this study.

MATERIALS AND METHODS

Sample Collection. The AFFF sample was a 3 M electrochemical fluorination product that had been used historically at a U.S. Department of Defense site. The container had been opened previously and could have contained impurities from other PFAS formulations.

The NOM sample contained dissolved organic matter (~8 mg C/L) from a high-elevation free-flowing channel in a mixed conifer forest located in Colorado, U.S.A. A surface grab sample was collected in an acid-washed and combusted glass amber bottle, filtered through a 0.2-μm poly(ether sulfone) filter, and stored at 4 °C. PFASs are ubiquitous in the environment[52−54] and found in many common laboratory supplies and equipment.[55] Nevertheless, the NOM sample was presumed to be free from PFAS contamination to facilitate its use as a negative control.

Sample Analysis and Spectral Processing. The AFFF sample was diluted 1:1000 in ultrahigh-purity HPLC-grade methanol (J.T. Baker, Phillipsburg, NJ) prior to 21 T FT-ICR MS analysis in negative-ion mode electrospray ionization (ESI^-). The NOM sample was prepared for the same analysis using a well-established solid-phase extraction (SPE) method.[56] Briefly, the NOM sample was acidified to pH 2 using trace metal-grade HCl (Sigma-Aldrich Chemical Co., St. Louis, MO), loaded onto an Agilent Bond Elut PPL cartridge (3 cc, 200 mg) conditioned with 15 mL of methanol and 15 mL of pH 2 water, rinsed with 15 mL of pH 2 water to remove salts, and eluted with 2 mL of HPLC-grade methanol (Sigma-Aldrich Chemical Co., St. Louis, MO).

The samples were analyzed in negative electrospray ionization mode with a custom-built hybrid linear ion trap FT-ICR mass spectrometer equipped with a 21 T superconducting solenoid magnet,[34,51] as detailed in the Supporting Information. Positive electrospray ionization mode was not used for this study, although certain species (e.g., cationic PFASs) can only be detected in positive-ion mode. Mass spectra were phase-corrected and internally calibrated with 10−15 highly abundant homologous series that span the entire molecular weight distribution (~150 calibrant peaks) based on the walking calibration method.[57,58] Peaks with signal magnitude >6 times the baseline root-mean-square (rms) noise at m/z 500 were exported as peak lists.[59]

Databases. The NIST PFAS Suspect List (https://github.com/usnistgov/NISTPFAS), which contains 3 925 unique formulas and many (if not most) PFASs identified in previous studies, was used for suspect screening. Summary statistics about the PFAS formulas, including box plots of the molecular formulas' element numbers and histograms of their mass and mass defect distributions, can be found in Figures S1 and S2.

The AFFF sample was also screened for known surfactants using the Surfactant Suspect List from the Environmental Institute (EI, SK) and the German Federal Environmental Agency (UBA, DE). The EI-UBA Surfactant Suspect List contains 817 unique formulas.

For batch formula assignment, a database of F-containing formulas was produced using the library creation scripts from UltraMassExplorer (UME).[60] $C_{2-\infty}$, $H_{0-\infty}$, Cl_{0-5}, $F_{0-\infty}$, N_{0-6}, $O_{0-\infty}$, P_{0-3}, S_{0-5}, $^{13}C_{0-2}$, $^{15}N_{0-1}$, and $^{34}S_{0-2}$ were used as elements, and the maximum mass was 865 Da. The resulting database contained 301 205 645 molecular formulas. For individual formula assignments, we used the Predator Molecular Formula Calculator (https://nationalmaglab.org/user-facilities/icr/icr-software).

Data Analysis. The data analysis (shown in Figure 2) was primarily performed in the R programming environment, as detailed in the Supporting Information.

RESULTS AND DISCUSSION

Mass Spectral Analysis. ESI^- FT-ICR MS analyses detected 9 247 peaks (>6 rms noise) in the AFFF sample and 27 229 peaks (>6 rms noise) in the NOM sample (Figures S3 and S4). Both samples span approximately the same molecular weight distribution, but <2% of the detected ions make up 75% of the total abundance in the AFFF sample and ~22% of the detected ions make up 75% of the total abundance in the NOM sample. Importantly, most of the anions detected in the AFFF sample were present at low relative abundances compared to the most abundant peak, highlighting the advantage of the 21 T system, which reports the highest dynamic range (ratio of highest to lowest peak) of any mass analyzer. The most abundant peak was putatively identified as perfluorooctanesulfonic acid (PFOS, m/z 498.93022, mass error = 0.005 ppm) based in part on its common occurrence in electrochemical fluorination AFFFs.[61,62]

https://doi.org/10.1021/acs.est.1c08143
Environ. Sci. Technol. 2022, 56, 2455−2465

Negative mass defects (exact mass − nominal mass) are useful when screening for PFASs.[63,64] Substantial F-for-H substitution causes many PFAS molecules to have low or negative mass defects because F has a negative mass defect, H has a positive mass defect, and ^{12}C has no mass defect by definition. As a result, 43.5% of the compounds in the known PFAS database have negative mass defects (Figure S2). In this study, 17.6% of the detected peaks in the AFFF sample had negative mass defects (Figure S3), compared to 4% of the detected peaks in the NOM sample (Figure S4). In the AFFF sample, the proportion of peaks with negative mass defects is far greater than that in the NOM sample but far lower than in the known PFAS database. This suggests that many of the AFFF constituents are not PFASs or they contain enough hydrocarbon substituents to yield positive mass defects. In fact, hydrocarbon surfactants are known constituents of many AFFFs.[65]

Mass Difference Statistics. Mass difference statistics[66] were computed for the AFFF and NOM samples by subtracting each detected m/z from every other detected m/z in the sample and rounding to 1 mDa (Table S2). In the AFFF sample, only one of the 10 most frequent mass differences was associated with the mass difference of CF_2 (1 527 occurrences among 9 247 detected ions). The most abundant mass difference was C_2H_4O (2 487 occurrences), and 5 more of the 10 most frequent were multiples or variations of C_2H_4O, suggesting that the AFFF sample contains polyethoxylates.

In the NOM sample, the 10 most frequent mass differences were variations of C, H, and O. However, the C_2H_4O mass difference was the 11th most frequent mass difference (16 383 occurrences among 27 229 detected ions), and the mass difference of CF_2 (49.997 Da) was detected 3 555 times, even though the NOM sample was believed to be PFAS-free. This suggests that mass differences between 49.9965 and 49.9975 Da occur among molecules in complex environmental samples because the number of detected ions per nominal mass is so large (averaging 22.6 in the NOM sample). Importantly, these results suggest a potential for false-positive PFAS and ethoxylate identifications in environmental samples.

Suspect Screening. The detected ions were screened against the combined database of known PFASs using a ±0.2 ppm mass error window (±0.15 mDa at 750 Da) based on the rms error for the 21 T FT-ICR MS. When suspects were identified, the detected ions were screened again for ^{13}C, ^{34}S, and ^{37}Cl isotopologues using a ±0.2 ppm mass error window and an isotope ratio tolerance equal to 25−200% of the theoretical ratio. This ratio was deemed appropriate for screening purposes, particularly considering the relatively low ratio of $^{34}S_1/^{32}S_1$ isotopes (0.045/1 = 4.5%) and the low expected number of S atoms (interquartile range = 0−2, Figure S1).

In the AFFF sample, 163 PFAS suspects were identified using the NIST PFAS Suspect List (Table S3), and 129 (79.1%) of them had negative mass defects. The identified PFAS suspects corresponded to 259 possible structures in the PFAS Suspect List (Table S4). In addition, 47 surfactant suspects were identified using the EI-UBA Surfactant Suspect List (Table S5), corresponding to 72 possible structures (Table S6). Only 10 PFAS suspects and 9 surfactant suspects had relative abundances >1 (Figure 3). Together, they comprised 45.3% of the detected abundance in the AFFF sample and corresponded to only 30 possible structures (Table S7). Although relative abundances are subject to differences in ionization efficiency and matrix effects, the AFFF sample's composition appears to be dominated by a small number of PFASs and surfactants. Through ion suppression, the presence of a few highly abundant peaks can limit the total number of peaks detected by direct-infusion HRMS.[67] Chromatography (online or offline) can minimize ion suppression if the analyte mixture can be chromatographically resolved. However, 9 247 ions were detected in the AFFF sample by direct-infusion FT-ICR MS in negative-ion mode using a conservative (6 rms) noise level, highlighting the dynamic range of the 21 T system.

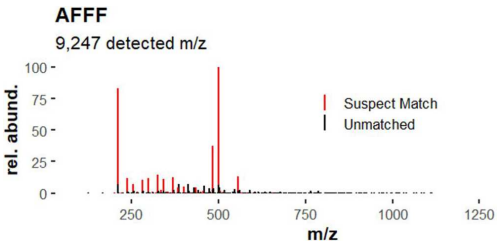

Figure 3. Mass spectrum of the AFFF sample identifying the ions (in red) that matched (±0.2 ppm) formulas in either the NIST PFAS Suspect List (163 matches) or the EI-UBA Surfactant Suspect List (47 matches).

A Kendrick mass defect analysis identified 21 homologous series with $-CF_2-$ as the repeating unit and at least 3 homologues (Table S8). The longest and most abundant homologous series had 15 consecutive members and was putatively identified as $CF_3(CF_2)_nSO_3H$, the perfluoroalkane sulfonic acid (PFSA) series that includes PFOS (Table S9). Notably, this series includes short-chain (C2 and C3) and long-chain (up to C16) PFSAs not typically reported with other MS techniques. All of the most abundant PFSAs were associated with ^{13}C (10) and ^{34}S (8) isotopologues, supporting the class's putative identification. Although calibrant-free internal calibration is difficult without *a priori* knowledge of at least some sample constituents,[68] the ppm errors of the putative PFSA series ranged from −0.167 to 0.154 ppm, demonstrating that a ± 0.2 ppm mass error window was appropriate for formula assignment in the AFFF sample.

In another example, a low-abundance chloroperfluoroalkyl sulfonic acid (Cl-PFSA) series (see Figure 1) with 6 consecutive members was putatively identified with the support of ^{13}C, ^{34}S, and ^{37}Cl isotopes from its most abundant homologues (Table S10). Their ppm errors ranged from −0.024 and 0.020 ppm across a more limited mass range.

In the NOM sample, fluorine-containing molecular formulas were assigned to 30 of the 27 229 detected ions (Table S11). However, no ^{34}S or ^{37}Cl isotopologues were detected within the specified range for any S-containing or Cl-containing suspect (25−200% of the isotopologue's expected abundance). In addition, no suspect had a negative mass defect, and the longest CF_2-homologous series contained only 2 members ($C_{17}H_{22}F_{13}N_2O_3S$ and $C_{19}H_{22}F_{17}N_2O_3S$). Moreover, 16 of the 30 PFAS suspects were assigned conflicting formulas in a separate study characterizing the NOM sample's composition (Table S11).[69] Taken together, these results suggest that the 30 PFAS suspects were false-positive identifications and that false-positive PFAS identifications in complex, NOM-containing samples can be mitigated by requiring that PFAS suspects

https://doi.org/10.1021/acs.est.1c08143
Environ. Sci. Technol. 2022, 56, 2455−2465

(1) appear in perfluoroalkyl homologous series (e.g., CF_2 or C_2F_4) with at least 3 members or (2) have negative mass defects.

Beyond Suspect Screening. After the suspect screening, the putatively identified PFASs and their isotopologues were removed from the list of detected ions, and formulas were assigned to the remaining ions using the F-containing formula database with an upper limit of 700 m/z and a ±0.5 ppm mass error window. Known PFASs occur at higher molecular weights, but the number of potential formula assignments increases dramatically with molecular weight and the number of assignable elements,[22,30,31] complicating formula assignment with the best available HRMS data. In the AFFF sample, 194 284 molecular formulas were assigned to 4 987 detected ions, for an average of 39.0 formulas per ion. No formula was assigned to any ion greater than 699.92084 m/z, and the greatest number of formulas (374) was assigned to 698.93168 m/z. These results clearly evidence the difficulty with formula assignment by accurate mass alone: a large number of prospective formulas is generated, even when the analytical mass error window is small (±0.5 ppm), the number of assignable elements is restricted (C, H, Cl, F, N, O, P, S) and the mass range is limited to ≤700 m/z.

To focus on the formulas of potential PFASs within a more limited, but appropriate, mass error window, the assigned formulas were filtered using a mass error of ±0.2 ppm, a minimum of 3 F atoms, and additional criteria based on the known PFAS database (Figures S1 and S2): $N \leq 3$, $S \leq 3$, $P \leq 1$, and $O \geq 3$ when $P = 1$, DBE < 6, and $N + O + S > 0$. After filtering, 5 965 molecular formulas were assigned to 2 468 detected ions, for an average of 2.4 formulas per m/z. The greatest number of formulas (11) was assigned to 693.00799 m/z, and 1 032 detected ions had only 1 formula assignment. These are unequivocal formula assignments, but only based on the designated elements and filtering criteria used. They still require further support from isotopologues, homologues, and other sources.

Because the AFFF sample in this study is an electrochemical fluorination product, a Kendrick mass defect analysis was performed next using CF_2 (49.99681 Da) as the repeating unit. Only 30 CF_2-homologous series contained at least 1 unique molecular formula and either (a) 3 or more consecutive homologues (e.g., 150−200−250) or (b) at least 3 members, with 2 or more consecutive homologues and no more than 1 missing homologue for each additional member (e.g., 150−200−missing−300−350). The unique molecular formulas (generally the smallest m/z values) were expected to putatively identify the series, and the requirement for 3 or more homologues was intended to reduce the possibility of false-positive identifications. There were a total of 134 detected ions in the 30 CF_2-homologous series (Table S12). After their identification, the remaining ions were screened for their ^{13}C, ^{34}S, and ^{37}Cl isotopologues using a ±0.2 ppm mass error window and the same isotope ratio tolerance that was used for suspect screening (25−200% of the theoretical ratio).

The longest CF_2-homologous series contained 8 members, and the four most abundant were associated with ^{34}S isotopologues, consistent with a perfluoroalkyl sulfonyl amino series ($C_9H_{15}F_5N_2O_4S$, Table S13). Eight more CF_2-homologous series contained at least 6 members. One 6-member series was putatively identified as a $CF_3(CF_2)_nC_4H_{11}N_2O_2S$ series (Table S14), supported with one ^{34}S and three ^{13}C isotopologues. In contrast, another 6-member series was putatively identified as a $CClF_2(CF_2)_nC_9H_{15}ClN_3$ series (Table S15), but no ^{37}Cl isotopologue was associated with any member despite sufficient abundance (e.g., 484.04114 m/z had a relative abundance of 0.448). This suggests that the second series was falsely identified and demonstrates that unequivocal formula assignments can be incorrect when the identities and numbers of assignable elements are too constrained. In fact, several CF_2 series were assigned Cl-containing formulas, but no ^{37}Cl isotopologues were detected above the study's noise levels, despite sufficient molecular ion abundances. This highlights the importance of using isotopologues (e.g., ^{34}S) to support formula assignments whenever possible. Because some elements have low abundance (e.g., ^{15}N and ^{18}O) or no isotopologues (e.g., F and P), different information may be required in those cases.

Even if no unique molecular formulas have been identified, the presence of a CF_2-homologous series with 3 or more members is still relevant when screening for PFASs. Accordingly, we also identified CF_2-homologous series with no unique molecular formulas and either (a) 3 or more consecutive homologues or (b) at least 3 members, with 2 or more consecutive homologues and no more than 1 missing homologue for each additional member (i.e., the same criteria used when at least 1 unique molecular formula was identified). Under these criteria, 567 formulas were assigned to 175 detected ions in 77 CF_2-homologous series, none of which contained >5 detected ions (Table S16). The remaining detected ions were screened for their ^{13}C, ^{34}S, and ^{37}Cl isotopologues using a ±0.2 ppm mass error window and the same isotope ratio tolerance that was used for suspect screening (25−200% of the theoretical ratio).

In one 5-member CF_2-homologous series (Table S17), the most abundant homologue had 3 conflicting formulas ($C_{11}H_{13}ClF_{12}N_2O_2S$, $C_{12}H_{20}ClF_6N_2O_4PS_2$, and $C_{12}H_{11}F_{10}N_2O_6P$) and was associated with a ^{37}Cl isotopologue. When viewing the 5-member homologous series and the Cl isotopologue together, only one conflicting formula was consistent with all homologues, and the 5-member series was putatively identified as $CClF_2(CF_2)_nC_5H_{13}N_2O_2S$.

Kendrick-Analogous Mass Difference Networks. To produce the KAMDNs, each detected m/z value was subtracted from every other detected m/z value in the sample, creating a large matrix. Next, the mass differences were screened for 11 characteristic mass differences (Table 1), based in part on reported variations in perfluoroalkane sulfonic acids (PFSAs) and perfluoroalkyl carboxylic acids (PFCAs).[4] If the mass difference matched one of the characteristic mass differences within the allowed tolerance (±0.00015 Da = ±0.2 ppm at 750 Da), then it was replaced by the characteristic mass difference. Otherwise, it was replaced by zero. Finally, a network graph was assembled using the experimental m/z values as nodes and the characteristic mass differences as weighted edges.

AFFF Networks. Initially, we created a network graph for the AFFF sample (9 247 detected ions). After removing 3 491 disconnected nodes (m/z values that were not linked to any other m/z value by at least one characteristic mass difference), the AFFF network graph contained 5 629 nodes, 7 974 edges, and 542 components (clusters or networks of connected nodes). The largest component contained 1 393 nodes, and the next largest contained 1 329 nodes, indicating that a large number of the detected m/z values are connected by the relatively small number of characteristic mass differences in

https://doi.org/10.1021/acs.est.1c08143
Environ. Sci. Technol. 2022, 56, 2455−2465

Table 1. Characteristic Mass Differences Used To Produce the Kendrick-Analogous Mass Difference Network and Their Occurrence in the AFFF and NOM Samples

mass difference	description	ΔDa	AFFF counts	NOM counts
$-CF_2-$	fluoroalkyl repeating unit	49.99681	1234	700
$-CH_2-$	methyl repeating unit	14.01565	861	15091
$-C_2H_4O-$	ethoxy repeating unit	44.02621	1882	13408
F_2	fluoroalkyl double bond	37.99681	290	706
H_2	alkyl double bond	2.01565	369	15366
+Cl/−F	chlorine-for-fluorine substitution	15.97045	144	1551
+F/−H	fluorine-for-hydrogen substitution	17.99058	488	387
$+SF_5/-CF_3$	pentafluorosulfanyl end group	57.96888	98	2448
$+^{13}C/-^{12}C$	^{13}C isotopologue	1.00335	1670	2319
$+^{34}S/-^{32}S$	^{34}S isotopologue	1.99580	813	388
$+^{37}Cl/-^{35}Cl$	^{37}Cl isotopologue	1.99705	125	2006

Table 1. Consistent with the mass-difference analysis, the ethoxy repeating unit (1 882 counts) was more common than ^{13}C isotopes (1 670 counts) and the fluoroalkyl repeating unit ($-CF_2-$, 1 234 counts) (Table 1), even after a smaller mass error window was used (0.15 vs 1 mDa).

Next, we created a subgraph for the AFFF sample containing only fluoroalkyl repeating units and produced a histogram that summarized the network components by chain length (Figure S5). The longest chain length was 15 nodes, corresponding to the PFSA series that was putatively identified during suspect screening (Table S9). Most of the CF_2-homologous series with 7 or more nodes corresponded to PFASs that were putatively identified during suspect screening, but many other series corresponded to their isotopologues and unidentified CF_2-homologous series. When the same subgraph was created with a greater allowed tolerance (±0.0015 Da = ±2 ppm at 750 Da), some of the clusters exhibited branching, where more than 1 detected ion was linked to the same position in the homologous series (Figure S6). This suggests that KAMDNs will be more difficult to interpret when using larger mass error windows but also that they will still provide useful information.

Because the number of ethoxy repeating units in the AFFF sample was large, we also created a subgraph containing only ethoxy repeating units and produced a similar histogram (Figure S7). The longest chain length was 19 nodes, but few of the C_2H_4O-homologous series with 15 or more members were putatively identified during suspect screening, creating an opportunity for future work.

NOM Networks. Next, we created a network graph for the NOM sample (27 229 detected ions) using the same characteristic mass differences. After removing 3 153 disconnected nodes, the NOM network graph contained 24 076 nodes, 54 370 edges, and 577 components. The largest component contained 22 095 nodes, and the next largest contained 69 nodes, indicating that >81% of the detected m/z values are linked by the relatively small number of characteristic mass differences. The alkyl double bond (15 366 counts), methyl repeating unit (15 091 counts), and ethoxy repeating unit (13 408 counts) were by far the most common mass differences (Table 1), consistent with prior knowledge about NOM samples.[70] Even with the smaller mass error window, the mass difference of CF_2 (49.99681 ± 0.00015 Da) occurred 700 times, although none of the associated ions had negative mass defects. In addition, only 16 components contained 3 or more members, and 8 of them contained NOM formula assignments that were unrelated to PFASs (Figure S8). As suggested earlier, molecules in complex environmental samples can produce mass differences that approximate the CF_2 mass difference simply because the number of detected ions at every nominal mass is large (averaging 22.6 in the NOM sample). Accordingly, the KAMDN analysis supports our recommendation that false-positive PFAS identifications can be mitigated by requiring that PFAS suspects (1) appear in perfluoroalkyl homologous series (e.g., CF_2 or C_2F_4) with at least 3 members or (2) have negative mass defects.

AFFF Subnetworks. Figure 4 shows perfluoroalkyl repeating units, Cl-for-F substitutions, and ^{37}Cl isotopologues.

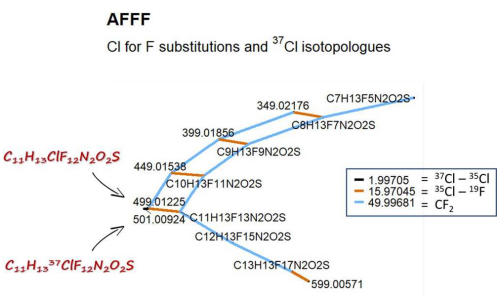

Figure 4. AFFF network containing a putatively identified CF_2-homologous series ($CF_3(CF_2)_nC_5H_{13}N_2O_2S$) and an unidentified CF_2-homologous series, with characteristic mass differences evidencing different numbers of CF_2 repeating units (Δ m/z = 49.99681), Cl-for-F substitutions (Δ m/z = 15.97045), and a ^{37}Cl isotopologue (Δ m/z = 1.99705).

One 7-member CF_2-homologous series (labeled with elemental compositions) was putatively identified during the suspect screening process as a $CF_3(CF_2)_nC_5H_{13}N_2O_2S$ series, possibly corresponding to an *N*-dimethyl ammonio propyl perfluoroalkane sulfonamide (AmPr-FASA) series. The second CF_2-homologous series corresponded to the 5-member $CClF_2(CF_2)_nC_5H_{13}N_2O_2S$ series described earlier (see Table S17). Because all 5 members of the series differ from the AmPr-FASA series by a chlorine-for-fluorine substitution (15.97045 Da) and the most abundant homologue (499.01225 m/z at a relative abundance of 0.121) is associated with a ^{37}Cl isotopologue, the same putative identification can be made with the KAMDN analysis.

Finally, Figure 5A is composed of perfluoroalkyl and ethoxy repeating units and ^{34}S isotopologues. None of the detected ions were putatively identified during suspect screening or formula assignment, in part because all but 2 of them exceeded the 700 m/z limit imposed during formula assignment. However, the component ions created a web of apparent CF_2- and C_2H_4O-homologous series where the number of perfluoroalkyl repeating units remained fixed as the number of ethoxy repeating units varied and vice versa. This suggests the presence of a polyethoxylated PFAS series, which have been previously reported, although with different composition and not in AFFF.[71−73] Several of the nodes in Figure 5A are associated with ^{34}S isotopologues, and none were associated with ^{37}Cl isotopologues. Because no P-containing formulas

https://doi.org/10.1021/acs.est.1c08143
Environ. Sci. Technol. 2022, 56, 2455−2465

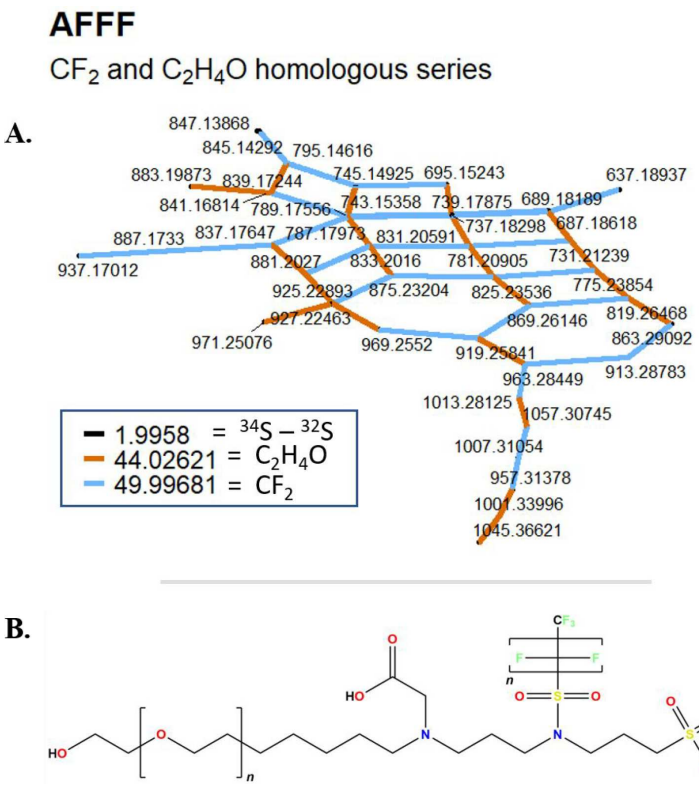

Figure 5. (A) AFFF network containing fluoroalkyl ($\Delta m/z$ = 49.99681) and ethoxy ($\Delta m/z$ = 44.02621) repeating units and ^{34}S isotopologues ($\Delta m/z$ = 1.99580) and (B) one possible structure for the resulting, putatively identified $C_{16}H_{31}F_3N_2O_8S_2(CF_2)_x(C_2H_4O)_y$ series.

were identified in the AFFF sample during suspect screening, molecular formulas were calculated for the series using $C_{0\text{-}\infty}$, $H_{0\text{-}\infty}$, $F_{0\text{-}\infty}$, $N_{0\text{-}6}$, $O_{0\text{-}\infty}$, and $S_{0\text{-}5}$ as elements and a mass error window of ±0.2 ppm. Unique formula assignments were generated for several homologues, and the series was putatively identified as $C_{16}H_{31}F_3N_2O_8S_2(CF_2)_x(C_2H_4O)_y$. Then, a suspect list was created for the putatively identified series ($C_{16}H_{31}F_3N_2O_8S_2(CF_2)_{1-10}(C_2H_4O)_{1-10}$), and a new suspect screening procedure was performed. Within the ±0.2 ppm mass error window, 25 molecular formulas in the suspect list were identified in the AFFF sample (Table S18), together with 13 ^{13}C isotopologues and 7 ^{34}S isotopologues, 6 of which corresponded to the most abundant molecular formulas in the series. Notably, several of the CF_2 series possessed >3 homologues.

Direct-infusion HRMS data cannot be used to determine molecular structures without complementary information, which may require isolation, purification, and detailed chemical analysis if the structures are novel,[29] but the $C_{16}H_{31}F_3N_2O_8S_2(CF_2)_x(C_2H_4O)_y$ series is consistent with a polyethoxylated perfluoroalkane sulfonamide structure (Figure 5B), which functionally resembles many known PFASs. This series might be a candidate for further analysis and structure elucidation, including to eliminate the possibility of adduct formation between PFASs and polyethoxylated hydrocarbon surfactants.

Putatively Identified PFASs via ESI⁻ FT-ICR MS. Tables S2, S11, and S15 contain comprehensive lists of the putatively identified PFASs in the AFFF sample, with varying degrees of support and confidence, including 163 known PFASs from suspect screening (Tables S2 and S3), 134 putative PFAS formulas in 30 CF_2-homologous series with at least 1 unique molecular formula assignment and at least 3 CF_2-homologues (Table S12), and 567 formulas assigned to 175 detected ions in 77 conflicting CF_2-homologous series with no unique molecular formula assignments and at least 3 CF_2-homologues (Table S16).

Implications. One purpose of this study was to demonstrate the power of direct-infusion FT-ICR MS when applied to HRMS suspect and nontargeted screening for PFAS in a complex AFFF mixture. HRMS PFAS screening does not rely on existing MS/MS databases or the deconvolution of LC-MS/MS spectra. Instead, it relies on the ability to detect homologues and isotopologues using only molecular ions. When leveraged with the unrivaled mass-resolving power, mass accuracy, and dynamic range achievable by 21 T FT-ICR MS, multitudes of homologues and isotopologues can be detected. Direct-infusion MS with any mass analyzer does not provide definitive structural identifications for the detected ions, but

https://doi.org/10.1021/acs.est.1c08143
Environ. Sci. Technol. 2022, 56, 2455−2465

these can be determined in subsequent analyses using accepted structural identification standards,[27,29] extending the list of known PFASs.

Another purpose of this study was to introduce targeted formula databases and KAMDNs as tools for nontargeted PFAS screening. These approaches can be used to narrow the enormous number of candidates that is generated during formula assignment, even with extremely small mass error windows and a limited number of assignable elements. Molecular formula assignments are always putative,[27,29] but they can be coupled with isotopologues, homologues, and mass defect data to improve confidence in the putative identifications (i.e., isotopologues > no isotopologues, more homologues > fewer homologues, and negative mass defects > positive mass defects). Figure S6 illustrates that KAMDNs can provide useful information when using ppm (vs sub-ppm) mass error windows, but they may be difficult to interpret in complex mixtures with many detected ions per nominal mass. Other HRMS systems with lower mass-resolving power and dynamic range (e.g., LC-TOF and LC-Orbitrap) may detect fewer homologues and isotopologues in AFFF, environmental samples, and other complex matrices, but it is also challenging to collect unconvoluted LC-MS/MS spectra in these matrices. Accordingly, the screening methods in this study provide a useful alternative approach for any HRMS system.

Additionally, KAMDNs offer a unique ability to visualize associations of homologous series by characteristic mass differences (e.g., isotopologues and F substitutions), facilitating the use of known PFASs to identify previously unknown PFASs, as well as the coordinated use of homologues and isotopologues to support putative identifications during suspect screening and molecular formula assignment.

The global concern over PFASs has spurred considerable research into PFAS mixture characterization,[41] PFAS source attribution,[13] PFAS environmental fate and transport,[9,14] PFAS exposure,[74,75] and other important issues. When employed during suspect and nontargeted PFAS screening, the methods described in this study can putatively identify known, novel, and low-abundance PFASs, providing suspects for targeted, quantitative analyses and novel PFAS suspects for structure elucidation.

■ ASSOCIATED CONTENT

Supporting Information

The Supporting Information is available free of charge at https://pubs.acs.org/doi/10.1021/acs.est.1c08143.

PFAS database analysis; ESI⁻ FT-ICR MS spectra and analyses; Kendrick-analogous mass difference network analyses; and statistical peak and KMD series analyses (PDF)

Complete lists of all putatively identified PFASs (XLSX)

■ AUTHOR INFORMATION

Corresponding Author

Jens Blotevogel − *Department of Civil and Environmental Engineering, Colorado State University, Fort Collins, Colorado 80523, United States*; Phone: +1-970-491-8880; Email: jens.blotevogel@colostate.edu; Fax: +1-970-491-8224

Authors

Robert B. Young − *Chemical Analysis & Instrumentation Laboratory, New Mexico State University, Las Cruces, New Mexico 88003, United States*; orcid.org/0000-0001-7485-0604

Nasim E. Pica − *Department of Civil and Environmental Engineering, Colorado State University, Fort Collins, Colorado 80523, United States; Weston Solutions, Lakewood, Colorado 80401, United States*; orcid.org/0000-0002-3745-8723

Hamidreza Sharifan − *Department of Civil and Environmental Engineering, Colorado State University, Fort Collins, Colorado 80523, United States; Department of Natural Science, Albany State University, Albany, Georgia 31705, United States*; orcid.org/0000-0002-6990-0635

Huan Chen − *National High Magnetic Field Laboratory, Florida State University, Tallahassee, Florida 32310, United States*; orcid.org/0000-0002-6032-6569

Holly K. Roth − *Department of Chemistry, Colorado State University, Fort Collins, Colorado 80523, United States*; orcid.org/0000-0003-2733-517X

Greg T. Blakney − *National High Magnetic Field Laboratory, Florida State University, Tallahassee, Florida 32310, United States*; orcid.org/0000-0002-4205-9866

Thomas Borch − *Department of Civil and Environmental Engineering, Colorado State University, Fort Collins, Colorado 80523, United States; Department of Chemistry and Department of Soil & Crop Sciences, Colorado State University, Fort Collins, Colorado 80523, United States*; orcid.org/0000-0002-4251-1613

Christopher P. Higgins − *Department of Civil and Environmental Engineering, Colorado School of Mines, Golden, Colorado 80401, United States*; orcid.org/0000-0001-6220-8673

John J. Kornuc − *NAVFAC EXWC, Port Hueneme, California 93041, United States*

Amy M. McKenna − *National High Magnetic Field Laboratory, Florida State University, Tallahassee, Florida 32310, United States; Department of Soil & Crop Sciences, Colorado State University, Fort Collins, Colorado 80523, United States*; orcid.org/0000-0001-7213-521X

Complete contact information is available at: https://pubs.acs.org/10.1021/acs.est.1c08143

Author Contributions

#R.B.Y. and N.E.P. contributed equally to this work. R.B.Y. wrote the manuscript with contributions from N.E.P. and J.B. All authors reviewed and edited the manuscript. J.B. and A.M.M. designed and directed the project. T.B. and H.K.R. collected and extracted the NOM sample. H.C. and A.M.M. performed the FT-ICR MS analysis and internal calibration. G.T.B. augmented the Predator Molecular Formula Calculator for PFAS analysis. N.E.P. produced the F-containing formula database with UltraMassExplorer. N.E.P. and H.S. produced the formula assignments for unknown PFASs using UltraMassExplorer and Colorado State University's high-performance computing system. R.B.Y. performed the suspect screening, network, and other data analyses and produced the tables and figures.

Notes

The authors declare no competing financial interest.

The data underlying this study are available in the published article and its online Supporting Information or are publicly available through the Open Science Framework at https://osf.io/f3m9n.

■ ACKNOWLEDGMENTS

Financial support for this research was provided by the U.S. Department of Defense's Strategic Environmental Research and Development Program (SERDP) under Project ER20-1265. Partial support was provided through SERDP Project ER-2718. The Ion Cyclotron Resonance user facility located at the National High Magnetic Field Laboratory in Tallahassee, FL (Florida State University), is supported by the National Science Foundation Division of Chemistry and Division of Materials Research through DMR 16-44779 and the State of Florida. The authors thank Paul Hatzinger (APTIM) for donating the AFFF sample and Boris P. Koch (Alfred Wegener Institute Helmholtz Centre for Polar and Marine Research) for assisting with UltraMassExplorer.

■ REFERENCES

(1) Wang, Z.; Dewitt, J. C.; Higgins, C. P.; Cousins, I. T. A Never-Ending Story of Per- and Polyfluoroalkyl Substances (PFASs)? *Environ. Sci. Technol.* **2017**, *51* (5), 2508−2518.

(2) Tokranov, A. K.; Nishizawa, N.; Amadei, C. A.; Zenobio, J. E.; Pickard, H. M.; Allen, J. G.; Vecitis, C. D.; Sunderland, E. M. How Do We Measure Poly- and Perfluoroalkyl Substances (PFASs) at the Surface of Consumer Products? *Environ. Sci. Technol. Lett.* **2019**, *6* (1), 38−43.

(3) Houtz, E. F.; Sutton, R.; Park, J. S.; Sedlak, M. Poly- and Perfluoroalkyl Substances in Wastewater: Significance of Unknown Precursors, Manufacturing Shifts, and Likely AFFF Impacts. *Water Res.* **2016**, *95*, 142−149.

(4) Barzen-Hanson, K. A.; Roberts, S. C.; Choyke, S.; Oetjen, K.; McAlees, A.; Riddell, N.; McCrindle, R.; Ferguson, P. L.; Higgins, C. P.; Field, J. A. Discovery of 40 Classes of Per- and Polyfluoroalkyl Substances in Historical Aqueous Film-Forming Foams (AFFFs) and AFFF-Impacted Groundwater. *Environ. Sci. Technol.* **2017**, *51* (4), 2047−2057.

(5) Lang, J. R.; Allred, B. M.; Field, J. A.; Levis, J. W.; Barlaz, M. A. National Estimate of Per- and Polyfluoroalkyl Substance (PFAS) Release to U.S. Municipal Landfill Leachate. *Environ. Sci. Technol.* **2017**, *51* (4), 2197−2205.

(6) Backe, W. J.; Day, T. C.; Field, J. A. Zwitterionic, Cationic, and Anionic Fluorinated Chemicals in Aqueous Film Forming Foam Formulations and Groundwater from U.S. Military Bases by Nonaqueous Large-Volume Injection HPLC-MS/MS. *Environ. Sci. Technol.* **2013**, *47* (10), 5226−5234.

(7) Washington, J. W.; Rosal, C. G.; McCord, J. P.; Strynar, M. J.; Lindstrom, A. B.; Bergman, E. L.; Goodrow, S. M.; Tadesse, H. K.; Pilant, A. N.; Washington, B. J.; Davis, M. J.; Stuart, B. G.; Jenkins, T. M. Nontargeted Mass-Spectral Detection of Chloroperfluoropolyether Carboxylates in New Jersey Soils. *Science (New York, N.Y.)* **2020**, *368* (6495), 1103−1107.

(8) Wang, Z.; Cousins, I. T.; Scheringer, M.; Buck, R. C.; Hungerbühler, K. Global Emission Inventories for C4−C14 Perfluoroalkyl Carboxylic Acid (PFCA) Homologues from 1951 to 2030, Part I: Production and Emissions from Quantifiable Sources. *Environ. Int.* **2014**, *70*, 62−75.

(9) Sharifan, H.; Bagheri, M.; Wang, D.; Burken, J. G.; Higgins, C. P.; Liang, Y.; Liu, J.; Schaefer, C. E.; Blotevogel, J. Fate and Transport of Per- and Polyfluoroalkyl Substances (PFASs) in the Vadose Zone. *Science of The Total Environment* **2021**, *771*, 145427.

(10) D'Agostino, L. A.; Mabury, S. A. Identification of Novel Fluorinated Surfactants in Aqueous Film Forming Foams and Commercial Surfactant Concentrates. *Environ. Sci. Technol.* **2014**, *48* (1), 121−129.

(11) Charbonnet, J. A.; Rodowa, A. E.; Joseph, N. T.; Guelfo, J. L.; Field, J. A.; Jones, G. D.; Higgins, C. P.; Helbling, D. E.; Houtz, E. F. Environmental Source Tracking of Per- and Polyfluoroalkyl Substances within a Forensic Context: Current and Future Techniques. *Environ. Sci. Technol.* **2021**, *55*, 7237.

(12) Nickerson, A.; Maizel, A. C.; Kulkarni, P. R.; Adamson, D. T.; Kornuc, J. J.; Higgins, C. P. Enhanced Extraction of AFFF-Associated PFASs from Source Zone Soils. *Environ. Sci. Technol.* **2020**, *54* (8), 4952−4962.

(13) Benotti, M. J.; Fernandez, L. A.; Peaslee, G. F.; Douglas, G. S.; Uhler, A. D.; Emsbo-Mattingly, S. A Forensic Approach for Distinguishing PFAS Materials. *Environmental Forensics* **2020**, *21* (3−4), 319−333.

(14) Ahrens, L.; Bundschuh, M. Fate and Effects of Poly- and Perfluoroalkyl Substances in the Aquatic Environment: A Review. *Environ. Toxicol. Chem.* **2014**, *33* (9), 1921−1929.

(15) Mejia-Avendaño, S.; Munoz, G.; Vo Duy, S.; Desrosiers, M.; Benoît, P.; Sauvé, S.; Liu, J. Novel Fluoroalkylated Surfactants in Soils Following Firefighting Foam Deployment During the Lac-Mégantic Railway Accident. *Environ. Sci. Technol.* **2017**, *51* (15), 8313−8323.

(16) Jacob, P.; Barzen-Hanson, K. A.; Helbling, D. E. Target and Nontarget Analysis of Per- and Polyfluoroalkyl Substances in Wastewater from Electronics Fabrication Facilities. *Environ. Sci. Technol.* **2021**, *55*, 2346.

(17) Wang, X.; Yu, N.; Qian, Y.; Shi, W.; Zhang, X.; Geng, J.; Yu, H.; Wei, S. Non-Target and Suspect Screening of per- and Polyfluoroalkyl Substances in Chinese Municipal Wastewater Treatment Plants. *Water Res.* **2020**, *183*, 115989.

(18) Dubocq, F.; Wang, T.; Yeung, L. W. Y.; Sjöberg, V.; Kärrman, A. Characterization of the Chemical Contents of Fluorinated and Fluorine-Free Firefighting Foams Using a Novel Workflow Combining Nontarget Screening and Total Fluorine Analysis. *Environ. Sci. Technol.* **2020**, *54*, 245.

(19) McCord, J.; Strynar, M. Identification of Per- and Polyfluoroalkyl Substances in the Cape Fear River by High Resolution Mass Spectrometry and Nontargeted Screening. *Environ. Sci. Technol.* **2019**, *53* (9), 4717−4727.

(20) Luo, Y.-S.; Aly, N. A.; McCord, J.; Strynar, M. J.; Chiu, W. A.; Dodds, J. N.; Baker, E. S.; Rusyn, I. Rapid Characterization of Emerging Per- and Polyfluoroalkyl Substances in Aqueous Film-Forming Foams Using Ion Mobility Spectrometry−Mass Spectrometry. *Environ. Sci. Technol.* **2020**, *54* (23), 15024−15034.

(21) Gago-Ferrero, P.; Krettek, A.; Fischer, S.; Wiberg, K.; Ahrens, L. Suspect Screening and Regulatory Databases: A Powerful Combination to Identify Emerging Micropollutants. *Environ. Sci. Technol.* **2018**, *52* (12), 6881−6894.

(22) Schrimpe-Rutledge, A. C.; Codreanu, S. G.; Sherrod, S. D.; McLean, J. A. Untargeted Metabolomics Strategies—Challenges and Emerging Directions. *J. Am. Soc. Mass Spectrom.* **2016**, *27* (12), 1897−1905.

(23) Nason, S. L.; Koelmel, J.; Zuverza-Mena, N.; Stanley, C.; Tamez, C.; Bowden, J. A.; Godri Pollitt, K. J. Software Comparison for Nontargeted Analysis of PFAS in AFFF-Contaminated Soil. *J. Am. Soc. Mass Spectrom.* **2021**, *32* (4), 840−846.

(24) Andra, S. S.; Austin, C.; Patel, D.; Dolios, G.; Awawda, M.; Arora, M. Trends in the Application of High-Resolution Mass Spectrometry for Human Biomonitoring: An Analytical Primer to Studying the Environmental Chemical Space of the Human Exposome. *Environ. Int.* **2017**, *100*, 32−61.

(25) Koelmel, J. P.; Paige, M. K.; Aristizabal-Henao, J. J.; Robey, N. M.; Nason, S. L.; Stelben, P. J.; Li, Y.; Kroeger, N. M.; Napolitano, M. P.; Savvaides, T.; Vasiliou, V.; Rostkowski, P.; Garrett, T. J.; Lin, E.; Deigl, C.; Jobst, K.; Townsend, T. G.; Godri Pollitt, K. J.; Bowden, J. A. Toward Comprehensive Per- and Polyfluoroalkyl Substances Annotation Using FluoroMatch Software and Intelligent High-Resolution Tandem Mass Spectrometry Acquisition. *Anal. Chem.* **2020**, *92* (16), 11186−11194.

(26) Bristow, A. W. T. Accurate Mass Measurement for the Determination of Elemental Formula - A Tutorial. *Mass Spectrom. Rev.* **2006**, *25* (1), 99−111.
(27) Schymanski, E. L.; Jeon, J.; Gulde, R.; Fenner, K.; Ruff, M.; Singer, H. P.; Hollender, J. Identifying Small Molecules via High Resolution Mass Spectrometry: Communicating Confidence. *Environ. Sci. Technol.* **2014**, *48* (4), 2097−2098.
(28) Viant, M. R.; Sommer, U. Mass Spectrometry Based Environmental Metabolomics: A Primer and Review. *Metabolomics* **2013**, *9*, 144−158.
(29) Sumner, L. W.; Amberg, A.; Barrett, D.; Beale, M. H.; Beger, R.; Daykin, C. A.; Fan, T. W. M.; Fiehn, O.; Goodacre, R.; Griffin, J. L.; Hankemeier, T.; Hardy, N.; Harnly, J.; Higashi, R.; Kopka, J.; Lane, A. N.; Lindon, J. C.; Marriott, P.; Nicholls, A. W.; Reily, M. D.; Thaden, J. J.; Viant, M. R. Proposed Minimum Reporting Standards for Chemical Analysis. *Metabolomics* **2007**, *3* (3), 211−221.
(30) Koch, B. P.; Dittmar, T.; Witt, M.; Kattner, G. Fundamentals of Molecular Formula Assignment to Ultrahigh Resolution Mass Data of Natural Organic Matter. *Anal. Chem.* **2007**, *79* (4), 1758−1763.
(31) Kind, T.; Fiehn, O. Metabolomic Database Annotations via Query of Elemental Compositions: Mass Accuracy Is Insufficient Even at Less than 1 Ppm. *Bmc Bioinformatics* **2006**, *7*, 10.
(32) Kind, T.; Fiehn, O. Seven Golden Rules for Heuristic Filtering of Molecular Formulas Obtained by Accurate Mass Spectrometry. *BMC Bioinformatics* **2007**, *8*, 105.
(33) Marshall, A. G.; Hendrickson, C. L.; Jackson, G. S. Fourier Transform Ion Cyclotron Resonance Mass Spectrometry: A Primer. *Mass Spectrom. Rev.* **1998**, *17* (1), 1−35.
(34) Smith, D. F.; Podgorski, D. C.; Rodgers, R. P.; Blakney, G. T.; Hendrickson, C. L. 21 T FT-ICR Mass Spectrometer for Ultrahigh-Resolution Analysis of Complex Organic Mixtures. *Anal. Chem.* **2018**, *90*, 2041.
(35) Huang, D.; Bouza, M.; Gaul, D. A.; Leach, F. E.; Amster, I. J.; Schroeder, F. C.; Edison, A. S.; Fernández, F. M. Comparison of High-Resolution Fourier Transform Mass Spectrometry Platforms for Putative Metabolite Annotation. *Anal. Chem.* **2021**, *93*, 12374.
(36) Weber, R. J. M.; Southam, A. D.; Sommer, U.; Viant, M. R. Characterization of Isotopic Abundance Measurements in High Resolution FT-ICR and Orbitrap Mass Spectra for Improved Confidence of Metabolite Identification. *Anal. Chem.* **2011**, *83* (10), 3737−3743.
(37) Rowland, S. M.; Smith, D. F.; Blakney, G. T.; Corilo, Y. E.; Hendrickson, C. L.; Rodgers, R. P. Online Coupling of Liquid Chromatography with Fourier Transform Ion Cyclotron Resonance Mass Spectrometry at 21 T Provides Fast and Unique Insight into Crude Oil Composition. *Anal. Chem.* **2021**, *93* (41), 13749−13754.
(38) van Agthoven, M. A.; Lam, Y. P. Y.; O'Connor, P. B.; Rolando, C.; Delsuc, M.-A. Two-Dimensional Mass Spectrometry: New Perspectives for Tandem Mass Spectrometry. *Eur. Biophys. J.* **2019**, *48*, 213−229.
(39) Hughey, C. A.; Hendrickson, C. L.; Rodgers, R. P.; Marshall, A. G.; Qian, K. N. Kendrick Mass Defect Spectrum: A Compact Visual Analysis for Ultrahigh-Resolution Broadband Mass Spectra. *Anal. Chem.* **2001**, *73* (19), 4676−4681.
(40) Bahureksa, W.; Tfaily, M. M.; Boiteau, R. M.; Young, R. B.; Logan, M. N.; McKenna, A. M.; Borch, T. Soil Organic Matter Characterization by Fourier Transform Ion Cyclotron Resonance Mass Spectrometry (FTICR MS): A Critical Review of Sample Preparation, Analysis, and Data Interpretation. *Environ. Sci. Technol.* **2021**, *55* (14), 9637−9656.
(41) Xiao, F. Emerging Poly- and Perfluoroalkyl Substances in the Aquatic Environment: A Review of Current Literature. *Water Res.* **2017**, *124*, 482−495.
(42) Kendrick, E. A Mass Scale Based on CH2 = 14.0000 for High Resolution Mass Spectrometry of Organic Compounds. *Anal. Chem.* **1963**, *35* (13), 2146.
(43) Bugsel, B.; Zwiener, C. LC-MS Screening of Poly- and Perfluoroalkyl Substances in Contaminated Soil by Kendrick Mass Analysis. *Anal. Bioanal. Chem.* **2020**, *412* (20), 4797−4805.
(44) Stenson, A. C.; Marshall, A. G.; Cooper, W. T. Exact Masses and Chemical Formulas of Individual Suwannee River Fulvic Acids from Ultrahigh Resolution Electrospray Ionization Fourier Transform Ion Cyclotron Resonance Mass Spectra. *Anal. Chem.* **2003**, *75* (6), 1275−1284.
(45) Hsu, C. S.; Qian, K.; Chen, Y. C. An Innovative Approach to Data Analysis in Hydrocarbon Characterization by On-Line Liquid Chromatography-Mass Spectrometry. *Anal. Chim. Acta* **1992**, *264* (1), 79−89.
(46) Tziotis, D.; Hertkorn, N.; Schmitt-Kopplin, P. Kendrick-Analogous Network Visualisation of Ion Cyclotron Resonance Fourier Transform Mass Spectra: Improved Options for the Assignment of Elemental Compositions and the Classification of Organic Molecular Complexity. *European Journal of Mass Spectrometry* **2011**, *17* (4), 415−421.
(47) Longnecker, K.; Kujawinski, E. B. Using Network Analysis to Discern Compositional Patterns in Ultrahigh-Resolution Mass Spectrometry Data of Dissolved Organic Matter. *Rapid Commun. Mass Spectrom.* **2016**, *30* (22), 2388−2394.
(48) Myers, A. L.; Jobst, K. J.; Mabury, S. A.; Reiner, E. J. Using Mass Defect Plots as a Discovery Tool to Identify Novel Fluoropolymer Thermal Decomposition Products. *Journal of Mass Spectrometry* **2014**, *49* (4), 291−296.
(49) Getzinger, G. J.; Higgins, C. P.; Ferguson, P. L. Structure Database and *In Silico* Spectral Library for Comprehensive Suspect Screening of Per- and Polyfluoroalkyl Substances (PFASs) in Environmental Media by High-Resolution Mass Spectrometry. *Anal. Chem.* **2021**, *93* (5), 2820−2827.
(50) Tam, J. Y. C.; Lorsbach, T.; Schmidt, S.; Wicker, J. S. Holistic Evaluation of Biodegradation Pathway Prediction: Assessing Multi-Step Reactions and Intermediate Products. *J. Cheminform* **2021**, *13* (1), 63.
(51) Hendrickson, C. L.; Quinn, J. P.; Kaiser, N. K.; Smith, D. F.; Blakney, G. T.; Chen, T.; Marshall, A. G.; Weisbrod, C. R.; Beu, S. C. 21 T Fourier Transform Ion Cyclotron Resonance Mass Spectrometer: A National Resource for Ultrahigh Resolution Mass Analysis. *J. Am. Soc. Mass Spectrom.* **2015**, *26* (9), 1626−1632.
(52) Pan, Y.; Zhang, H.; Cui, Q.; Sheng, N.; Yeung, L. W. Y.; Sun, Y.; Guo, Y.; Dai, J. Worldwide Distribution of Novel Perfluoroether Carboxylic and Sulfonic Acids in Surface Water. *Environ. Sci. Technol.* **2018**, *52* (14), 7621−7629.
(53) Stock, N. L.; Furdui, V. I.; Muir, D. C. G.; Mabury, S. A. Perfluoroalkyl Contaminants in the Canadian Arctic: Evidence of Atmospheric Transport and Local Contamination. *Environ. Sci. Technol.* **2007**, *41* (10), 3529−3536.
(54) Shimizu, M. S.; Mott, R.; Potter, A.; Zhou, J.; Baumann, K.; Surratt, J. D.; Turpin, B.; Avery, G. B.; Harfmann, J.; Kieber, R. J.; Mead, R. N.; Skrabal, S. A.; Willey, J. D. Atmospheric Deposition and Annual Flux of Legacy Perfluoroalkyl Substances and Replacement Perfluoroalkyl Ether Carboxylic Acids in Wilmington, NC, USA. *Environ. Sci. Technol. Lett.* **2021**, *8* (5), 366−372.
(55) Martin, J. W.; Kannan, K.; Berger, U.; Voogt, P. D.; Field, J.; Franklin, J.; Giesy, J. P.; Harner, T.; Muir, D. C. G.; Scott, B.; Kaiser, M.; Järnberg, U.; Jones, K. C.; Mabury, S. A.; Schroeder, H.; Simcik, M.; Sottani, C.; Bavel, B. V.; Kärrman, A.; Lindström, G.; Leeuwen, S. V. Peer Reviewed: Analytical Challenges Hamper Perfluoroalkyl Research. *Environ. Sci. Technol.* **2004**, *38*, 248A−255A.
(56) Dittmar, T.; Koch, B.; Hertkorn, N.; Kattner, G. A Simple and Efficient Method for the Solid-Phase Extraction of Dissolved Organic Matter (SPE-DOM) from Seawater. *Limnology and Oceanography-Methods* **2008**, *6*, 230−235.
(57) Savory, J. J.; Kaiser, N. K.; McKenna, A. M.; Xian, F.; Blakney, G. T.; Rodgers, R. P.; Hendrickson, C. L.; Marshall, A. G. Parts-per-Billion Fourier Transform Ion Cyclotron Resonance Mass Measurement Accuracy with a "Walking" Calibration Equation. *Anal. Chem.* **2011**, *83* (5), 1732−1736.
(58) Xian, F.; Hendrickson, C. L.; Blakney, G. T.; Beu, S. C.; Marshall, A. G. Automated Broadband Phase Correction of Fourier

https://doi.org/10.1021/acs.est.1c08143
Environ. Sci. Technol. 2022, 56, 2455−2465

Transform Ion Cyclotron Resonance Mass Spectra. *Anal. Chem.* **2010**, *82* (21), 8807−8812.
(59) Corilo, Y. E. *PetroOrg*; The Florida State University: 2012.
(60) Leefmann, T.; Frickenhaus, S.; Koch, B. P. UltraMassExplorer - a Browser-Based Application for the Evaluation of High-Resolution Mass Spectrometric Data. *Rapid Commun. Mass Spectrom.* **2019**, *33* (2), 193−202.
(61) Place, B. J.; Field, J. A. Identification of Novel Fluorochemicals in Aqueous Film-Forming Foams Used by the US Military. *Environ. Sci. Technol.* **2012**, *46* (13), 7120−7127.
(62) Interstate Technology & Regulatory Council, PFAS Team. *PFAS Technical and Regulatory Guidance Document*; Interstate Technology & Regulatory Council: Washington, DC, 2020.
(63) Sleno, L. The Use of Mass Defect in Modern Mass Spectrometry. *Journal of Mass Spectrometry* **2012**, *47* (2), 226−236.
(64) Trier, X.; Granby, K.; Christensen, J. H. Tools to Discover Anionic and Nonionic Polyfluorinated Alkyl Surfactants by Liquid Chromatography Electrospray Ionisation Mass Spectrometry. *J. Chromatogr. A* **2011**, *1218* (40), 7094.
(65) García, R. A.; Chiaia-Hernández, A. C.; Lara-Martin, P. A.; Loos, M.; Hollender, J.; Oetjen, K.; Higgins, C. P.; Field, J. A. Suspect Screening of Hydrocarbon Surfactants in AFFFs and AFFF-Contaminated Groundwater by High-Resolution Mass Spectrometry. *Environ. Sci. Technol.* **2019**, *53* (14), 8068−8077.
(66) Kunenkov, E. V.; Kononikhin, A. S.; Perminova, I. V.; Hertkorn, N.; Gaspar, A.; Schmitt-Kopplin, P.; Popov, I. A.; Garmash, A. V.; Nikolaev, E. N. Total Mass Difference Statistics Algorithm: A New Approach to Identification of High-Mass Building Blocks in Electrospray Ionization Fourier Transform Ion Cyclotron Mass Spectrometry Data of Natural Organic Matter. *Anal. Chem.* **2009**, *81* (24), 10106−10115.
(67) Young, R. B.; Avneri-Katz, S.; McKenna, A.; Chen, H.; Bahureksa, W.; Polubesova, T.; Chefetz, B.; Borch, T. Composition-Dependent Sorptive Fractionation of Anthropogenic Dissolved Organic Matter by Fe(III)-Montmorillonite. *Soil Systems* **2018**, *2* (1), 14.
(68) Sleighter, R. L.; McKee, G. A.; Liu, Z.; Hatcher, P. G. Naturally Present Fatty Acids as Internal Calibrants for Fourier Transform Mass Spectra of Dissolved Organic Matter. *Limnology and Oceanography-Methods* **2008**, *6*, 246−253.
(69) Roth, H. K.; McKenna, A. M.; Nelson, A. R.; Fegel, T. S.; Young, R. B.; Rhoades, C. C.; Wilkins, M. J.; Borch, T. Impact of Beaver Ponds on Biogeochemical Cycling of Organic Carbon and Nitrogen within a Fire-Impacted Watershed. *Org. Geochem.* (in review).
(70) Kujawinski, E. B.; Behn, M. D. Automated Analysis of Electrospray Ionization Fourier Transform Ion Cyclotron Resonance Mass Spectra of Natural Organic Matter. *Anal. Chem.* **2006**, *78* (13), 4363−4373.
(71) Frömel, T.; Knepper, T. P. Fluorotelomer Ethoxylates: Sources of Highly Fluorinated Environmental Contaminants Part I: Biotransformation. *Chemosphere* **2010**, *80* (11), 1387−1392.
(72) Gremmel, C.; Frömel, T.; Knepper, T. P. HPLC−MS/MS Methods for the Determination of 52 Perfluoroalkyl and Polyfluoroalkyl Substances in Aqueous Samples. *Anal. Bioanal. Chem.* **2017**, *409* (6), 1643−1655.
(73) Herkert, N. J.; Kassotis, C. D.; Zhang, S.; Han, Y.; Pulikkal, V. F.; Sun, M.; Ferguson, P. L.; Stapleton, H. M. Characterization of Per- and Polyfluorinated Alkyl Substances Present in Commercial Anti-Fog Products and Their *In Vitro* Adipogenic Activity. *Environ. Sci. Technol.* **2022**, *56*, 1162.
(74) Kato, K.; Wong, L. Y.; Jia, L. T.; Kuklenyik, Z.; Calafat, A. M. Trends in Exposure to Polyfluoroalkyl Chemicals in the U.S. Population: 1999−2008. *Environ. Sci. Technol.* **2011**, *45* (19), 8037−8045.
(75) Andrews, D. Q.; Naidenko, O. V. Population-Wide Exposure to Per- and Polyfluoroalkyl Substances from Drinking Water in the United States. *Environ. Sci. Technol. Lett.* **2020**, *7* (12), 931−936.

https://doi.org/10.1021/acs.est.1c08143
Environ. Sci. Technol. 2022, 56, 2455−2465

APPENDIX F: CO-AUTHOR CONTRIBUTIONS TO WILDFIRE MICROBIOME PAPER

Reprinted from [paper/copyright info].

According to CRediT criteria, my co-author contributions to this work included formal analysis, methodology, and writing/reviewing/editing.

nature microbiology

ARTICLES

https://doi.org/10.1038/s41564-022-01203-y

Check for updates

OPEN

Wildfire-dependent changes in soil microbiome diversity and function

Amelia R. Nelson[1], Adrienne B. Narrowe[1,2], Charles C. Rhoades[3], Timothy S. Fegel[3], Rebecca A. Daly[1], Holly K. Roth[4], Rosalie K. Chu[5], Kaela K. Amundson[1], Robert B. Young[6], Andrei S. Steindorff[7], Stephen J. Mondo[7,8], Igor V. Grigoriev[7,9], Asaf Salamov[7], Thomas Borch[1,4,10] and Michael J. Wilkins[1]✉

Forest soil microbiomes have crucial roles in carbon storage, biogeochemical cycling and rhizosphere processes. Wildfire season length, and the frequency and size of severe fires have increased owing to climate change. Fires affect ecosystem recovery and modify soil microbiomes and microbially mediated biogeochemical processes. To study wildfire-dependent changes in soil microbiomes, we characterized functional shifts in the soil microbiota (bacteria, fungi and viruses) across burn severity gradients (low, moderate and high severity) 1 yr post fire in coniferous forests in Colorado and Wyoming, USA. We found severity-dependent increases of Actinobacteria encoding genes for heat resistance, fast growth, and pyrogenic carbon utilization that might enhance post-fire survival. We report that increased burn severity led to the loss of ectomycorrhizal fungi and less tolerant microbial taxa. Viruses remained active in post-fire soils and probably influenced carbon cycling and biogeochemistry via turnover of biomass and ecosystem-relevant auxiliary metabolic genes. Our genome-resolved analyses link post-fire soil microbial taxonomy to functions and reveal the complexity of post-fire soil microbiome activity.

Changes in climate coupled with the effects of long-term fire suppression and shifting land use patterns have increased the frequency, severity and season length of wildfires in the western United States[1–3]. In 2020 and 2021, the western United States experienced severe, record-breaking wildfires[2]. High-severity wildfires cause greater erosion[4], soil carbon (C) and nitrogen (N) losses[5], and nutrient and sediment export in stream water[6], so the increasing occurrence of severe wildfires may have important consequences for both terrestrial and aquatic ecosystems. Shifting wildfire patterns have also been linked to slow post-fire revegetation and tree seedling recruitment[7] and thus delayed watershed recovery[8] in western US forests. Although ecosystem recovery from severe wildfires is closely linked to belowground biological processes, little is known about the impact of high-severity fire on soil microbiome function in high elevation, coniferous ecosystems.

The soil microbiome regulates soil organic matter (SOM) decomposition and stabilization[9], soil nutrient dynamics[10] and rhizosphere function[11]. During wildfires, the soil microbiome can be impacted immediately by the loss of heat-sensitive taxa and thereafter by lasting changes in soil chemistry and vegetation shifts[12]. Wildfires reduce soil microbial biomass and community diversity in numerous ecosystems[13–16] and such changes probably influence and inhibit post-fire plant recovery[17].

Post-fire shifts in soil microbiome composition[14,18,19] and assembly processes[20–22] are relatively well-characterized across different ecosystems, with some studies explicitly linked with corresponding shifts in microbially mediated C and N cycling[23–26]. This work has been complemented by laboratory studies with pure cultures of pyrophilous taxa that demonstrate their ability to persist during stressful conditions[27,28] and utilize aromatic C[29–32]. Metagenomic approaches can bridge insights between field-based compositional analyses and more controlled laboratory studies. So far, two studies have applied gene-resolved metagenomic analyses to post-fire soils[23,33]. Genome-resolved metagenomic tools can link potential pyrophilous traits (for example, fast growth rate, heat resistance) to specific organisms that thrive in burned soils and support laboratory observations[34]. Furthermore, this approach enables a broader understanding of microbiome function through identification of co-occurring functional traits, potential interspecies interactions, and viral-host dynamics.

Here we bridge laboratory studies and field-based compositional investigations through a genome-resolved multi-omic approach to characterize wildfire impacts on soil microbiome function. Furthermore, the work represents a holistic understanding of the post-fire soil microbiome, including comprehensive characterization of interacting bacterial, fungal and viral communities. We studied burn severity gradients in two recent forest wildfires to characterize how fire severity influences C composition and the intimately connected soil microbiome. We hypothesized that higher-severity wildfire results in an increasingly altered soil microbiome and that taxa colonizing burned soils would encode functional traits that favour their persistence. These analyses advance the understanding of linkages between the soil microbiome and post-fire forest biogeochemistry.

[1]Department of Soil and Crop Sciences, Colorado State University, Fort Collins, CO, USA. [2]Eastern Regional Research Center, Agricultural Research Service, Wyndmoor, PA, USA. [3]Rocky Mountain Research Station, U.S. Forest Service, Fort Collins, CO, USA. [4]Department of Chemistry, Colorado State University, Fort Collins, CO, USA. [5]Environmental Molecular Sciences Laboratory, Pacific Northwest National Laboratory, Richland, WA, USA. [6]Chemical Analysis and Instrumentation Laboratory, New Mexico State University, Las Cruces, NM, USA. [7]Department of Energy Joint Genome Institute, Lawrence Berkeley National Laboratory, Berkeley, CA, USA. [8]Department of Agricultural Biology, Colorado State University, Fort Collins, CO, USA. [9]Department of Plant and Microbial Biology, University of California Berkeley, Berkeley, CA, USA. [10]Department of Civil and Environmental Engineering, Colorado State University, Fort Collins, CO, USA. ✉e-mail: Mike.Wilkins@colostate.edu

Results

Fire decreases soil microbiome diversity and shifts composition. Near surface soils (0–5 cm depth) were collected approximately 1 yr post fire from four burn severity gradient transects (control, low, moderate and high burn severity) at two wildfires that occurred in 2018 along the Colorado-Wyoming border (Extended Data Fig. 1). Bacterial and fungal communities were profiled using marker gene analyses, while a subset of 12 samples (low or high severity-impacted Ryan fire soils) were additionally interrogated with metagenomic and metatranscriptomic sequencing. Bacterial and fungal communities were significantly different between burned ($n=144$) and unburned ($n=32$) soils (bacterial analyses of similarity (ANOSIM) $R=0.57$, $P<0.05$; fungal ANOSIM $R=0.72$, $P<0.05$) (Supplementary Fig. 2).

While shifts in community composition with burn were observed in both surface (0–5 cm) and deep (5–10 cm) soils (Supplementary Note 3 and Extended Data Fig. 2), surface soils were impacted to a greater extent. Microbial diversity generally decreased with increasing severity in surface soils, although differences between moderate and high severity were statistically indistinct (Fig. 1). Similarly, as fungal and bacterial diversity decreased with burn severity, beta dispersion ('distance to centroid') calculations revealed increasingly similar bacterial communities (Supplementary Fig. 3) with less complex community structures (via WGCNA; Supplementary Note 2, Supplementary Table 3). These shifts resulted in significant dissimilarity between microbial communities in surface soils impacted by either low ($n=24$) or high ($n=24$) severity wildfire (bacterial ANOSIM $R=0.15$, $P<0.05$; fungal ANOSIM $R=0.25$, $P<0.05$). In contrast, deep soils displayed an opposite effect, with increasing beta dispersion after wildfire signifying greater bacterial community dissimilarity (Supplementary Fig. 3). Stochastic community shifts in deep soils may follow a wildfire, potentially due to spatially heterogeneous changes in soil chemistry and nutrient availability. Combined amplicon sequencing data analyses highlight the susceptibility of surface soils to wildfire, resulting in less diverse and inter-connected microbial communities. In contrast, the microbiome in deep soil displays a more muted response to wildfire, potentially due to insulation from soil heating (dependent on soil moisture).

A comprehensive dataset from fire-impacted soils. While myriad studies have reported changes in microbial community composition following a wildfire[14,18,35], the functional implications of these shifts are difficult to infer from compositional data. We used genome-resolved metagenomics to generate a comprehensive, publicly accessible catalogue of post-fire bacterial, fungal and viral genomes from coniferous forest soils. From metagenomic sequencing of burned (low and high severity) soils, we reconstructed 637 medium- and high-quality bacterial metagenome-assembled genomes (MAGs) (Extended Data Fig. 3) that represent taxa shown to increase following a wildfire in complementary 16S ribosomal RNA gene sequencing data (for example, *Blastococcus*, *Arthrobacter*; Supplementary Note 1). The dataset spans 21 phyla and encompasses 237 MAGs from taxa within the Actinobacteria, 167 from the Proteobacteria, 62 from the Bacteroidota and 52 from the Patescibacteria. Furthermore, we recovered 2 fungal genomes from the Ascomycota, affiliated with *Leotiomycetes* and *Coniochaeata lignaria*. We additionally recovered 2,399 DNA and 91 RNA viral populations (vMAGs) (Supplementary Data 5).

Actinobacteria respond strongly to high-severity wildfire. On the basis of consistent high relative abundances across surface soils impacted by high-severity wildfire ('High S') that mirrored 16S rRNA gene data (Supplementary Note 1), 40 MAGs were selected for further genomic analyses. Combined, these MAGs accounted for an average relative abundance of ~60% in High S samples and ~34% in low severity-impacted surface soils ('Low S') and collectively represent the most abundant MAGs responding to altered soil conditions 1 yr post wildfire. Metatranscriptomic read mapping revealed activity of these MAGs in High S samples, accounting for an average of ~50% of total gene expression and 90% of differentially expressed genes in High S vs Low S soils (Supplementary Data 4). These MAGs were also active in Low S samples, albeit to a lesser extent (accounting for ~30% of gene expression). Most of these MAGs (28 of 40) were affiliated with the Actinobacteria phyla, specifically the genera *Arthrobacter* (8 MAGs), *Blastococcus* (5) and *SCTD01* (5) (Supplementary Data 2). Ten of these MAGs (Supplementary Data 2, Sheet D), including 9 Actinobacteria, were significantly enriched in High S relative to Low S samples (pairwise *t*-test, $P<0.05$; Extended Data Fig. 4), indicating a positive response 1 yr following high-severity wildfire. In general, Actinobacteria dominated the microbiome in burned surficial soils; all 237 Actinobacteria MAGs were responsible for ~56% of gene expression in High S samples and ~47% in Low S samples. Dominant MAGs in high severity-impacted deep samples ('High D') were more diverse (representing Actinobacteria, Eremiobacterota, Acidobacteriota and Proteobacteria), reflecting the probably more heterogeneous impact of wildfire on deeper soils (Supplementary Note 2).

The heat produced during wildfire exerts a pulse disturbance on soils and as such, the relative abundance of two groups of thermal resistance genes—sporulation and heat shock—increased significantly (Welch's *t*-test, $P<0.05$) from Low S to High S soils (42.8% and 20.4% increase, respectively). Nearly all the aforementioned MAGs (38/40) encoded sporulation genes, indicating that spore formation is probably a trait supporting survival and post-fire colonization. Many genomes (31/40) encoded heat shock proteins and molecular chaperones to further facilitate thermal resistance. In 16 MAGs, thermal resistance was complemented by genes for mycothiol biosysnthesis, mycothiol being a compound produced by Actinobacteria that aids in oxidative stress tolerance[36]. Genes for osmoprotectant (trehalose, *otsAB*, *treZY*[37]; glycine betaine, *betAB*[38]) synthesis were widespread among these 40 MAGs (17 and 38 MAGs encoded trehalose and glycine betaine synthesis genes, respectively), which could facilitate cell viability under low soil moisture conditions post fire. We recognize that many well-studied soil taxa encode genes for similar traits, but note that combinations of these traits are probably an emergent property of fire disturbance supporting post-fire dominance of these taxa. Further, MAGs recovered from High S samples also had significantly higher guanine-cytosine (GC) content, which has been linked to thermal stability[39,40], than MAGs from fire-impacted deeper soils (Extended Data Fig. 5; pairwise *t*-test, $P<0.05$). The lysing of microorganisms during soil heating represents sources of labile organic C and N associated with necromass[41]. All 40 featured MAGs expressed peptidase genes (2,721 total) in High S soils, of which approximately 41 were differentially expressed ($P<0.05$) between High S and Low S samples. These included genes responsible for peptidoglycan (component of bacterial cell walls) degradation, suggesting that taxa enriched post fire actively utilize microbial necromass.

The ability to grow quickly and occupy newly available niches is probably a key trait for microorganisms colonizing or growing in burned soils[18,26]. We inferred maximum growth rates using codon usage bias across our bacterial MAGs to determine whether colonizing taxa encoded the potential for rapid growth[42,43] (Supplementary Data 2). After removal of MAGs with doubling times >5 h due to model inaccuracies at slower growth rates[42], the average doubling time within our MAG dataset was found to be ~3.2 h. Twenty-two of the 40 MAGs of interest in High S samples had doubling times faster than the dataset average (ranging from ~0.3 to 4.7 h). Further, there was a significant negative correlation (Spearman's $\rho=-0.18$, $P<0.05$) between MAG relative abundance in High S samples and growth rate (measured as maximum doubling time), indicating that

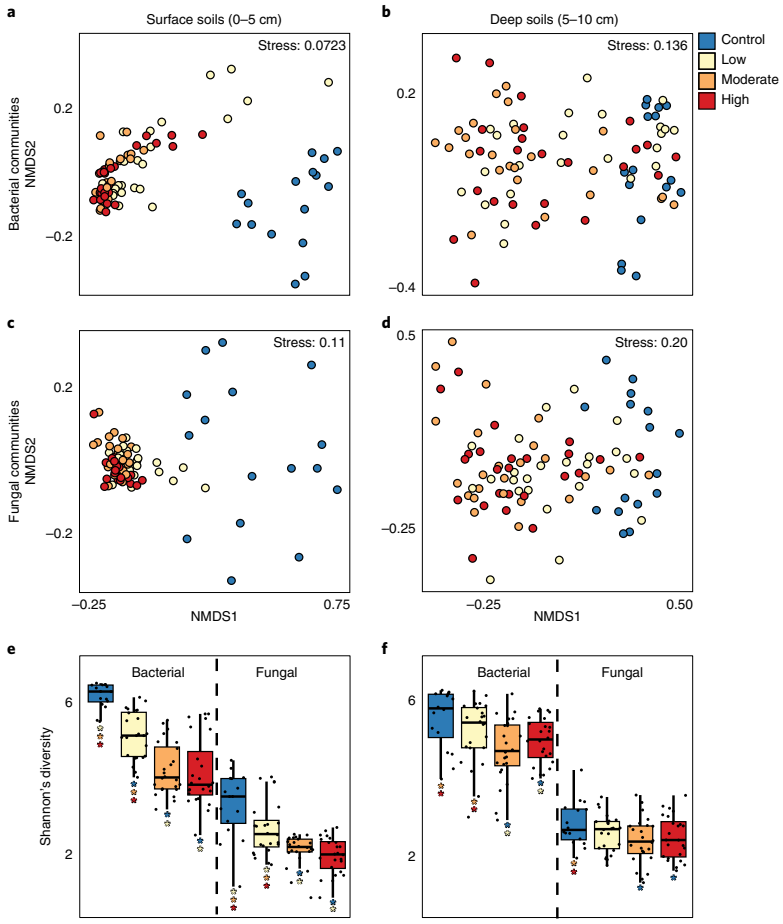

Fig. 1 | Surface soil microbiome undergoes homogenizing effect with burn. a–d, NMDS of surface (0–5 cm) (**a**,**c**) and deeper (5–10 cm) soil (**b**,**d**) bacterial (**a**,**b**) and fungal (**c**,**d**) communities shows increased separation of burned and unburned microbial communities in surface soils relative to deep soil communities. **e**,**f**, Shannon's diversity (H) calculated from 16S rRNA and ITS gene sequencing in surface (**e**) and deep soils (**f**) further shows the increased susceptibility of microbiomes in surface soils to wildfire. Asterisks in **e** and **f** denote significant differences (pairwise *t*-test; $P < 0.05$) between conditions ($n = 16$ for control S and D, $n = 24$ for low, moderate and high severity-impacted S and D samples). Corresponding *P* values are listed in Supplementary Table 1. The lower and upper hinges of the boxplots represent the 25th and 75th percentiles, respectively, and the middle line is the median. The whiskers extend from the median by 1.5× the interquartile range. Data points represent outliers.

High S conditions may select for microorganisms that can grow quickly (Fig. 2a). These insights suggest that abundant bacteria sampled 1 yr post wildfire occupied niches in the immediate aftermath of wildfire through strategies that probably include rapid growth. In contrast, these patterns were absent from MAGs recovered from other conditions (Fig. 2b–d). Emphasizing the importance of fast growth for colonizing severely burned soils, only 19 MAGs from High S samples had growth rates too slow to accurately estimate (249 MAGs with growth rates >5 h). To determine whether these same microorganisms were growing rapidly at the time of sampling (1 yr post wildfire), we investigated gene expression associated with rapid growth[44,45] (ribosomes, central metabolism) through MAG abundance-normalized transcripts (Supplementary Data 4). Results suggested diminished growth rates for the dominant High S bacteria at the time of sampling relative to other Actinobacteria MAGs that were highly expressing ribosomal and tricarboxylic acid cycle genes in High S samples. Together, these analyses indicate that potential rapid growth could enable these microorganisms to occupy free niche space in soil immediately following a wildfire, but this strategy may not be maintained once those niches are filled.

Actinobacteria process pyrogenic organic matter. During wildfire, SOM may be transformed to increasingly aromatic molecular structures that are commonly considered less available for microbial utilization[46]. Similar to other studies[47], mass spectrometry analyses of dissolved organic matter (DOM) revealed severity-dependent aromaticity increases in surface soils 1 yr post fire (Fig. 3). These aromaticity index trends were absent in DOM from more insulated

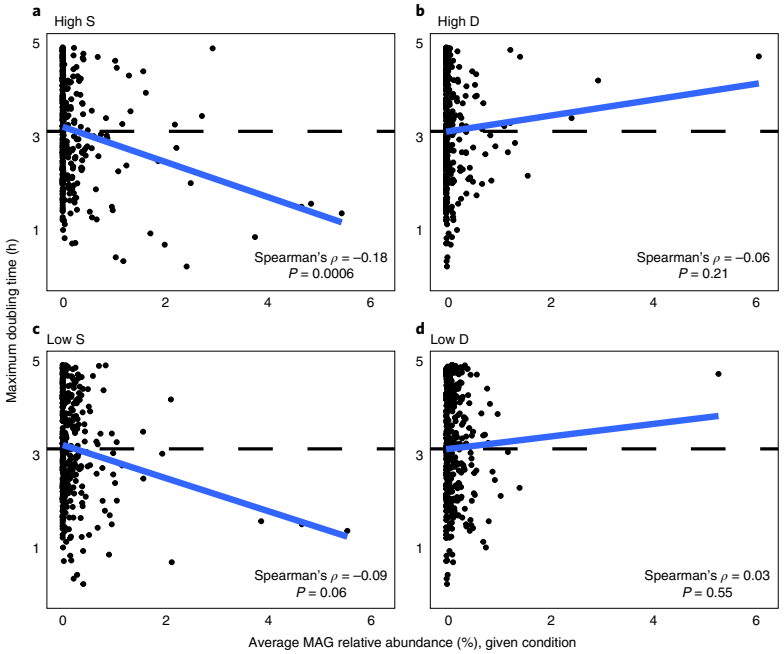

Fig. 2 | Potential fast growth rate favoured in soils impacted by high-severity wildfire. a–d, High S conditions (**a**) favour MAGs from organisms with faster potential growth rates (lower maximum doubling time, estimated using gRodon[42]), indicated here by a significant negative correlation (two-sided Spearman's rho test; Spearman's $\rho = -0.18$, $P < 0.05$). This trend is not present in the other three conditions (**b**–**d**). MAG average maximum doubling time is shown by the dashed line.

deep soils (Supplementary Fig. 4). Low-severity wildfire drives an increase in DOM aromaticity but also an accumulation of other unique compounds probably from incomplete combustion of SOM[48,49], whereas moderate and high-severity wildfire in surface soils resulted in the formation of unique aromatic organic compounds (Fig. 3a). The microbial transformation of these compounds is constrained by solubility and thermodynamic thresholds established by available electron acceptors[50] (for example, oxygen). To estimate the potential thermodynamic favourability of this DOM, we calculated the nominal oxidation state of carbon (NOSC); higher NOSC values theoretically yield a lower ΔG_{Cox} (that is, more favourable) when coupled to reduction of an electron acceptor[51]. Unique formulas in High S samples had significantly higher NOSC values, indicating increasing thermodynamic favourability for oxidation of DOM following severe wildfire (Fig. 3c; pairwise *t*-test, $P < 0.05$). Thus, thermodynamic limitations probably do not influence the lability of pyrogenic DOM in this system and other factors such as solubility or microbial community function probably govern compound processing.

We focused on microbial processing of catechol and protocatechuate—two intermediate products formed during aerobic degradation of diverse aromatic compounds[52]. The genomic potential for these reactions was present across severities and soil depths, and was dominated by Actinobacteria and Proteobacteria (Fig. 4); 80 and 226 MAGs encoded >50% of the catechol and protocatechuate ortho-cleavage pathways, respectively, including most of the featured High S and High D MAGs (Fig. 4c). Meta-cleavage pathways were also broadly represented within the MAGs (Extended Data Fig. 6). In High S samples, the *Arthrobacter* MAG RYN_101 alone was responsible for ~44% of *catA* (catechol 1,2-dioxygenase) gene expression, and therefore probably plays a key role in catechol degradation. Contrastingly, in High D samples, the Streptosporangiaceae MAG RYN_225 was responsible for ~46% and 23% of expression of *pcaGH* (protocatechuate 3,4-dioxygenase) and *pcaC* (4-carboxymuconolactone decarboxylase), respectively, that catalyses protocatechuate degradation (Fig. 4c). However, no MAGs of interest from High S or High D samples encoded the entire catechol or protocatechuate ortho-cleavage pathway (Fig. 4c), indicating that metabolic hand-offs between community members are probably important for complete compound degradation. Outside of catechol and protocatechuate, there was genomic evidence for the benzoyl-CoA and phenylacetyl-CoA oxidation pathways (Extended Data Fig. 7). These data indicate that post-fire soils support microbiomes that actively degrade some fire-derived aromatic compounds and have implications for C storage in wildfire-impacted ecosystems, since pyrogenic C compounds are considered largely resistant to decay and contribute to C storage[53]. Further work should integrate multi-omics data from field and laboratory studies into ecosystem models to refine the quantification of post-fire C fluxes.

Viruses impact burned soil microbiome structure and function. We recovered 2,399 distinct DNA and 91 distinct RNA viral populations (vMAGs) from the metagenomic and metatranscriptomic assemblies. Of these, 945 were previously undescribed (only clustering with other vMAGs from this study) and 92 were taxonomically assigned, with the majority ($n = 86$) within the *Caudovirales* order (Supplementary Data 5). DNA and RNA viral communities mirrored beta diversity trends observed in bacterial and fungal

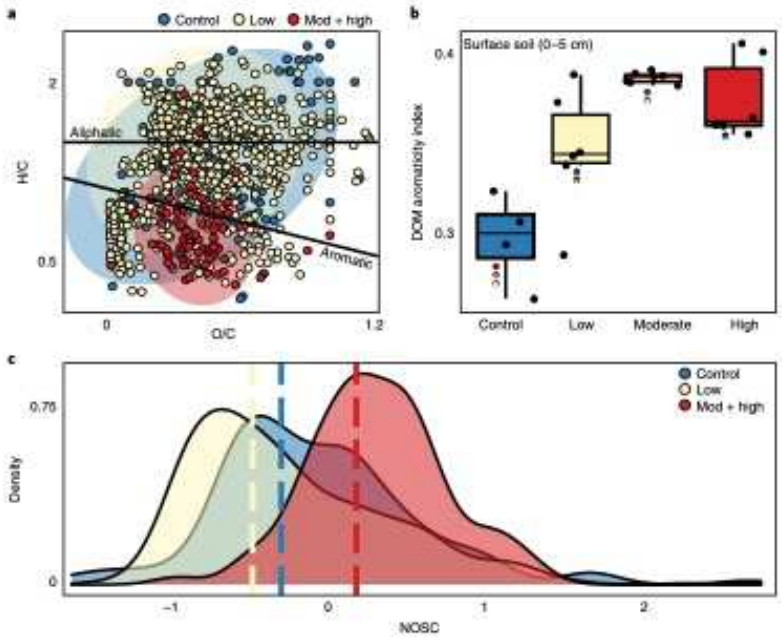

Fig. 3 | Pyrogenic dissolved organic matter becomes increasingly aromatic with wildfire burn severity. a, Van Krevelen diagram showing unique formulas in unburned, low, and moderate and high (combined) surface soils. **b**, Aromaticity index of DOM pools extracted from surface soils across the burn severity gradient ($n = 4$ for control, 6 for low, 5 for moderate and 6 for high severity). Corresponding P values are shown in Supplementary Fig. 4b from one-sided pairwise t-test. The lower and upper hinges of the boxplot represent the 25th and 75th percentiles, respectively, and the middle line is the median. The whiskers extend from the median by 1.5× the interquartile range. Data points represent outliers. Coloured asterisks indicate significant difference between the two conditions (pairwise t-test, $P < 0.05$). **c**, Density plot of unique formula NOSC value distributions between different conditions. Dashed line shows NOSC median for each condition.

communities; those in deep soils were less homogeneous compared with communities in surface soils, further highlighting the homogenizing influence of wildfire (Supplementary Fig. 5). Additionally, although DNA and RNA viral community composition was indistinct between low and high severity-impacted soils (ANOSIM $R = 0.007$ and -0.12, respectively; $P > 0.1$), we did measure significant differences between the two soil depths (ANOSIM $R = 0.59$ and 0.57, respectively; $P < 0.05$).

Given the importance of viral activity on soil microbiomes[14], we identified potential virus-host linkages that could offer insights into how viruses target bacteria. Many abundant and active MAGs ($n = 94$)—including 32 from the Actinobacteria—encoded CRISPR-Cas arrays with an average of ~18 spacers (max 210 spacers; Supplementary Data 2). By matching CRISPR spacers to protospacers in vMAGs, we linked 9 vMAGs with 4 bacterial hosts (RYN_115, RYN_242, RYN_436 and RYN_542) from the Actinobacteria, Planctomycetota and Proteobacteria. While each of these MAGs were active (expressing transcripts), the RYN_242 MAG (Solirubrobacteraceae) was among the top 3% most active MAGs across all conditions, suggesting that viruses are targeting active bacteria. We expanded upon potential virus-host linkages using VirHostMatcher[35] (d_2' value < 0.25), revealing higher numbers of viral linkages with more abundant host MAGs (Fig. 5). For example, the High S and High D MAGs of interest had above average numbers of putative viral linkages (average of 278 compared with the dataset-wide average of 196). Moreover, 129 vMAGs were linked to all 28 featured Actinobacteria MAGs from High S samples, potentially due to conserved nucleotide frequencies. These shared 129 vMAGs comprised ~7.6% of the viral community in High S samples, again suggesting that abundant and active bacteria in burned soils are actively targeted by abundant phage, potentially impacting soil C cycling via release of labile cellular components following cell lysis (that is, viral shunt)[36]. There is also evidence for the 'piggyback-the-winner' viral strategy, where lysogenic lifestyles are favoured at high microbial abundances and growth rates[37]. Of our 2,399 DNA vMAGs, 185 had putative lysogenic lifestyles based on gene annotations for integrase, recombinase or excisionase genes, and 25 of these had nucleotide frequency-based linkages to all the featured High S Actinobacteria MAGs.

To investigate potential viral roles in post-fire soil C cycling, we characterized the putative auxiliary metabolic genes (AMGs) repertoire of the vMAGs. Viruses use AMGs to 'hijack' and manipulate host metabolism; one permafrost soil study found AMGs associated with SOM degradation and central C metabolism, suggesting that viruses play a direct role in augmenting soil C cycling[38]. There were 773 total putative AMGs detected in 445 vMAGs, including 138 CAZymes targeting diverse substrates (for example, cellulose, chitin, pectin; Supplementary Data 5). Additionally, the AMGs included 105 genes related to growth (for example, ribosomal proteins, ribonucleoside-diphosphate reductase), 21 central C metabolism genes and 21 peptidases. Over 50 of these genes—including some related to SOM and necromass processing (for example, glycoside hydrolases, polysaccharide lyases) and cell growth (pyrimidine ribonucleotide biosynthesis)—were encoded within viral

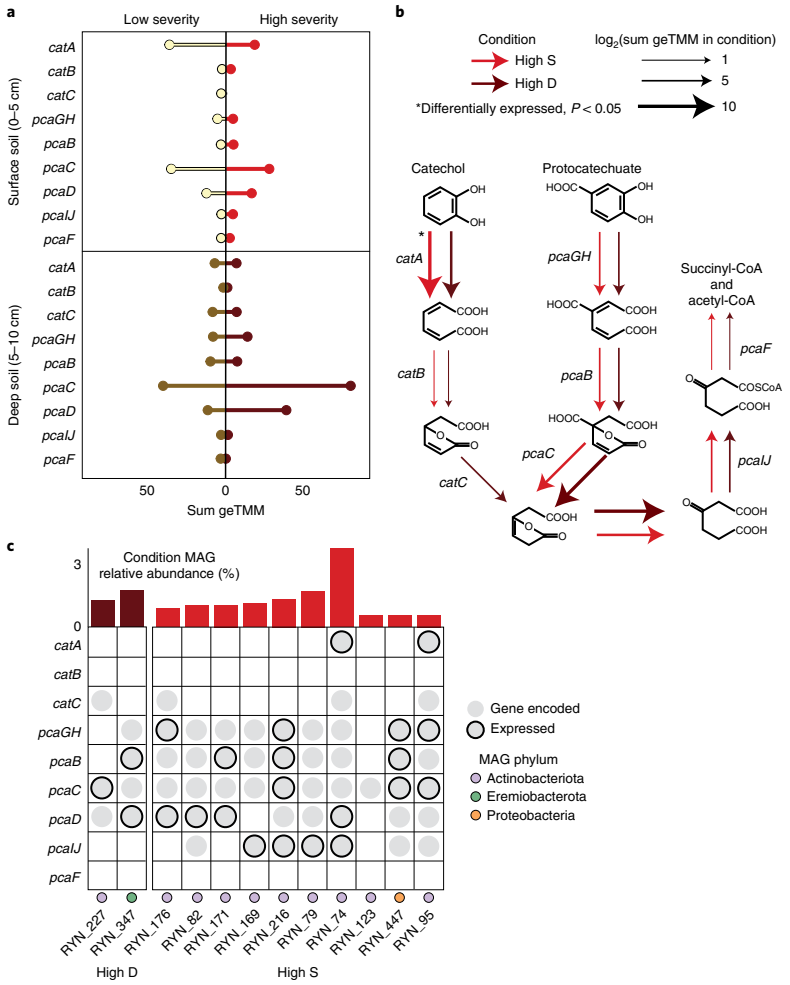

Fig. 4 | Dominant MAGs express genes for utilizing aromatic carbon. a, The summed geTMM of each gene for catechol and protocatechuate ortho-cleavage in each condition. **b**, The pathway for catechol and protocatechuate ortho-cleavage, with arrows indicating the log normalized sum geTMM of the gene for high severity surface and deep soils. Asterisk indicates genes that are differentially expressed in the condition (Wald's test in DESeq2; $P = 0.0055$ for *catA* in High S). **c**, The genomic potential and expression of each gene in the pathway for the MAGs of interest in High S and High D samples. The bar chart at the top shows the featured MAG relative abundance in that condition, coloured by featured condition.

genomes linked to all 28 of the featured High S Actinobacteria MAGs. Furthermore, metatranscriptomic analyses indicate that 13 of these AMGs were being actively transcribed, suggesting that prophage manipulate SOM degradation and potential cell growth in active bacteria in High S samples (Supplementary Data 5).

Fungi are active across burn conditions. Two fungal Ascomycota MAGs from known pyrophilous taxa, *Leotiomycetes* (R113–184) and *Coniochaeata ligniaria* (R110–5)[58–60], were reconstructed from metagenomes. These taxa were prominently represented in our internal transcribed spacer region (ITS) amplicons; the *Leotiomycetes* class increased in relative abundance by ~215% between control and High S samples (14% to 45%) and the *Coniochaeta* genus relative abundance increased from 0.003% to 1% from control to High D samples.

Complementing observations from bacterial MAGs, the fungal MAGs encoded and expressed genes for degrading aromatic compounds. Both expressed genes for degrading salicylate (salicylate hydroxylase), phenol (phenol 2-monooxygenase) and catechol (catechol 1,2-dioxygenase), and expression of all three genes increased with fire severity. The MAGs also encoded laccases, which are enriched in pyrophilous fungal genomes[61] and act on aromatic substrates[62]. The *Coniochaeta* MAG additionally encoded hydrophobic surface binding proteins (*hsbA*; PF12296), which may facilitate the degradation of fire-derived hydrophobic compounds and be critical to soil recovery[61]. To compare the fungal and bacterial contribution

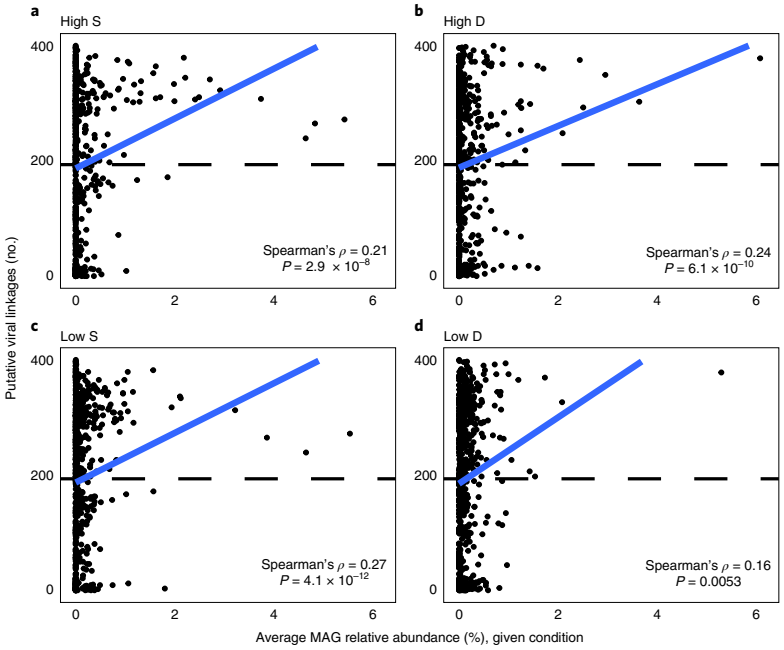

Fig. 5 | Dominant MAGs are increasingly targeted by viruses in post-fire soils. Each MAG's relative abundance within (**a**) High S and (**b**) D and (**c**) Low S and (**d**) D conditions plotted against the number of putative viral linkages identified by VirHostMatcher. Dashed line indicates the dataset average of 196 virus-host linkages. Correlation and significance between MAG relative abundance and number of putative viral linkages were assessed using the two-sided Spearman rho test.

to catechol degradation, we compared normalized transcriptomic reads recruited to the gene encoding catechol 1,2-dioxygenase, *catA*. In High S samples, the fungal MAGs generated more than twice the number of transcripts per gene compared with bacterial MAGs, indicating the important role that fungi probably play in aromatic DOM degradation in burned soils. Both fungal MAGs also expressed diverse peptidases (Supplementary Fig. 6), with increased expression from low to high fire severity in both surface and deep samples (~40.4% and 235%, respectively), which could degrade necromass from lysed microorganisms.

Ecosystem implications of soil microbiome changes. We observed short-term (1 yr post fire) differences in microbiome composition and function that probably alter biogeochemical cycling and initial post-fire vegetation recovery. We found no expression of the gene catalysing N fixation (*nifH*), despite the key role that N-fixing bacteria play in augmenting plant-available soil N pools[10] following disturbance, the pre- and post-fire abundance of actinorhizal shrubs (*Ceanothus velutinus, Shepherdia canadensis*) and the numerous leguminous forb species that form symbioses with N-fixing bacteria in these ecosystems. Nitrification is another key microbially mediated process that generally increases in post-fire soils due to an influx of ash-derived ammonium (also found here; Supplementary Data 1)[25,63]. Ammonia monooxygenase (*amoA*) transcripts were detected in deep soils but were absent in burned surface soils. Moreover, transcript abundances for both *amoA* and nitrite oxidoreductase (*nxrAB*) were significantly higher in Low D vs High D samples (Welch's *t*-test; $P < 0.05$) (Supplementary Data 4), potentially due to the inability of ammonia-oxidizing bacteria (for example, *Nitrospira*) to withstand post-fire soil conditions. Indeed, *Nitrospira* was present in both control and burned deep soils but absent in moderate and high severity-impacted surface soils. These observations are supported by other studies; short-term, post-fire decreases in the abundances of genes catalysing N fixation and ammonia-oxidization have been noted in a conifer forest following a wildfire[64].

While pyrophilous taxa were enriched post wildfire, the loss of other soil microorganisms may impact biogeochemical processes and associated soil health. Increasing wildfire severity (from low to high) resulted in large decreases in the relative abundances of both Acidobacteria and Verrucomicrobia in surface soils (Extended Data Fig. 2; relative abundance decreases of 37.6% and 63.6%, respectively). Members of the Acidobacteria frequently play an active role in soil C cycling via decomposition[65–67] and are considered a keystone taxa for SOM degradation[68]. Here, representative MAGs affiliated with Acidobacteria (RYN_25, RYN_26) from the Pyrinomonadaceae family (16S rRNA gene data; −94.9% from Low S to High S) and Verrucomicrobia from the Verrucomicrobiaceae family (16S rRNA gene data; −82.35% Low S to High S) all encoded CAZYmes for targeting complex plant-derived carbohydrate polymers (for example, cellulose, beta-mannans, beta-galactans, xylan). Furthermore, Acidobacteria MAGs RYN_25 and RYN_26 both encoded genes (for example, *epsH*) for the synthesis of exopolysaccharides that play critical roles in soil aggregate formation and SOM stabilization as mineral-associated OM[69]. The loss of these taxa following severe wildfire may reduce the potential for SOM degradation and stabilization in surface soils.

Ectomycorrhizal fungi (EMF) facilitate plant access to limiting nutrients and water in return for photosynthetically derived carbohydrates[70]. We observed a 99% decrease in EMF relative abundances across the burn severity gradient (Supplementary Table 4),

which could be due to heat-induced fungal mortality or plant host death[14]. This has implications for the re-establishment of obligate ectomycorrhizal host plants such as *Pinus contorta*, the dominant tree species in these forests. For example, *Cenoccum geophilum*, a known EMF symbiont of *P. contorta*[71] that is indicative of fast conifer growth[72], was present in unburned sites but absent after fire. Inoculation of *P. contorta* and most conifers with EMF is a standard forest nursery production and reforestation practice[73], but inoculating seedlings destined for post-fire landscapes[74] with a mixture of local EMF species[71] may increase lost soil microbial diversity.

Discussion

Here we present a genome-resolved multi-omics analysis of the impact of wildfire on the soil microbiome of conifer forest ecosystems, providing functional context to previously observed post-fire shifts in soil microbiome structure. Our results suggest that a combination of life strategies, including heat tolerance, fast growth and the utilization of pyrogenic substrates allow microorganisms to occupy available post-fire niche space. We found the widespread microbial processing of aromatic compounds that were probably generated during wildfire, which has implications for the residence time of pyrogenic C. Carbon processing in burned soils is also influenced by active viruses that target key bacterial community members through viral-mediated cell lysis and activity of AMGs. This rich genome-resolved multi-omic dataset provides invaluable insight into the impact of severe wildfire on the soil microbiome of western US forest ecosystems, which continue to experience unprecedented wildfire disturbances.

Methods

Field campaign. Sampling was conducted in old-growth, lodgepole pine-dominated (*P. contorta*) forests burned by the Badger Creek (8,215 ha) and Ryan (11,567 ha) fires during 2018 in the Medicine Bow National Forest. The average return interval for wildfire within these forests is about 200 yr[75] and the even-aged lodgepole pine stands sampled regenerated from stand-replacing wildfires. Total annual precipitation averages 467 mm and mean annual temperature is 1.9 °C, with average annual minima and maxima of −12.1 °C and 17.1 °C, respectively (Cinnabar Park, SNOTEL site 1046). Soils are formed in metamorphic and igneous parent material and are well-drained, with moderate to rapid permeability. The most abundant soil types are loamy-skeletal Ustic Haplocryepts and fine-loamy Ustic Haplocryalfs (Supplementary Data 1). The plots were at similar elevation (2,480–2,760 m) and on mainly gentle slopes (10/15 plots; little aspect influence). Microbial communities were not statistically different between gentle and moderate sloping plots (ANOSIM; $P < 0.05$) and north or south facing plots when slope was moderate (>10°; ANOSIM; $P < 0.05$). Four burn severity gradients comprising low, moderate and high severity sites and an unburned control were selected on the basis of remotely sensed comparisons of pre and post-fire greenness[76], and then field validated before sampling (early August 2019) using US Forest Service guidelines[77,78]. Low, moderate and high severity sites had >85%, 20–85% and <20% surficial organic matter cover, respectively[77], which we quantified visually within each plot using a point-intercept approach (Extended Data Fig. 1). Low-severity plots had sparse grass and low shrub (*Vaccinium myrtillu*) cover, which we avoided to ensure we sampled root-free soil. Low-severity sites also had a very small litter layer to a depth of <1 mm and Site #4 had live trees remaining but all were >2 m away from the sampling plot. Samples were collected on 16 and 19 August 2019, 2 d without any precipitation events, approximately 1 yr following containment of both fires. At each sampling site, a 3 m × 5 m sampling grid with 6 m^2 subplots was laid out perpendicular to the dominant slope (Extended Data Fig. 1). Surface (0–5 cm depth) and deeper soil (5–10 cm depth) was collected with a sterilized trowel in each subplot for DNA and RNA extractions and subsequent microbial analyses. Surface soil samples included thin O-horizon at control and low-severity plots and charred mineral soil at moderate and high-severity plots. Deeper (5–10 cm) samples were mineral soils. In three subplots of each plot, additional material was collected for chemical analyses. Samples for RNA analyses were immediately flash-frozen using an ethanol-dry ice bath and placed on dry ice to remain frozen in the field. Samples for DNA extractions and chemical analyses were immediately placed on ice and all samples were transported to the laboratory at Colorado State University (CSU). Soils for DNA and RNA extractions were stored at −80 °C in the laboratory until processing. A total of 176 soil samples were collected (Supplementary Data 1).

Soil chemistry. We evaluated soil nutrients and chemistry to gauge changes across a gradient of wildfire severity and to consider the implications of those conditions on microbial activity or substrate quality. Analyses of inorganic forms of soil N (NO_3-N and NH_4-N) were conducted on a subset of deep soil samples ($n = 12$ each for low, moderate and high severity, $n = 8$ for control). Samples were passed through a 4 mm mesh sieve and extracted with 2 M KCl within 24 h of sampling. Extracts were analysed for NO_3-N and NH_4-N by colorimetric spectrophotometry[79] (Lachat). A subset of surface ($n = 15$) and deep soil samples ($n = 45$) were dried (48 h at 60 °C), ground to a fine powder and analysed for total C and N by dry combustion (LECO). We analysed the NO_3–N and NH_4–N and dissolved organic C (DOC) and total dissolved N (TDN) released during warm water extraction[80] using ion chromatography (NH_4-N and NO_3-N; Thermo Fisher) and a Shimadzu TOC-VCPN analyser (DOC and TDN; Shimadzu). Soil pH was analysed in a 1:1 soil to deionized water slurry after 1 h of agitation[81] using a temperature-corrected glass electrode (Hach). Soil chemistry data are included in Supplementary Data 1 and discussed in Supplementary Note 1.

High-resolution carbon analyses by FTICR-MS. Water extractions were completed on a subset of 47 samples from the Ryan Fire for high-resolution C analyses using Fourier transform ion cyclotron resonance mass spectrometry (FTICR-MS) to analyse DOM. Briefly, 100 ml of milliQ water (>18 mΩ) was added to 50 g of sample in an acid-washed and combusted (400 °C for 6 h) 250 ml Erlenmeyer flask. These were placed on a shaker table for 10 h at 170 r.p.m. Following shaking, liquid was poured off into a 50 ml centrifuge tube and centrifuged for 10 min at 7,500 *g* and supernatant was filtered through a polypropylene 0.2 µm filter (polypropylene material). The extracts were acidified to pH 2 and additionally pre-treated with solid-phase extractions using Agilent Bond Elut-PPL cartridges (3 ml, 200 mg) (Agilent Technologies) following standard lab protocol[82] and subsequently diluted to 50 ppm. A 12 Tesla (12 T) Bruker SolariX FTICR-MS located at the Environmental Molecular Sciences Laboratory in Richland, Washington, USA was used to collect DOM high-resolution mass spectra from each DOM sample. Samples were injected into the instrument using a custom automated direction infusion cart that performed two offline blanks between each sample and using an Apollo II electrospray ionization source in negative ion mode with an applied voltage of −4.2 kV. Ion accumulation time was optimized between 50 and 80 ms. Transients (144) were co-added into a 4MWord time domain (transient length of 1.1 s) with a spectral mass window of 100–900 *m/z*, yielding a resolution at 400 K at 381 *m/z*. Spectra were internally recalibrated in the mass domain using homologous series separated by 14 Da (CH_2 groups). The mass measurement accuracy was typically within 1 ppm for singly charged ions across a broad *m/z* range (100 *m/z*–900 *m/z*). Bruker Daltonics DataAnalysis (version 4.2) was used to convert mass spectra to a list of *m/z* values by applying the FTMS peak picking module with a signal-to-noise ratio threshold set to 7 and absolute intensity threshold to the default value of 100. Chemical formulae were assigned with Formularity[83] on the basis of mass measurement error <0.5 ppm, taking into consideration the presence of C, H, O, N, S and P and excluding other elements. This open-access software was also used to align peaks with a 0.5 ppm threshold. Raw FTICR-MS data are provided in archive (doi:10.5281/zenodo.5182305). The R package ftmsRanalysis[84] was then used to remove peaks that either were outside the desired *m/z* range (200 *m/z*–900 *m/z*) or had a more abundant isotopologue, assign Van Krevelen compound classes and calculate nominal oxidation state of carbon (NOSC) and aromaticity index (AI) on the basis of the number of different atoms using equations (1) and (2) below:

$$\mathrm{NOSC} = 4 - \frac{5C + H - 3N - 20 - 2S}{C} \quad (1)$$

$$\mathrm{AI} = 4 - \frac{1 + C - O - S - 0.5H}{C - O - S - N - P} \quad (2)$$

Kendrick mass defect (KMD) analysis and plots were employed to identify potentially increasing polyaromaticity across the burn severity gradient. The KMD analysis was done using the C_4H_2 base unit (50 atomic mass units, amu) to represent the addition of benzene to a separate molecular benzene. The mass of each identified ion (*M*) was converted to its Kendrick mass (KM):

$$\mathrm{KM} = M\left(\frac{50\ \mathrm{amu}}{50.0587\ \mathrm{amu}}\right) \quad (3)$$

with 50 amu being the nominal mass of C_4H_2 and 50.0587 being the exact mass of C_4H_2. The final KMD was obtained by subtracting the KM from the nominal KM, which is the initial ion mass rounded to the nearest integer. Series were identified as 2 or more formulae with the same KMD and a nominal Kendrick mass (NKM) differing by the C_4H_2 base unit (50 g mol^{-1}). Series were retained if they were present across all four burn severity conditions (control, low, moderate and high), resulting in 64 total series in the final analysis (Supplementary Note 4).

DNA extraction, 16S rRNA gene and ITS amplicon sequencing. DNA was extracted from soil samples using the Zymobiomics Quick-DNA faecal/soil microbe kits (Zymo Research). 16S rRNA genes in extracted DNA were amplified and sequenced at Argonne National Laboratory on the Illumina MiSeq using

251 bp paired-end reads and the primers 515F/806R[85], targeting the V4 region of the 16S rRNA gene. For fungal community composition, the DNA was PCR amplified targeting the first nuclear ribosomal ITS using the primers (ITS1f/ITS2) and sequenced on the Illumina MiSeq platform at the University of Colorado using 251 bp paired-end reads.

For taxonomic assignment, we used the SILVA[86] (release 132) and UNITE[87] (v8.3) databases for bacteria and fungi, respectively. We employed the QIIME2 environment[88] (release 2018.11) for processing of reads, which are both deposited and are available at NCBI under BioProject PRJNA682830. DADA2[89] was used to filter, learn error rates, denoise and remove chimeras from reads. Following this step, 16S rRNA gene and ITS amplicon sequencing reads retained on average 48,379 and 34,004 reads per sample, respectively. Taxonomy was assigned using the QIIME2 scikit-learn classifier trained on the SILVA and UNITE databases for bacteria and fungi, respectively. Ecological guilds were assigned to fungal amplicon sequence variants (ASVs) using FUNGuild[90] (v1.2). Similar to FUNGuild creator recommendations, we accepted guild assignments classified as 'highly probable' or 'probable' to avoid possible overinterpretation and discarded any ASVs classified as multiple guilds.

To characterize how microbial populations differed across burn severities and depths, we used the R[91] vegan[92] (v2.5-7) and phyloseq[93] (v1.28.0) packages. Non-metric multidimensional scaling (NMDS) was conducted on Bray-Curtis dissimilarities to examine broad differences between microbial communities. ANOSIM (vegan) was utilized to test the magnitude of dissimilarity between microbial communities. Mean species diversity of each sample (alpha diversity) was calculated on the basis of species abundance, evenness or phylogenetic relationships using Shannon's diversity index, Faith's phylogenetic diversity and Pielou's evenness. Linear discriminant analysis with a score threshold of 2.0 was used to determine ASVs discriminant for unburned or burned soil[94].

Metagenomic assembly and binning. A subset of 12 Ryan Fire samples from a single transect representing low- and high-severity burn from surface and deep soils was selected for metagenomic sequencing to analyse changes in microbial community functional potential ($n=3$ per condition). The four different conditions are hereafter referred to as 'Low S' (low-severity surface soil), 'High S' (high-severity surface soil), 'Low D' (low-severity deep soil) and 'High D' (high-severity deep soil). Libraries were prepared using the Tecan Ovation Ultralow System V2 and were sequenced on the NovaSEQ6000 platform on an S4 flow cell using 151 bp paired-end reads at Genomics Shared Resource, Colorado Cancer Center, Denver, Colorado, USA. Sequencing adapter sequences were removed from raw reads using BBduk (https://jgi.doe.gov/data-and-tools/bbtools/bb-tools-user-guide/bbduk-guide/) and reads were trimmed with Sickle[95] (v1.33). For each sample, trimmed reads were assembled into contiguous sequences (contigs) using the de novo de Bruijn assembler MEGAHIT v1.2.9 using *k*mers[96] (minimum kmer of 27, maximum *k*mer of 127 with step of 10). Assembled contigs shorter than 2,500 bp were discarded for all downstream usages, including gene-resolved analyses for inorganic N cycling and binning into genomes. These assembled contigs (>2,500 bp) were binned using MetaBAT2 with default parameters[97] (v2.12). Metagenome-assembled genome (MAG) quality was estimated using checkM[98] (v1.1.2) and taxonomy was assigned using GTDB-Tk[99] (R05-RS95, v1.3.0). MAGs from all metagenomes were dereplicated using dRep[100] (default parameters, v2.2.3) to create a non-redundant MAG dataset. Low quality MAGs (<50% completion and >10% contamination) were excluded from further analysis[101]. Reads from all samples were mapped to the dereplicated MAGs using BBMap with default parameters (version 38.70, https://sourceforge.net/projects/bbmap/). Per-contig coverage across each sample was calculated using CoverM contig (v0.3.2) (https://github.com/wwood/CoverM) with the 'Trimmed Mean' method, retaining only those mappings with minimum percent identity of 95% and minimum alignment length of 75%. Coverages were scaled on the basis of library size and scaled per-contig coverages were used to calculate the mean per-bin coverage and relative abundance in each sample (Supplementary Data 2). The quality metrics and taxonomy of the subsequent 637 medium- and high-quality MAGs discussed here are included in the Supplementary Information (Supplementary Data 2) and are deposited at NCBI (BioProject ID PRJNA682830). Maximum cell doubling times were calculated from codon usage bias patterns in each MAG with >10 ribosomal proteins using gRodon[42] (Supplementary Data 2). Bacterial MAGs with an average relative abundance >0.5% across triplicates (with a standard deviation less than the average relative abundance) in both High S and High D were selected as MAGs of interest for further genome-resolved discussion and insight into the function of the post-fire microbiome in surface and deep soils (Supplementary Data 2).

Fungal MAGs (R113–184 and R110–5) were identified because they were abnormally large for bacterial MAGs and were confirmed as of eukaryotic origin on the basis of mmseqs2 searches for all available open reading frames in their contigs against the NCBI NR and MycoCosm databases, with best hits to *Coniochaeta ligniaria* and the *Leotiomycetes*/*Helotiales* clade. To identify taxonomy and precisely place the MAGs in the fungal tree (Supplementary Fig. 1), we used 867 single-copy orthogroups from OrthoFinder v2.5.4[102] using default parameters. The protein sequences in each orthogroup were aligned with MAFFT[103] (–maxiterate 1000–globalpair) and trimmed with TrimA1 v1.4.rev22[104] (-automated1). All the filtered MSAs were concatenated. The phylogenetic tree was built using iqtree v1.6.9[105] detecting the best model for each gene partition, 10,000 ultrafast bootstrap and 10,000 SH-like approximate likelihood ratio test (-m MFP -bb 10000 -alrt 10000 -safe). The tree was visualized using FigTree 1.4.4 (http://tree.bio.ed.ac.uk/software/figtree/) and the support values represent the ultrafast bootstraps/SH-aLRT. Completeness for both MAGs was assessed using BUSCO v4.0.6[106] and CEGMA[107].

MAG annotation. Eukaryotic MAGs were annotated using the JGI annotation pipeline, analysed with complementary metatranscriptomics assemblies[108] (RnaSPAdes, v3.13.0) and are deposited on MycoCosm[109] (https://mycocosm.jgi.doe.gov/ColoR110_1 and https://mycocosm.jgi.doe.gov/ColoR113_1). Bacterial MAGs were annotated using DRAM[110] (v1.0). In addition to the DRAM annotations, we used HMMER[111] against Kofamscan HMMs[112] to identify genes for catechol and protocatechuate meta- and ortho-cleavage, naphthalene transformations and inorganic N cycling (Supplementary Data 3).

Metatranscriptomics. RNA was extracted from the subset of 12 samples utilized for metagenomics using the Zymobiomics DNA/RNA mini kit (Zymo Research) and RNA was cleaned, DNase treated and concentrated using the Zymobiomics RNA Clean & Concentrator kit (Zymo Research). The Takara SMARTer Stranded Total RNA-Seq kit v2 (Takara Bio) was used to remove ribosomal RNA from total RNA and construct sequencing libraries. Samples were sequenced on the NovaSEQ6000 platform on an S4 flow cell using 151 bp paired-end reads at Genomics Shared Resource, Colorado Cancer Center, Denver, Colorado, USA. Adapter sequences were removed from raw reads using Bbduk (https://jgi.doe.gov/data-and-tools/bbtools/bb-tools-user-guide/bbduk-guide/) and sequences were trimmed with Sickle v1.33[95]. Trimmed reads were mapped to metagenome assemblies using BBMap (parameters: ambiguous, random; idfilter, 0.95; v38.70). Mappings were filtered to 95% identity and counts were generated using HTSeq[113]. For differential expression analysis, the dataset was filtered to transcripts which were successfully annotated by DRAM ($n=132{,}665$) and DESeq2[114] was used to identify transcripts that were differentially expressed in any condition (Supplementary Data 4). The same analysis was also run on the combined HMM output described above (1,189 total transcripts). We normalized our dataset by calculating the gene length-corrected trimmed mean of *M* values[115] (geTMM) using edgeR[116] to normalize for library depth and gene length (Supplementary Data 4). To identify transcripts that were highly expressed in any given condition, we filtered the data to transcripts that were in the upper 20% of TMM for 2 of the 3 samples in any one condition (Supplementary Table 2). To compare bacterial and fungal expression data for individual genes, we normalized the number of either fungal or bacterial transcript reads to the gene coverage in each sample to compare the number of transcripts recruited per gene.

Viruses. Viral contigs were recovered from the metagenomic assemblies using VirSorter2[117] (v2.2.2) and only contigs ≥10 kb with a VirSorter2 score >0.5 were retained. Viral contigs were trimmed using checkV[118] (v0.4.0) and the final contigs were clustered using the CyVerse app ClusterGenomes (v1.1.3) requiring an average nucleotide identity of 95% or greater over at least 80% of the shortest contig. The final DNA viral metagenome-assembled genome (vMAG) dataset was manually curated using the checkV, VIRSorter2 and DRAM-v annotation outputs according to protocol[119]. RNA vMAGs were also recovered from metatranscriptome assemblies using VIRSorter2[117] (v2.2.2). The resulting sequences were clustered using ClusterGenomes (v1.1.3) on CyVerse using the aforementioned parameters. To quantify relative abundance of DNA and RNA vMAGs across the 12 samples, we mapped the metagenomic and metatranscriptomic reads to the vMAGs using BBMap with default parameters (v38.70). To determine vMAGs that had reads mapped to at least 75% of the vMAG, we used CoverM (v0.6.0) in contig mode to find vMAGs that passed this 75% threshold (–min-covered-fraction 75). We then used CoverM (v0.6.0) in contig mode to output reads per base and used this to calculate final DNA and RNA vMAG relative abundance in each metagenome and metatranscriptome. vConTACT2 (v0.9.8; CyVerse) was used to determine vMAG taxonomy. Final viral sequences are deposited on NCBI (BioProject ID PRJNA682830 - BioSamples SAMN20555178, SAMN20555179; Supplementary Data 5). We used DRAM-v[110] (v1.2.0) to identify AMGs within the final viral dataset (Supplementary Data 5).

CRISPR-Cas protospacers were found and extracted from MAG sequences using the CRISPR Recognition Tool[120] (minimum of 3 spacers and 4 repeats) in Geneious (v2020.0.3) and CRisprASSembler[121] with default parameters (v1.0.1). BLASTn was used to compare MAG protospacer sequences with protospacer sequences in vMAGs, with matches only retained if they were 100% or contained ≤1 bp mismatch with an *e*-value ≤ 1×10^{-5}. To identify putative vMAG-MAG linkages, we used an oligonucleotide frequency dissimilarity measure (VirHostMatcher v1.0.0) and retained only linkages with a d_2^* value <0.25[55] (Supplementary Data 5).

Reporting summary. Further information on research design is available in the Nature Research Reporting Summary linked to this article.

Data availability

The metagenomic reads, metatranscriptomic reads, bacterial and viral MAGs, 16S rRNA gene sequencing reads and ITS amplicon reads reported in this paper have been deposited in National Center for Biotechnology Information BioProject PRJNA682830. The two fungal MAGs and corresponding annotations are deposited in the Joint Genome Institute (JGI) MycoCosm portal and can be assessed at https://mycocosm.jgi.doe.gov/ColoR113_1 and https://mycocosm.jgi.doe.gov/ColoR110_1. FTICR-MS data have been deposited in the Zenodo archive with identifier https://doi.org/10.5281/zenodo.5182305. The following databases were also used: Silva (release 132), UNITE (v8.3) and GTDB-Tk (v1.3.0). Processed data are included in the Supplementary Data files which are detailed in the Supplementary Information.

Received: 1 September 2021; Accepted: 18 July 2022;
Published online: 25 August 2022

References

1. Dennison, P. E., Brewer, S. C., Arnold, J. D. & Moritz, M. A. Large wildfire trends in the western United States, 1984–2011. *Geophys. Res. Lett.* **41**, 2928–2933 (2014).
2. Higuera, P. E. & Abatzoglou, J. T. Record-setting climate enabled the extraordinary 2020 fire season in the western United States. *Glob. Change Biol.* https://doi.org/10.1111/gcb.15388 (2020).
3. Parks, S. A. & Abatzoglou, J. T. Warmer and drier fire seasons contribute to increases in area burned at high severity in western US forests from 1985 to 2017. *Geophys. Res. Lett.* **47**, e2020GL089858 (2020).
4. Benavides-Solorio, J. D. D. & MacDonald, L. H. Measurement and prediction of post-fire erosion at the hillslope scale, Colorado Front Range. *Int. J. Wildl. Fire* **14**, 457–474 (2005).
5. Pierson, D. N., Robichaud, P. R., Rhoades, C. C. & Brown, R. E. Soil carbon and nitrogen eroded after severe wildfire and erosion mitigation treatments. *Int. J. Wildl. Fire* **28**, 814–821 (2019).
6. Rhoades, C. C., Entwistles, D. & Butler, D. The influence of wildfire extent and severity on streamwater chemistry, sediment and temperature following the Hayman Fire, Colorado. *Int. J. Wildl. Fire* **20**, 430–442 (2011).
7. Chambers, M. E., Fornwalt, P. J., Malone, S. L. & Battaglia, M. A. Patterns of conifer regeneration following high severity wildfire in ponderosa pine – dominated forests of the Colorado Front Range. *For. Ecol. Manage.* **378**, 57–67 (2016).
8. Rhoades, C. C. et al. The legacy of a severe wildfire on stream nitrogen and carbon in headwater catchments. *Ecosystems* **22**, 643–657 (2019).
9. Strickland, M. S., Lauber, C., Fierer, N. & Bradford, M. A. Testing the functional significance of microbial community composition. *Ecology* **90**, 441–451 (2009).
10. van der Heijden, M. G. A., Bardgett, R. D. & van Straalen, N. M. The unseen majority: soil microbes as drivers of plant diversity and productivity in terrestrial ecosystems. *Ecol. Lett.* **11**, 296–310 (2008).
11. Mendes, R. et al. Deciphering the rhizosphere microbiome for disease-suppressive bacteria. *Science* **332**, 1097–1100 (2011).
12. Hart, S. C., DeLuca, T. H., Newman, G. S., MacKenzie, M. D. & Boyle, S. I. Post-fire vegetative dynamics as drivers of microbial community structure and function in forest soils. *For. Ecol. Manage.* **220**, 166–184 (2005).
13. Pressler, Y., Moore, J. C. & Cotrufo, M. F. Belowground community responses to fire: meta-analysis reveals contrasting responses of soil microorganisms and mesofauna. *Oikos* **128**, 309–327 (2019).
14. Pulido-Chavez, M. F., Alvarado, E. C., DeLuca, T. H., Edmonds, R. L. & Glassman, S. I. High-severity wildfire reduces richness and alters composition of ectomycorrhizal fungi in low-severity adapted ponderosa pine forests. *For. Ecol. Manage.* **485**, 118923 (2021).
15. Villadas, P. J. et al. The soil microbiome of the Laurel Forest in Garajonay National Park (La Gomera, Canary Islands): comparing unburned and burned habitats after a wildfire. *Forests* **10**, 1051 (2019).
16. Dove, N. C. & Hart, S. C. Fire reduces fungal species richness and in situ mycorrhizal colonization: a meta-analysis. *Fire Ecol.* **13**, 37–65 (2017).
17. Ibáñez, T. S., Wardle, D. A., Gundale, M. J. & Nilsson, M.-C. Effects of soil abiotic and biotic factors on tree seedling regeneration following a boreal forest wildfire. *Ecosystems* https://doi.org/10.1007/s10021-021-00666-0 (2021).
18. Whitman, T. et al. Soil bacterial and fungal response to wildfires in the Canadian boreal forest across a burn severity gradient. *Soil Biol. Biochem.* **138**, 107571 (2019).
19. Brown, S. P. et al. Context dependent fungal and bacterial soil community shifts in response to recent wildfires in the Southern Appalachian Mountains. *For. Ecol. Manage.* **451**, 117520 (2019).
20. Ferrenberg, S. et al. Changes in assembly processes in soil bacterial communities following a wildfire disturbance. *ISME J.* **7**, 1102–1111 (2013).
21. Knelman, J. E., Schmidt, S. K., Garayburu-Caruso, V., Kumar, S. & Graham, E. B. Multiple, compounding disturbances in a forest ecosystem: fire increases susceptibility of soil edaphic properties, bacterial community structure, and function to change with extreme precipitation event. *Soil Syst.* **3**, 1–1, 40 (2019).
22. Zhang, L. et al. Habitat heterogeneity induced by pyrogenic organic matter in wildfire-perturbed soils mediates bacterial community assembly processes. *ISME J.* **5**, 1943–1955 (2021).
23. Tas, N. et al. Impact of fire on active layer and permafrost microbial communities and metagenomes in an upland Alaskan boreal forest. *ISME J.* https://doi.org/10.1038/ismej.2014.36 (2014).
24. Yang, S. et al. Fire affects the taxonomic and functional composition of soil microbial communities, with cascading effects on grassland ecosystem functioning. *Glob. Change Biol.* **26**, 431–442 (2020).
25. Dove, N. C., Safford, H. D., Bohlman, G. N., Estes, B. L. & Hart, S. C. High-severity wildfire leads to multi-decadal impacts on soil biogeochemistry in mixed-conifer forests. *Ecol. Appl.* **30**, eap.2072 (2020).
26. Pérez-Valera, E., Goberna, M. & Verdú, M. Fire modulates ecosystem functioning through the phylogenetic structure of soil bacterial communities. *Soil Biol. Biochem.* **129**, 80–89 (2019).
27. SantaCruz-Calvo, L., González-López, J. & Manzanera, M. *Arthrobacter siccitolerans* sp. nov., a highly desiccation-tolerant, xeroprotectant-producing strain isolated from dry soil. *Int. J. Syst. Evol. Microbiol.* **63**, 4174–4180 (2013).
28. Mongodin, E. F. et al. Secrets of soil survival revealed by the genome sequence of *Arthrobacter aurescens* TC1. *PLoS Genet.* **2**, 2094–2106 (2006).
29. Bourguignon, N., Isaac, P., Alvarez, H., Amoroso, M. J. & Ferrero, M. A. Enhanced polyaromatic hydrocarbon degradation by adapted cultures of actinomycete strains. *J. Basic Microbiol.* **54**, 1288–1294 (2014).
30. Fischer, M. S. et al. Pyrolyzed substrates induce aromatic compound metabolism in the post-fire fungus, *Pyronema domesticum*. *Front. Microbiol.* **12**, 729289 (2021).
31. Arora, P. K. & Sharma, A. New metabolic pathway for degradation of 2-nitrobenzoate by *Arthrobacter* sp. SPG. *Front. Microbiol.* **6:551**, 1–6 (2015).
32. Ren, L. et al. Insight into metabolic versatility of an aromatic compounds-degrading *Arthrobacter* sp. YC-RL1. *Front. Microbiol.* **9:2438**, 1–15 (2018).
33. Cobo-Díaz, J. F. et al. Metagenomic assessment of the potential microbial nitrogen pathways in the rhizosphere of a mediterranean forest after a wildfire. *Microb. Ecol.* **69**, 895–904 (2015).
34. Dove, N. C., Taş, N. & Hart, S. C. Ecological and genomic responses of soil microbiomes to high-severity wildfire: linking community assembly to functional potential. *ISME J.* https://doi.org/10.1038/s41396-022-01232-9 (2022).
35. Adkins, J., Docherty, K. M., Gutknecht, J. L. M. & Miesel, J. R. How do soil microbial communities respond to fire in the intermediate term? Investigating direct and indirect effects associated with fire occurrence and burn severity. *Sci. Total Environ.* **745**, 140957 (2020).
36. Newton, G. L., Buchmeier, N. & Fahey, R. C. Biosynthesis and functions of mycothiol, the unique protective thiol of Actinobacteria. *Microbiol. Mol. Biol. Rev.* **72**, 471–494 (2008).
37. Reina-Bueno, M. et al. Role of trehalose in heat and desiccation tolerance in the soil bacterium *Rhizobium etli*. *BMC Microbiol.* **12**, 207 (2012).
38. Schimel, J. P. Life in dry soils: effects of drought on soil microbial communities and processes. *Annu. Rev. Ecol. Evol. Syst.* **49**, 409–432 (2018).
39. Musto, H. et al. Correlations between genomic GC levels and optimal growth temperatures in prokaryotes. *FEBS Lett.* **573**, 73–77 (2004).
40. Yakovchuk, P. Base-stacking and base-pairing contributions into thermal stability of the DNA double helix. *Nucleic Acids Res.* **34**, 564–574 (2006).
41. Mooshammer, M. et al. Decoupling of microbial carbon, nitrogen, and phosphorus cycling in response to extreme temperature events. *Sci. Adv.* **3**, e1602781 (2017).
42. Weissman, J. L., Hou, S. & Fuhrman, J. A. Estimating maximal microbial growth rates from cultures, metagenomes, and single cells via codon usage patterns. *Proc. Natl Acad. Sci. USA* **118**, 1–10 e2016810118 (2020).
43. Long, A. M., Hou, S., Ignacio-Espinoza, J. C. & Fuhrman, J. A. Benchmarking microbial growth rate predictions from metagenomes. *ISME J.* **15**, 183–195 (2021).
44. Karlin, S., Mrázek, J., Campbell, A. & Kaiser, D. Characterizations of highly expressed genes of four fast-growing bacteria. *J. Bacteriol.* **183**, 5025–5040 (2001).
45. Scott, M., Gunderson, C. W., Mateescu, E. M., Zhang, Z. & Hwa, T. Interdependence of cell growth and gene expression: origins and consequences. *Science* **330**, 1099–1102 (2010).
46. Faria, S. R. et al. Wildfire-induced alterations of topsoil organic matter and their recovery in Mediterranean eucalypt stands detected with biogeochemical markers. *Eur. J. Soil Sci.* **66**, 699–713 (2015).

47. Chen, H., Rhoades, C. C. & Chow, A. T. Characteristics of soil organic matter 14 years after a wildfire: a pyrolysis-gas-chromatography mass spectrometry (Py-GC-MS) study. *J. Anal. Appl. Pyrolysis* **152**, 104922 (2020).
48. Knicker, H. Pyrogenic organic matter in soil: its origin and occurrence, its chemistry and survival in soil environments. *Quat. Int.* **243**, 251–263 (2011).
49. Bahureksa, W. et al. Nitrogen enrichment during soil organic matter burning and molecular evidence of Maillard reactions. *Environ. Sci. Technol.* https://doi.org/10.1021/acs.est.1c06745 (2022).
50. Boye, K. et al. Thermodynamically controlled preservation of organic carbon in floodplains. *Nat. Geosci.* **10**, 415–419 (2017).
51. LaRowe, D. E. & Van Cappellen, P. Degradation of natural organic matter: a thermodynamic analysis. *Geochim. Cosmochim. Acta* **75**, 2030–2042 (2011).
52. Fuchs, G., Boll, M. & Heider, J. Microbial degradation of aromatic compounds – from one strategy to four. *Nat. Rev. Microbiol.* **9**, 803–816 (2011).
53. Pingree, M. R. A. & DeLuca, T. H. Function of wildfire-deposited pyrogenic carbon in terrestrial ecosystems. *Front. Environ. Sci.* https://doi.org/10.3389/fenvs.2017.00053 (2017).
54. Trubl, G. et al. Soil viruses are underexplored players in ecosystem carbon processing. *mSystems* **3**, 1–21 e00076-18 (2018).
55. Ahlgren, N. A., Ren, J., Lu, Y. Y., Fuhrman, J. A. & Sun, F. Alignment-free d_2^* oligonucleotide frequency dissimilarity measure improves prediction of hosts from metagenomically-derived viral sequences. *Nucleic Acids Res.* **45**, 39–53 (2017).
56. Kuzyakov, Y. & Mason-Jones, K. Viruses in soil: nano-scale undead drivers of microbial life, biogeochemical turnover and ecosystem functions. *Soil Biol. Biochem.* **127**, 305–317 (2018).
57. Knowles, B. et al. Lytic to temperate switching of viral communities. *Nature* **531**, 466–470 (2016).
58. Hewelke, E. et al. Soil functional responses to natural ecosystem restoration of a pine forest peucedano-pinetum after a fire. *Forests* **11**, 286 (2020).
59. Mahoney, D. P. & LaFavre, J. S. *Coniochaeta extramundana*, with a synopsis of other *Coniochaeta* species. *Mycologia* **73**, 931–952 (1981).
60. Yang, T. et al. Distinct fungal successional trajectories following wildfire between soil horizons in a cold-temperate forest. *New Phytol.* **227**, 572–587 (2020).
61. Steindorff, A. S. et al. Comparative genomics of pyrophilous fungi reveals a link between fire events and developmental genes. *Environ. Microbiol.* **23**, 99–109 (2021).
62. Viswanath, B., Rajesh, B., Janardhan, A., Kumar, A. P. & Narasimha, G. Fungal laccases and their applications in bioremediation. *Enzyme Res.* **2014**, 1–21 163242 (2014).
63. Bouskill, N. J., Mekonnen, Z., Zhu, Q., Grant, R. & Riley, W. J. Microbial contribution to post-fire tundra ecosystem recovery over the 21st century. *Commun. Earth Environ.* **3**, 26 (2022).
64. Yeager, C. M., Northup, D. E., Grow, C. C., Barns, S. M. & Kuske, C. R. Changes in nitrogen-fixing and ammonia-oxidizing bacterial communities in soil of a mixed conifer forest after wildfire. *Appl. Environ. Microbiol.* **71**, 2713–2722 (2005).
65. Ward, N. L. et al. Three genomes from the Phylum Acidobacteria provide insight into the lifestyles of these microorganisms in soils. *Appl. Environ. Microbiol.* **75**, 2046–2056 (2009).
66. García-Fraile, P., Benada, O., Cajthaml, T., Baldrian, P. & Lladó, S. *Terracidiphilus gabretensis* gen. nov., sp. nov., an abundant and active forest soil acidobacterium important in organic matter transformation. *Appl. Environ. Microbiol.* **82**, 560–569 (2016).
67. Eichorst, S. A., Kuske, C. R. & Schmidt, T. M. Influence of plant polymers on the distribution and cultivation of bacteria in the Phylum Acidobacteria. *Appl. Environ. Microbiol.* **77**, 586–596 (2011).
68. Banerjee, S. et al. Network analysis reveals functional redundancy and keystone taxa amongst bacterial and fungal communities during organic matter decomposition in an arable soil. *Soil Biol. Biochem.* **97**, 188–198 (2016).
69. Costa, O. Y. A., Raaijmakers, J. M. & Kuramae, E. E. Microbial extracellular polymeric substances: ecological function and impact on soil aggregation. *Front. Microbiol.* **9**, 1–14 (2018).
70. Smith, S. E. & Read, D. Mycorrhizal symbiosis. *Soil Sci.* **137**, 204 (1984).
71. Douglas, R. B., Parker, V. T. & Cullings, K. W. Belowground ectomycorrhizal community structure of mature lodgepole pine and mixed conifer stands in Yellowstone National Park. *For. Ecol. Manage.* **208**, 303–317 (2005).
72. Anthony, M. A. et al. Forest tree growth is linked to mycorrhizal fungal composition and function across Europe. *ISME J.* https://doi.org/10.1038/s41396-021-01159-7 (2022).
73. Marx, D. H., Bryan, W. C. & Cordell, C. E. Survival and growth of pine seedlings with *Pisolithus* ectomycorrhizae after two years on reforestation sites in North Carolina and Florida. *For. Science.* **23**, 363–373 (1977).
74. Franco, A. R., Sousa, N. R., Ramos, M. A., Oliveira, R. S. & Castro, P. M. L. Diversity and persistence of ectomycorrhizal fungi and their effect on nursery-inoculated *Pinus pinaster* in a post-fire plantation in Northern Portugal. *Microb. Ecol.* **68**, 761–772 (2014).
75. Kipfmueller, K. F. & Baker, W. L. A fire history of a subalpine forest in south-eastern Wyoming, USA. *J. Biogeogr.* **27**, 71–85 (2000).
76. Key, C. H. & Benson, N. C. *Landscape Assessment (LA) Sampling and Analysis Methods* General Techical Report (USDA Forest Service, 2006).
77. Parson, A., Robichaud, P. R., Lewis, S. A., Napper, C. & Clark, J. T. *Field Guide for Mapping Post-fire Soil Burn Severity* General Technical Report (USDA Forest Service, 2010); https://doi.org/10.2737/RMRS-GTR-243
78. Miesel, J. R., Hockaday, W. C., Kolka, R. K. & Townsend, P. A. Soil organic matter composition and quality across fire severity gradients in coniferous and deciduous forests of the southern boreal region. *J. Geophys. Res. Biogeosci.* **120**, 1124–1141 (2015).
79. Bundy, L. G. & Meisinger, J. J., Weaver, R. W., Angle, S., Bottomley, P., Bezdicek, D., Smith, S., Tabatabai, A., Wollum, A. (Eds.) in *Methods of Soil Analysis: Part 2 Microbiological and Biochemical Properties* 951–984 (Macmillan, 2018). https://doi.org/10.2136/sssabookser5.2.c41
80. McDowell, W. H. et al. A comparison of methods to determine the biodegradable dissolved organic carbon from different terrestrial sources. *Soil Biol. Biochem.* **38**, 1933–1942 (2006).
81. Thomas, G. W., Sparks, D. L., Page, A. L., Helmke, P. A., Loeppert, R. H., Soltanpour, P. N., Tabatabai, M. A., Johnston, C. T., Sumner, M. E. (Eds.) in *Methods of Soil Analysis: Part 3 Chemical Methods*, **5.3** 475–490 (1996).
82. Dittmar, T., Koch, B., Hertkorn, N. & Kattner, G. A simple and efficient method for the solid-phase extraction of dissolved organic matter (SPE-DOM) from seawater. *Limnol. Oceanogr. Methods* **6**, 230–235 (2008).
83. Tolić, N. et al. Formularity: software for automated formula assignment of natural and other organic matter from ultrahigh-resolution mass spectra. *Anal. Chem.* **89**, 12659–12665 (2017).
84. Bramer, L. M. et al. ftmsRanalysis: an R package for exploratory data analysis and interactive visualization of FT-MS data. *PLoS Comput. Biol.* **16**, e1007654 (2020).
85. Caporaso, J. G. et al. Ultra-high-throughput microbial community analysis on the Illumina HiSeq and MiSeq platforms. *ISME J.* **6**, 1621–1624 (2012).
86. Quast, C. et al. The SILVA ribosomal RNA gene database project: improved data processing and web-based tools. *Nucleic Acids Res.* **41**, D590–D596 (2012).
87. Kõljalg, U. et al. UNITE: a database providing web-based methods for the molecular identification of ectomycorrhizal fungi. *New Phytol.* **166**, 1063–1068 (2005).
88. Bolyen, E. et al. Reproducible, interactive, scalable and extensible microbiome data science using QIIME 2. *Nat. Biotechnol.* **37**, 852–857 (2019).
89. Callahan, B. J. et al. DADA2: high-resolution sample inference from Illumina amplicon data. *Nat. Methods* **13**, 581–583 (2016).
90. Nguyen, N. H. et al. FUNGuild: an open annotation tool for parsing fungal community datasets by ecological guild. *Fungal Ecol.* **20**, 241–248 (2016).
91. R Core Team. R: A Language and Environment for Statistical Computing (R Foundation for Statistical Computing, 2021).
92. Oksanen, J. et al. (2020). vegan: Community Ecology Package. R package version 2.5-7. https://CRAN.R-project.org/package=vegan
93. McMurdie, P. J. & Holmes, S. phyloseq: an R package for reproducible interactive analysis and graphics of microbiome census data. *PLoS ONE* **8**, e61217 (2013).
94. Segata, N. et al. Metagenomic biomarker discovery and explanation. *Genome Biol.* **12**, R60 (2011).
95. Joshi, N. & Fass, J. Sickle: A Sliding-window, Adaptive, Quality-based Trimming Tool for Fastq Files, v1.33 (2011).
96. Li, D., Liu, C.-M., Luo, R., Sadakane, K. & Lam, T.-W. MEGAHIT: an ultra-fast single-node solution for large and complex metagenomics assembly via succinct de Bruijn graph. *Bioinformatics* **31**, 1674–1676 (2015).
97. Kang, D. D. et al. MetaBAT 2: an adaptive binning algorithm for robust and efficient genome reconstruction from metagenome assemblies. *PeerJ* **7**, e7359 (2019).
98. Parks, D. H., Imelfort, M., Skennerton, C. T., Hugenholtz, P. & Tyson, G. W. CheckM: assessing the quality of microbial genomes recovered from isolates, single cells, and metagenomes. *Genome Res.* **25**, 1043–1055 (2015).
99. Chaumeil, P.-A., Mussig, A. J., Hugenholtz, P. & Parks, D. H. GTDB-Tk: a toolkit to classify genomes with the Genome Taxonomy Database. *Bioinformatics* **36**, 1925–1927 (2019).
100. Olm, M. R., Brown, C. T., Brooks, B. & Banfield, J. F. dRep: a tool for fast and accurate genomic comparisons that enables improved genome recovery from metagenomes through de-replication. *ISME J.* **11**, 2864–2868 (2017).
101. Bowers, R. M. et al. Minimum information about a single amplified genome (MISAG) and a metagenome-assembled genome (MIMAG) of bacteria and archaea. *Nat. Biotechnol.* **35**, 725–731 (2017).
102. Emms, D. M. & Kelly, S. OrthoFinder: phylogenetic orthology inference for comparative genomics. *Genome Biol.* **20**, 238 (2019).

103. Katoh, K. MAFFT: a novel method for rapid multiple sequence alignment based on fast Fourier transform. *Nucleic Acids Res.* **30**, 3059–3066 (2002).
104. Capella-Gutierrez, S., Silla-Martinez, J. M. & Gabaldon, T. trimAl: a tool for automated alignment trimming in large-scale phylogenetic analyses. *Bioinformatics* **25**, 1972–1973 (2009).
105. Nguyen, L. T., Schmidt, H. A., Von Haeseler, A. & Minh, B. Q. IQ-TREE: a fast and effective stochastic algorithm for estimating maximum-likelihood phylogenies. *Mol. Biol. Evol.* **32**, 268–274 (2015).
106. Seppey, M., Manni, M. & Zdobnov, E. M., Walker, J. M. (Ed.) BUSCO: assessing genome assembly and annotation completeness. *Gene prediction* 227–245 (Humana Press, 2019). https://doi.org/10.1007/978-1-4939-9173-0_14
107. Parra, G., Bradnam, K. & Korf, I. CEGMA: a pipeline to accurately annotate core genes in eukaryotic genomes. *Bioinformatics* **23**, 1061–1067 (2007).
108. Bushmanova, E., Antipov, D., Lapidus, A. & Prjibelski, A. D. RnaSPAdes: a de novo transcriptome assembler and its application to RNA-Seq data. *Gigascience* **8**, 1–13 (2019).
109. Grigoriev, I. V. et al. MycoCosm portal: gearing up for 1000 fungal genomes. *Nucleic Acids Res.* **42**, 699–704 (2014).
110. Shaffer, M. et al. DRAM for distilling microbial metabolism to automate the curation of microbiome function. *Nucleic Acids Res.* **48**, 8883–8900 (2020).
111. Eddy, S. R. Accelerated profile HMM searches. *PLoS Comput. Biol.* **7**, e1002195 (2011).
112. Aramaki, T. et al. KofamKOALA: KEGG ortholog assignment based on profile HMM and adaptive score threshold. *Bioinformatics* **36**, 2251–2252 (2020).
113. Anders, S., Pyl, P. T. & Huber, W. HTSeq–a Python framework to work with high-throughput sequencing data. *Bioinformatics* **31**, 166–169 (2015).
114. Love, M. I., Huber, W. & Anders, S. Moderated estimation of fold change and dispersion for RNA-seq data with DESeq2. *Genome Biol.* **15**, 550 (2014).
115. Smid, M. et al. Gene length corrected trimmed mean of M-values (GeTMM) processing of RNA-seq data performs similarly in intersample analyses while improving intrasample comparisons. *BMC Bioinformatics* **19**, 236 (2018).
116. Robinson, M. D., McCarthy, D. J. & Smyth, G. K. edgeR: a Bioconductor package for differential expression analysis of digital gene expression data. *Bioinformatics* **26**, 139–140 (2010).
117. Guo, J. et al. VirSorter2: a multi-classifier, expert-guided approach to detect diverse DNA and RNA viruses. *Microbiome* **9**, 37 (2021).
118. Nayfach, S. et al. CheckV assesses the quality and completeness of metagenome-assembled viral genomes. *Nat. Biotechnol.* **39**, 578–585 (2021).
119. Guo, J., Vik, D., Pratama, A. A., Roux, S. & Sullivan, M. B. Viral Sequence Identification SOP with VirSorter2 (2021); protocols.io. https://doi.org/10.17504/protocols.io.btv8nn9w
120. Bland, C. et al. CRISPR recognition tool (CRT): a tool for automatic detection of clustered regularly interspaced palindromic repeats. *BMC Bioinformatics* **8**, 209 (2007).
121. Skennerton, C. T., Imelfort, M. & Tyson, G. W. Crass: identification and reconstruction of CRISPR from unassembled metagenomic data. *Nucleic Acids Res.* **41**, e105 (2013).

Acknowledgements

This work was supported through a USDA NIFA award (2021-67019-34608) to M.J.W. FTICR-MS analyses were performed under the Facilities Integrating Collaborations for User Science (FICUS) initiative and used resources at the Environmental Molecular Sciences Laboratory (proposal ID 49615), which is a DOE Office of Science User Facility. This facility is sponsored by the Office of Biological and Environmental Research and operated under contract number DE-AC05-76RL01830. Metagenomic and metatranscriptomic sequencing was performed at the University of Colorado Cancer Center's Genomics Shared Resource, which is supported by the Cancer Center Support Grant P30CA046934. This work utilized resources from the University of Colorado Boulder Research Computing Group, which is supported by the National Science Foundation (awards ACI-1532235 and ACI-1532236), the University of Colorado Boulder and Colorado State University. The work conducted by the US Department of Energy Joint Genome Institute, a DOE Office of Science User Facility, is supported by the Office of Science of the US Department of Energy under Contract No. DE-AC02-05CH11231. We thank F. Pulido-Chavez for help with processing the ITS amplicon sequencing data, and J. Emerson and S. Geonczy for discussions on viral analyses.

Author contributions

A.R.N., C.C.R. and M.J.W. designed the field sampling and downstream analyses. A.R.N., K.K.A. and M.J.W. performed field sampling, while A.R.N. and R.A.D. performed laboratory sample processing. A.R.N. and A.B.N. led the microbial analyses, with assistance from S.J.M., A.S.S., I.V.G. and A.S. for fungal genomics. H.K.R., T.B., R.K.C. and R.B.Y. contributed to high-resolution carbon measurements and analyses. T.S.F. performed bulk soil geochemistry measurements. A.R.N., C.C.R. and M.J.W. wrote the manuscript, with assistance and input from all co-authors.

Competing interests

The authors declare no competing interests.

Additional information

Extended data is available for this paper at https://doi.org/10.1038/s41564-022-01203-y.

Supplementary information The online version contains supplementary material available at https://doi.org/10.1038/s41564-022-01203-y.

Correspondence and requests for materials should be addressed to Michael J. Wilkins.

Peer review information *Nature Microbiology* thanks Janet Jansson and the other, anonymous, reviewer(s) for their contribution to the peer review of this work. Peer reviewer reports are available.

Reprints and permissions information is available at www.nature.com/reprints.

Publisher's note Springer Nature remains neutral with regard to jurisdictional claims in published maps and institutional affiliations.

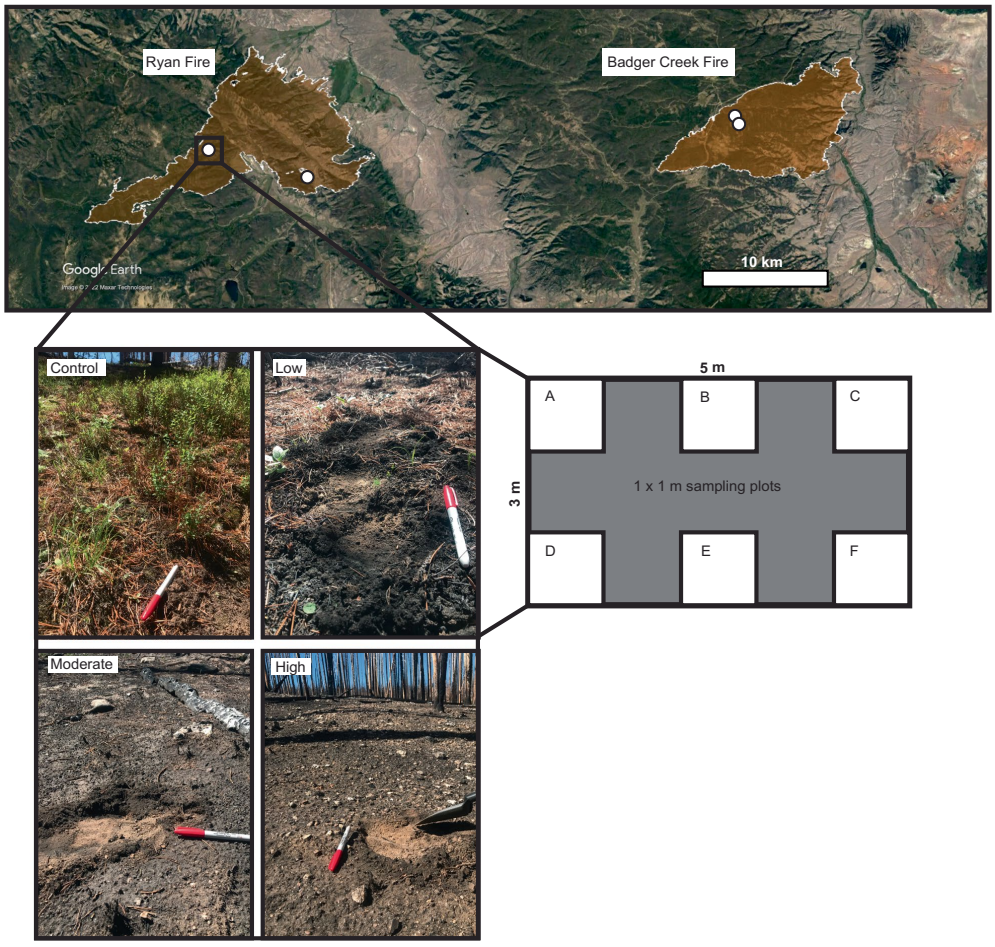

Extended Data Fig. 1 | Overview of field sampling design. There were four replicate burn severity gradients (two at Ryan Fire and two at Badger Creek Fire); six subsamples were collected in each burn condition at each gradient.

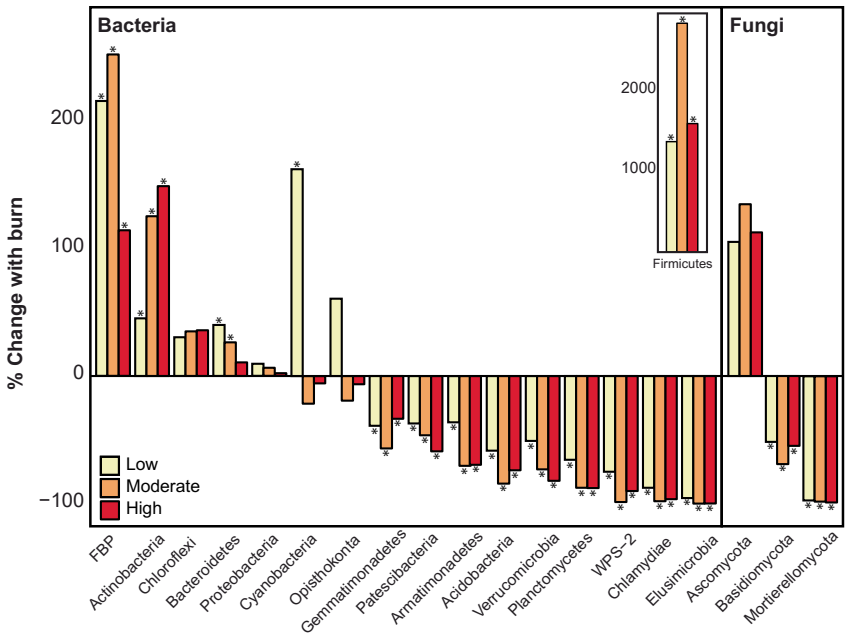

Extended Data Fig. 2 | Shifting soil microbiome composition with wildfire burn severity. The percent change in relative abundance from control to low, moderate, and high severity in surface soil of each main bacterial and fungal phylum. Phyla with relative abundance less than 0.5% were discarded for this analysis. Note that although the *Firmicutes* have the largest increase with burn (inset) their overall relative abundance in burned samples is still low relative to *Actinobacteria* (1.21% vs 25.6% relative abundance). Phyla with significant (one-sided pairwise t-test; $p < 0.05$) differences in relative abundance between the unburned and burned conditions are denoted with an asterisk.

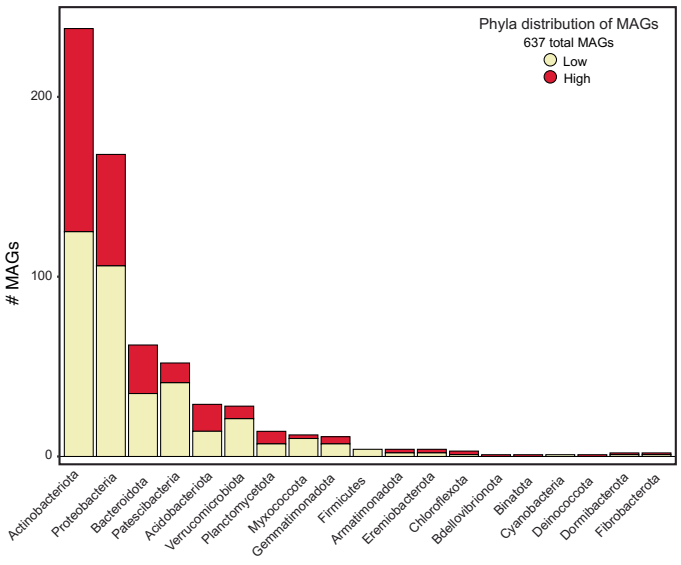

Extended Data Fig. 3 | Phyla distribution of bacterial metagenome-assembled genomes (MAGs). Phyla distribution of the 637 medium- and high-quality MAGs (> 50% completion, <10% contamination) from burned surface and deep soils.

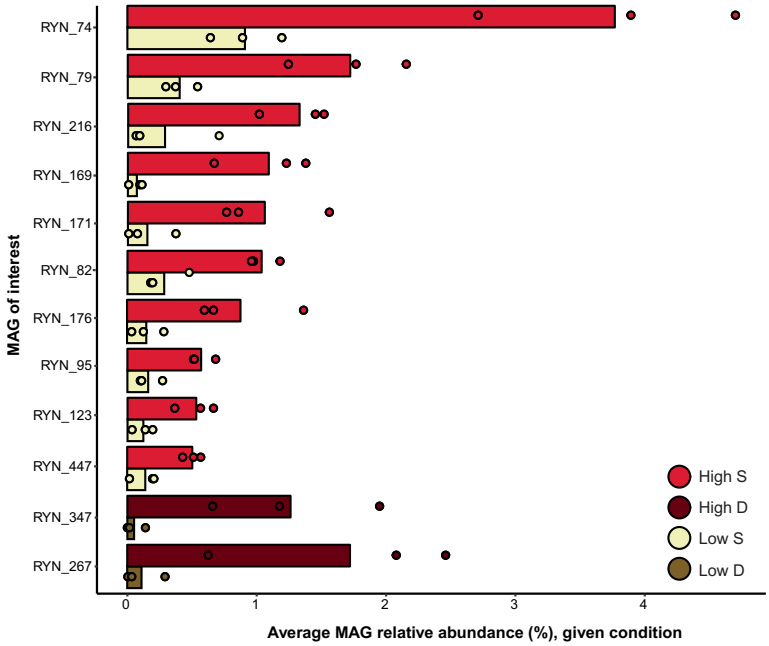

Extended Data Fig. 4 | Average relative abundance of MAGs of interest across severities. The relative abundances in Low and high severity of MAGs that are significantly enriched (one-sided pairwise t-test; $p < 0.05$; p-values in Supplementary Data 2) in High S vs. Low S (7 MAGs) or High D vs. Low D (2 MAGs) that match the designated criteria for discussion in the text (average relative abundance > 0.05% and standard deviation less than average relative abundance). Overlayed points show relative abundance of MAGs in each samples ($n = 3$ for each condition).

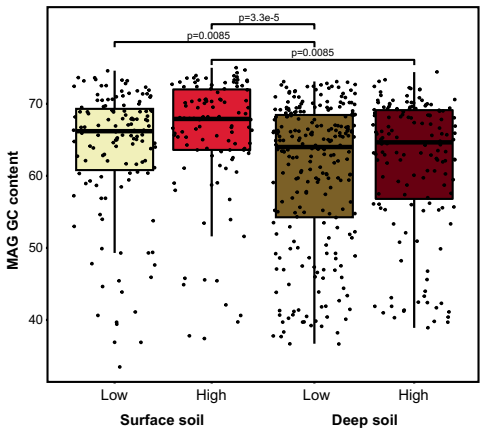

Extended Data Fig. 5 | MAG GC content higher in MAGs reconstructed from high severity-impacted surface soils. GC content of MAGs reconstructed from each condition. P-values are indicated between conditions if there are significant differences (one-sided pairwise t-test, $p < 0.05$). The lower and upper hinges of the boxplots represent the 25th and 75th percentile and the middle line is the median. The upper whisker extends to the median plus 1.5x interquartile range and the lower whisker extends to the median minus 1.5x interquartile range. Jittered points represent individual MAGs (n = 131 reconstructed from Low S samples, n = 111 from High S, n = 247 from Low D, n = 148 from High D).

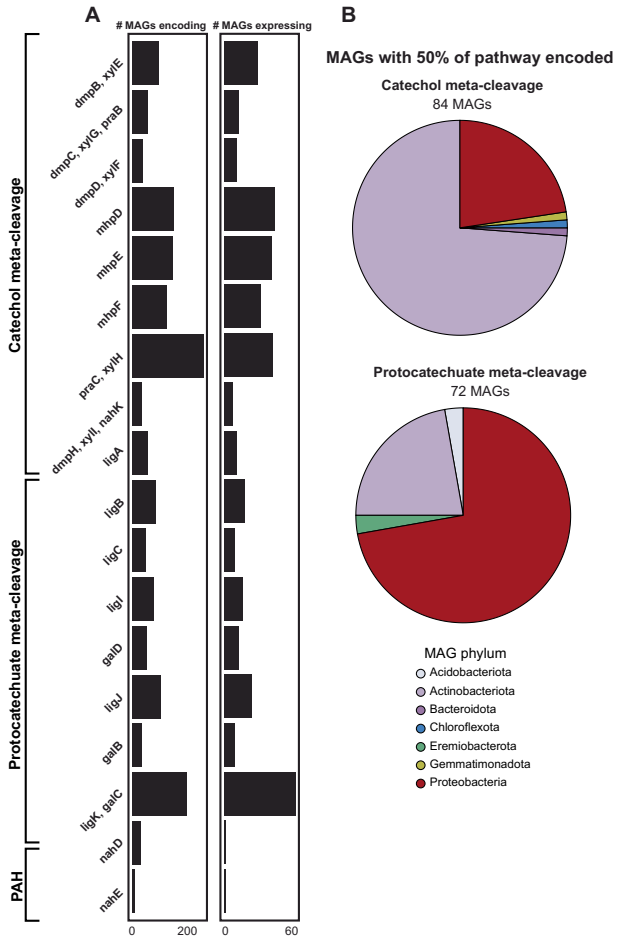

Extended Data Fig. 6 | Widespread potential and expression of catechol and protocatechuate meta-cleavage in MAG dataset. (**a**) Number of MAGs encoding and expressing each gene of the catechol and protocatechuate meta-cleavage pathways. (**b**) Phyla distribution of MAGs encoding 50% of either pathway.

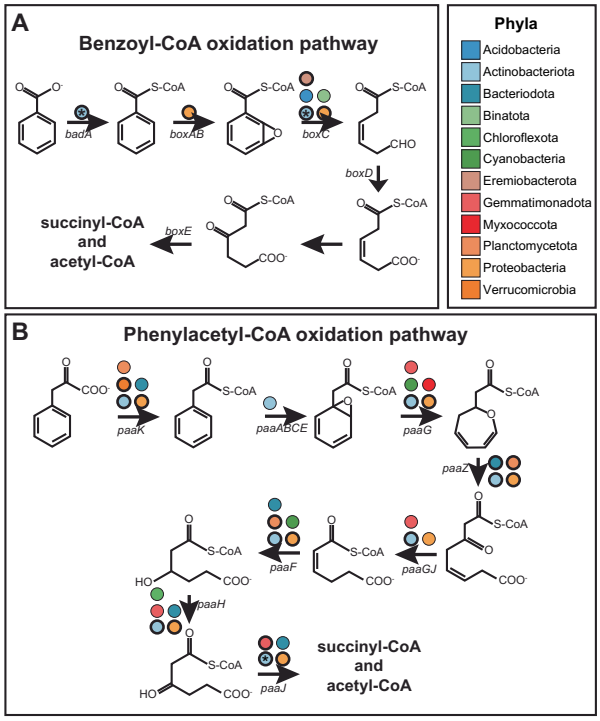

Extended Data Fig. 7 | Genomic evidence of other aerobic aromatic C degradation pathways. The benzoyl-CoA oxidation pathway (**a**) and phenylacetyl-CoA oxidation pathway (**b**) with overlaid gene names and whether there was encoded or expressed evidence of these genes. Colored circles indicate whether a MAG from that phyla encoded that gene, bolded circles indicate that metatranscriptomic reads mapped to the gene, and asterisks indicate the gene was being highly expressed in any given condition.